DEVELOPMENT OF A GENERAL DYNAMIC HYSTERETIC LIGHT-FRAME STRUCTURE MODEL AND STUDY ON THE TORSIONAL BEHAVIOR OF OPEN-FRONT LIGHT-FRAME STRUCTURES

By

JIAN XU

A dissertation submitted in partial fulfillment of
the requirements for the degree of

DOCTOR OF PHILOSOPHY IN CIVIL ENGINEERIING

WASHINGTON STATE UNIVERSITY
Department of Civil & Environmental Engineering

DECEMBER 2006

To the Faculty of Washington State University:

The members of the Committee appointed to examine the dissertation of JIAN XU find it satisfactory and recommend that it be accepted.

Chair

ACKNOWLEDGMENT

My advisor, committee chair, Dr. J. Daniel Dolan, made all research purposes clear, had all research tools and testing data available, and made everything easier for me. Without his guidance and encouragement, this dissertation would not have been possible. I am especially thankful for his lenience and patience. Thank you for being such a wonderful advisor.

Further acknowledgement is extended to Dr. William F. Cofer, Dr. David Pollock, Dr. David McLean, and Kelly Cobeen for serving on my committee and providing warmhearted support. I also thank all the persons that gave me help and encouragement during this exceptional research journey.

I am especially indebted to my parents and my wife for their abiding love. This dissertation is dedicated to them.

Development of a General Dynamic Hysteretic Light-frame Structure Model and Study on the Torsional Behavior of Open-front Light-frame Structures

Abstract

by Jian Xu, Ph.D.
Washington State University
December 2006

Chair: James D. Dolan

Open-front light-frame structures may have significant torsional problems when attacked by intense earthquakes. Full-size testing is a good tool to be employed to understand their performance under significant seismic events, but it is limited due to the high expense. So, a model, which is able to accurately represent the hysteretic dynamic performance of light-frame structural systems under lateral loads is in demand.

All previous testing showed that the hysteretic behavior of nailed wood joints governs the response of many wood systems when subjected to lateral loadings. Unfortunately, commercially available software does not have an appropriate hysteretic element for a nailed wood joint, and the accuracy and versatility of previously developed nail joint elements are not satisfactory. A general hysteretic model, BWBN, was modified to represent the hysteretic behavior of a nailed joint. Based on test data, suitable parameters for different joint configurations can be estimated using a Genetic Algorithm. This model was embedded in ABAQUS/Standard (Version 6.5), as a user-defined element, which accounted for the coupling property of the nail joint action. Detailed shear walls were simulated and analyzed, and the results agreed well with the test data.

With some modifications on the nailed wood joint model, a super shear wall model was developed, which describes the behavior of a whole shear wall line. This super shear wall model consists of two diagonal hysteretic springs, along with the frame members in the wall, and can predict racking and overturning behavior of shear walls at the same time. Using this model, a 3-D 2-story building model, which was developed to simulate the building tested in the CUREE shake table test (Fischer et al. 2001), was analyzed in ABAQUS/Standard. Comparison of the results validated the accuracy and efficiency of this super shear wall model.

Using this super shear wall model, a parametric study was conducted to benchmark current design methods. The parameters included floor or roof diaphragm aspect ratios, open-front ratios, and possible inclusion of gypsum partition walls. The study shows that the elastic torsional design method is not satisfactory for open-front light-frame structures, and design method improvement comments were made accordingly.

TABLE OF CONTENTS

Page

LIST OF TABLES

LIST OF FIGURES

NOTATION

$BWBN$ = a hysteretic model named after the four developers' last name initials;

c = linear viscous damping coefficient;

e_r = eccentricity between mass center and stiffness center;

F = nail joint force vector in the global coordinate;

F' = nail joint force vector in the local coordinate of Oriented Spring Pair Model;

$F(t)$ = time-dependant forcing function;

F_u = nail joint force along the moving trajectory;

F_v = nail joint force perpendicular to the moving trajectory;

$f(t)$ = mass-normalized forcing function;

g = acceleration of gravity (32.2 ft/s^2 or 9.8 m/s^2);

H = restoring force in the hysteretic spring;

$h(z)$ = pinching function;

[K] = nail joint stiffness matrix in the global coordinate;

[K'] = nail joint stiffness matrix in the local coordinate of Oriented Spring Pair Model;

K_0 = initial lateral stiffness of structure;

K_{11}, K_{12}, K_{22} = terms in the nail joint stiffness matrix in the global coordinate;

K_u = tangent stiffness of the nonlinear spring along the moving trajectory;

K_v = tangent stiffness of the nonlinear spring perpendicular to the moving trajectory;

k_t = total tangent stiffness of the elastic and hysteretic springs;

L = building dimension in the direction perpendicular to ground motion;

m = mass;

M_Dis = the maximum positive displacement (when u>0) or absolute value of the minimum displacement (when u≤0)

Max_Dis = the maximum positive displacement;

Min_Dis = the minimum displacement;

n = hysteresis shape parameters (controls curve smoothness)

p = rate of change of ζ_1;

q = fraction of ultimate hysteretic strength, z_u, where pinching occurs;

R = total restoring force from both the linear and hysteretic springs;

r = mass-normalized restoring force;

ratio = ratio of the displacement at unloading position to the experienced maximum displacement in the same direction;

S = restoring force in the linear spring;

sgn(.) = the signum function;

[T] = stiffness transform matrix

T = torsion moment;

u = relative displacement of the mass to the base;

$\dot{u}$ = relative velocity of the mass to the base;

$\ddot{u}$ = relative acceleration of the mass to the base;

$V_{//}$ = total parallel design resistance;

$V_{\perp}$ = imposed load in perpendicular walls;

W = building dimension in the direction parallel to ground motion;

z = hysteretic displacement;

z_u = ultimate hysteretic displacement;

α = rigidity ratio;

β = hysteresis shape parameters

γ = hysteresis shape parameters

δ_η = stiffness degradation rate;

δ_ν = strength degradation rate;

δ_ψ = rate of change of ζ_2;

ε = hysteretic energy dissipation;

ζ_1 = pinching parameter controls the pinching stiffness ($0.0<\zeta_1<1.0$);

ζ_{10} = basic magnitude of ζ_1;

ζ_2 = pinching parameter controls the rate of change of the slope, *dz/du*;

η = stiffness degradation parameters;

θ = angle between the nail joint moving trajectory and horizontal direction;

θ_{SW} = angle between super shear wall hysteretic springs and horizontal direction;

λ = parameter that controls the rate of change of ζ_2 as ζ_1 changes;

ν = strength degradation parameters;

ξ = structural elastic damping ratio (ξ=1%);

ξ_0 = viscous damping ratio;

ψ_0 = basic magnitude of ζ_2;

ω = pseudo-natural frequency of the non-linear system, ω^2 is mass-normalized stiffness;

ω_1 = circular frequency of the structural fundamental vibration mode;

ω_{xi} = value of parameter, ω of the i^{th} shear wall parallel to the ground motion direction;

ω_{yi} = value of parameter, ω of the i^{th} shear wall perpendicular to the ground motion direction;

To My Parents, Jiuying Liu & Xiangming Xu

To My Wife, Xiaohui Huang

Chapter 1
Introduction

1.1 General

In the past few decades, many severe earthquakes were recorded all around the world. The Northridge earthquake (USA, 1994) statistics include 56 dead, 25,000 dwellings uninhabitable, and $10 billion in damage. In the Chichi earthquake (Taiwan, 1999), the death toll surpassed 2,400 and more than 10,700 people were injured. Over 8,500 buildings were destroyed and another 6,200 were seriously damaged, a majority of which were reinforced concrete structures with poorly designed columns that failed at the first story. The Turkey (1999) and Pakistan earthquakes (2005) killed more than 80,000 people. The significant losses caused by these earthquakes have raised the public's concern about improving the engineering and reliability of structures.

Recently, research in the area of structural disaster resistance has changed from static to dynamic, from monotonic loading to reversed cyclic loading, and from element level to system level. These changes are due to the fact that the structural behavior under natural disasters is more dynamic based, and the structures behaved more as a whole system than as several separate parts. Connections between members and the structural configurations govern the structural behavior much more than the response of single members. Without a theoretical understanding of the real dynamic performance of the structure in ultimate situations, designs can be unsafe and even ridiculous.

Low-rise residential houses and small commercial buildings in North America are generally light-frame structures constructed using steel and/or wood-based materials.

Typically, frames are used to resist the vertical loading, and the roof, floors, and shear walls form the lateral force resisting system. The high strength-to-weight ratio of wood-based materials, the ductility of connectors, and the high redundancy of the system are three main reasons that light-frame structures perform well when subjected to seismic events.

1.2 Open Front Light-frame Structure

Post event damage reports show irregular structural configurations are likely contributors to the failure of a large number of buildings during earthquakes. Open front construction is a common plan irregular case.

Because of plan irregularity, open-front light-frame structures will suffer from torsion problems when subjected to major seismic events if not designed properly. The methodology used in the current codes for the structures with torsional irregularity is in the elastic domain, and the design requirements are not detailed enough. On the other hand, design in areas with significant seismic risk relies on inelastic response, which means that the assumptions of the elastic analysis are not valid. The displacement mode and distribution of lateral loads in shear walls of open front structures can be very different from those determined using elastic analysis. Besides, the displacement ductility demand on certain elements may be significantly larger than the demand imposed on the system as a whole. The elastic design methods can be unsafe and sometimes misleading.

1.3 Objectives

Full-size testing is a good tool to show the real performance of open-front light-frame structure systems under significant lateral loadings. However, it is not possible to test structures of all configurations. To better understand the behavior of open-front light-frame structures under significant lateral loadings, a numerical model, which can accurately predict the dynamic hysteretic performance of light-frame structures under lateral dynamic loads, is needed. Unfortunately, commercially available software does not have the appropriate elements which are able to accurately describe the hysteretic behavior of light-frame systems. The accuracy and versatility of the models developed and used in most available research tools are not satisfactory. So developing a more accurate and reliable model is one of the objectives of this study.

Using this developed model as a tool, a parametric study was completed to quantify the responses of open-front light-frame buildings under significant lateral loadings (the parameters include the open-front ratio or irregular degree, building aspect ratio, and the presence of nonstructural partition walls or not). Time history analysis was conducted on a series of models with different configurations. The curves describing structural behavior based on the parametric study are used as a reference to real design practice, and some design recommendations are made at the end.

1.4 Scope and Limitations

Although the model developed in this study is a general one that can be employed to represent many different kinds of structures with some parameter modifications, this study focuses on low-rise wood light-frame structures.

In this study, only the short-duration behavior is considered. Effects attributed to 'time effects' such as moisture content variations, as well as creep, weathering, or aging, are not considered.

The procedure of the research includes the following steps.

1. Modify BWBN (a mathematical model which used a series of differential equations to describe the hysteretic rules) to make it suitable for nailed wood joints and light-frame shear walls.
2. Employ an optimization method to estimate the parameters associated with relevant joint configurations.
3. Embed the nailed wood joint model into ABAQUS/Standard and simulate detailed shear wall models in ABAQUS.
4. Develop a super shear wall model (consists of frame members and a pair of diagonal hysteresis springs), which can also take overturning into account.
5. Simulate the 2-story full-scale building tested in UC, San Diego for CUREE with the super shear wall model and validate the proposed super shear wall model through the comparison of the experimental and simulation results.
6. Build a series of models with different aspect ratios and open-front ratios, and run nonlinear time history analysis. Then complete a parametric study on the torsional behavior of open-front light-frame structures subjected to lateral forces (the possible parameters include the open-front ratio or irregularity degree, building length-width ratio, and diaphragm rigidity, etc.).
7. Develop curves and tables based on the parametric study results, which can be used as a reference in real design practice.

Chapter 2
Background and Literature Review

2.1 Introduction

In a wood-frame structural system, shear wall is the most important lateral-resistant element. The ductility of a wood-frame shear wall is from the hysteretic behavior of nailed wood joints between sheathing panels and framing members. Many studies have been conducted on numerical simulation of the hysteretic behavior of nailed wood joints and shear walls. Some important researches were briefly introduced in this chapter.

2.2 Nailed Wood Joint

Hysteretic performance of nailed wood joints is quite complicated. It primarily depends on the nail material and manufacture, and the embedment property of the wood. Friction between nail and wood, and between wood members also affects the joint performance to some extent.

For decades, many researchers have conducted work to find a way to accurately describe the mechanical behavior of a nail joint. Based on the Takeda model, which was developed to model the hysteretic rule of reinforced concrete members under reversed lateral loading (briefly described in Loh et al 1990), Kivell et al. (1981) derived a hysteresis model suitable for moment resisting nailed timber joints. This model uses a pair of symmetric bi-linear paths as the backbone curve. The track between the maximum deflection on the positive backbone curve and that on the negative part is described with a tri-linear path. The end points of the three lines are defined by a cubic function that passes through the maximum deflections. This model was used to analyze the dynamic performance of two simple timber portal frames with nailed beam-to-column connections. Pinching could be represented in this model, however, the system degradation was not considered.

Polensek and Laursen (1984) developed a hysteresis model for nailed plywood-to-wood connections based on test data. The model is similar to that of Kivell et al. (1981). The difference is that a tri-linear curve is used as the backbone curve and the governing points on the tri-linear trace between positive maximum deflection and negative maximum deflection are obtained using a statistical fit of test data.

Instead of multiple-linear curves, Dolan (1989) derived a hysteresis model described by an exponential backbone curve and four unloading and reloading sections, which are defined by different exponential equations. The backbone curve equation was first developed by Foschi (1977). Dolan modified it to take strength degradation into account. The parameters used in this model are based on a statistical fit of test data.

Ceccotti and Vignoli (1990) developed a hysteresis model for moment-resisting semi-rigid wood joints that are normally used in glulam portal frames in Europe. The pinching and stiffness degradation are considered in this model, and the element was incorporated into the commercial non-linear dynamic analysis program DRAIN-2D.

Chui et al (1997, 1998) developed a finite-element model for nailed wood joints under cyclic load. Three types of elements are used in this model: a beam element to represent the nail, a spring element for embedment, and a linkage element for friction between nail and wood. The method developed by Dolan (1989) was employed to describe the embedment spring element.

Foschi (2000) represented the nail with a beam element and the embedment action between nail and wood with a nonlinear spring element. The embedment property is determined from test data. The gap between nail and wood is considered explicitly (i.e., the force will not be built in the spring between nail and wood until the deflection of the nail is beyond the gap size). This model ignored the friction between fastener and wood, and the withdrawal effect of the fastener, which are important for the nail joint performance under cyclic loading. He et al. (2001) modified and used this model in the modeling of three-dimensional timber light-frame buildings.

All these hysteresis models for nailed wood joints were derived from specific joint or system configurations and were expressed with either a complex set of force-history rules or limited empirical relations. To overcome these disadvantages, a general hysteresis model, which can simulate a wide variety of nailed wood joints, is needed.

2.3 Wood-frame Shear Wall

2.3.1 General

Wood-frame Shear Walls are mainly designed to resist in-plane lateral loads caused by wind or earthquakes. A typical wood-frame shear wall is built using wood framing members (studs, sill plates, and top plates) and sheathing panels (plywood or OSB panels, etc). The wood framing members form a stand on which the sheathing panels are attached by nails or other types of discrete fasteners. The framing members are used to resist vertical loads and the out-of-plane loading (e.g. the wind flowing perpendicular the wall face). The in plane lateral loads are resisted by the racking of the sheathing panels. Tests have shown that the most common failure mode of a shear wall under lateral loads is the tearing and pullout of the sheathing fasteners. On the other hand, the sheathing fasteners are also the source of the ductility of the shear wall. Basically, the performance of the sheathing fasteners controls the shear wall behavior.

Since shear walls are the most important component within the light-frame building system, modeling of shear walls is the most important part in modeling of the whole system. To simulate shear walls accurately and efficiently through the finite element method (FEM) is one of the main objectives of this study.

2.3.2 Previous Research on Wood-Frame Shear Walls

To understand the characteristics of shear wall performance better, large numbers of studies, including testing and modeling, have been completed. Some of the more recent studies will be described here.

Heine (1997) tested sixteen full-scale wall specimens using monotonic and sequential phased displacement (SPD) patterns. A total of five different wall configurations, five anchorage, and two loading conditions were used. All walls were 2.4 m (8 ft) high. Straight wall specimens were 12.2 m (40 feet) long, whereas specimens with return corner walls measured 3.7 m (12 ft) in length. He investigated the monotonic and cyclic response of light-frame wood shear walls with and without openings. The test results show that the amount of overturning restraint is positively correlated with ultimate capacity and elastic stiffness. The influence magnitude is related to the opening ratio of the shear walls (i.e., the bigger the opening, the more the stiffness and capacity improvement is affected). Furthermore, effects of overturning restraint in the form of tie-down anchors and corner segments on light-frame shear walls with and without door and window openings were quantified. He also found that, without overturning restraints, shear walls exhibit a pronounced rigid-body rotation arising from uplift and separation along the bottom plate. The main failure mode was sheathing and stud separation from the bottom plate.

Salenikovich (2000) studied the response of light-frame timber shear walls to lateral forces. He obtained performance characteristics of shear walls with various aspect ratios and overturning restraint via experimental testing and analytical modeling. Fifty-six light-frame timber shear walls with aspect ratios of 4:1, 2:1, 1:1, and 2:3 were tested. Overturning restraint conditions of engineered construction (walls were attached to the base through tie-down anchors and shear bolts) and conventional construction practices (walls were attached to the base through nails or shear bolts only) were investigated. To remove the influence of self-weight, the specimens were tested in a horizontal position with OSB sheathing on one side. The nail-edge distance across the top and bottom plates varied from 10 mm (3/8 in.) to 19 mm (3/4 in.). A mechanics-based model was advanced to predict the racking resistance of conventional multi-panel shear walls using simple formulae. The deflections of engineered and conventional shear walls were predicted using the energy method combined with empirical formulae to account for load deformation characteristics of sheathing-to-framing connections and overturning restraint.

The study prepared by McKee, et al. (1998) focused on the performance of perforated shear walls with narrow wall segments. The objective of this study was to understand the influence of the width of the full-height segments, the reduced base restraint and alternative framing methods on the performance of light-frame shear walls.

In this study, 7 light-frame shear wall specimens were tested. The first specimen was a fully sheathed one and was tied down at both ends with two hold-down anchors, which was used as a control. The rest of the walls were constructed with different opening ratios, different opening configurations, different base restraints, and different framing methods.

The test results validated a conservative capacity estimation for perforated shear wall method (Sugiyama and Matsumoto, 1994). An alternative prediction equation for shear load ratio was presented and was proved to be more accurate than the former one. The test data showed that a significant portion of the load was shared with the rest of the full-height wall segments because of the shear transfer through the sheathing above and below the openings. The tests showed that the initial stiffness was proportional to the sheathing area ratio. The truss plate reinforcement placed at wall corners and opening corners increased the initial stiffness, the ultimate capacity, and the energy dissipation capacity of the wall significantly. The strap wrapped over the header and top plate increased the ultimate capacity and the energy dissipation, and reduced the end stud's uplift significantly. The wall with wider segments (1219 mm, 4 ft) had a slightly greater ultimate capacity and initial stiffness than did that with narrower segments (610mm, 2 ft) (They had same opening ratio). However, the energy dissipation capacity of the former is much lower that the later. Results also show that the increased anchor bolt spacing had little effect on the specimen's stiffness and energy dissipation. All walls tested had similar failure characteristics. The initial loading was highly linear until the screws began to pull through the GWB. Racking of full height OSB panels was observed, while the OSB above and below openings acted as a rigid body. As failure progressed the nails failed along the bottom plate in the walls with openings. This failure was more prevalent in the wall section that had no hold-down anchor to resist overturning on the tension (uplift) side of the wall specimen.

Kochkin, et al. (2001) conducted another testing study, which focused on the performance of wood shear walls with corners. In this research, the researchers did some monotonic-loading tests on 11 wood shear wall specimens (20ft X 8ft), one of which was engineered (including hold-downs at both ends), and the others are perforated or non-perforated (fully sheathed) conventional ones (no hold-downs) with 2-foot or 4-foot corner return walls. The objectives of this research included: 1. Measuring the performance of conventional wood shear walls (no hold-downs) and comparing results with the data for engineered wood shear walls (including hold-downs). 2. Investigate the restraining effect of the return corner on the lateral response of conventional wood shear walls. 3. Examining the applicability of innovative design methods to conventional wood shear walls restrained against overturning by corner framing.

The conclusions drawn from this research included: The corner-restrained conventional walls have equivalent elastic stiffness as the engineered walls. Separation of the sheathing panel from the bottom plate near the corner and bending failure of the bottom plate were the typical failure modes for the bolted walls. Withdrawal of the bottom plate nails from the platform was the typical failure mode for the nailed walls. The failure of each wall was accompanied with an uplift failure of the return corner. The corners provided the uplift resistance through the nails along the bottom plate. The remaining sheathing nails of the corner panel showed little degradation. The walls with 4-foot corners approached or exceeded capacity of an engineered shear wall. However, the ductility of the conventional walls decreased compared with engineered ones because of the change of failure modes. The fully sheathed walls with the 4-foot corners reached higher capacities and showed larger ductility characteristics than the fully sheathed walls with the 2-foot corners. The perforated walls restrained with corners showed higher ductility as compared to fully sheathed walls. The corner width had little influence on the elastic stiffness. The Perforated Shear Wall (PSW) method considerably underestimated capacity of the perforated shear walls restrained with corner returns but estimated the stiffness well. The method proposed by Ni et al. (1998) provided more accurate results and is more suitable for the analysis of conventional shear walls. The equation showed that the ratio of the lateral load capacity of walls with partial uplift restraint to capacity of wall with full uplift restraint is inversely proportional to the wall aspect ratio, which means that the larger the wall aspect ratio is, the decrease in wall capacity caused by lack of uplift restraint is greater. The effect of the door openings was not considered in this study, which was thought to weaken the shear wall even more than windows do.

In accordance with the research of Ni and Karacabeyli (2000), a vertical load of 17.5 kN/m (1.2 kips/ft) on unrestrained walls was required to provide the same performance as the wall with hold-downs. However, vertical load of 4.38 kN/m (0.3 kips/ft), which counteracted 25% of the overturning moment, allowed the unrestrained wall to develop 80% of its full capacity and ultimate displacement (Validated for shear walls with aspect ratio of 1).

Toothman (2003) did a series of 1219 × 2438 mm (4 × 8 ft) light-frame shear walls with tie-downs and without tie-downs. The sheathing materials investigated included OSB, hardboard, fiberboard, and gypsum wallboard. This study obtained and compared performance characteristics of each sheathing material, and especially investigated the contribution of gypsum in walls with dissimilar sheathing materials on opposite sides of the wall. It also investigated the effects of monotonic loading versus the cyclic loading response and the effects of using overturning anchors.

In addition to experimental studies, many researchers have made great efforts to model the shear walls numerically. Tarabia and Itani (1997) accomplished modeling a whole 3-D light-frame building using FEM. In this model, diaphragm elements are used to represent walls. Master DOF's were assigned to the connecting nodes among the diaphragms. They also were assigned to the nodes with lumped masses for the dynamic analysis. Three translational degrees-of-freedom were assigned to each master node. The stiffness matrix of a diaphragm was divided into two parts, which were shear and bending respectively (no coupling between these two actions). In this model, buckling of sheathing panels was not considered, and 5 elements were used to represent the shear wall. A 2-node linear element with two translational DOF at each end was used for the frame. The DOF connected with master DOF through linear shape functions. For sheathing, 2D plane elements were employed, which could deform in shear only with the capacity to model openings within the sheathing panel. Sheathing interface elements were used to prevent overlapping of adjacent sheathing panels. The stiffness values of these springs were equal to zero in the case of separation, and higher values in the case of contact. Linear springs with different values in tension, compression, and shear were used for framing connectors. Sheathing-frame fasteners were modeled as a two-perpendicular decoupled nonlinear spring system connecting sheathing and framing elements. A lumping technique was used to evaluate the stiffness matrix of each group of nails located on one line as a single element. The fastener stiffness was assumed to distribute along the wall line and a numerical integration method was used to evaluate the total stiffness matrix. Kivell et al.'s hysteretic model was used to represent the hysteretic performance of nail connections and inter-component connections. Axial stiffness of inter-component elements was based on the hysteresis rule developed in Tarabia (1994). The out-of-plane bending deformations were assumed to be small and the behavior was assumed to be linear. Rotational DOFs were condensed out using the static condensation process. When considering out-of-plane bending action, the sheathing elements were modeled with 4-node thin plate elements. Two rotational DOFs and one out-of-plane translational DOF were assigned to each node. The bending stiffness matrix of the framing elements was calculated first as a grid element with two rotational and one translational degrees of freedom in the local coordinates axes and then transformed and condensed to retain the master DOFs only. For out-of-plane action, the slippage between framing members and sheathing panels was ignored.

Folz and Filiatrault (2001, 2004) formulated a FEM model to predict the hysteretic performance of light-frame shear walls and formed the "pancake model" to simulate the performance of a whole building. In this model, the connector and shear wall hysteresis loops were composed of a backbone curve and some straight lines between maximum displacement and minimum displacement. The parameters of nail connectors were obtained from test data, and the shear wall spring's parameters were based on the cyclic analysis of shear walls which were composed of elastic shell elements, rigid frame elements, and nonlinear nail connector elements between frames and shells. The straight lines used in describing hysteresis loops could cause inaccuracy. Another problem is that the same backbone is used for both monotonic and hysteresis curves. This usually is not true for nail connector and shear wall performance. Actually, the monotonic capacity is usually higher than the hysteretic capacity, especially when the number of loading cycles is large, the capacity will degrade as the dissipated energy increases (Heine 1997, Dinehart et al.1998).

This light-frame structure model simplified the 3D structural into a 2D planar model composed of zero-height shear wall spring elements that connect the floor and roof diaphragms together or to the foundation. All the horizontal diaphragms were assumed in-plane rigid. This model has been incorporated into the computer program SAWS (Seismic Analysis of Wood-frame Structures). The most obvious advantage of this model is that it is very simple, and computer time is saved. The model predictions of both the dynamic characteristics and seismic response of the structures are relatively accurate. However, it cannot show the influence of the diaphragm rigidity on the torsional effect of the structures. It cannot represent the influence of the roof slope effect, the out-of-plane stiffness of the shear wall, or the interaction between intersecting shear walls, which are generally perpendicular to each other. The most important thing is that it cannot capture the overturning and flexural response of a structure. (Actually for low-rise light-frame structures, the flexural response is not so apparent given enough hold-down capacity.) Also, SAWS has limited functions compared with general commercial FEM software.

Collins, et al (2005) built a light-frame structure model in ANSYS, a commercial FEM software. In this study, the nail connector model is based on a phenomenological model presented by Dolan (1989) and Kasal and Xu (1997), which could exhibit the key properties of the hysteretic response of these elements. In this shear wall model, a pair of diagonal hysteretic nonlinear springs instead of one zero-height spring, which was employed by Folz and Filiatrault (2004), was used to represent the in-plane action of shear walls, and the hysteresis parameters for these springs were energetically equivalent to experimental results or detailed FE models of individual walls, which are composed of shells, beams, and nonlinear nail connection elements. Shell elements were used to represent the sheathing, and beam elements were used to represent the framing. The shell element used here has no membrane stiffness, so actually it is a plate element. Shell elements and beam elements provide the out-of-plane resistance of the wall assembly. A shell element layer accounts for the bending action of all the existing sheathing layers. The moment of inertia is calculated using the parallel axis theorem. This simplification does not account for slippage between the framing and sheathing. The axial resistance is provided by the beam elements representing the studs. Unlike the sheathing elements (with plate stiffness only), the beam elements retain all their DOF (3 DOF per node) thus representing actual studs. The beam elements use the same nodes as the sheathing elements except at geometrical intersections such as a wall-to-wall or a wall-to-floor connection. The frame intersections (e.g. between sill plates and studs) are modeled as pinned connections. The limitation of this shear wall model is the decoupling of in-plane and out-of-plane responses. The other limitation is the hysteretic response of shear wall is affected by boundary conditions. A small segment of an intersecting wall could increase the shear wall's capacity and ductility. However, it is not easy to determine the boundary conditions. The authors thought the effect of boundary conditions may be more significant at lower load and displacement levels while ultimate and post-ultimate behavior may be less significantly influenced. Actually, based on the tests referred before, if two ends are tied down, the intersecting wall does not help much. However, if no tie downs are used, the difference with and without intersecting wall segments in both capacity and stiffness will be huge. This model is relatively detailed and could reflect the axial and out-of-plane action of shear walls. It could accurately represent the distribution of the mass, which will give more accurate results for seismic analysis. However, there are many drawbacks too. The coupling of nail connections is not taken into account in the detailed shear wall model. The diagonal springs could only represent the isolated shear wall's in-plane action and could not represent the effect of intersecting shear walls. The hysteretic performance of the inter-component connections could not be represented. The slippage between sheathing and frames is not considered when the out-of-plane stiffness of the shear walls is considered.

Lindt (2004) did a summary of the evolution of wood shear wall testing, modeling, and reliability analysis. In this review, the studies of last two decades were presented in chronological order. In the part of "Conclusion and Recommendations", the author attached importance on the development of damage models for light-frame wood structures that can be used to assess performance in terms of losses to owners.

2.3.3 The Rationale of this study

The logic brought forward by Collins, et al. (2005) is a reasonable way since it is relatively simple and comprehensive. In this study, the change is that the modified BWBN element, instead of the element based on the phenomenological models, is used in the detailed shear wall and super shear wall models.

2.4 Summary

The literature shows that quite a few test and numerical simulation studies have been completed on the performance of nailed wood joints and wood-frame shear walls under monotonic and cyclic loading conditions. The studies showed that characteristics of the hysteretic responses of the nail joints and shear wall are similar, which are nonlinear, history-dependant, and include stiffness and strength degradation, and pinching. Many models have been developed to predict the hysteretic behavior of nail joints and shear walls. However, each model has its obvious disadvantages. A more accurate and reliable numerical model is in need and put forth in this dissertation.

Chapter 3
Development of Nailed Wood Joint Element in ABAQUS/Standard

3.1 General

For decades, tests have been conducted to investigate the performance of light-frame shear walls subjected to monotonic and cyclic lateral loads (Dolan 1989, Heine 1997, Lam et al 1997, He et al 1999, Salenikovich 2000, Durham et al 2001, Kochkin et al 2001, etc). Recently, several full-scale house tests were employed to examine the system performance of light-frame structures. A simplified full-scale two-story single-family house was tested on a shake table (Fischer et al. 2001)). A three-story wood-frame building with tuck-under parking at the ground level was tested on a shake table (Mosalam et al. 2002), and a full-scale one-story L-shaped woodframe house, which represents a typical North American single-story stud-framed house, was tested under cyclic loading (Paevere et al 2003). A common observation from these tests is that the hysteretic response of a wood subassembly, even a wood system, is governed by the hysteretic behavior of the nail connectors. To model the behavior of light-frame structures when subjected to lateral loading accurately, the behavior of the nail connectors must be modeled correctly.

Unfortunately, commercially available software does not have the appropriate element to accurately describe the hysteretic behavior of a nailed wood joint, and the accuracy and versatility of the nailed wood joint elements developed and used in most available research tools (e.g. Dolan 1989; Chui et al 1998; He et al 2001) are not satisfactory. In this research, a nailed wood joint element which is coupled, nonlinear, history-dependent, and includes stiffness and strength degradation and pinching, will be introduced. Furthermore, the element has been embedded into the commercial general finite element analysis software, ABAQUS/Standard, as a user-defined element.

3.2 A General Nailed Wood Joint Hysteretic Model

3.2.1 Introduction

Bouc (1967) suggested a versatile, smoothly varying hysteresis model for a Single Degree of Freedom (SDF) mechanical system under forced vibration. The mechanical model is shown in Figure 3.1. Wen (1976, 1980) extended Bouc's model and made it capable to represent a wide variety of hardening or softening, smoothly varying or nearly bilinear hysteresis with a considerable range of cyclic energy dissipations. Baber and Wen (1981) modified the model to include the system degradation (stiffness and/or strength) as a function of the hysteretic energy dissipation, and extended the model to multi-degree-of-freedom (MDOF) shear beam structure systems. Baber and Noori (1985) further extended the model to incorporate pinching. This model is so called BWBN model.

Foliente (1993) first applied the BWBN model for wood systems and generalized the pinching function, which meets the criteria of wood joints. In this model, 14 parameters are used to represent the hysteretic properties of joints.

The basis of this model is the equation of motion for a single-degree-of-freedom system (Equation (3-1)) consisting of a mass connected in parallel to a viscous damper, a linear spring and a non-linear, hysteretic spring (Figure 3.1).

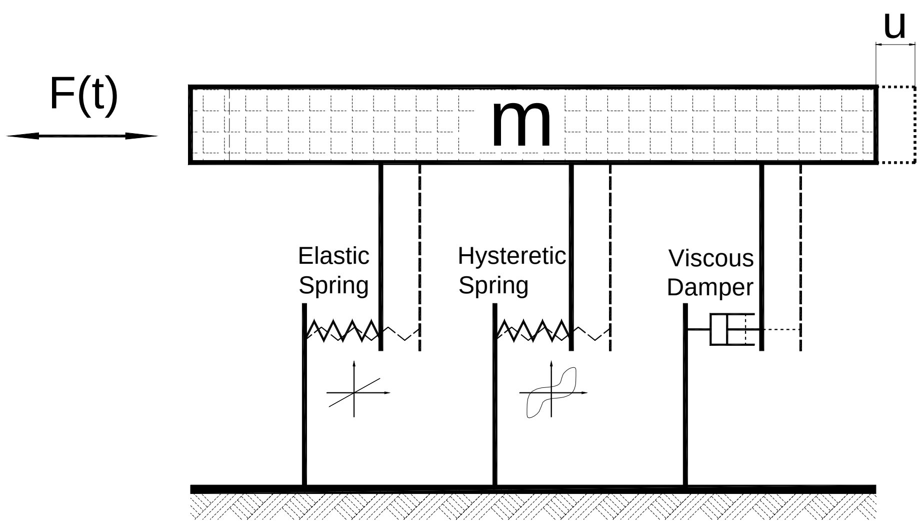

Figure 3.1 Schematic Model

$$\begin{cases} m \cdot \ddot{u}(t) + c \cdot \dot{u}(t) + R(u,z,t) = F(t) \\ R(u,z,t) = S(u,t) + H(z,t) = \alpha \cdot m \cdot \omega^2 \cdot u(t) + (1-\alpha) \cdot m \cdot \omega^2 \cdot z(t) \end{cases} \tag{3-1}$$

Where u is the relative displacement of the mass to the base; c is the linear viscous damping coefficient; F is the time-dependant forcing function; R is the total restoring force from both the linear and hysteretic springs; S is the restoring force in the linear spring, and H is the restoring force in the hysteretic spring; ω is the pseudo-natural frequency of the non-linear system, and ω^2 is the mass-normalized stiffness; α is the rigidity ratio; z is the hysteretic displacement, which is expressed with the following differential equation (the relevant parameters in the equation will be introduced later).

$$\dot{z}(t) = h(z) \cdot \left\{ \frac{\dot{u}(t) - \nu\left(\beta \cdot |\dot{u}(t)| \cdot |z(t)|^{n-1} \cdot z(t) + \gamma \cdot \dot{u}(t) \cdot |z(t)|^{n}\right)}{\eta} \right\} \tag{3-2}$$

After normalizing with respect to the mass, Equation (3-1) becomes:

$$\begin{cases} \ddot{u}(t) + 2 \cdot \xi_0 \cdot \omega \cdot \dot{u}(t) + r(u,z,t) = f(t) \\ r(u,z,t) = s(u,t) + h(z,t) = \alpha \cdot \omega^2 \cdot u(t) + (1-\alpha) \cdot \omega^2 \cdot z(t) \end{cases} \tag{3-3}$$

Where ξ_0 is the linear viscous damping ratio, which equals $\frac{C}{2 \cdot m \cdot \omega}$; f is the mass-normalized forcing function; *r* is the mass-normalized restoring force.

The hysteretic energy dissipation is used in this model to approximate system degradation. The energy dissipated by the hysteretic spring is the continuous integral of the hysteretic force, *h*, over the total displacement *u*. The hysteretic energy dissipation may be expressed as (Foliente 1993):

$$\varepsilon(t) = \int_{u(0)}^{u(t)} h \cdot du = (1.0 - \alpha) \cdot \omega^2 \cdot \int_{u(0)}^{u(t)} z(u,t) \cdot du \cdot \frac{dt}{dt} = (1.0 - \alpha) \cdot \omega^2 \cdot \int_0^t z(u,t) \cdot \dot{u}(t) \cdot dt \qquad (3\text{-}4)$$

3.2.2 The parameters

1. Stiffness and Damping Parameters: ω, ξ_0

ω is the pseudo-natural frequency of the non-linear system, and ω^2 is the mass-normalized stiffness. ξ_0 is the linear viscous damping ratio.

2. Stiffness Ratio Parameter: α

α is the stiffness ratio, which determines the ratio of the final asymptote tangent stiffness to the initial stiffness. In the original BWBN model, this parameter is a constant. However, tests by Smart (2002) showed that the strength of the connections would not keep increasing, which means that the connections will lose their stiffness. Besides, if α is set to zero, the stiffness and strength of the connections at small displacement level will be underestimated. So a function of the experienced maximum absolute displacement, *M_Dis*, is used to define this parameter:

$$\alpha = \alpha_0 \cdot e^{(-0.08 \cdot M\_Dis)} \qquad (3\text{-}5)$$

When u>0, *M_Dis* is the maximum positive displacement. When u≤0, *M_Dis* is the absolute value of the maximum negative displacement.

The pinching stiffness (minimum tangent stiffness of the curve section where unloading finishes and reloading begins) is almost equal to $(\alpha \cdot \omega^2)$ because nail connections have a great degree of pinching. This stiffness value decreases with the development of maximum displacement, so the model using varying α is more accurate (Figure 3.2).

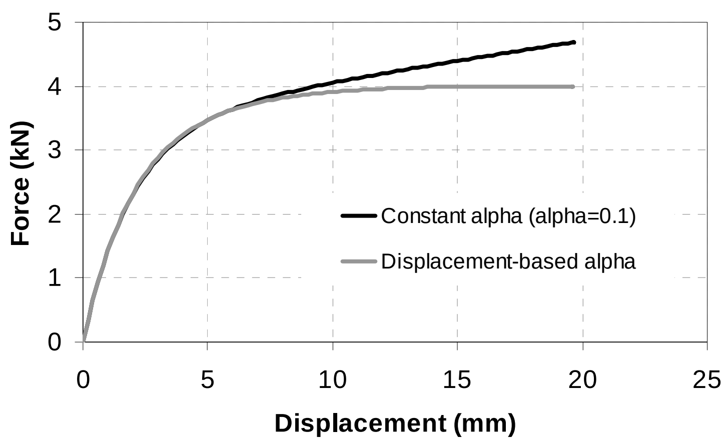

(a) Monotonic Loading

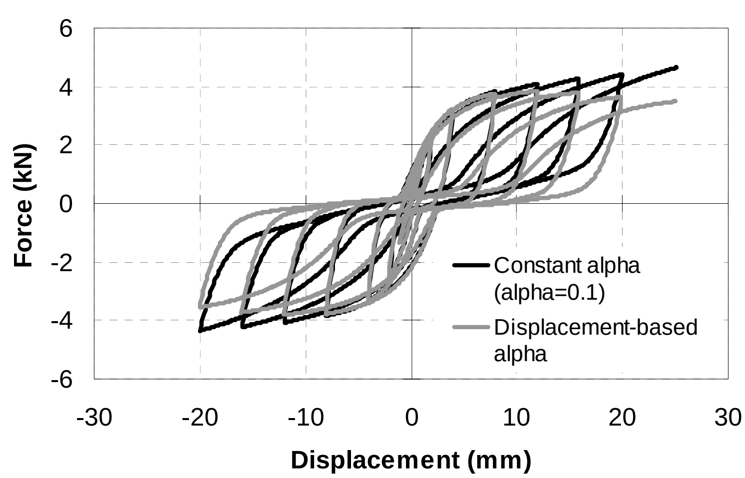

(b) Hysteretic Loading

Figure 3.2 Effect of α

3. Shape Parameters: β , γ , and n

β and γ act as a couple and determine whether the curve is hardening or softening (Figure 3.3).

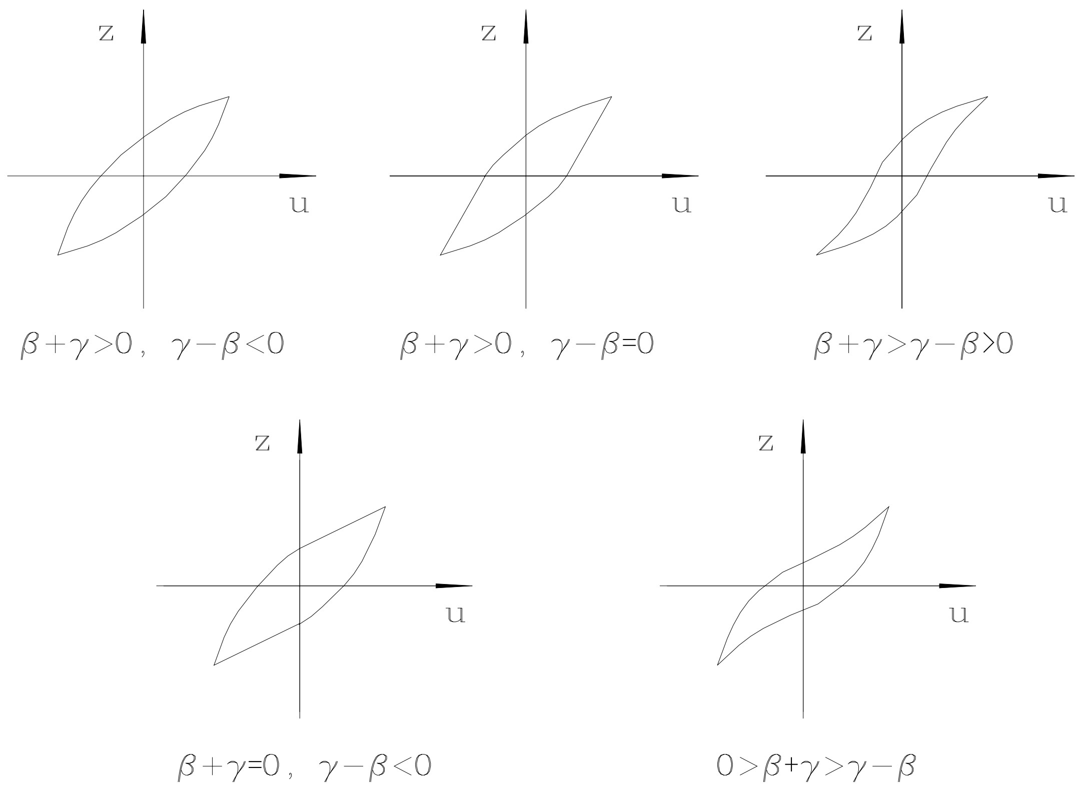

Figure 3.3 Effect of b and g on the Shape of the Hysteretic Curve

The hysteretic performance of a wood structure most resembles weak softening, and the suitable couple is:

$$\begin{cases} \beta + \gamma > 0.0 \\ \gamma - \beta < 0.0 \end{cases} \tag{3-6}$$

The parameter n, during loading, determines the sharpness of the transition from initial slope to the slope of the asymptote (Figure 3.4). For increasing values of n, the loading path of a softening hysteresis approaches the ideal elastic-plastic function while the unloading path approaches a straight line.

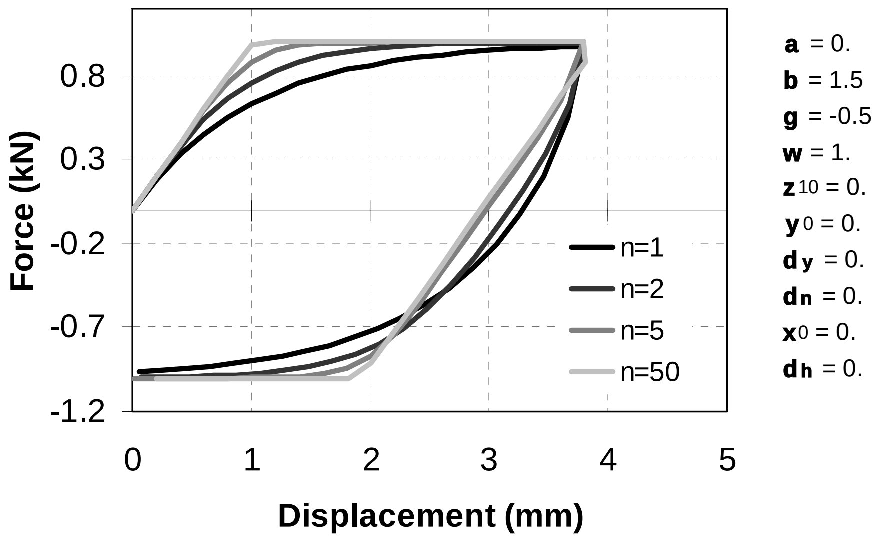

Figure 3.4 Effect of *n* on the Shape of the Hysteretic Curve

4. Degradation Parameters: η and ν

The total tangent stiffness k_t of the elastic and hysteretic springs (Figure 3.1) is:

$$k_t = \frac{dr}{du} = \alpha \cdot \omega^2 + (1-\alpha) \cdot \omega^2 \cdot \frac{dz}{du} \tag{3-7}$$

Where,

$$\frac{dz}{du} = \frac{\dot{z}(t)}{\dot{u}(t)} = h(z) \cdot \left\{ \frac{1 - \nu\left(\beta \cdot \mathrm{sgn}(\dot{u}(t)) \cdot |z(t)|^{n-1} \cdot z(t) + \gamma \cdot |z(t)|^{n}\right)}{\eta} \right\} \tag{3-8}$$

Where *sgn* is the signum function (i.e., when a is positive, zero, or negative, sgn(a) gives the value of –1, 0, or 1 respectively.).

The ultimate hysteretic spring force is $[(1-\alpha)\cdot\omega^2\cdot z_u]$, where z_u is the ultimate hysteretic displacement. z_u is reached when $\frac{dz}{du} = \frac{\dot{z}(t)}{\dot{u}(t)} = 0$ (i.e., $\dot{z}(t) = 0$). It follows,

$$z_u = \pm \left(\frac{1}{\nu(\beta + \gamma)} \right)^{\frac{1}{n}} \tag{3-9}$$

In the equations above, η and ν are stiffness and strength degradation parameters respectively and are linearly energy-based:

$$\eta = 1.0 + \delta_\eta \cdot \varepsilon(t) \tag{3-10}$$

$$\nu = 1.0 + \delta_\nu \cdot \varepsilon(t) \tag{3-11}$$

Where δ_η and δ_ν are the degradation rates (Figures 3.5, 3.6).

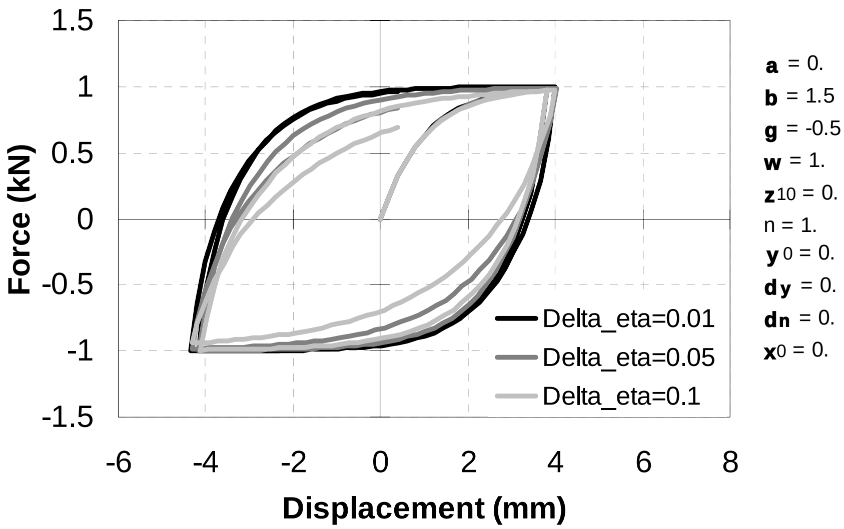

Figure 3.5 Effect of d_h on the Shape of the Hysteresis

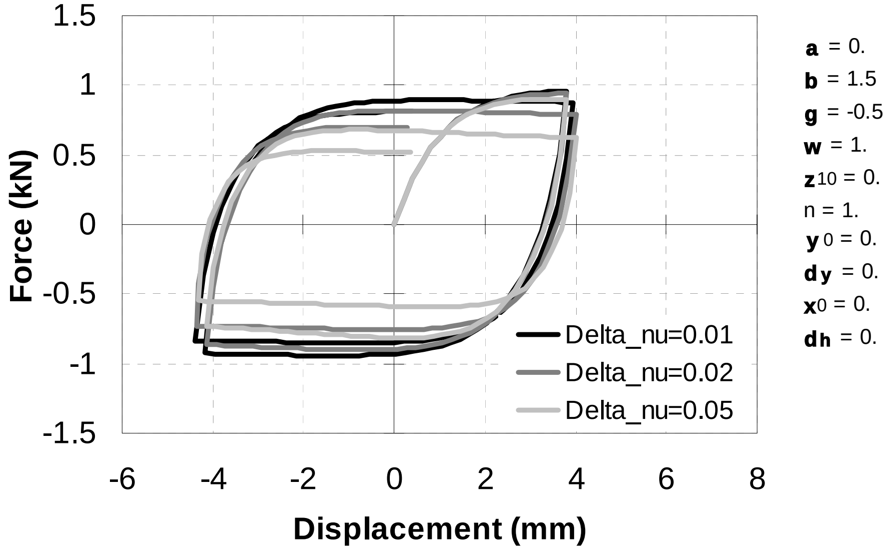

Figure 3.6 Effect of d_n on the Shape of the Hysteresis

5. Pinching Parameters: ζ_1, ζ_2, q, etc

h(z) is the pinching function. In the BWBN model, the dissipated hysteresis energy is considered as the only factor that affects the pinching development. Foliente (1993) took the residual force of the wood connectors into account and incorporated q to present this effect. When z equals $q \cdot z_u$, the pinching is maximized. The expressions of the pinching function are:

$$h(z) = 1.0 - \zeta_1 \cdot e^{[-(z \cdot \mathrm{sgn}(\dot{u}(t)) - q \cdot z_u)^2 / \zeta_2{}^2]} \tag{3-12}$$

$$\zeta_1(\varepsilon) = \zeta_{10} \cdot [1.0 - e^{(-p \cdot \varepsilon)}] \tag{3-13}$$

$$\zeta_2(\varepsilon) = (\psi_0 + \delta_\psi \cdot \varepsilon) \cdot (\lambda + \zeta_1) \tag{3-14}$$

Where, ζ_1 ($0.0 < \zeta_1 < 1.0$) controls the pinching stiffness (minimum tangent stiffness of the hysteretic loop, which occurs where unloading finishes and reloading begins). The greater ζ_1 is, the greater the initial drop in slope, *dz/du*, is. ζ_2 controls the rate of change of the slope, *dz/du*. Graphically, it controls the range of the pinching (from the beginning point of pinching to the stiffness recovery point). The greater ζ_2 is, the larger the pinching range is. ζ_{10} and p are the parameters that affect the basic magnitude and the rate of change of ζ_1 based on ε respectively. ψ_0 and δ_ψ are the parameters that affect the basic magnitude and the rate of change of ζ_2 based on ε respectively; λ is the parameter that controls the rate of change of ζ_2 as ζ_1 changes.

However, the main reason for the pinching phenomenon in nailed wood joints is the gap developed between nail and wood during cyclic loading. The test data collected by Dolan and Carradine (2003) show that the pinching developed very little after the joints experienced considerable low-level load and displacement loops. So the dissipated energy has little, if any, effect on the pinching development in nailed wood joints. Pinching will be overestimated if the energy dissipation was taken as the only factor, especially for low-displacement-level performance.

The other problem this model must address is the pinching lag phenomenon. As mentioned before, q controls the position where the maximum pinching occurs. At unloading points (definition is expressed by Equations 3-15 and 3-16), if the current displacement is less than the maximum previously experienced displacement in the same direction, a constant q postpones the maximum pinching location in the opposite direction, which causes the pinching lag (Figure 3.7).

$$\dot{u}(i-1) > 0,\ \ \dot{u}(i) < 0,\ \ u(i-1) > 0 \text{, or} \tag{3-15}$$

$$\dot{u}(i-1) < 0,\ \ \dot{u}(i) > 0,\ \ u(i-1) < 0 \tag{3-16}$$

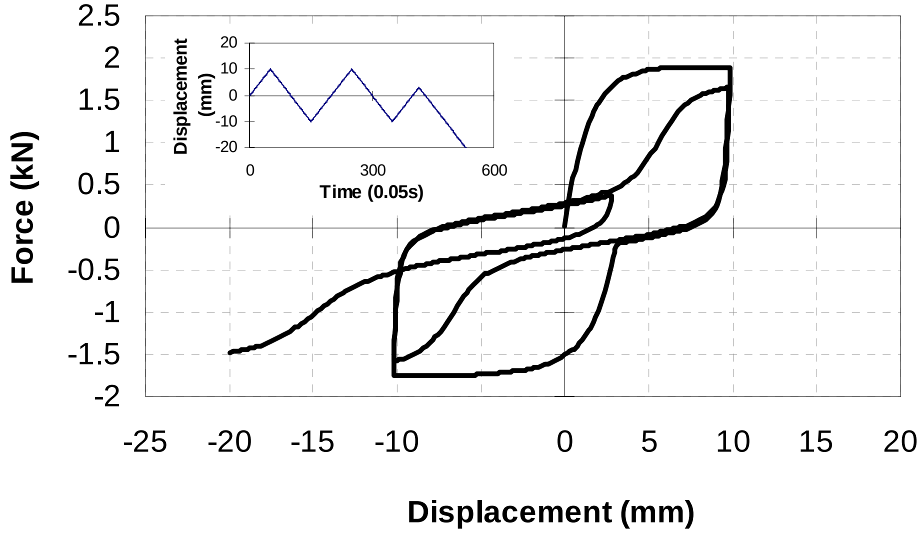

Figure 3.7 Pinching Lag Phenomenon

To make the pinching displacement-based and eliminate the pinching lag phenomenon, Equations (3-12), (3-13), and (3-14) are replaced by (3-17), (3-18), and (3-19) respectively:

$$h(z) = 1.0 - \zeta_1 \cdot e^{[-(z \cdot \mathrm{sgn}(\dot{u}(t)) - ratio \cdot q \cdot z_u)^2 / \zeta_2{}^3]} \tag{3-17}$$

$$\zeta_1(M\_Dis) = \zeta_{10} \cdot [1.0 - e^{(-p \cdot M\_Dis)}] \tag{3-18}$$

$$\zeta_2(M\_Dis) = \psi_0 + \delta_\psi \cdot M\_Dis \tag{3-19}$$

Where *ratio* represents the ratio of the displacement at the unloading position to the previously experienced maximum displacement in the same direction.

$$ratio = \begin{cases} \left| \dfrac{u}{Max\_Dis} \right|, & u \geq 0 \\ \left| \dfrac{u}{Min\_Dis} \right|, & u < 0 \end{cases}$$

The *ratio* is always greater than or equal to 0. It is set equal to 1.0 when it is greater than 1.0. In another words, *ratio* will take effect only when small loops exist in the loading history. To give the hysteresis the ability to merge to the former trajectory, *ratio* is used to reduce the q value and thus decrease the absolute z value where the maximum z_1 occurs. Accordingly the maximum pinching point occurs earlier. To improve the loop merge, z_{10} is set to $(\zeta_{10} \cdot ratio^{0.11})$ when unloading occurs. In this model, *M_Dis* is set to the maximum positive displacement when $(z > ratio \cdot q \cdot z_u)$ and before $(z < -ratio \cdot q \cdot z_u)$, and it is set to the absolute value of the minimum displacement when $(z < -ratio \cdot q \cdot z_u)$ and before $(z > ratio \cdot q \cdot z_u)$. This setting means that when z reaches the value of the positive pinching point or when z decreases to a value less than the value at the positive pinching point but before z develops to the negative pinching point value, the nail connection performs in the positive scope. In another words, in this case, the performance of the nail connection is based on the maximum experienced displacement in the positive direction, and vice versa.

The effect of these modifications can be seen in Figure 3.8.

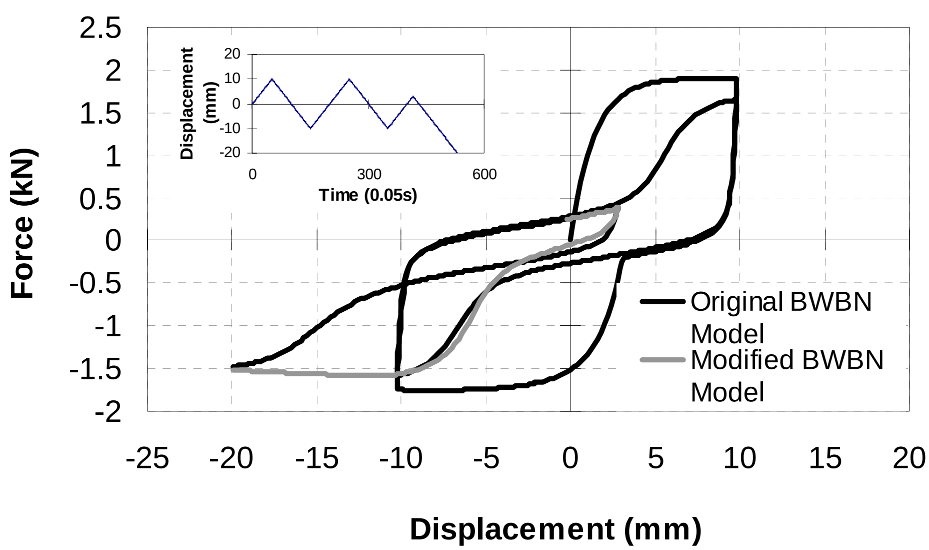

Figure 3.8 Elimination of Pinching Lag Phenomena

Another apparent shortcoming of the original BWBN model is that it is not capable of representing the small loop during partial loading-reloading circles. This limitation will cause big problems in the large-displacement scope. The model will seriously underestimate the energy-dissipation capacity of the joints. Casciati (1987) proposed a modification which added two terms in the hysteretic constitutive equation. This modification increases the stiffness in the loading and reloading sections, which causes an inaccurate shape change of the whole hysteretic loop.

To overcome this limitation, some other modifications are applied at the reloading points (definition is expressed by Equations 3-20 and 3-21) and the original parameter values will be recovered at the following unloading points if there are any.

$$\dot{u}(i-1) < 0,\ \ \dot{u}(i) > 0,\ \ u(i-1) > 0\text{, or} \tag{3-20}$$

$$\dot{u}(i-1) > 0,\ \ \dot{u}(i) < 0,\ \ u(i-1) < 0 \tag{3-21}$$

The changes are different for situations without load sign reversal (Figure 3.9a) versus situations with load sign reversal (Figure 3.9b).

When the reloading happens at the positive displacement range, the *ratio* is defined as below for the without-load-sign-reversal (Force≥0) and with-load-sign-reversal (Force<0) cases respectively.

$$ratio = \begin{cases} \left|\dfrac{z}{q \cdot z_u}\right| \ , & Force \geq 0 \\ -\left|\dfrac{z}{q \cdot z_u}\right| \ , & Force < 0 \end{cases} \tag{3-22}$$

To eliminate the unreal pinching, ζ_{10} is changed at the same time for both cases,

$$\zeta_{10} = \begin{cases} -2 \ , \ Force \geq 0 \\ (1 - \left| \dfrac{u}{Min\_Dis} \right|)^4 \cdot \zeta_{10} \ , \ Force < 0 \end{cases} \tag{3-23}$$

When the reloading happens in the negative displacement range, the *ratio* is defined as below for the without-load-sign-reversal (Force≤0) and with-load-sign-reversal (Force>0) cases respectively.

$$ratio = \begin{cases} \left| \dfrac{z}{q \cdot z_u} \right| \ , \ Force \leq 0 \\ -\left| \dfrac{z}{q \cdot z_u} \right| \ , \ Force > 0 \end{cases} \tag{3-24}$$

ζ_{10} is changed at the same time for both cases,

$$\zeta_{10} = \begin{cases} -2 \ , \ Force \leq 0 \\ (1 - \dfrac{|u|}{Max\_Dis})^4 \cdot \zeta_{10} \ , \ Force > 0 \end{cases} \tag{3-25}$$

These changes make the reloading point become a pinching point and reduce the unreal pinching as well. They can eliminate the unreal pinching effect and produce a small loop. (Figure 3.9)

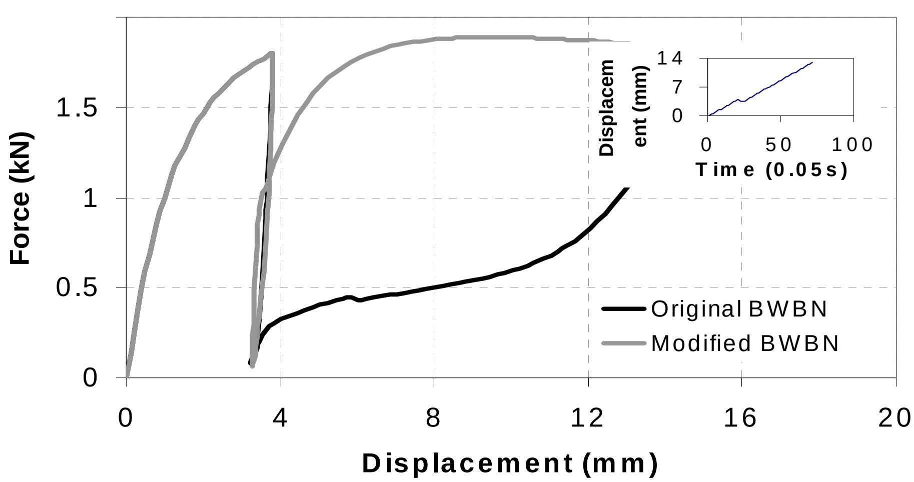

(a) Without Load Reversed

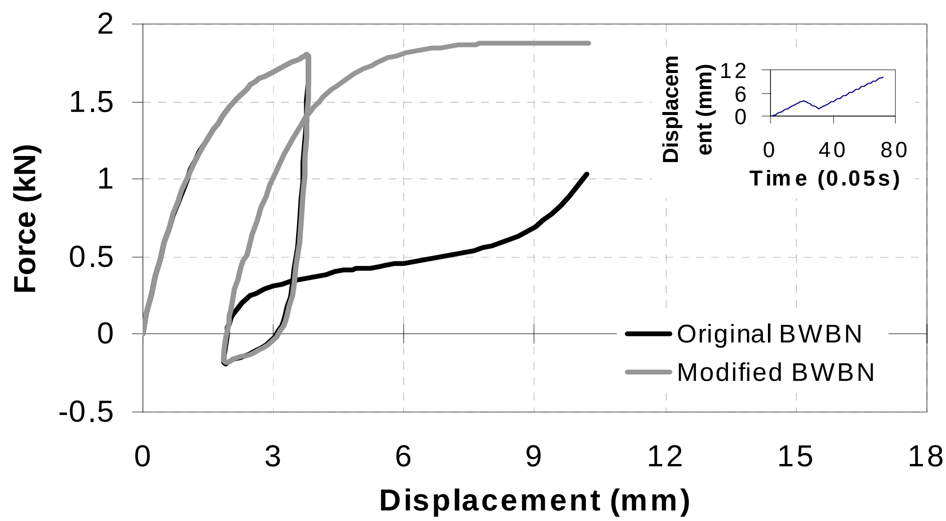

(b) With Load Reversed

Figure 3.9 Realization of Small Loops

3.2.3 Model Solving

The model uses the relation (Baber and Noori 1985, Foliente 1993)

$$\begin{Bmatrix} y_1(t) \\ y_2(t) \\ y_3(t) \end{Bmatrix} = \begin{Bmatrix} u(t) \\ z(t) \\ \varepsilon(t) \end{Bmatrix} \tag{3-26}$$

The model for the restoring elements is composed with several differential equations (the time dependencies are excluded for simplicity):

$$\begin{cases} \dot{y}_1 = V \\ \dot{y}_2 = (1.0 - \zeta_1 \cdot e^{[-(y_2 \cdot \mathrm{sgn}(V) - ratio \cdot q \cdot z_u)^2 / \zeta_2^{\,3}]}) \cdot \left[\dfrac{\dot{y}_1 - (1.0 + \delta_\eta \cdot y_3) \cdot \left(\beta \cdot |V| \cdot |y_2|^{n-1} \cdot y_2 + \gamma \cdot V \cdot |y_2|^n \right)}{1.0 + \delta_\nu \cdot y_3} \right] \\ \dot{y}_3 = (1.0 - \alpha) \cdot \omega^2 \cdot y_2 \cdot V \end{cases}$$

(3-27)

Where,

$$
\begin{cases}
\left.\begin{aligned}
\zeta_1 &= \zeta_{10} \cdot [1.0 - e^{(-p \cdot \max(y_1))}], \\
\zeta_2 &= \psi_0 + \delta_\psi \cdot \max(y_1)
\end{aligned}\right\} & when\ \ y_2 \geq ratio \cdot q \cdot z_u\ \ and\ \ before\ \ y_2 < -ratio \cdot q \cdot z_u \\
\left.\begin{aligned}
\zeta_1 &= \zeta_{10} \cdot [1.0 - e^{(-p \cdot |\min(y_1)|)}], \\
\zeta_2 &= \psi_0 + \delta_\psi \cdot |\min(y_1)|
\end{aligned}\right\} & when\ \ y_2 < -ratio \cdot q \cdot z_u\ \ and\ \ before\ \ y_2 \geq ratio \cdot q \cdot z_u
\end{cases}
\tag{3-28}
$$

All the derivatives in Equations (3-26) and (3-27) appear in the first power and variables vary with time at highly different rates. Hence, this model is composed of a stiff set of linear ordinary differential equations (ODE). Heine (2001) used the Livermore Solver for Ordinary Differential Equations (LSODE) to solve the model of a single bolt which is similar to this nail model. LSODE is employed in this study as well. LSODE solves a wide range of ODEs including stiff systems for which it uses the Gear Method and it is capable of internally computing the full Jacobian matrix. Moreover, input functions such as displacing or forcing functions do not have to be continuous functions. Instead discrete data points can be read in from an external file. In this solver, displacement is the input variable. For a displacement history, the velocity of each time interval is computed based on the displacement and time period of this interval and input into the solver. The force corresponding to each displacement is then output.

3.2.4 Parameter Estimation

In this model, 13 parameters need to be identified. The hysteresis performance is not only dependent on each of them, but also on their interaction. Foliente (1993) gave a suitable set of values for wood nail connectors, which was obtained by repeated trials and comparison with experimental data. However, there are too many types of nailed wood joints which may have much different performance. Therefore a system identification procedure is essential to estimate the parameters for different joints and make this model applicable to a wide range of problems.

Minimizing the difference between the model results and the experimental results makes the parameter estimation an optimization problem. There is a wealth of information reported in the literature on optimization techniques in general, and system identification or parameter estimation methods in particular. Heine (2001) chose Genetic Algorithms (GA) as the optimization method in his multiple-bolt model. GAs are versatile, and most importantly, they always converge, which means it does not require the objective function to be differentiable. Unlike calculus-based methods which are ill-suited for noisy data, GAs can handle any type of data. They also can handle any objective function with or without constraints, linear or nonlinear. The solution space may be n-dimensional where n can theoretically reach infinity. Another great advantage of GAs is that no initial parameter estimation needs to be made if there is no knowledge of the possible values of the parameters. However, if the initial parameters' ranges are supplied, the convergence of the procedure will be speeded. The smaller the ranges are, the faster the convergence occurs. Based on the GA developed by Lybanon and Messa (1999), which was specifically developed for model fitting to solve a satellite altimetry problem, Heine (2001) developed an efficient and highly robust GA written in FORTRAN that successfully estimates parameters for his multiple-bolt model. In this program, 4 loops are included. The 1st loop (the outermost one) is used to shift the parameter intervals, and the 2nd loop is used to shrink the parameter intervals. The 3rd loop is used to generate a number of GA "population", and the 4th loop (the innermost one) is the core one, which is used to check the solver results and select the "good organisms" based on least squares method, then "crossover" and "mutate" these "organisms" within the "population". When the intervals of the parameters shrink to a certain percentage of the original ranges, the program stops. Because of the excellent performance of GAs and the similarity between Heine's model and the nail joint model in this research, his program was modified and used in the parameter estimation for this nailed wood joint hysteresis model. The detail description of the program's organization could be found in Heine (2001).

Dolan and Carradine (2003) conducted a series of cyclic tests on nail connections. The nail connection specimens were fabricated by attaching a piece of 15 mm (19/32 in.) thick oriented strand board (OSB) to a 150 mm (6 in.) long section of nominal 2x4 lumber (Douglas Fir-Larch No. 2 or better) with a single nail. Nails utilized for the tests were 63 mm (2-1/2 in.) by 2.9 mm (0.113 in.) diameter (8d box), 63 mm (2-1/2 in.) by 3.3 mm (0.131 in.) diameter (8d common), 76 mm (3 in.) by 3.3 mm (0.128 in.) diameter (10d box), and 76 mm (3 in.) by 3.8 mm (0.148 in.) diameter (10d common). The lumber used was either kiln dried or green at the time of fabrication. All test specimens were fabricated and then placed in a 70º F, 65% relative humidity conditioning chamber until the moisture content of the green wood stabilized at 12%. The GA program was run for each type of nail connection based on the test data to find the proper parameter set for each.

Validations are illustrated in Figure 3.10. The correlation coefficients (definition and equations are shown in Appendix A) for specimens of (a) to (f) are 0.946, 0.935, 0.919, 0.956, 0.949, and 0.922 respectively. The figures show that most of the tested nail connectors have similar performance characteristics and parameters. The suitable parameter set for one nail joint configuration could be found through the testing of a series of specimens and averaging the parameter values obtained from these testing specimens.

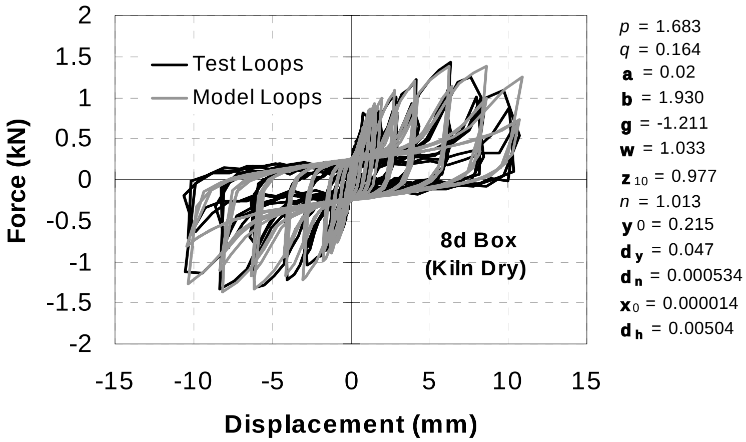

(a) Kiln-dry 8d Box Nail Joint

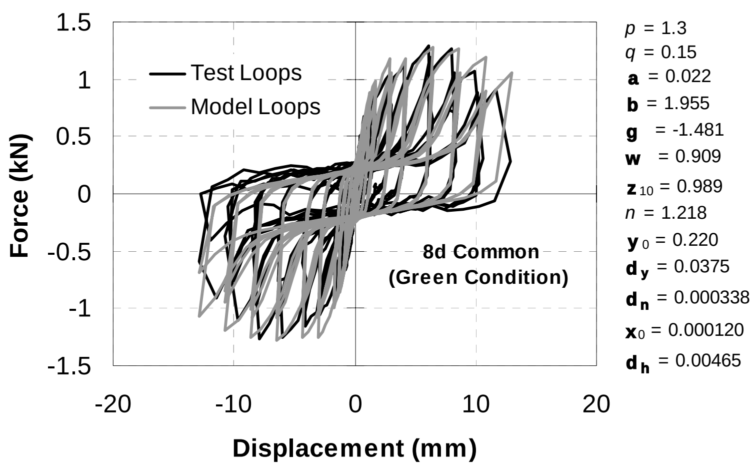

(b) Green-condition 8d Common Nail Joint

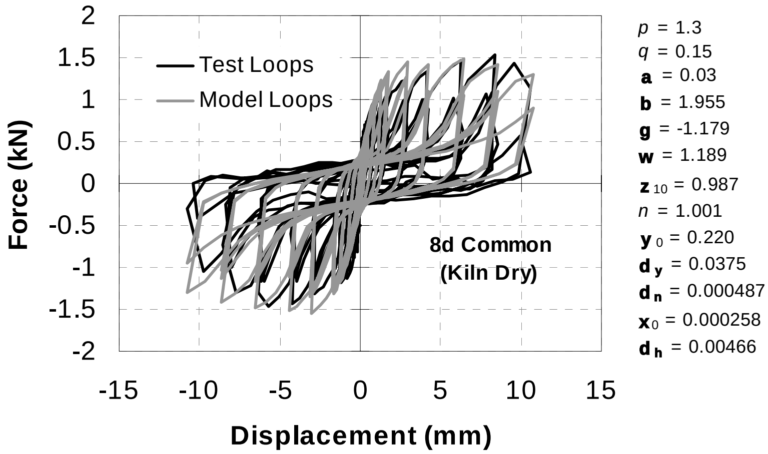

(c) Kiln-dry 8d Common Nail Joint

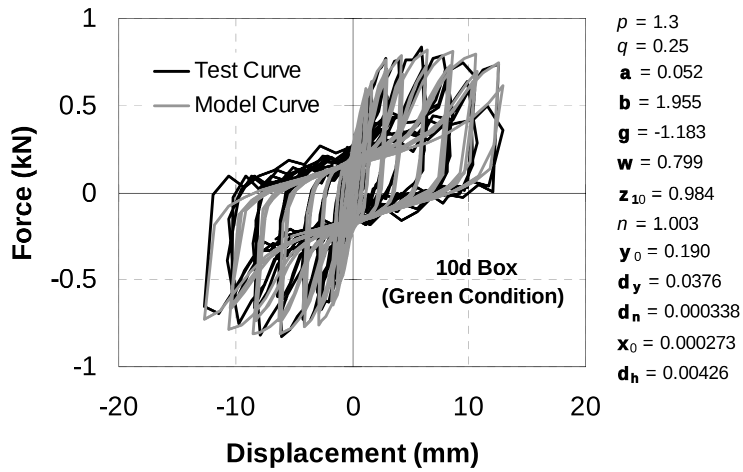

(d) Green-condition 10d Box Nail Joint

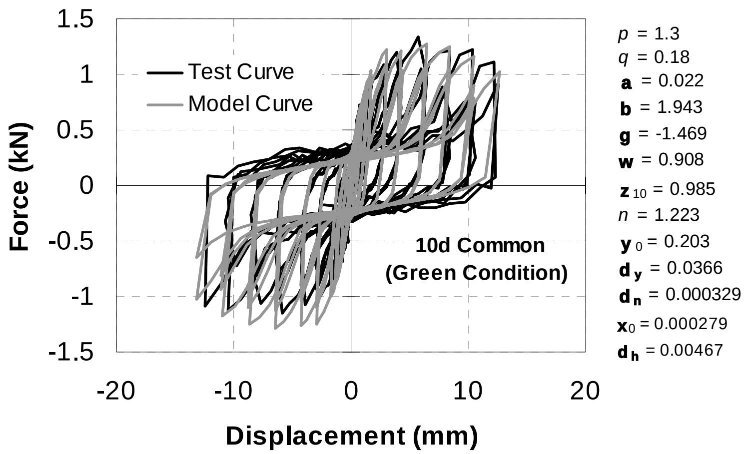

(e) Green-condition 10d Common Nail Joint

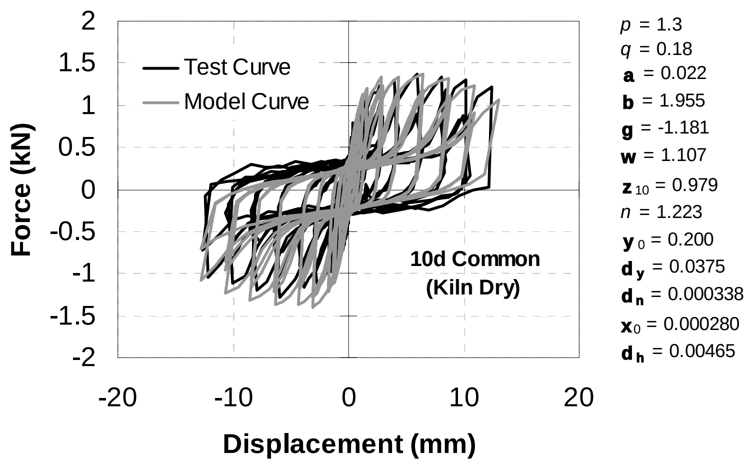

(f) Kiln-dry 10d Common Nail Joint

Figure 3.10 Validations of the Nailed Wood Joint Model

3.2.5 Coupling Character

The performance of nailed connections is coupled about the orthogonal directions. Since the joint performance is nonlinear, it is not reasonable to model the connectors as a pair of uncoupled orthogonal nonlinear springs.

Foschi (1977a), based on the virtual work theory, developed a FE method to represent the coupling character of nail connections. The vector of the virtual work derivatives was split into a linear and a nonlinear part before assembly into the global system. After assembly into the global system, the nonlinear part assembled into a nonlinear vector, which is a function of the global deformation vector, and the linear part is the product of global stiffness matrix and deformation vector. The orthotropic property of connections was also considered in this method. However, in this method, the nail connection springs could be oriented in any direction. It is hard to trace the trajectory and record the maximum experienced displacement of each nail in each direction. So, it is difficult to describe the pinching degree of each nail connection at certain displacement.

Furthermore, this method considered not only the nonlinearity caused by the spring itself but also the nonlinearity caused by coupling, and the linear part of the stiffness matrix remains unchanged all the time after assembly, which is similar to the modified Newton-Raphson method. So, it will take significant computer time to make the problem converge, especially for the hysteresis problem, which is much more complicated than the monotonic problem.

F. Fonseca and J. Judd (2004) presented an Oriented Spring Pair Model (Figure 3.11).

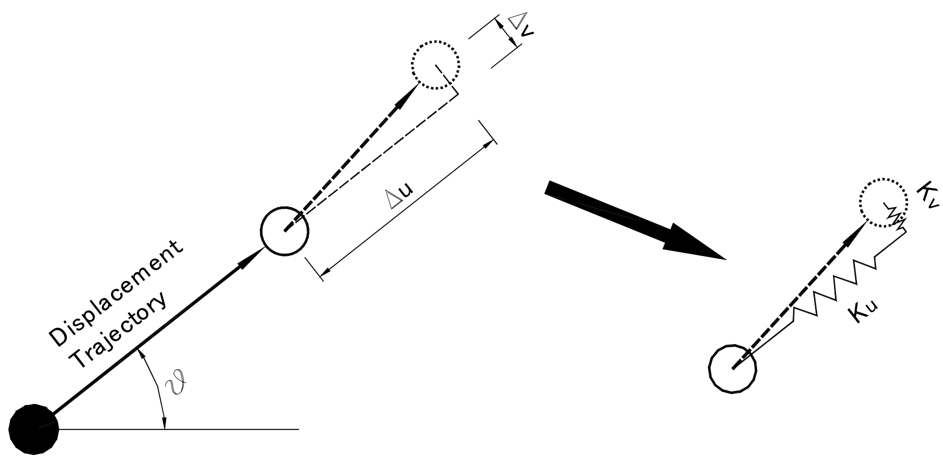

Figure 3.11 Oriented Spring Pair Model

In this model, “each nailed connection is represented using two nonlinear springs that are oriented using the initial linear deformation trajectory of the connection.” This model can represent actual connection behavior because “tearing through sheathing panels is a dominant failure mode observed during reversed-cyclic loading of wood shear walls, and tearing of the sheathing restricts the movement of the nail to a relatively narrow path.”

The orthotropic property is negligible for nails (diameter < 0.25 inch).

The following equations show the formation of the stiffness matrix for each nailed connection element. K_u is the tangent stiffness of the nonlinear spring along the moving trajectory. K_v represents the tangent stiffness in the orthogonal direction, which is perpendicular to the initial trajectory. The modified BWBN model is used for both springs, and this method can significantly relieve uncoupled problems.

$$[K'] = \begin{bmatrix} K_u & 0 & -K_u & 0 \\ & K_v & 0 & -K_v \\ & & K_u & 0 \\ sym. & & & K_v \end{bmatrix} \tag{3-29}$$

$$[T] = \begin{bmatrix} \cos\theta & \sin\theta & 0 & 0 \\ -\sin\theta & \cos\theta & 0 & 0 \\ 0 & 0 & \cos\theta & \sin\theta \\ 0 & 0 & -\sin\theta & \cos\theta \end{bmatrix} \tag{3-30}$$

$$[K] = [T]^T \cdot [K'] \cdot [T] = \begin{bmatrix} K_{11} & K_{12} & -K_{11} & -K_{12} \\ & K_{22} & -K_{12} & -K_{22} \\ & & K_{11} & K_{12} \\ sym. & & & K_{22} \end{bmatrix} \tag{3-31}$$

Where,

$$K_{11} = K_u \cdot \cos^2\theta + K_v \cdot \sin^2\theta \tag{3-32}$$

$$K_{12} = K_u \cdot \cos\theta \cdot \sin\theta - K_v \cdot \cos\theta \cdot \sin\theta \tag{3-33}$$

$$K_{22} = K_u \cdot \sin^2\theta + K_v \cdot \cos^2\theta \tag{3-34}$$

The forces acting on the element are:

$$F' = \begin{Bmatrix} F_u \\ F_v \\ -F_u \\ -F_v \end{Bmatrix} \tag{3-35}$$

$$F = [T]^T \cdot F' = \begin{Bmatrix} F_u \cdot \cos\theta - F_v \cdot \sin\theta \\ F_u \cdot \sin\theta + F_v \cdot \cos\theta \\ -F_u \cdot \cos\theta + F_v \cdot \sin\theta \\ -F_u \cdot \sin\theta - F_v \cdot \cos\theta \end{Bmatrix} \tag{3-36}$$

3.2.6 Modeling in ABAQUS/Standard

3.2.6.1 Introduction of ABAQUS/Standard

ABAQUS/Standard (2005) is a general purpose, finite element analysis system. The Standard is the implicit version of ABAQUS, which has a special feature that allows users to define elements not included in the ABAQUS element library. The user-defined element is implemented as a user subroutine called UEL (Programmed in Visual Fortran) and works just in the same way as the existing elements in ABAQUS/Standard. All material behavior is defined in subroutine, UEL, based on the material constants defined via UEL PROPERTY data and on solution-dependent state variables associated with the element. The ABAQUS/Standard invokes the subroutine once per iteration for each element. As introduced in ABAQUS Analysis User's Manual (2005), at each such call, ABAQUS/Standard provides the values of the nodal coordinates and of all solution-dependent nodal variables (displacements, incremental displacements, velocities, accelerations, etc.) at all degrees of freedoms associated with the element, as well as values, at the beginning of the current increment, of the solution-dependent state variables associated with the element. ABAQUS/Standard also provides the values of all element parameters associated with this element that have been defined in the *UEL PROPERTY option and a control flag array indicating what functions the user subroutine must perform. Depending on this set of control flags, the subroutine must define the contribution of the element to the residual vector, define the contribution of the element to the Jacobian (stiffness) matrix, update the solution-dependent state variables associated with the element, form the mass matrix, and so on. Often, several of these functions must be performed in a single call to the routine. ABAQUS/Post is used to produce the output plots and extract data.

3.2.6.2 Hysteretic Nailed Wood Joint Model in ABAQUS/Standard

A nonlinear hysteretic nailed wood joint element was built as a UEL subroutine in ABAQUS/Standard (Version 6.5) and was integrated into ABAQUS/Standard through the statements in the developed ABAQUS input file. This subroutine was written in Compaq Visual FORTRAN (Version 6.6).

In this subroutine, the Newton-Raphson method is used to iterate to a solution. To avoid the possible divergence problem at the unloading or reloading points, the theoretical tangent stiffness was assigned at the beginning of each unloading and reloading step. Automatic Time Increment was selected in ABAQUS, i.e., if solution does not converge within 16 iterations in each time increment, or if the solution appears to diverge, ABAQUS/STANDARD abandons the increment and starts again with a new time increment that is 25% of the previous value. By default, 5 reductions of increment size are allowed; however, if 2 consecutive increments require fewer than 5 iterations to obtain a converged solution, ABAQUS/STANDARD automatically increases the time increment size by 50%.

3.3 Summary

A general hysteresis model for nail connections, which is based on the modified BWBN model, was presented. The hysteretic constitutive law is characterized by a series of Ordinary Differential Equations and produces versatile and smoothly varying hysteresis curves. The model is nonlinear, history-dependant, and includes stiffness and strength degradation, and pinching. The parameters of the model can be estimated through Genetic algorithms based on the test data. The comparison between the model and test data shows good agreement. This model was embedded in commercially available software, ABAQUS/Standard (Version 6.5), as a user-defined element. This element also took the coupling property of the nail action into account.

Chapter 4
Detailed Shear Wall Modeling

4.1 General

In this study, both detailed and super shear wall models (see Chapter 5) are simulated in the general FEM software, ABAQUS/Standard (Version 6.5).

In the Detailed FEM shear wall model, a B31 beam element is used to represent studs and top and bottom plates. A S4 shell element is used to represent sheathing panels. The modified BWBN nail joint element, which was embedded in ABAQUS through a UEL subroutine, is used to connect the sheathing panels and framing members. B31 is a 2-node 3-D linear beam element, and each node has 6 degrees of freedom. S4 is a 4-node doubly curved general-purpose shell element with finite membrane strains permitted, and each node has 6 degrees of freedom. This element includes bending, shear, and membrane stiffness at the same time. In this study, it is assumed that the framing members and sheathing panels act linear elastically. The orthotropic characteristic of the sheathing material was considered through defining a different elastic modulus in two orthogonal directions.

To show the accuracy and reliability of the detailed shear wall model, two detailed shear wall models were simulated in ABAQUS/Standard. One was a 1219×2438 mm (4×8 ft) wood-frame shear wall without openings, and the other was a 3658×2438 mm (12×8 ft) shear wall with an opening. Overturning restraint conditions of engineered construction (walls were attached to the base through tie-down anchors and shear bolts) and conventional construction practices (walls were attached to the base with shear bolts only) were considered.

4.2 The 1219×2438 mm (4×8 ft) Shear Wall Model (without opening)

4.2.1 Introduction

The fabrication of this shear wall is same as the relevant specimens tested by Salenikovich (2000). The framing for each specimen consisted of 38×89 mm (2×4 in.-nominal) spruce-pine-fir (SPF) stud grade members spaced 406 mm (16 in.) on centers. End studs consisted of two members fastened by two 16d (Φ4.1×89 mm) common nails every 0.6 m (2 ft.). The studs were attached to the single bottom plate and the double top plate with two 16d common nails at each end. A single layer of OSB sheathing, 11 mm (7/16 in.) thick, was attached to one wall side by power-driven 8d (Φ3.3×63.5 mm) common SENCO® nails at 152 mm (6 in.) on centers along the edges and 305 mm (12 in.) on centers along intermediate studs. The long dimension of the sheathing was oriented parallel to the studs. The structural details of the wall specimen can be seen in Table 4.1. The wall assembly can be seen in Figure 4.1.

In this testing study, to prevent the effect of walls' self-weight, the shear walls were tested in a horizontal position, as is shown in Figure 4.2.

Three series with various anchorage conditions were tested with the purpose to estimate the change in racking performance of shear walls due to varying construction practices. These anchorage conditions were 'full anchorage' (FA), 'no anchorage' (NA), and 'intermediate anchorage' (IA), respectively. The detailed conditions can be seen in Table 4.2. However, since the test results showed that for the anchorage condition of NA overturning resistance of shear walls under the lateral load was governed by withdrawal resistance of the nails attaching the shear wall to the base, and there are few data about the hysteretic performance of nail withdraw action available, the NA condition will not be modeled in this study.

Table 4.1 Structural details of wall specimens tested by Salenikovich (2000)

Component	Fabrication and materials
Framing	Spruce-Pine-Fir, Stud grade, S-Dry, 38×89 mm (2×4 in.-nominal); Intermediate studs at 406 mm (16 in.) o. c.; Double studs at the ends of wall segments; Single bottom plate, double top plate.
Sheathing	Structural oriented strandboard (OSB), 11 mm (7/16 in.) thick, 1219×2438 mm (4×8 ft.) sheets installed with the long side parallel to studs; Attached on one side.
Framing attachment	Plate to plate: Two 16d (∅4.1×89 mm) bright common nails per foot; Stud to stud: Two 16d bright common per foot; Plate to stud: Two 16d bright common each end.
Sheathing attachment	Power driven 8d (∅3.3×63.5 mm) SENCO® nails at 152 mm (6 in.) o. c. (edge), 305 mm (12 in.) o. c. (field).
'Full anchorage'	Simpson HTT 22 Tie-down, nailed to end studs with 32 16d (∅3.8×82.6 mm) sinker nails; 15.9-mm (5/8-in.) diameter A307 bolt to connect to foundation; 15.9-mm (5/8-in.) diameter A307 bolts at 610 mm (24 in.) o. c. with 64×64×6.4 mm (2.5×2.5×0.25 in.) steel plate washers.
'No anchorage'	Three rows of 16d (∅4.1×89 mm) common nails at 76 mm (3 in.) o. c.;
'Intermediate anchorage'	15.9-mm (5/8-in.) diameter A307 bolts at 610 mm (24 in.) o. c. with 64×64×6.4 mm (2.5×2.5×0.25 in.) steel plate washers.

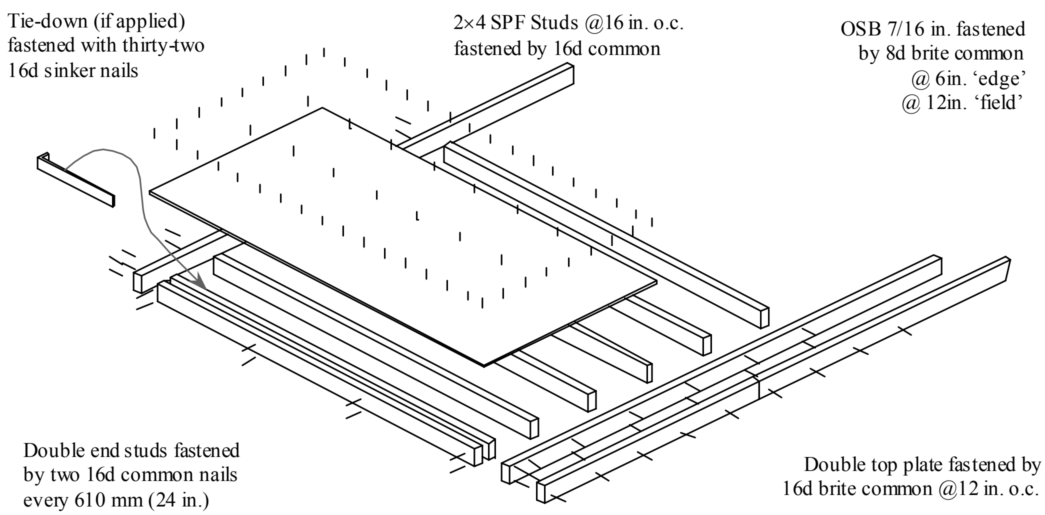

Figure 4.1 Typical Wall assembly (Courtesy of Heine (1997))

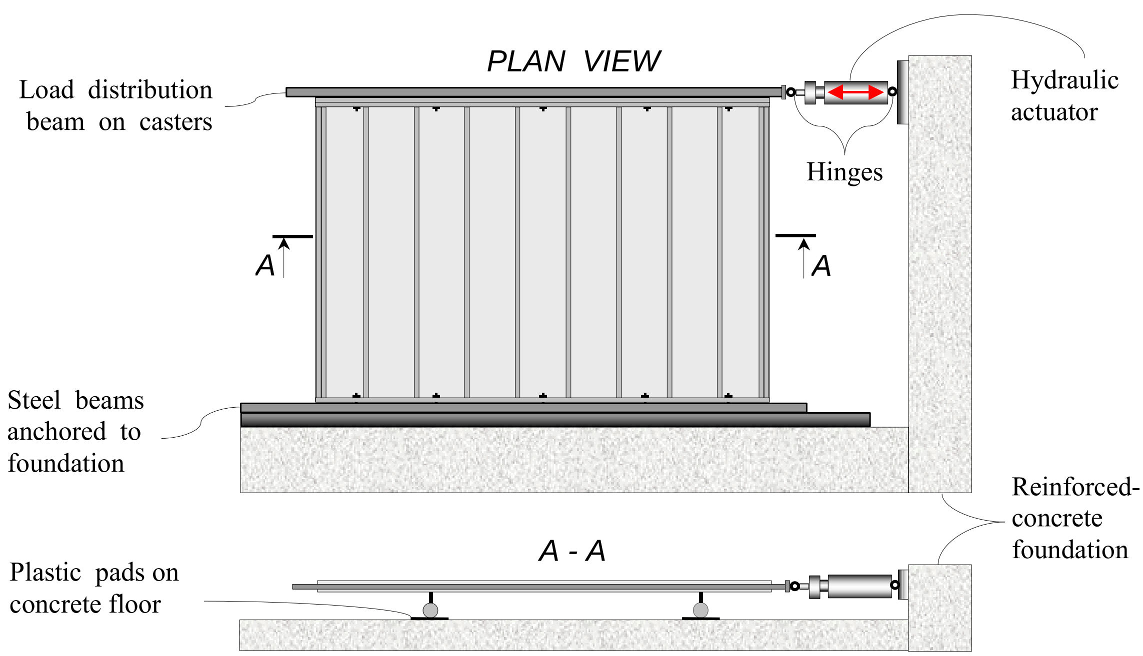

Figure 4.2 Testing Plan (Courtesy of Heine(1997))

Table 4.2 Anchorage conditions for model and tested by Salenikovich (2000)

Series		Description	Rationale
FA	Full anchorage (maximum restraint)	5/8 in. bolts at 24 in. o. c., Simpson Tie-down HTT22 with 32 16d sinker nails and 5/8-in. bolt.	Typical engineered construction practice; Maximum hold-down restraint possible; Possibility to compare with previous tests according to ASTM E564.
NA	No anchorage (minimum restraint)	16d bright common nails	Typical conventional construction; Minimum hold-down restraint possible.
IA	Intermediate anchorage	5/8 in. bolts at 24 in. o. c.	Often used in practice; Represent intermediate restraint.

The detailed FEM models were simulated in accordance with the fabrications of the Specimens, 04FAc3 (full anchorage) and 04IAc1 (intermediate anchorage) tested by Salenikovich (2000), which was shown in Figure 4.3. The MOE of the stud and the plate used in the test Specimens was 8.757 kN/mm^2 (1.27×10^6 psi). Since the in-plane properties of OSB panels were most important, the MOE values of the OSB panel were based on the panel axial stiffness, EA (Table 4.3). The MOE was 4.99 kN/mm^2 and 3.81 kN/mm^2 in strong axis and weak axis, respectively.

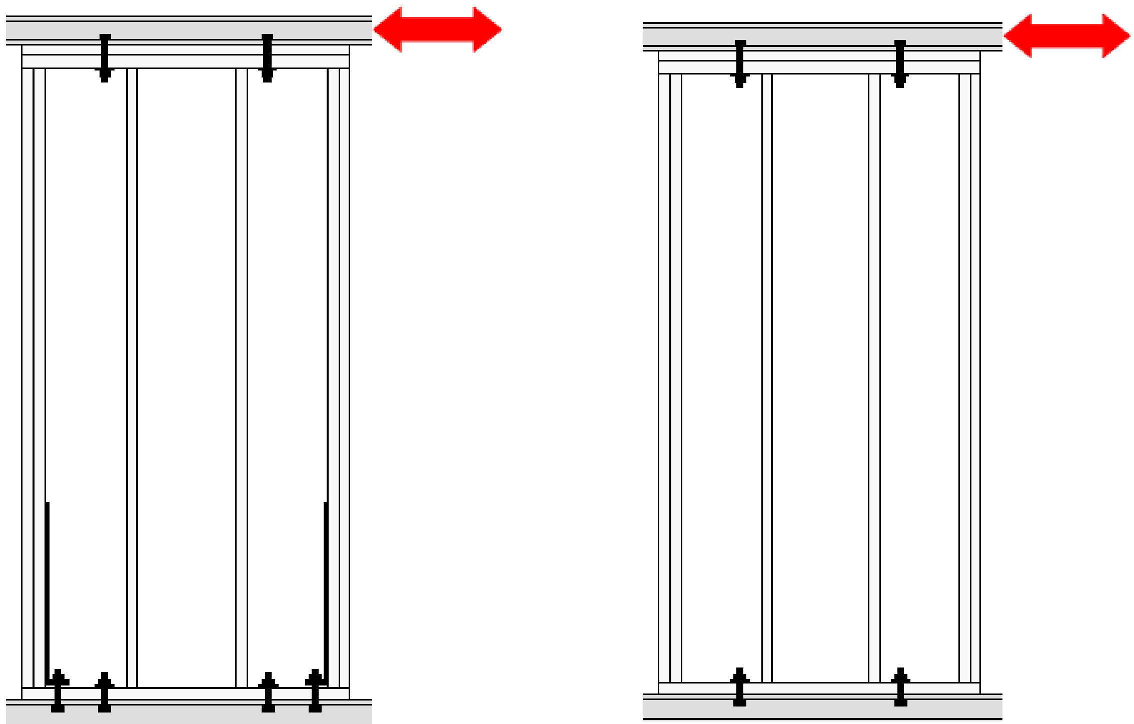

(a) Specimen 04FAc3 **(b) Specimen 04IAc1**

Figure 4.3 4×8 ft Shear Wall Specimens (Courtesy of Salenikovich (2000))

Table 4.3 Mechanical Properties of OSB Panels (Courtesy of Salenikovich (2000))

Mechanical Property	Units	Stress applied parallel to strength axis	Stress applied perpendicular to strength axis
Panel bending stiffness, *EI*	kN-mm^2/m width	734,000	152,000
	Lb-in^2/ft width	78,000	16,000
Panel axial stiffness, *EA*	kN/m	55,400	42,300
	lb/ft	3,800,000	2,900,000
Panel rigidity through thickness, $G_v t_v$	N/mm of depth	14,700	14,700
	Lb/in of depth	83,700	83,700

The framing connector elements used to simulate the nailed connectors attaching studs to top or bottom plates take both shear and bearing, while no end withdrawal resistance, actions into account. Since studs and top or bottom plates were also connected with sheathing panels through many sheathing nails, and the analysis showed that the results were not sensitive to the frame connectors' shear stiffness, to simplify the model, a constant shear stiffness of 3 kN/mm was used instead of a hysteretic rule. The meshing of the elements is shown in Figure 4.4.

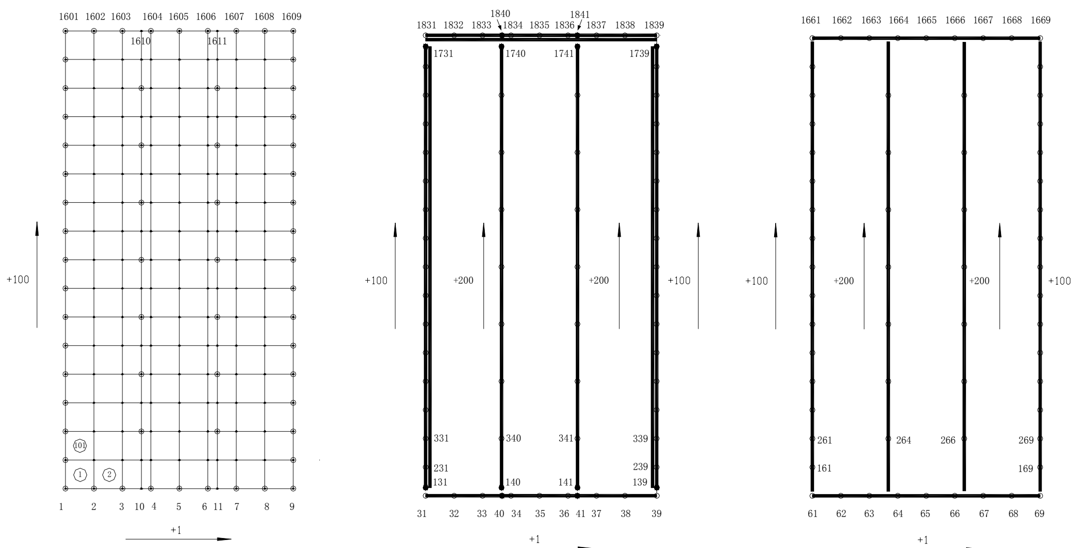

Sheathing Framing Nails

Figure 4.4 Meshing of Detailed model in ABAQUS

There were monotonic test results but no hysteretic test results available for the sheathing-to-framing nailed connectors used in the testing. The parameters derived from the CUREE project (Dolan and Carradine, 2003) were modified somewhat to match the monotonic test curve of the connectors used in this testing. These parameter values are:

p =1.3, q= 0.14, $\mathbf{a}$ = 0.03, $\mathbf{b}$ = 0.637, $\mathbf{g}$ = -0.0808, $\mathbf{w}$ = 0.82, $\mathbf{z}_0$ = 0.965, n =1.00,

$\mathbf{y}$ =0.285, $\mathbf{d}_\mathbf{y}$ = 0.0488, $\mathbf{d}_\mathbf{n}$ = 0.00487, $\mathbf{x}$ = 0.000280, $\mathbf{d}_\mathbf{h}$=0.00510.

The comparison between the simulated and experimental results can be seen in

Figure 4.5. The same International Standards Organization (ISO) loading protocol (Figure.4.6) used in the testing was applied to the top plate of the detailed shear wall model.

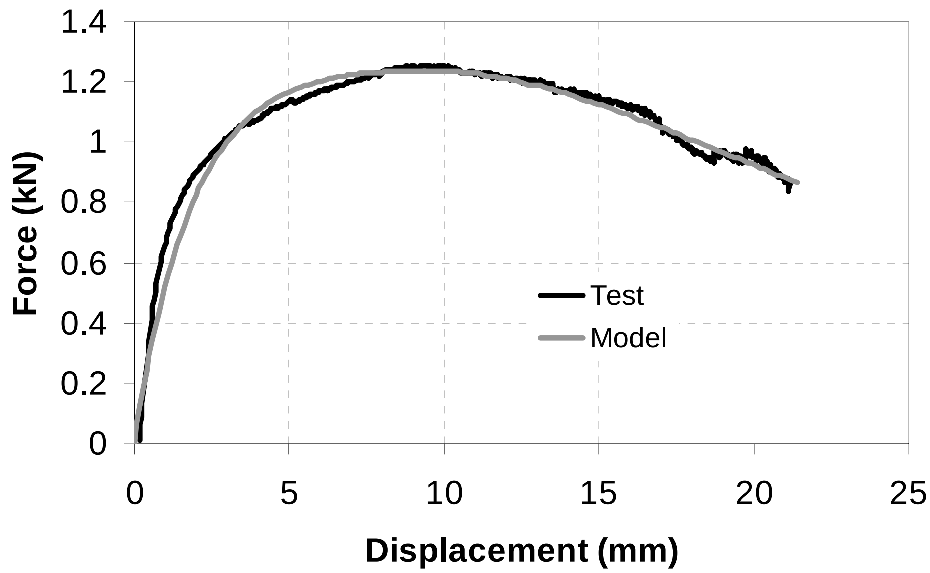

Figure 4.5 Sheathing-framing Nail Connector Parameter Estimation

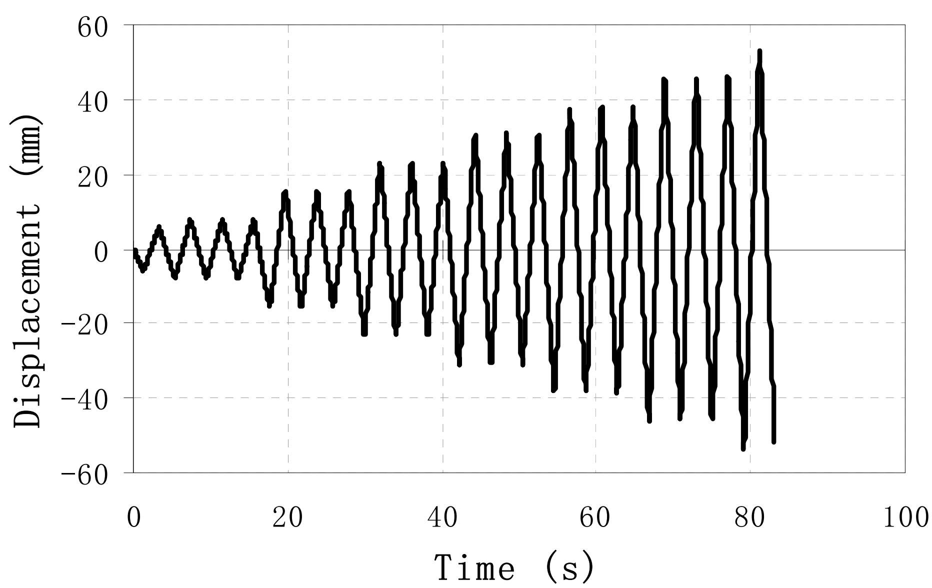

Figure 4.6 International Standards Organization (ISO) loading protocol

4.2.2 Shear Wall with Full Anchorage

The end studs' uplifts were restricted at the corners, where tie-down anchors were applied, in the model. The hysteretic loops from the test result were shown in Figure 4.7, and the hysteretic loops from the simulation were shown in Figure 4.8. The comparison of the hysteretic loops is shown in Figure 4.9. The maximum experimental and simulated resistances were 9.5 kN and 9.8 kN respectively (error is 3%). The comparison of the hysteretic energy dissipated in the protocol is shown in Figure 4.10. The maximum dissipated energy from the experiment and simulation were 3847 kN-mm and 3778 kN-mm respectively (error is –2%). From these comparisons, the accuracy of the model is obvious. All the characters of the shear wall's hysteretic performance were represented in the model results. From Figure 4.9, The strength of the modeled shear wall, in early stage, is a little higher than that in the test results and decreases earlier than the tested wall does. The reason is that stiffness of the tie-down anchors was not infinite, while the displacements of the tie-down anchors were ignored in the model. Besides, the joint parameters were derived based on the monotonic test results. Generally speaking, the strength of shear walls drops in ultimate stage more slowly in a hysteretic loading protocol than in a monotonic one.

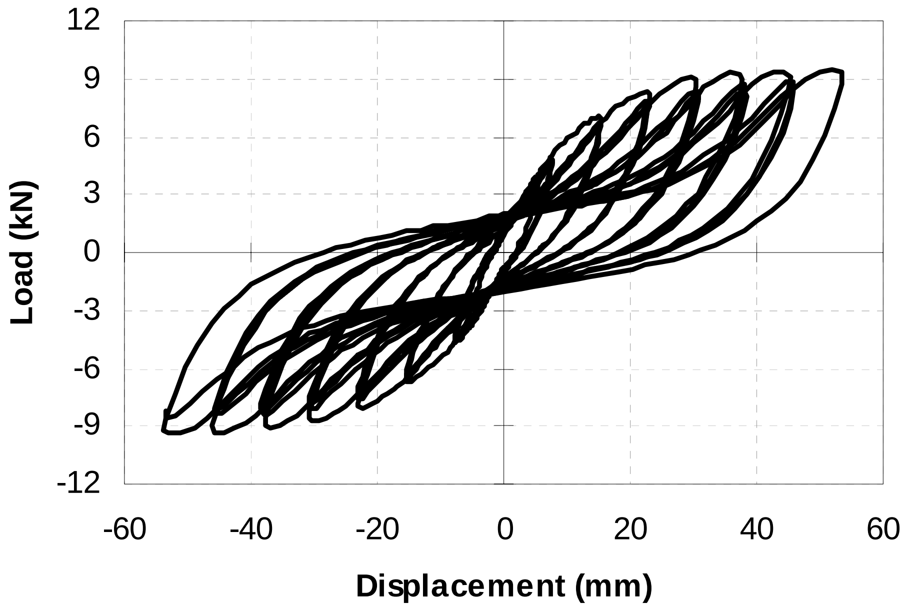

Figure 4.7 4×8 ft Shear Wall Hysteretic Loops from Testing (w/ tie downs)

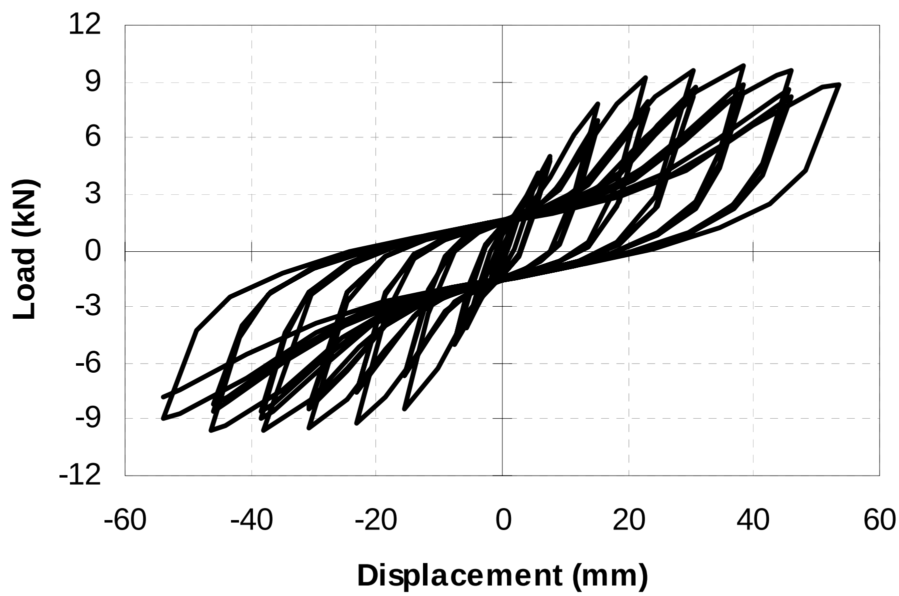

Figure 4.8 4×8 ft Shear Wall Hysteretic Loops from Model Analysis (w tie downs)

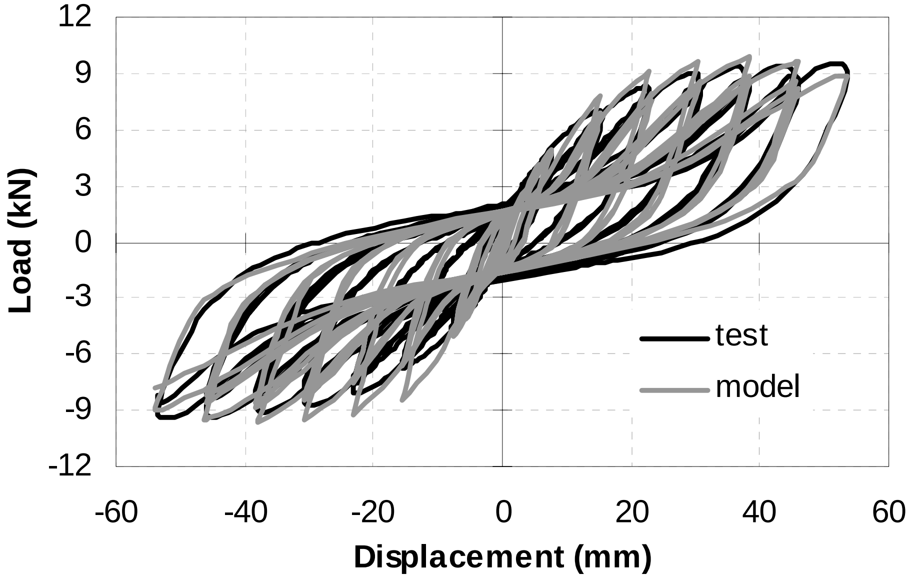

Figure 4.9 Comparison of 4×8 ft Shear Wall Hysteretic Loops (w/ tie downs)

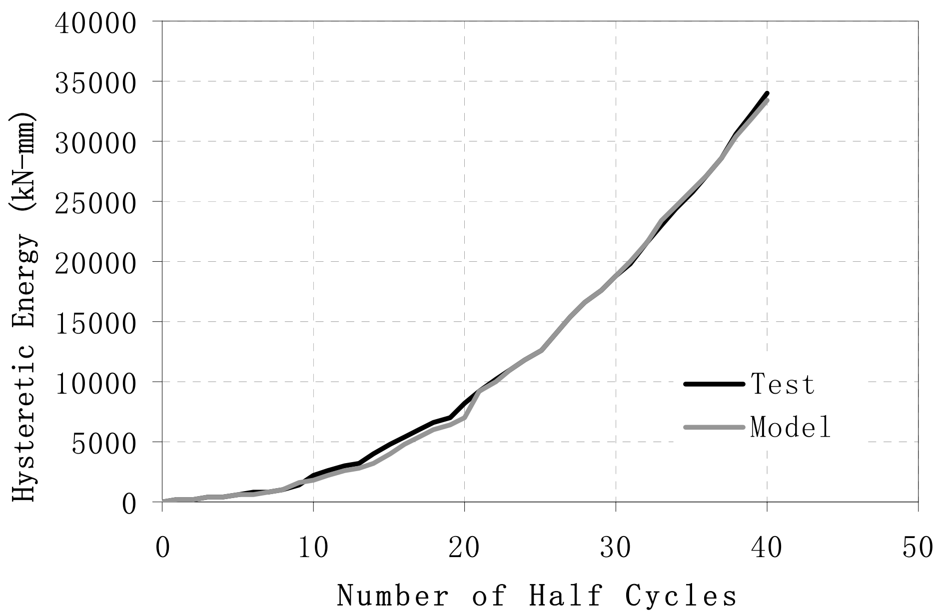

Figure 4.10 Comparison of 4×8 ft Shear Wall Hysteretic Energy (w/ tie downs)

The deformed shape that is exported from the ABAQUS/Viewer, a subset of

ABAQUS/CAE that contains only the post-processing capabilities of the Visualization module, is shown in Figure 4.11. The corresponding sheathing panel Mises Stress distribution diagram is shown in Figure 4.12. Those small Xs represent nail connectors, which stay at the positions on the framing element nodes where they were nailed originally.

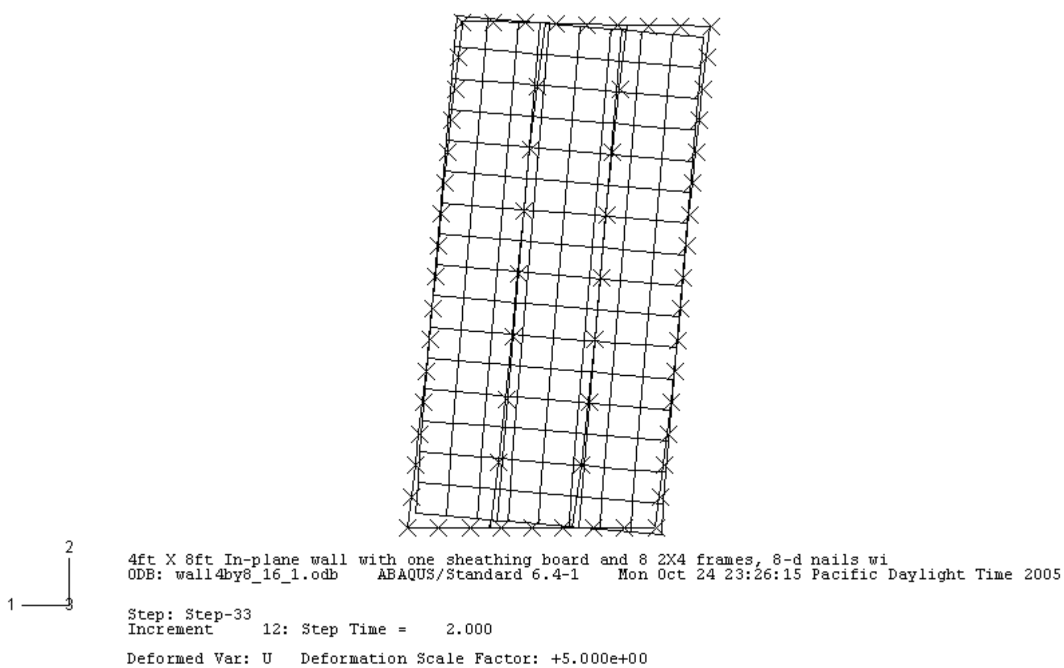

Figure 4.11 4×8 ft Shear Wall Deformed Shape (w/ tie downs)

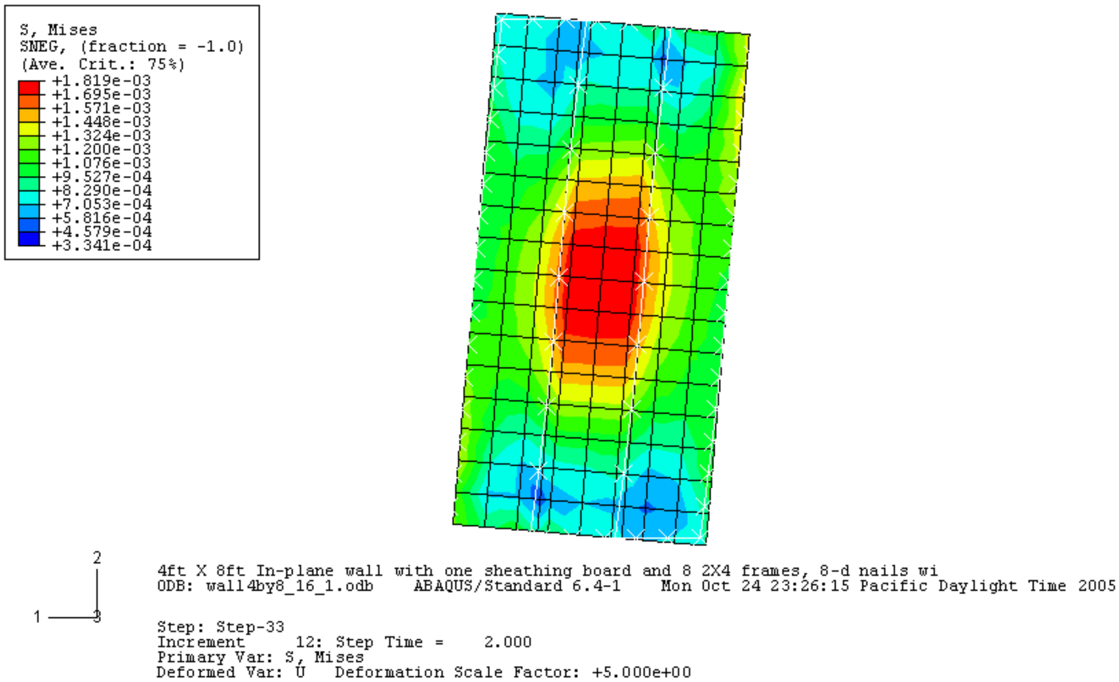

Figure 4.12 4×8 ft Shear Wall Sheathing Panel Mises Stress Contour (w/ tie downs)

4.2.3 Shear Wall with Intermediate Anchorage

The only difference between the model with intermediate anchorage and the one with full anchorage is that no restraint was applied between the end studs and the base in the former while restraint applied in the latter. The specimen of 04IAc1 tested by Salenikovich (2000) was simulated. The corresponding experimental hysteretic loops are shown in Figure 4.13, and the hysteretic loops from simulation are shown in Figure 4.14. They both are shown in Figure 4.15 for the comparison purposes.

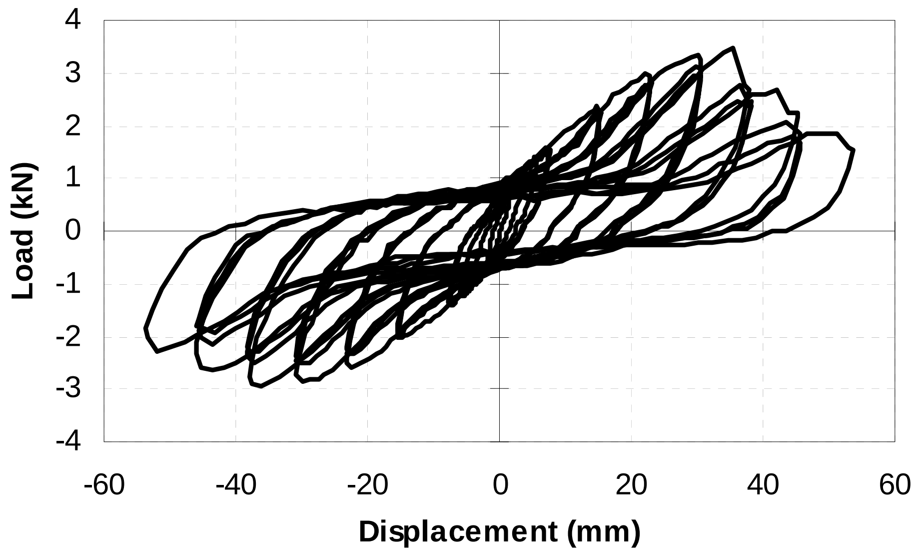

Figure 4.13 4×8 ft Shear Wall Hysteretic Loops from Testing (w/o tie downs)

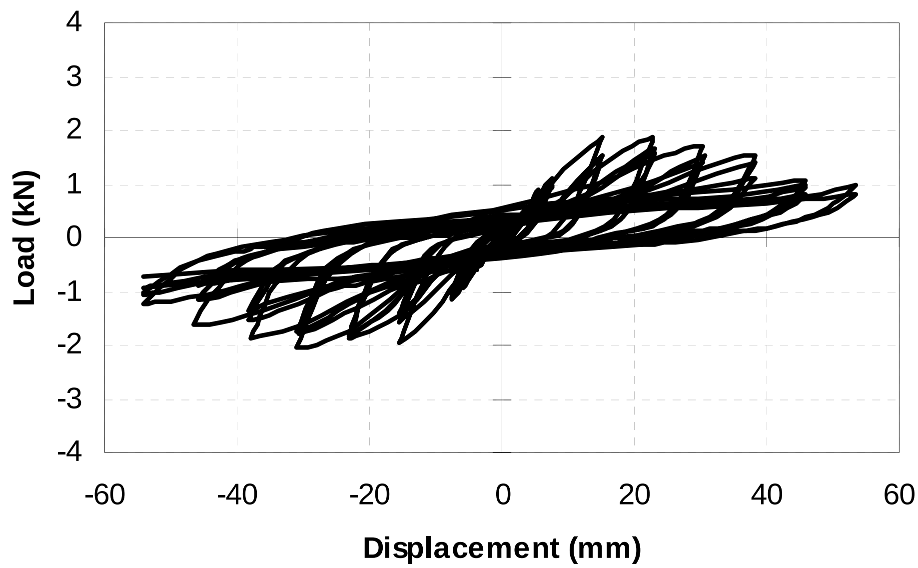

Figure 4.14 4×8 ft Shear Wall Hysteretic Loops from Model Analysis (w/o tie downs)

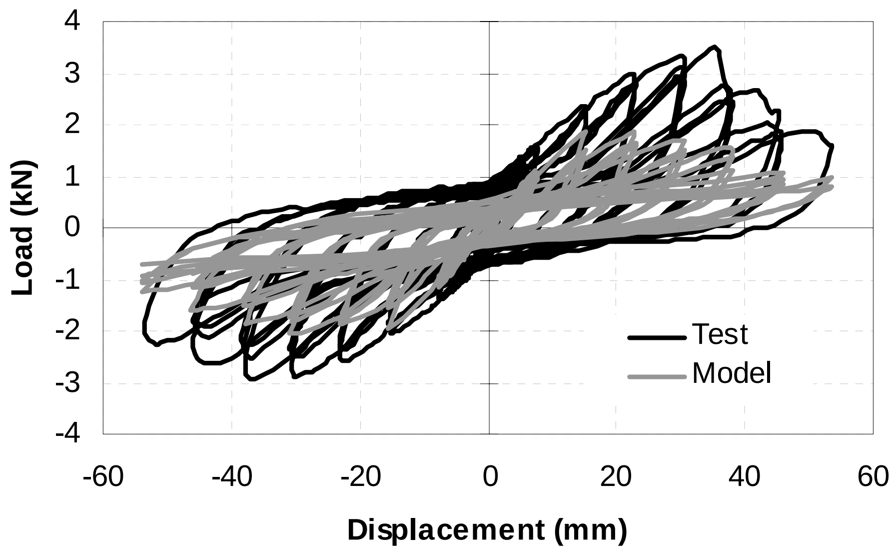

Figure 4.15 Comparison of 4×8 ft Shear Wall Hysteretic Loops (w/o tie downs)

The shape of the model loops is similar to the test ones. However, the strength, stiffness, and residual force of the model results are much lower than those from the test results.

There are two reasons for the large difference. First, in this model, the effect of the end-grain-withdraw capacity supplied by the 16d common nail connections was not considered. This effect was always ignored in the modeling and/or design process because the end-grain-withdraw capacity will be lost very rapidly in real construction with repeated shrinkage and swelling of wood caused by moisture content variation. However, the specimens in the testing condition did not experience this process. Second, the tested shear wall has a relatively low capacity because of the high height-to-width configuration and low restraint conditions. So the end-grain-withdraw connections could contribute a large capacity percentage to the whole system.

To show the difference caused by the end-grain-withdraw contribution, a test that included 5 specimens was conducted. Each specimen was constructed with two pieces of 1-foot-long 38×89 mm (2×4 in.-nominal) SPF that were connected with one 16d common nail and formed a “T” shape. Since only the capacity, stiffness, and the residual capacity are concerned, only one cycle of 1-in displacement was applied to each specimen. To make the results more comparable to the relative shear wall test data, the loading rate was 0.1 in/sec, which was based on the initial loading rate in the relative shear wall tests. The load-displacement curves are shown in Figure 4.16, and the statistics of the data are listed in Table 4.4.

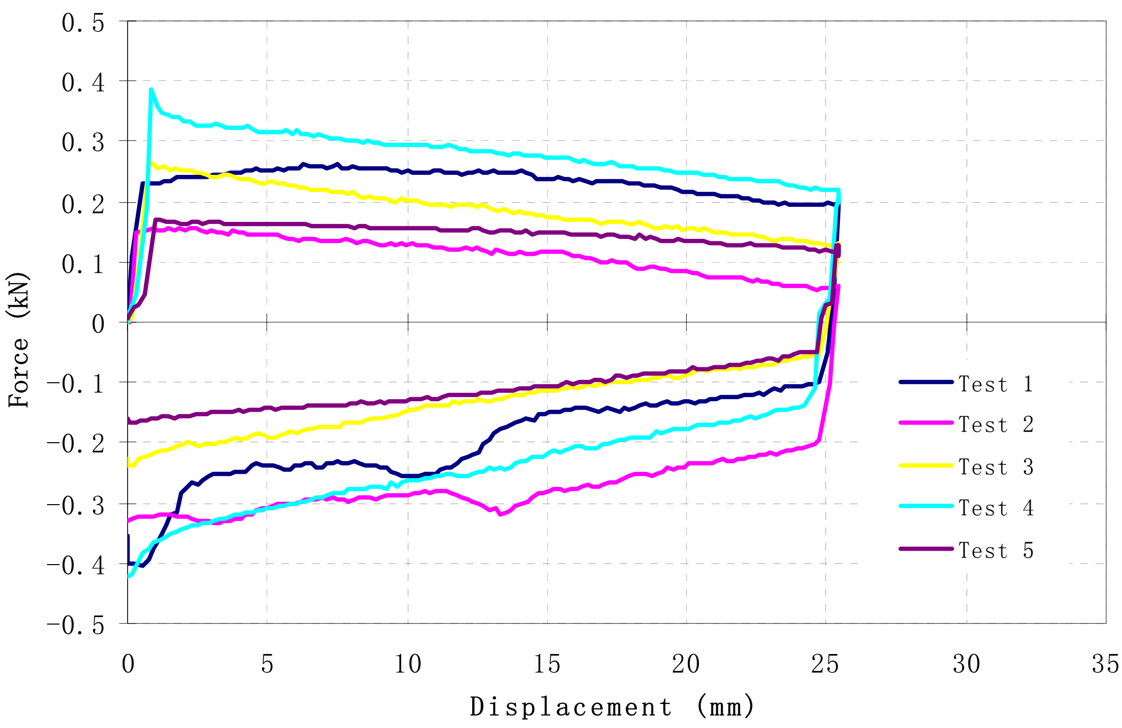

Figure 4.16 End-grain-withdraw Load-Displacement Curves

Table 4.4 End-grain-withdraw Performance Statistics

	Test 1	Test 2	Test 3	Test 4	Test 5	AVG	Standard Deviation
Load at Turning point (kN)	0.23	0.15	0.26	0.39	0.17	0.24	0.08
Displacement at Turning Point (mm)	0.53	0.28	0.74	0.84	0.97	0.67	0.24
Capacity (kN)	0.26	0.16	0.26	0.39	0.17	0.25	0.08
Displacement at the capacity point (mm)	6.30	2.41	0.74	0.84	0.97	2.25	2.11
Residual Force (kN)	-0.40	-0.33	-0.24	-0.42	-0.17	-0.31	0.10
Initial Stiffness or Static friction coefficient (kN/mm)	0.44	0.53	0.36	0.46	0.18	0.39	0.12

The results showed that the end-grain-withdraw connection performed just like a friction element. The variability of the outcome data is very large. From the results, the average capacity of one end-grain-withdraw connection was 0.25 kN (55.73 lb). In the real test, because of the transverse shear applied between studs and sill plate, the friction capacity of the nail joints could be strengthened. Four 16d common nails were used between the end studs and the sill plate and two used between the intermediate studs and the sill plate in the shear wall test specimens, which means that more than 1.0 kN (223 lb) extra capacity could be employed between the end studs and the sill plate and more than 0.5 kN (111.5 lb) between the intermediate studs and the sill plate on average. Compared with the capacity of each 8d common sheathing nail applied between sheathing panels and sill plate, which is about 1.24 kN (280 lb), the contribution of the end-grain-withdraw performance to the ultimate shear wall capacity is pretty large. Besides the capacity, the contributions to the shear wall residual capacity and the stiffness from the end-grain-withdraw performance are also very large when the test results are considered. This explained where the big difference between test and model results is from. From the pictures (Figure 4.17) of the tested specimens, partly because of the large end-grain-withdraw capacity, one of the end studs was not even separate from the sill plate before the cross-grain flexural failure and the along-grain split failure occurred in the sill plate.

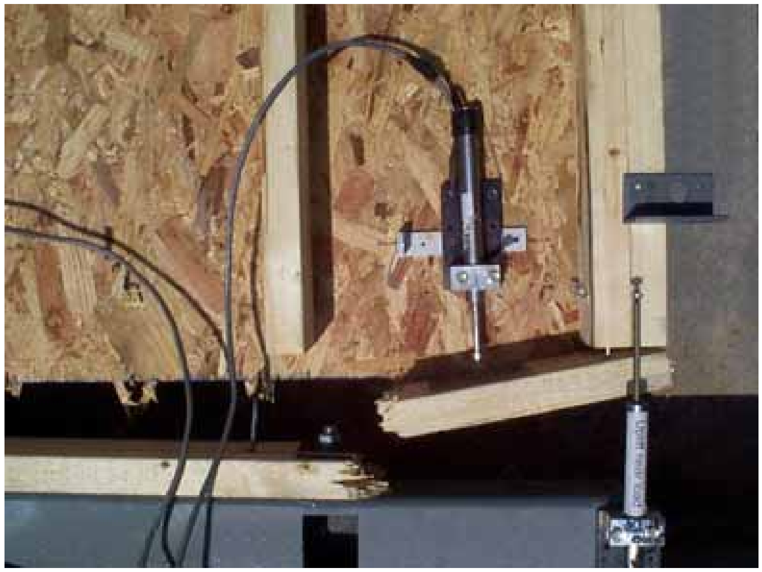

(a) Cross-grain Flexural Failure in Specimen 04Iac1

(b) Along-grain Split Failure in Specimen 04Iac1re

Figure 4.17 Pictures of the 4×8 ft Shear Walls with Intermediate Anchorage tested by Salenikovich (2000)

The cross-grain flexural failure and the along-grain split failure in the sill plate is also the reason why the hysteretic loops of the shear wall test results were not symmetric. However, in the model, the beam elements were all considered as linear elastic, and these failure modes were not considered.

The end-grain-withdraw capacity will decrease to a negligible level in real buildings because of the moisture content fluctuation in wood members. So the end-grain-withdraw issue will not affect real structures like mentioned above, and the model analysis without considering it will end up with conservative results. So it will be neglected in the following study.

The along-grain split failure and cross-grain flexural failure of the sill plate should be forbidden through construction improvement since these two failure modes are brittle and need to be prevented in real practice. In modeling, it can be represented through applying some nonlinear-inelastic material properties to the sill-plate beam elements. However, since it is not the main interest of this study, and the modification will increase the complication of the model and the computer time, the model was not modified.

The deformed shape and Mises Stress Contour are shown in Figures 4.18 and 4.19, respectively. The Mises Stress in the sheathing elements is much lower than that in the shear wall with tie-down anchors. This is because the shear wall with tie-down anchors resists lateral loads with the racking performance of the sheathing panel, while the sheathing performance in the shear wall without tie-down anchors is more like a rigid body rotation. The only attachment between the upper wall and the sill plate is the sheathing nails between sheathing panels and the sill plate.

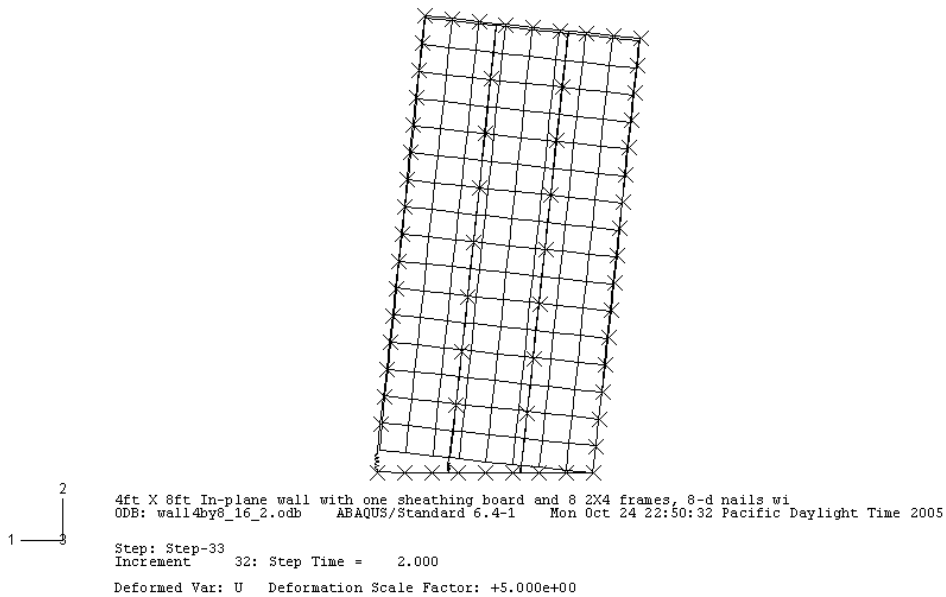

Figure 4.18 4×8 ft Shear Wall Deformed Shape (w/o tie downs)

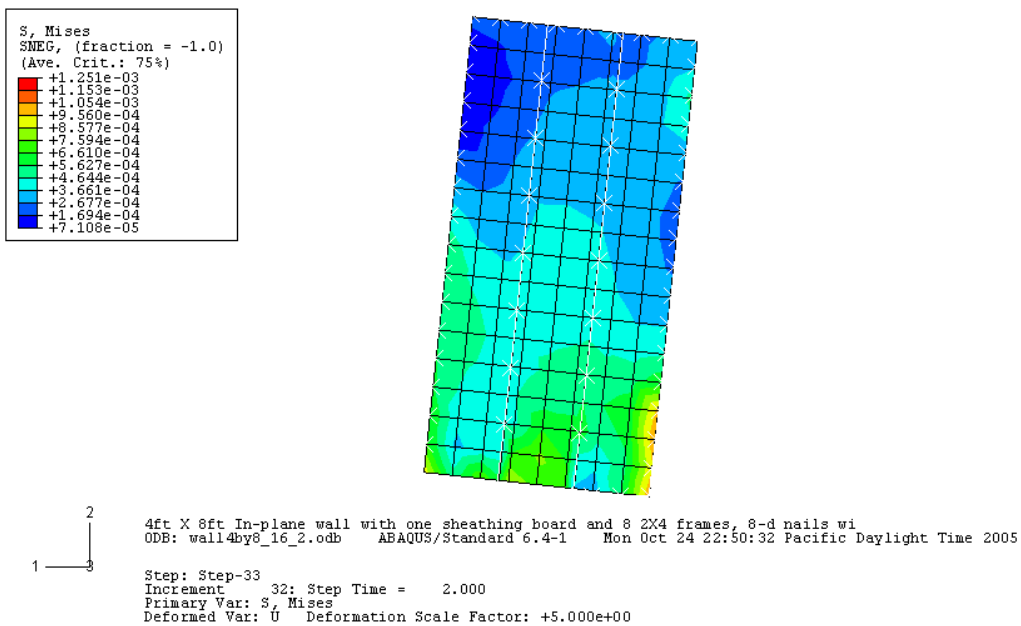

Figure 4.19 4×8 ft Shear Wall Sheathing Panel Mises Stress Contour (w/o tie downs)

4.3 12×8 ft Shear Wall Model (with an opening)

4.3.1 Introduction

To show the accuracy of the detailed model when used in shear walls with openings, a 3658×2438 mm (12×8 ft) wood-frame shear wall with an opening was simulated, and the outcome results were compared with the experimental results.

The tests were conducted for ***Simpson Strong Tie***. The framing for each specimen consisted of 38×89 mm (2×4 in.- Nominal) dry Douglas-fir (DF) lumber. End studs consisted of two members fastened by 10d (Φ3.8×76 mm) common nails every 0.6 m (2 ft.). The double top plate also consisted of two members, which were connected by 16d (Φ4.1×89 mm) common nails every 0.6 m (2 ft.). The header was constructed with two 38×286 mm (2×12 in.- Nominal) DF #2 boards with a 12 mm (15/32 in.) thick OSB spacer between. The lumbers and the OSB spacer were built up with 16d common nails at 406 mm (16 in.) on centers along each edge. The studs were attached to the single bottom plate and the double top plate with two 16d common nails at each end. A layer of 11 mm (7/16 in.) thick OSB sheathing (Rated Sheathing, Span Rating 24/16, Exposure 1) and a layer of 13 mm (1/2 in.) thick Gypsum board were attached to each wall side respectively. The OSB panels were attached by power-driven 8d (Φ3.3×63.5 mm) common nails at 152 mm (6 in.) on centers along the edges and 305 mm (12 in.) on centers along intermediate studs (Shown in Figure 4.20). The long dimension of the sheathing was oriented parallel to the studs on the two segments standing beside the opening symmetrically and perpendicular to the studs on the patch beneath the opening (Figure 4.19). The layout of the structural elements is shown in Figure 4.21. The Gypsum board panels were attached by $1\frac{1}{4}$-in Type W gypsum board screws at 304 mm (12 in.) on centers along the edges and 76 mm (3 in.) on centers at the opening corner areas (Shown in Figure 4.22). The structural details of the wall specimen can be seen in Table 4.5.

Two specimens were tested, one with tie-down anchors and the other without. The shear walls were tested in a vertical position, so the self-weights of the wall and the steel tube, which is attached to the top plates to apply the load, affected the test results of the specimen without tie-down anchors.

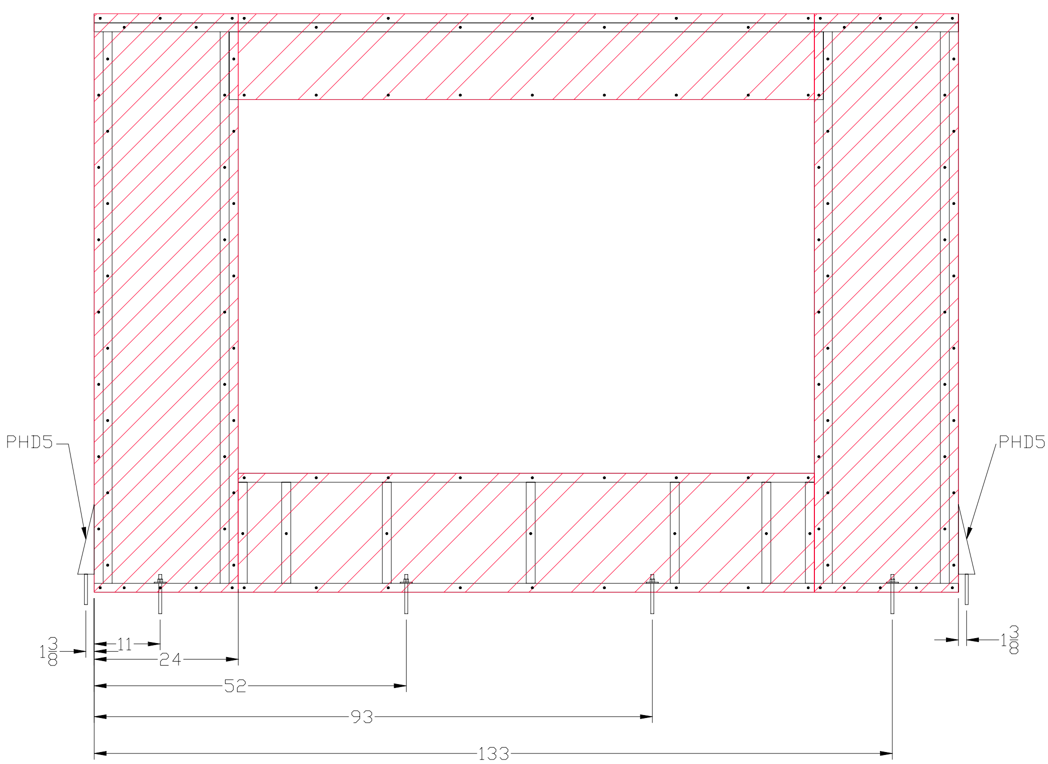

Figure 4.20 12×8 ft Shear Wall Fabrication

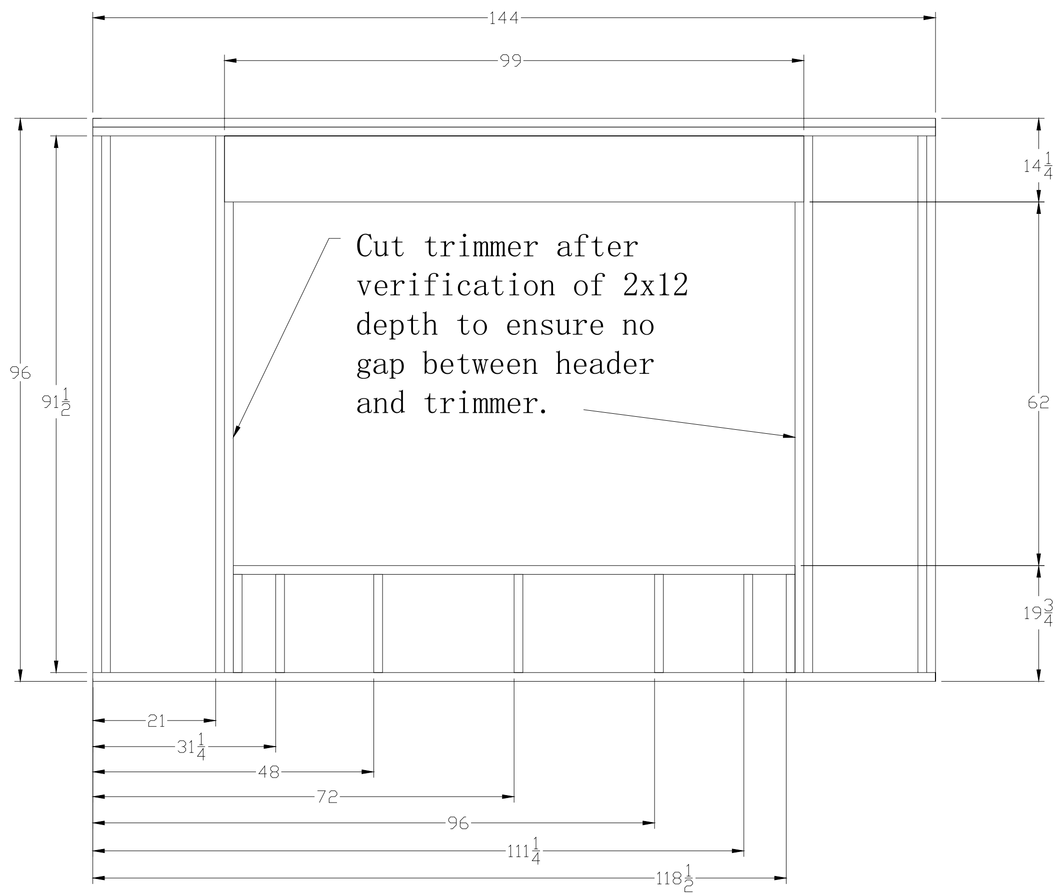

Figure 4.21 12×8 ft Shear Wall Element Layout

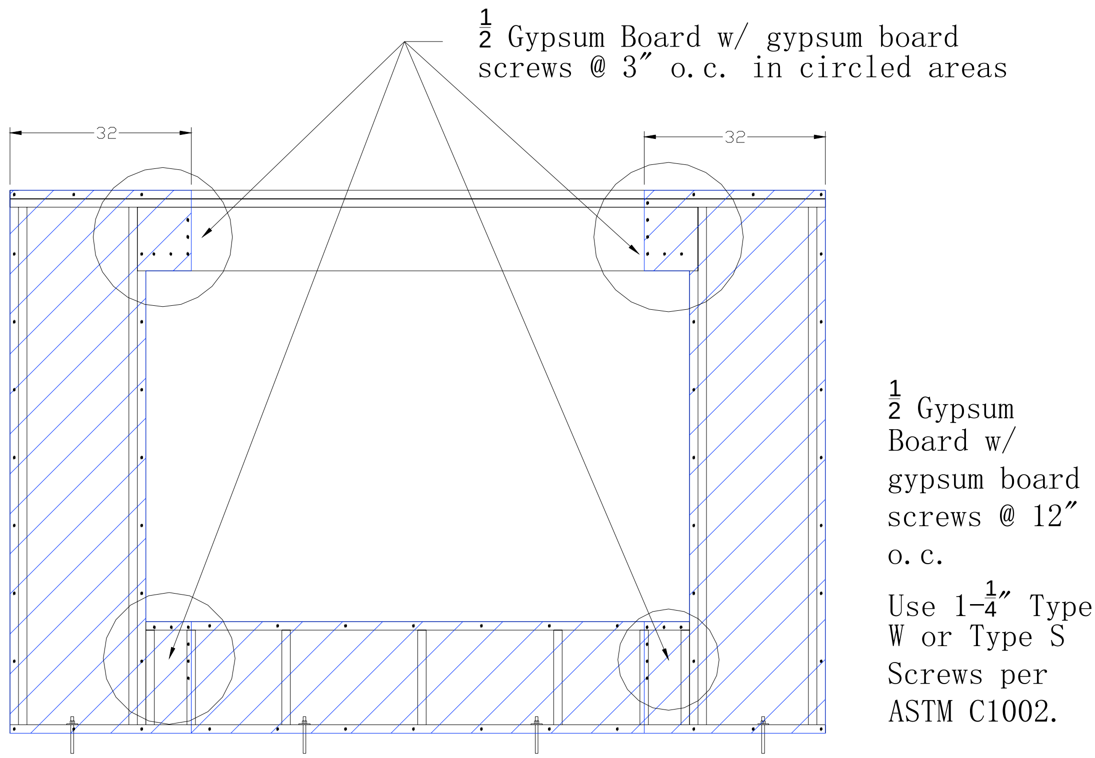

Figure 4.22 Gypsum Boards Installation in 12×8 ft Shear Wall

Table 4.5 Structural details of wall specimens

Component	Fabrication and materials
Framing	Douglas-Fir, S-Dry, 38×89 mm (2×4 in.-nominal); Intermediate studs at 610 mm (24 in.) o. c. Two extra studs at the both sides of the patch underneath the opening; Double studs at the ends of wall segments; Single bottom plate, double top plate.
Header	Two 38×286 mm (2×12 in.- Nominal) DF #2 lumbers with 12 mm (15/32 in.) thick OSB spacer between.
Sheathing	Non Structural I (OSB), 11 mm (7/16 in.) thick, two 610×2438mm (2×8 ft.), one 502×2438mm (1.65×8 ft.), and one 362×2438mm (1.19×8 ft.) sheets installed on the side segment, bottom segment, and the header face respectively; Attached on one side. 13 mm (1/2 in.) thick Gypsum boards, attached to the other side.
Framing attachment	Plate to plate: One 16d (∅4.1×89 mm) common nails each 2 feet; Stud to stud: One 10d common each 2 feet; Plate to stud: Two 16d common each end. Header: Two 16d (∅4.1×89 mm) common nails each 16 in.;
Sheathing attachment	For OSB: Power driven 8d (∅3.3×63.5 mm) nails at 152 mm (6 in.) o. c. (edge), 305 mm (12 in.) o. c. (field). For Gypsum Board: $1\frac{1}{4}$-in Type W or S gypsum board screws at 304 mm (12 in.) on centers along the edges and 76 mm (3 in.) on centers at the opening corner areas.
‘Full anchorage’	Simpson PHD5-SDS3 (See Simpson Strong-Tie Catalog C-2005 for installation requirements). 13-mm (1/2-in.) diameter A307 bolt to connect to foundation; 13-mm (1/2-in.) diameter A307 bolts at 1041 mm (41 in.) o. c. with 51×51×4.8 mm (2×2×0.188 in.) flat plate washers and standard size nuts.
‘Intermediate anchorage’	13-mm (1/2-in.) diameter A307 bolts at 1041 mm (41 in.) o. c. with 51×51×4.8 mm (2×2×0.188 in.) flat plate washers and standard size nuts.

4.3.2 Shear Wall with Full Anchorage

The same framing, sheathing, and nail connector elements were used in this model as those used in the former 1219×2438 mm (4×8 ft) shear wall model. The end studs’ uplifts were restricted at the corners where tie-down anchors are used.

In this model, since there is no data available for the hysteretic performance of the gypsum board screw connectors, the gypsum sheathing panels were not included. The same sequential phased displacement (SPD) protocol used in the testing (shown in Figure

4.23) was applied on the top plates of the modeled shear wall. The hysteretic loops of the test result are shown in Figure 4.24, and the outcome hysteretic loops from the model analysis are shown in Figure 4.25. The comparison between test results and model analysis results is shown in Figure 4.26. These diagrams showed that the load capacity, stiffness, and energy-dissipation capacity of the modeled shear wall are all lower than those from the test results. This is because that the effect of the gypsum sheathing was not taken into account.

The deformed shape is shown in Figure 4.27. The corresponding Mises Stress distribution diagram is shown in Figure 4.28.

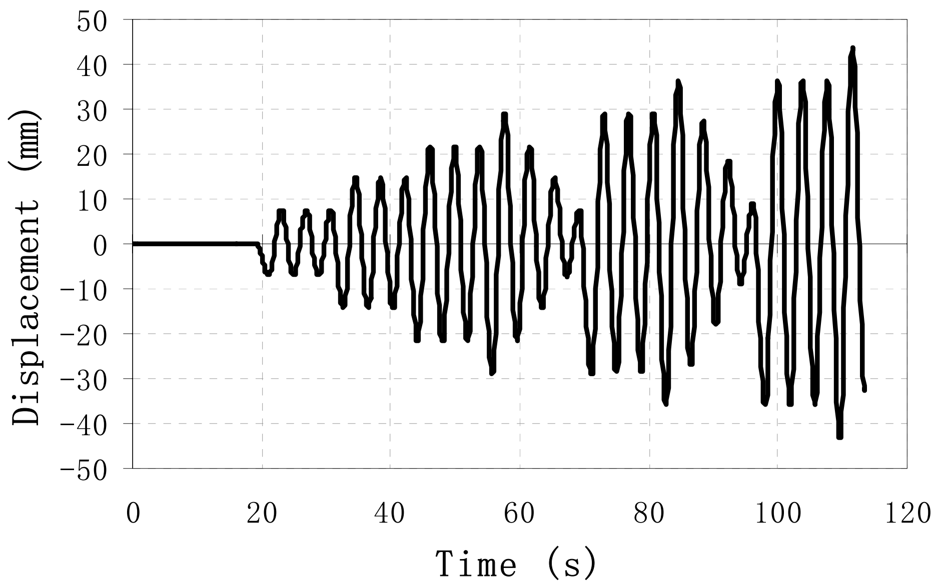

Figure 4.23 Sequential Phased Displacement (SPD) Protocol

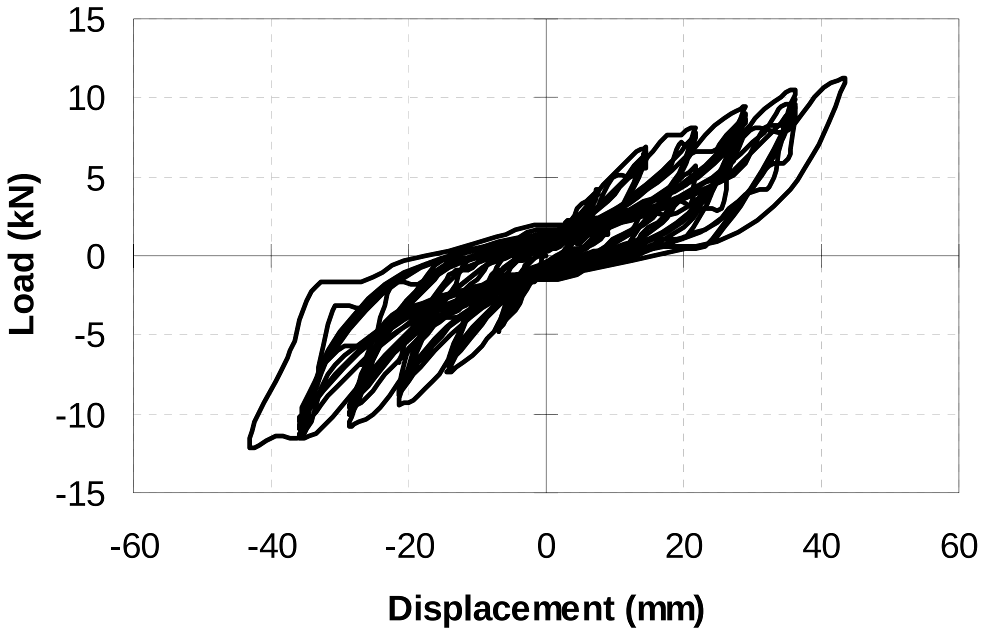

Figure 4.24 12×8 ft Shear Wall Hysteretic Loops from Testing (w/ tie downs)

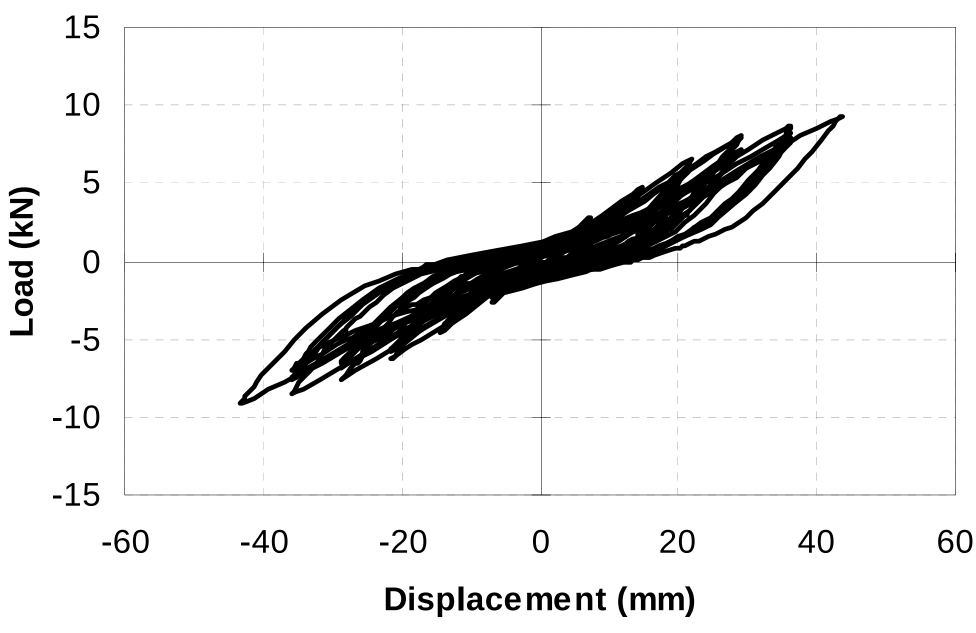

Figure 4.25 12×8 ft Shear Wall Hysteretic Loops from Model Analysis (w/ tie downs)

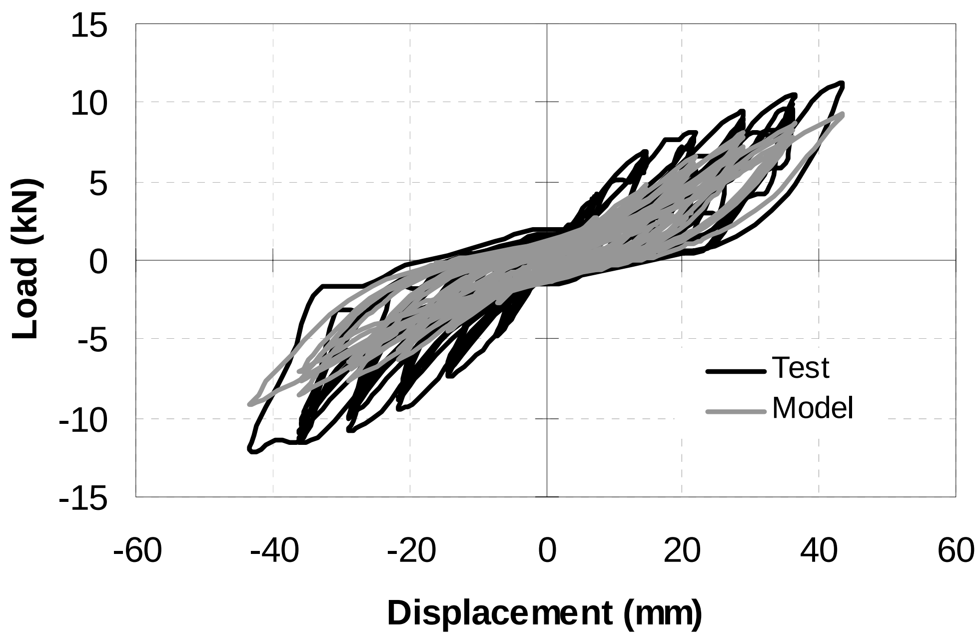

Figure 4.26 Comparison of 12×8 ft Shear Wall Hysteretic Loops (w/ tie downs)

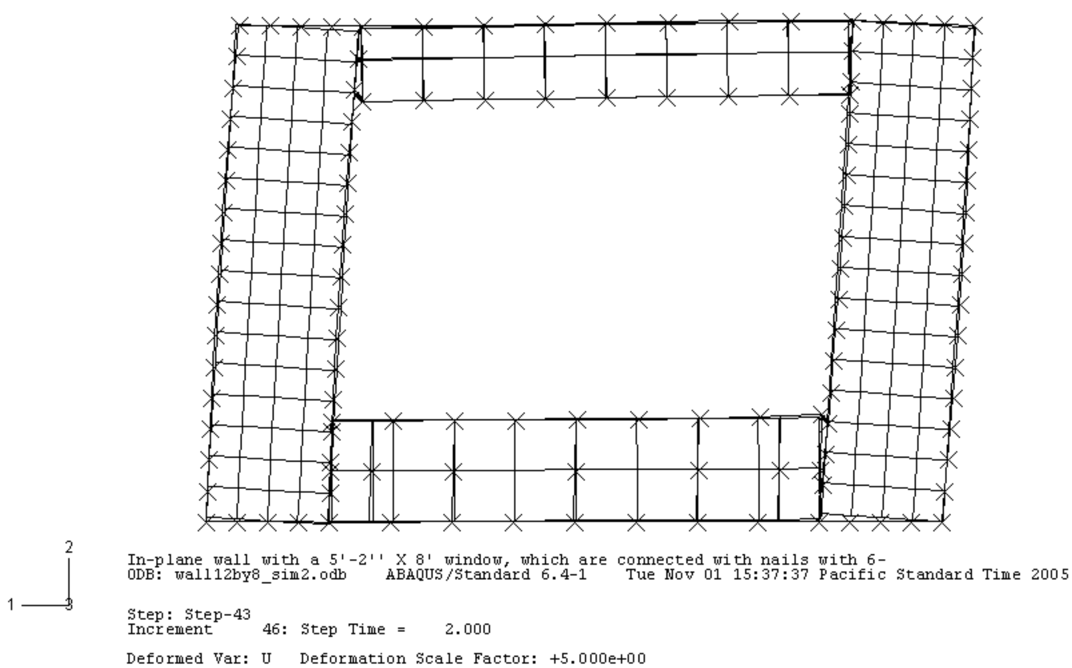

Figure 4.27 12×8 ft Shear Wall Deformed Shape (w/ tie downs)

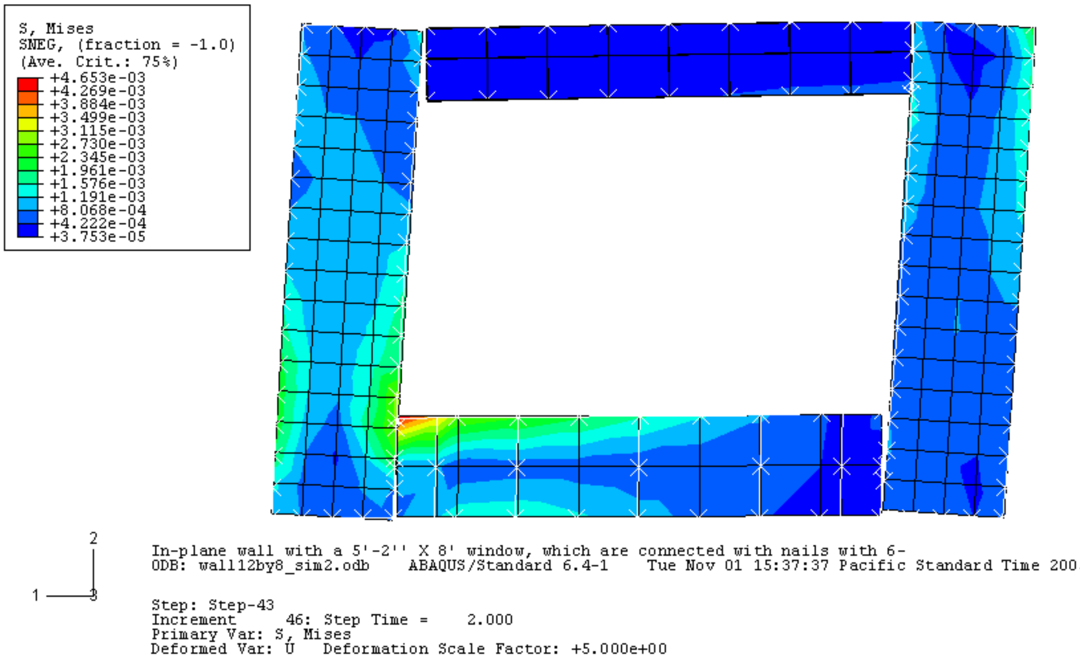

Figure 4.28 12×8 ft Shear Wall Sheathing Panel Mises Stress Contour (w/ tie downs)

The contribution of the gypsum board to the shear wall performance can be shown through tests of two shear walls, one with only OSB sheathing attached and the other with both OSB and gypsum board attached. Toothman (2003) did a series of 1219×2438 mm (4×8 ft) light-frame shear walls with tie-downs and without tie-downs. The sheathing materials investigated included OSB, hardboard, fiberboard, and gypsum wallboard. This study obtained and compared performance characteristics of each sheathing material, especially investigated the contribution of gypsum in walls with dissimilar sheathing materials on opposite sides of the wall. The sheathing materials and nailing schedule are shown in Table 4.6. The same OSB sheathing panels and sheathing nailing schedule was used on the OSB sheathing side as those used in the 3658×2438 mm (12×8 ft) shear wall tests, while different fasteners and spacing schemes were used on the gypsum sheathing side. Other detailed shear wall construction information can be found in Toothman's thesis (2003). Since this is the only relevant test data available at hand, although there were some differences in the gypsum board attachment from the modeled 3658×2438 mm (12×8 ft) shear wall, the test results are employed here to represent the capacity contribution percentage from gypsum board.

The 1219×2438 mm (4×8 ft) shear wall test results are shown in Figure 4.29. The load envelopes of the walls with both OSB and gypsum board and with OSB only are shown in Figure 4.30. To be comparable, the envelopes for the 3658×2438 mm (12×8 ft) shear wall tests are presented in Figure 4.31. The ratios of the envelope loads at different displacements for both the 1219 × 2438 mm (4 × 8 ft) shear wall and the 3658 × 2438 mm (12 × 8 ft) shear wall are shown in Figure 4.32. From the comparison, if it is assumed that the contribution percentage from gypsum attachment is similar for the two wall configurations, the hysteresis obtained from the simulation is reasonable.

Table 4.6 Sheathing materials and nailing schedule (courtesy to Toothman (2003))

Sheathing Type		**Nail Spacing (o.c.)**		
Material	**Thickness**	**Edge**		**Field**
OSB	11mm (7/16 in.) per US VPA DOC PS-2	8d common (φ3.33mm x 63.5mm long) (φ0.131” x 2 ½” long)	152mm (6in.)	305mm (12in.)
Gypsum (GWB)	12mm (½ in.) per ASTM C36	11ga. Galv. roofing nail (φ3 x 38mm long x φ9.5mm head) (0.12”φ x 1 ½”long x 3/8”φ head)	178mm (7in.)	406mm (16in.)

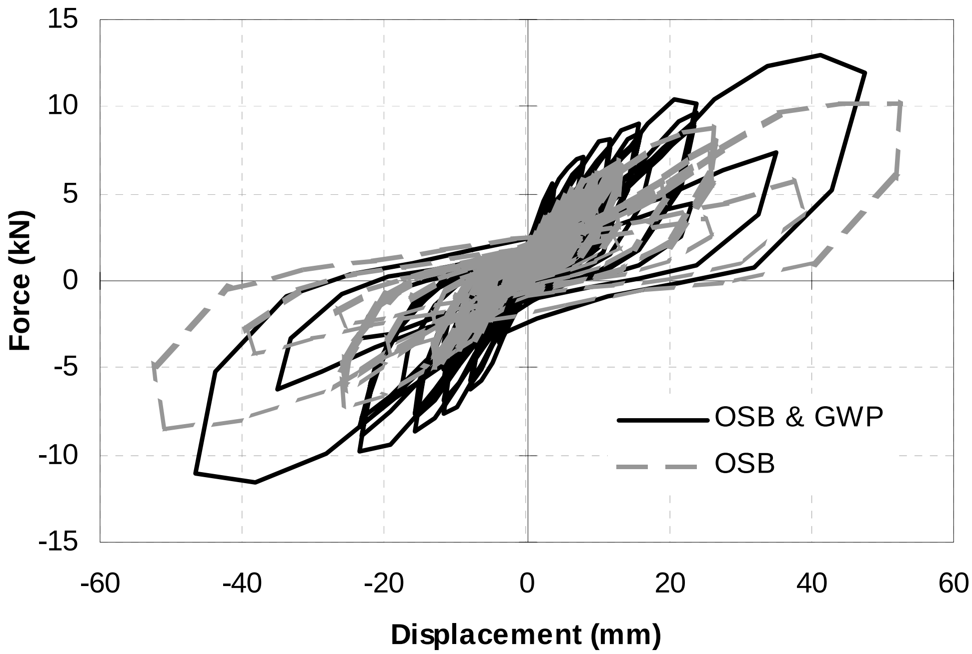

Figure 4.29 Tested 4×8 ft Shear Wall Hysteretic Loops (w/ tie downs)

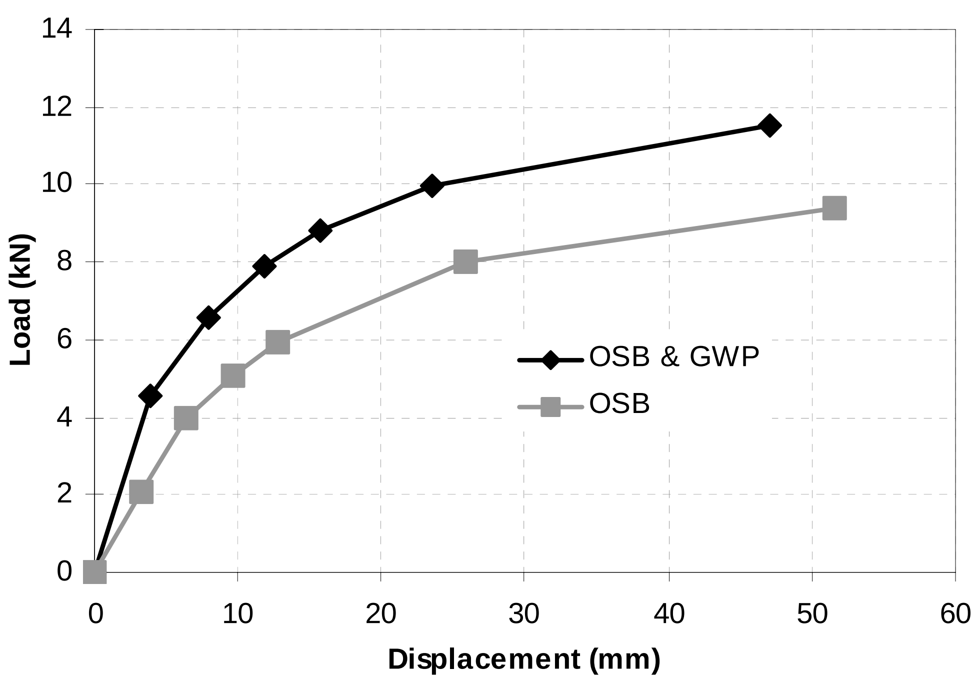

Figure 4.30 Tested 4×8 ft Shear Wall Load Envelopes (w/ tie downs)

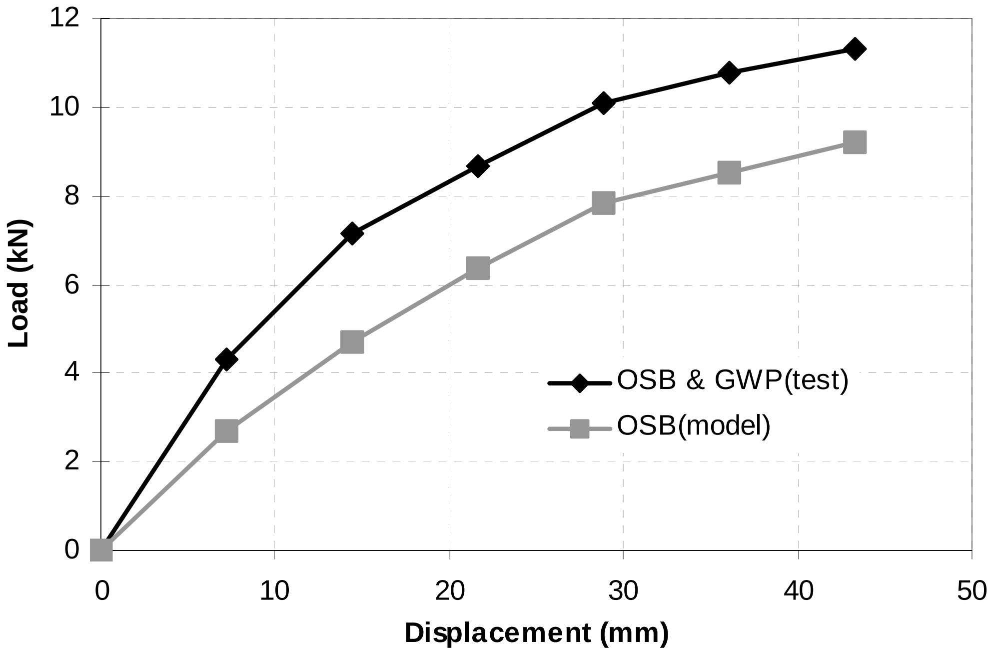

Figure 4.31 12×8 ft Shear Wall Load Envelopes (w/ tie downs)

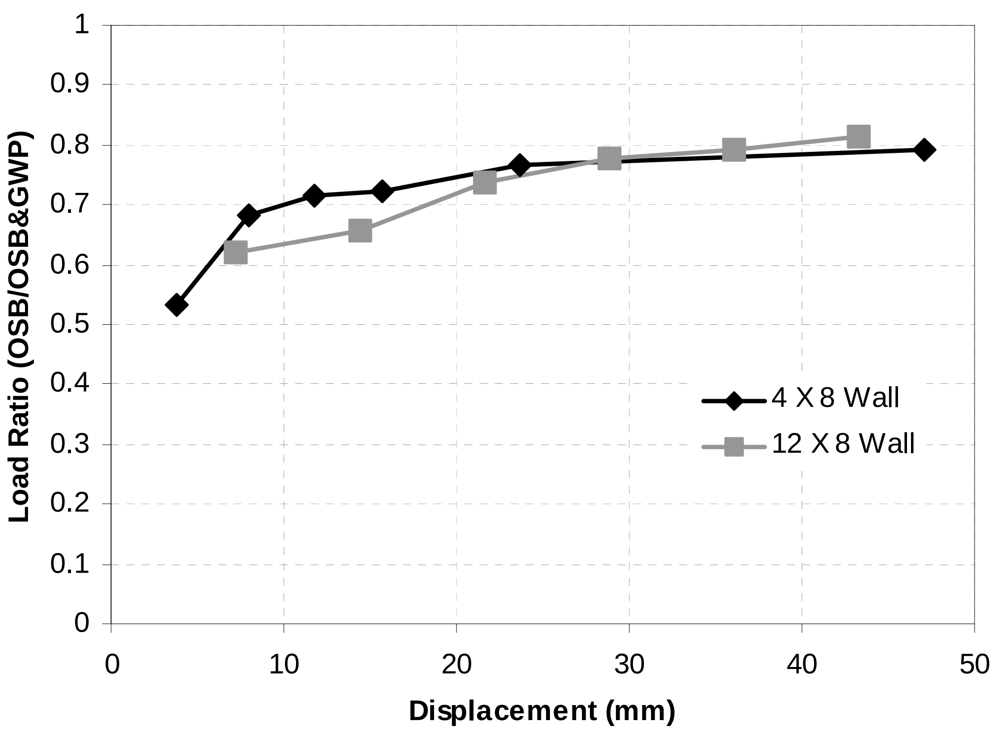

Figure 4.32 Load Ratio Comparison (w/ tie downs)

4.3.3 Shear Wall with Intermediate Anchorage

Since the shear wall was tested in the vertical position, the weight of the wall and the steel tube (load distributor) can be beneficial to the shear wall's performance when there are no tie-down anchors presented. The self-weight was taken into account by adding a nonlinear spring between each stud and sill plate besides the bearing spring. The stiffness of the spring was set to be large before uplift load reaches the self-weight portion assigned to the relevant stud and to be equal to zero after that.

The comparison of test and model results can be seen in Figure 4.33. The deformed shape and Mises stress contour in the sheathing panels can be seen in Figures 4.34 and 4.34 respectively.

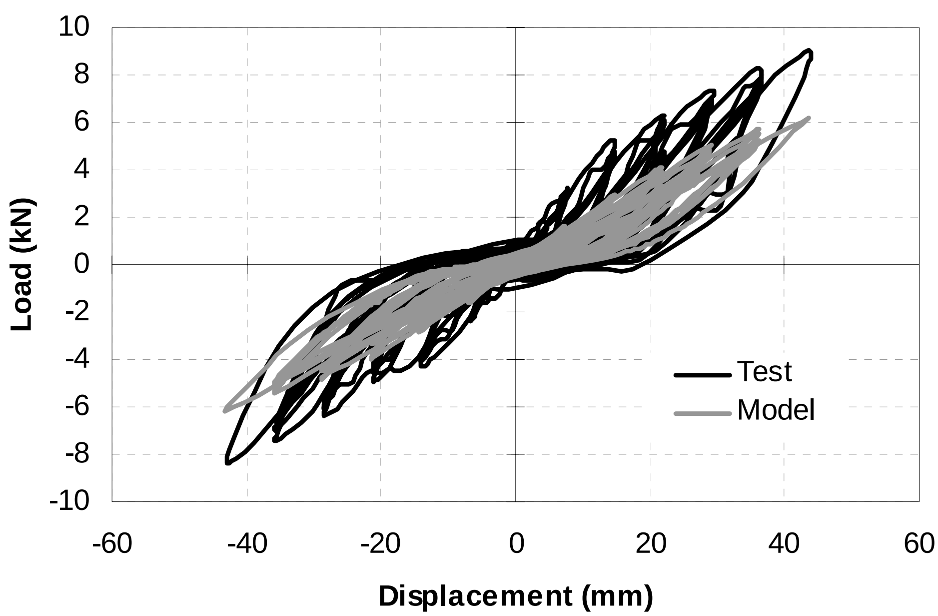

Figure 4.33 Comparison of 12×8 ft Shear Wall Hysteretic Loops (w/o tie downs)

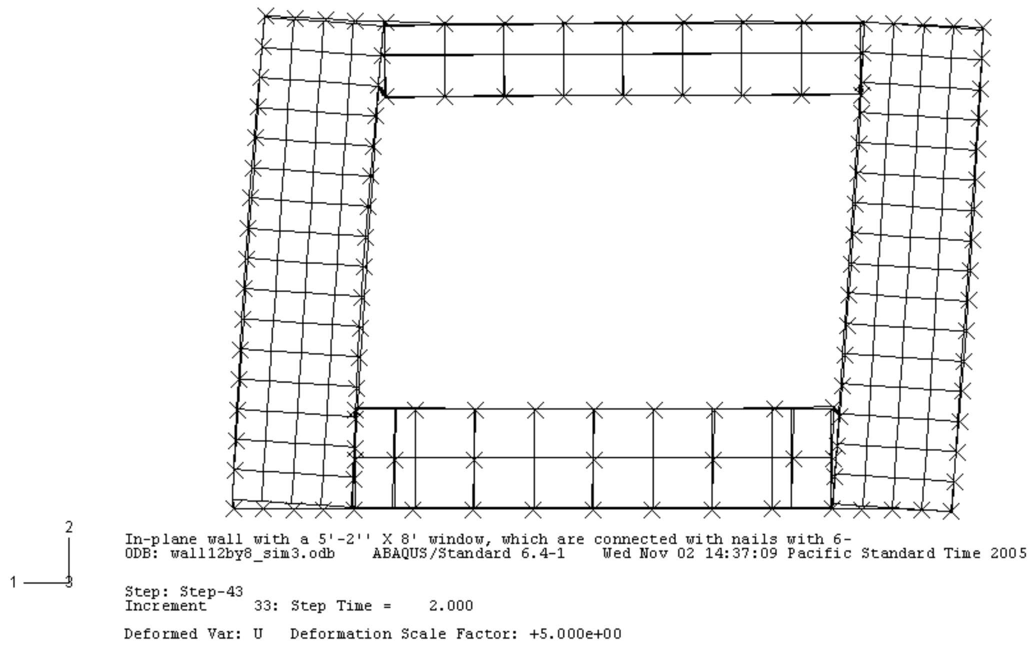

Figure 4.34 12×8 ft Shear Wall Deformed Shape (w/o tie downs)

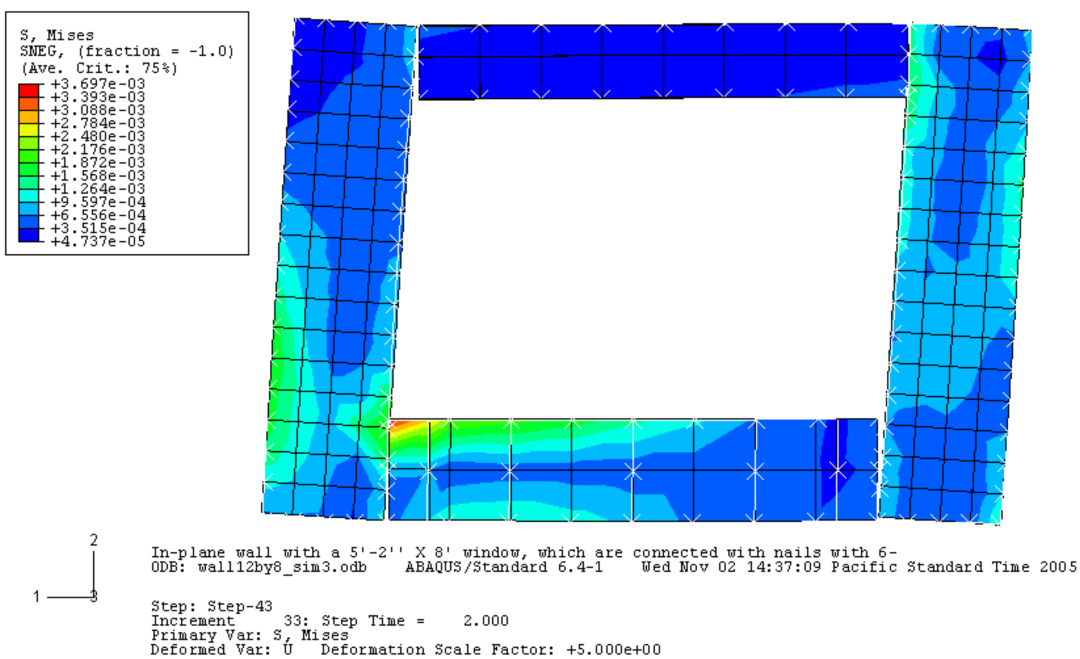

Figure 4.35 12×8 ft Shear Wall Sheathing Panel Mises Stress Contour (w/o tie downs)

The tested ultimate capacity of the shear wall with intermediate anchorage is only 20% less than that of the specimen with full anchorage. This reduction is much less than what occurred in the 1219 × 2438 mm (4 × 8 ft) solid shear wall case (63%) because only one side of each vertical segment was tied down and the intermediate lateral segment can restrain the uplift of vertical segments.

The difference between the experimental and model results of the 3658×2438 mm (12×8 ft) shear wall is due to ignorance of the contribution from end-grain withdraw capacity and the connectors between gypsum boards and sill plate, etc. Because of the complexity of the wall layout (e.g. it is hard to know the exact interaction behavior between vertical segments and intermediate segments), it is hard to accurately analyze the difference theoretically.

4.4 Summary

Using the developed nail joint element, two detailed shear wall configurations were simulated in ABAQUS/Standard. Two boundary conditions (full anchorage and intermediate anchorage) were considered for both shear wall configurations. The comparison between the experimental and numerical results proved the accuracy of the hysteretic nail joint element.

Chapter 5
Super FEM Shear Wall Model

5.1 General

In a detailed wood-frame shear wall or a whole 3-D building model, hundreds or even thousands of nail connector elements must be used. This is not computationally efficient to model every nail connector independently. A super shear wall model is the model that can represent the hysteretic behavior of a whole shear wall when subjected to lateral loads.

The super shear wall model can consist of the framing members and a single hysteretic spring connecting top plate and sill plate (Figure 5.1). This modeling method is simple. However, this model can only represent the racking behavior of the shear wall and cannot take the overturning into account.

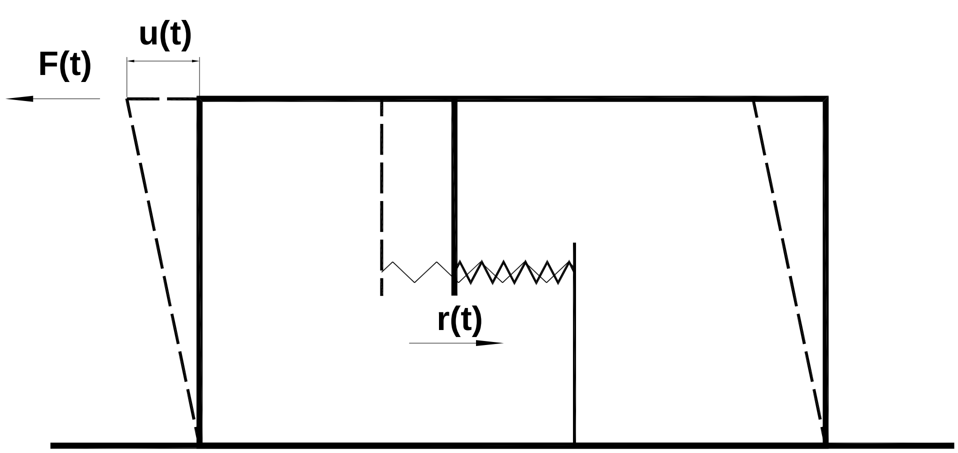

Figure 5.1 Single-spring Super Shear Wall Model

Another method is to represent the shear wall as a pair of diagonal hysteretic springs

(Figure 5.2), which was put forward by Kasal (1992, 1994). This method was also used by Du (2003) in her study on the evaluation of embedded fluid dampers within light-frame structures under seismic loading.

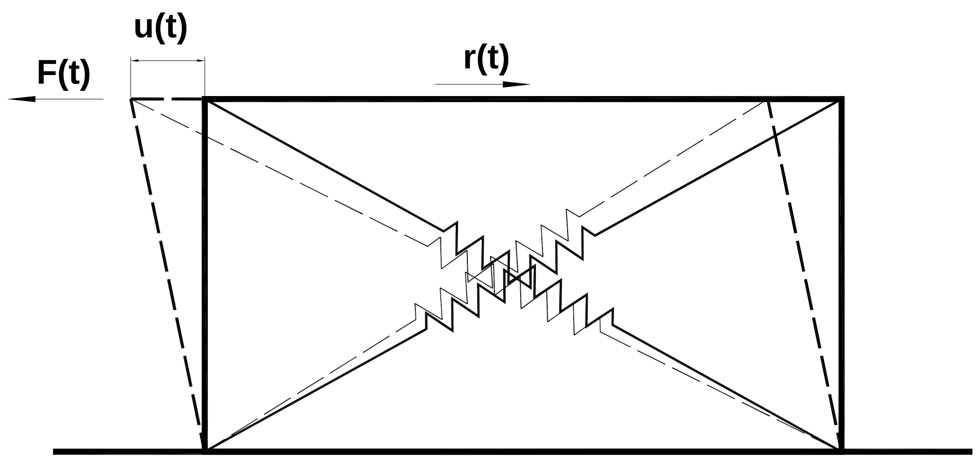

Figure 5.2 Diagonal-spring Super Shear Wall Model

In this study, the super shear wall model consists of all the framing elements and a pair of diagonal hysteretic spring elements which connect the 4 ends of the end studs. The overturning behavior can be considered by putting hysteretic springs between the bottom of studs and the sill plate (Figure 5.3). The properties of these springs are based on the type and number of the nails connecting sheathing panels to the sill plate. The forces within the diagonal springs tend to pull the studs at one side and push the studs at the other side to the sill plate when shear wall is subjected to lateral loads. So the model can take the racking and overturning behavior into account at the same time. With this model, the restraint effect supplied by the perpendicular walls at the corners can be represented accurately.

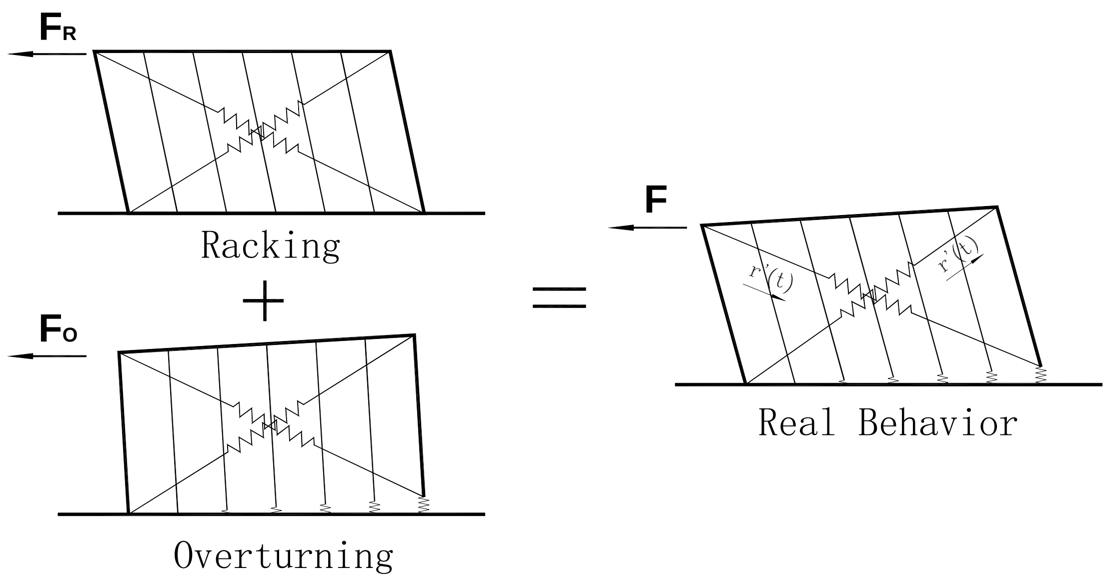

Figure 5.3 Super Shear Wall Model Considering Overturning Effect

5.2 Model Development

Since the hysteretic behavior of a wood-frame shear wall is governed by the behavior of the nail connectors, the model used for a single nail connector can also be employed in the super shear wall model with some modifications, which are:

Equation 3-5 being changed into:

$$\alpha = \alpha_0 \cdot e^{(-0.01 \cdot M\_Dis)} \tag{5-1}$$

Equation 3-17 being changed into:

$$h(z) = 1.0 - \zeta_1 \cdot e^{[-(z \cdot \mathrm{sgn}(\dot{u}(t)) - ratio \cdot q \cdot z_u)^2 / \zeta_2^{1.5}]} \tag{5-2}$$

The other equations remain the same.

It is easy to estimate the parameters for the hysteretic spring in the single-spring model (Figure 5.1) based on the hysteresis drawn from experimental results or detailed shear wall model analysis results because the displacement and force in the single spring are the same as those of the global shear wall. The same GA program used for single nail connector element can be employed for the parameter estimation purpose. The stiffness and force at time, t, in the spring are *K(t)* and *r(t)* respectively.

The parameters estimated for the single-spring shear wall model can be employed for each diagonal hysteretic spring in the diagonal-spring shear wall model directly. The racking performance and the force distribution in springs was shown in Figure 5.4. However, some modifications were made on the stiffness and resistant force in each diagonal spring based on the geometry of the shear wall. In the solver for each diagonal spring, the shear wall drift *u(t)* is used as the input, and the resultant force and stiffness of the spring are divided by ($2 \cdot |\cos(\theta_{SW})|$), which means the resistant stiffness and the resistant force within each diagonal spring are:

$$K'(t) = \frac{K(t)}{2 \cdot |\cos(\theta_{SW})|} \tag{5-3}$$

$$r'(t) = \frac{r(t)}{2 \cdot |\cos(\theta_{SW})|} \tag{5-4}$$

According to the geometry conditions, the stiffness and the force of the super shear wall will be just *K(t)* and *r(t)* respectively.

Two assumptions were made as the basis of the modifications: 1) The shear wall's racking displacement amount is far less than the height and the length of the walls; 2) The stretches and withdraws of the frame members are very small compared with the shear wall's racking displacement. For most shear walls, the assumptions stand. In accordance with the two assumptions above, $\Delta\theta_{SW}$ (Figure 5.4) is pretty small, so its influence on the geometry is negligible, and the vertical displacement of the wall caused by the tension and compression in frames are negligible.

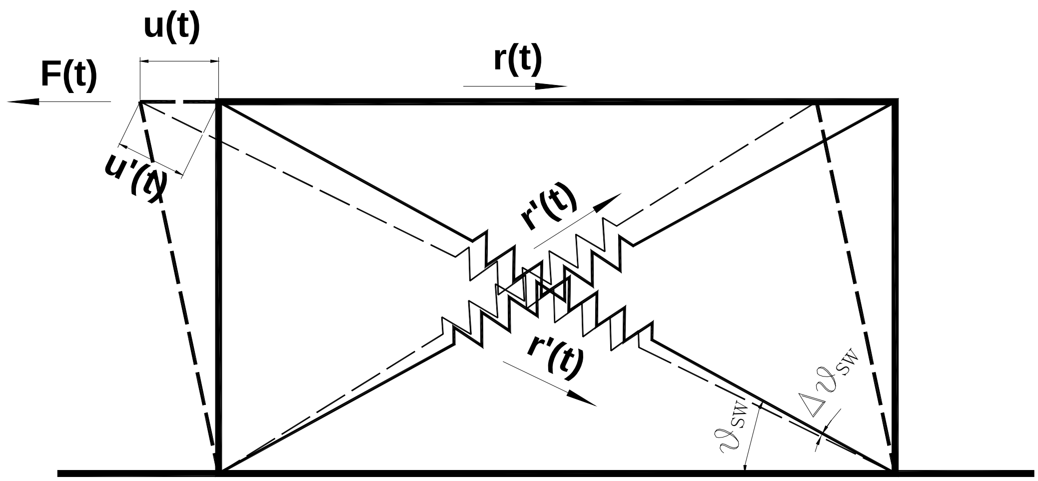

Figure 5.4 Racking of Diagonal-Spring Shear Wall Model

5.3 Model Validation

Experimental and detailed model analysis results of the two shear wall configurations mentioned in Chapter 4 were used here for the super shear wall model validation.

Figures 5.5 through 5.8 show the comparison of the hysteretic loops and hysteretic energy between the test results or detailed shear wall model analysis results and the super shear wall model results. The suitable parameter sets for each super shear wall spring were also presented in the relevant figures. The parameter estimations in Figures 5.5 and 5.6 are in accordance with the test data (shown in Figures 4.7 and 4.24, respectively), and the parameter estimations in Figures 5.7 and 5.8 are in accordance with the detailed shear wall analysis results (shown in Figures 4.8 and 4.25, respectively).

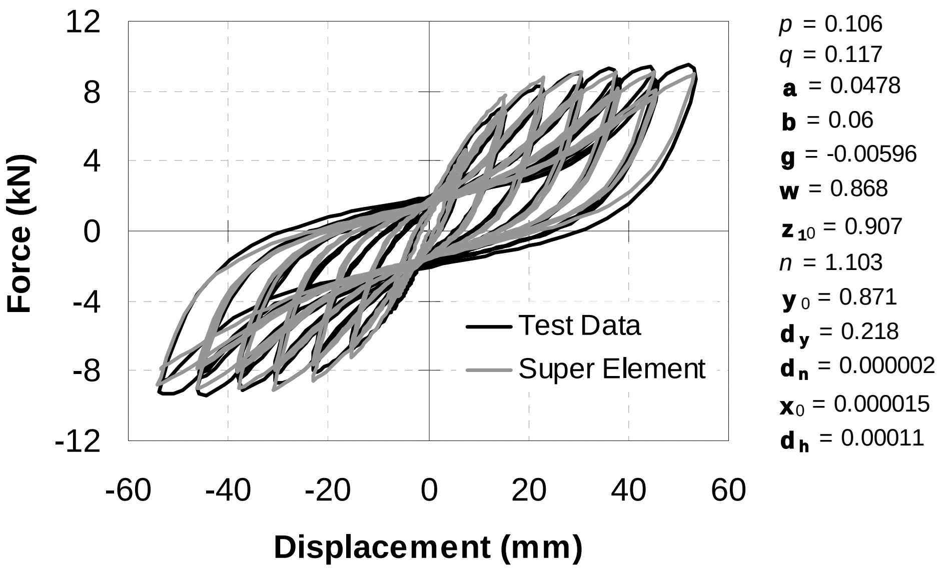

(a) Parameter Estimation & Comparison of Hysteretic Loops

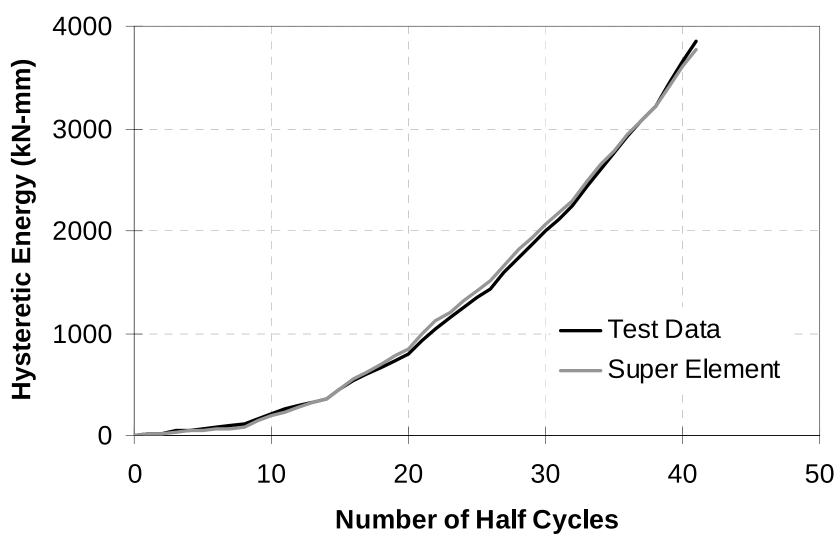

(b) Comparison of Hysteretic Energy

Figure 5.5 4×8 ft Solid Shear Wall Validation (according to test data w/ hold downs)

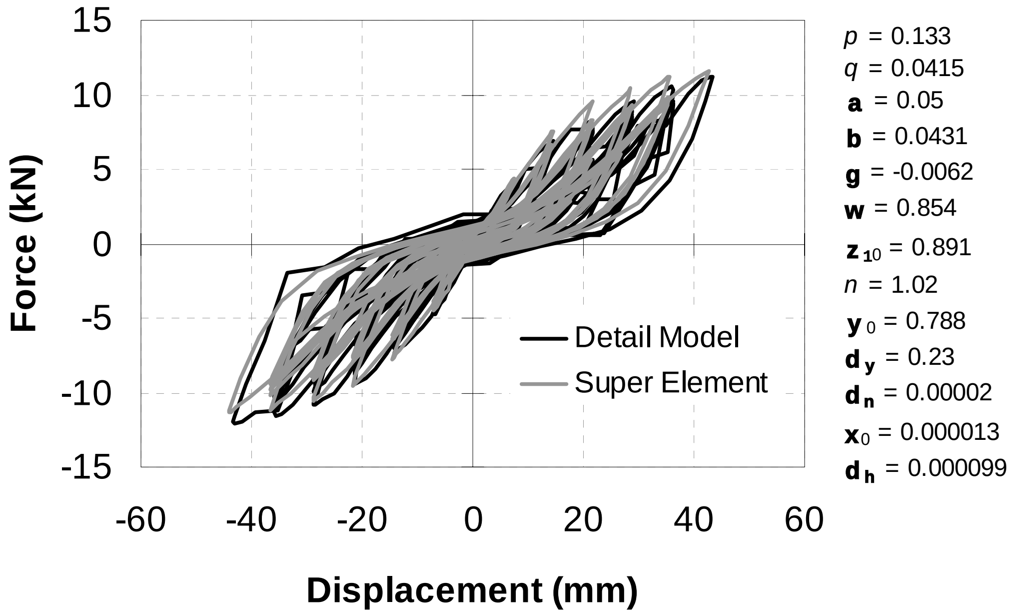

(a) Parameter Estimation & Comparison of Hysteretic Loops

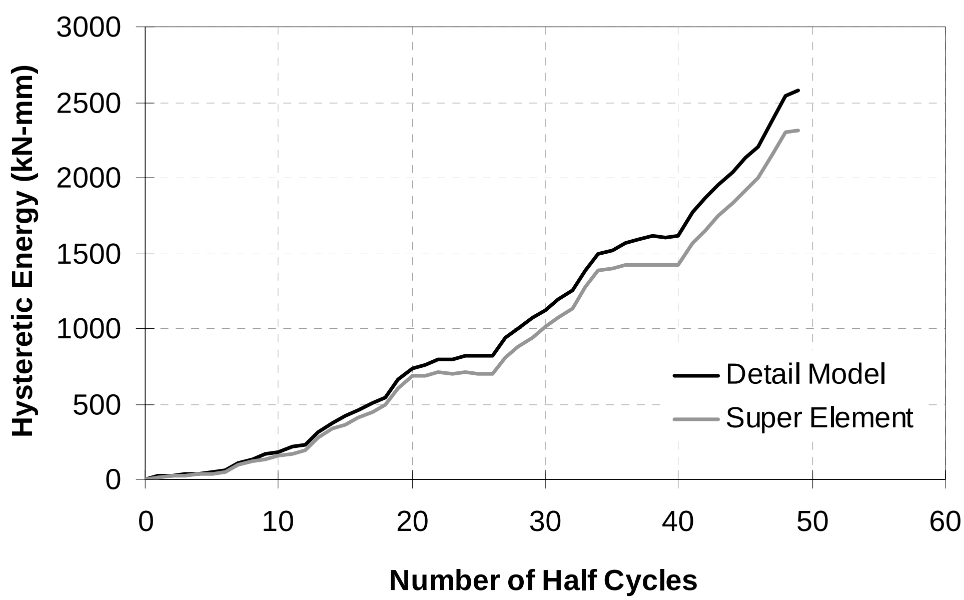

(b) Comparison of Hysteretic Energy

Figure 5.6 12×8 ft Open Shear Wall Validation (according to test data w/ hold downs)

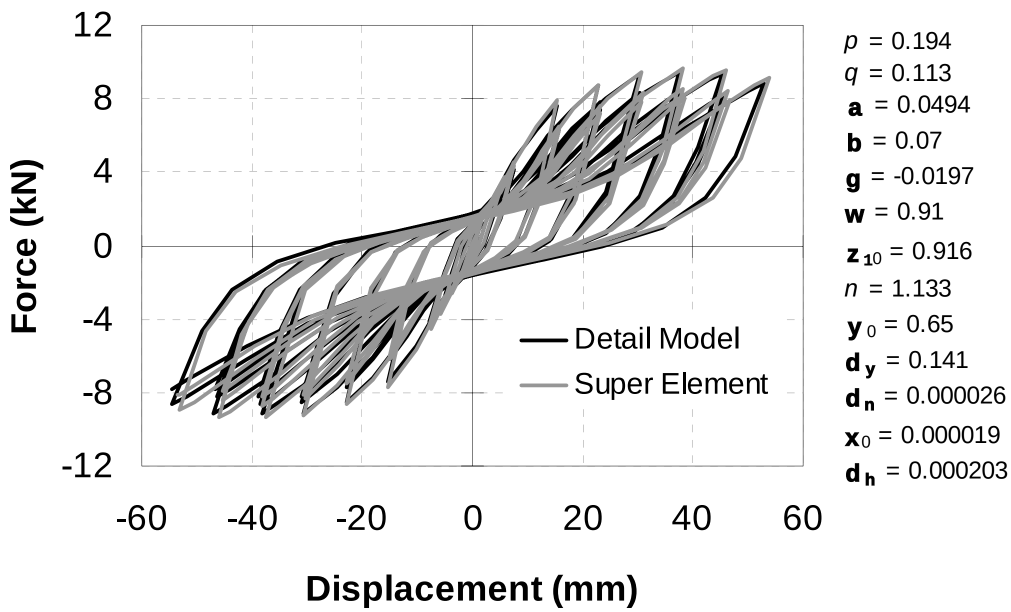

(a) Parameter Estimation & Comparison of Hysteretic Loops

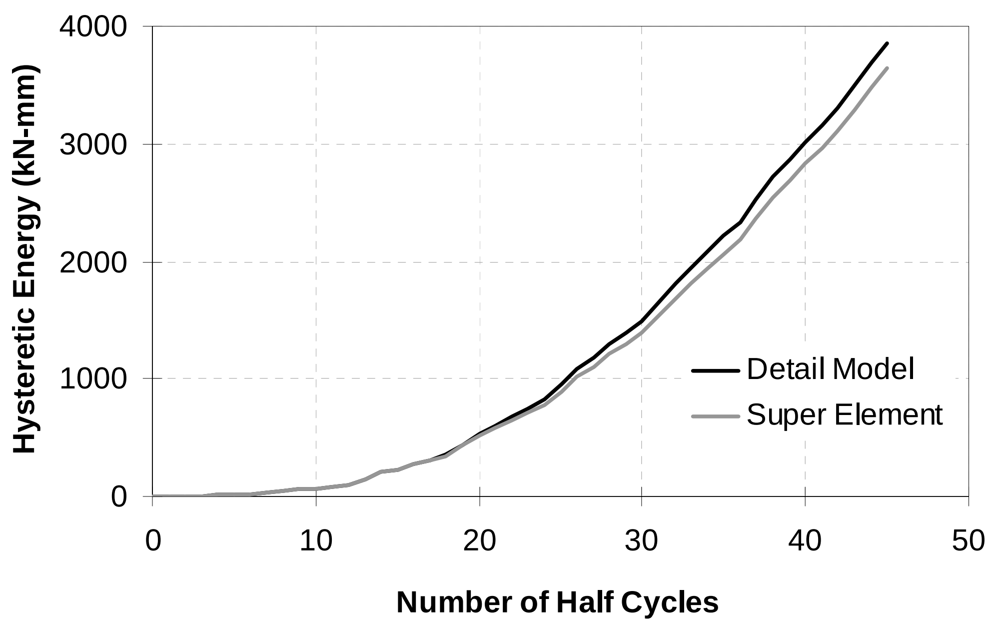

(b) Comparison of Hysteretic Energy

Figure 5.7 4×8 ft Solid Shear Wall Validation (according to detailed wall model analysis results w/ hold downs)

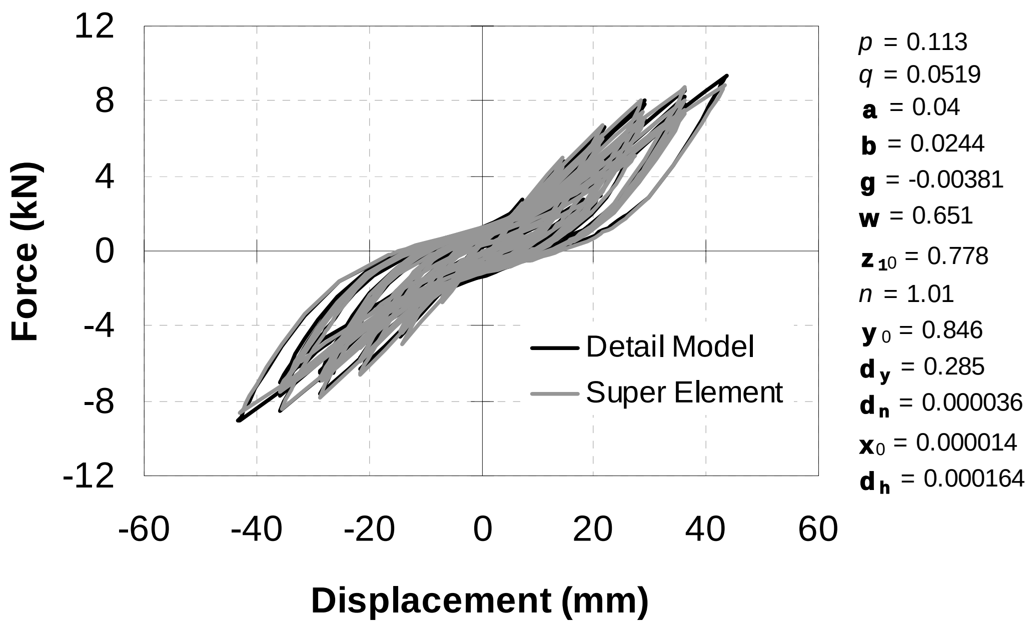

(a) Parameter Estimation & Comparison of Hysteretic Loops

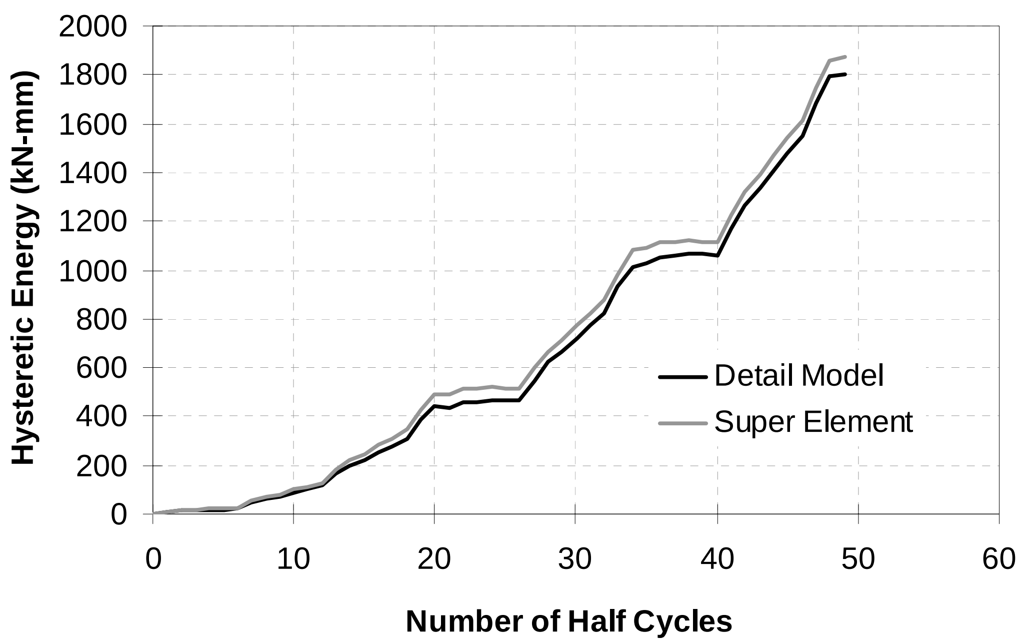

(b) Comparison of Hysteretic Energy

Figure 5.8 12×8 ft Open Shear Wall Validation (according to detailed wall model analysis results w/ hold downs)

The accuracy of the model was quantified through the comparison of peak load, peak hysteretic energy, and the correlation coefficient (definition and equations are shown in Appendix A) between the experimental and simulation results (Table 5.1).

Table 5.1 Quantification of Model Accuracy

Case	4×8 ft Wall		12×8 ft Wall	
	From test data	From detailed shear wall analysis	From test data	From detailed shear wall analysis
Error in Peak Force	-3.71%	1.72%	3.58%	-5.09%
Error in Peak Hysteretic Energy	-1.94%	-5.54%	-10.01%	3.94%
Correlation Coefficient	0.997	0.999	0.995	0.998

The comparisons showed a satisfactory performance of the super shear wall model.

With this super shear wall model, it will be much easier to simulate a whole 3-D wood-frame structure with sufficient accuracy, and the research on the system response to various lateral loadings can be handled efficiently.

5.4 Summary

With some modifications being made on the nail joint model, a super shear wall model was developed. Experimental and detailed shear wall model analysis results of the two shear wall configurations simulated in Chapter 4 were used for the purposes of the super shear wall model validation. The comparisons showed that the super shear wall model can simulate shear wall hysteretic response very well.

Chapter 6
3-D Wood-frame Structure Modeling

6.1 Brief Introduction of the CUREE-Caltech Woodframe Project

In Element 1 of the CUREE-Caltech Woodframe Project, shake table tests were conducted on three full-scale wood-frame structures with different configurations to investigate the performance of wood-frame structures under seismic events at the system level.

The three full-scale wood-frame structures were a two-story single-family house (Task 1.1.1), a three-story apartment building with parking on the first story (Task 1.1.2), and a simplified box-shaped wood-frame structure (Task 1.1.3). Figure 6.1 shows a flowchart of the organization of the various tasks.

Compared to the structures tested in Tasks 1.1.2 and 1.1.3, the test structure considered in Task 1.1.1 of the CUREE-Caltech Woodframe Project represents a simplified full-scale two-story single-family house incorporating several characteristics of recent California residential construction. The emphasis was put on simpler construction for which the results could more easily be interpreted, rather than incorporating complicated geometry features such as floor cantilevers and roof offsets. For the same reason, it is chosen for the purpose of 3-D model validation.

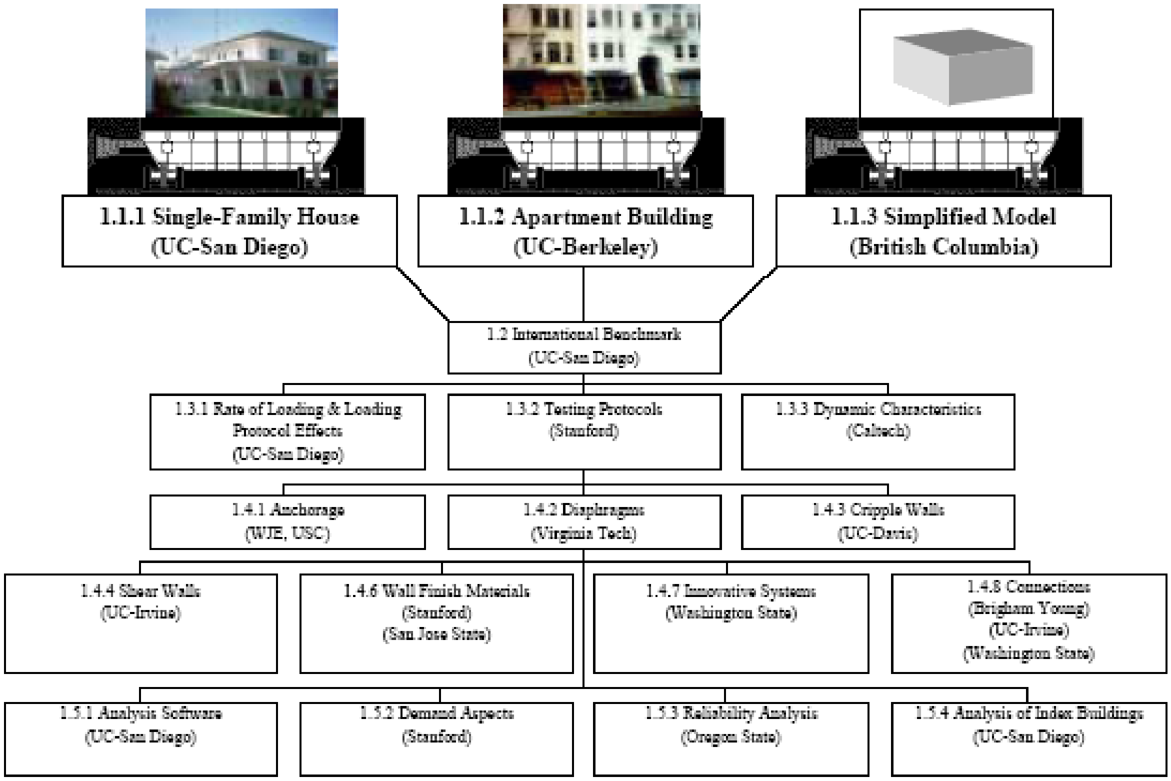

Figure 6.1 Flowchart of the Organization of the Various Tasks

6.2 CUREE 2-Story Wood-Frame Structure Test at UCSD

This two-story single-family wood-frame house was tested using the UC San Diego uniaxial earthquake simulation system under Task 1.1.1 of the CUREE-Caltech Wood-frame Project. The main objectives of the study were to determine the dynamic characteristics and the seismic performance of the test structure under various levels of seismic shaking and structural configurations (Fischer et al. 2001). The structure was tested during 10 phases of construction to determine the performance of the structure with fully sheathed shear walls, symmetrical and unsymmetrical door and window openings, perforated shear wall construction, conventional construction, and with and without non-structural wall finish materials. Four types of shake table tests were performed: quasi-static in-plane floor diaphragm tests, frequency evaluation tests, damping evaluation tests, and seismic tests (Fischer, et al. 2001).

Phase 9 is the final configuration without finish material applied. The torsional irregularity is the most significant compared to the other phases without finish material applied. So the configuration in Phase 9 is ideal for the 3-D model validation in this study. Besides, the hysteresis data for the connections between finish layers to the shear wall are not easy to find, and the relevant model parameters cannot be estimated currently, so the building configuration in phase 10 was not simulated.

The architectural and structural plan for the configuration in Phase 9 of the test structure is shown in Figure 6.2.

6.3 Detailed Shear Wall Modeling

6.3.1 Material Properties

The studs and the plates used in this test were Douglas Fir, and the grade was "Stud". From Table 4A in NDS (2001), the MOE is 1.4×10^6 psi (9.65 kN/mm^2), and the poisson's ratio was assumed to be 0.3.

The OSB's mechanical properties were based on those for the structural panels with the span rating of 24/16 (Table 3.2 2001 ASD Supplements). The MOE was assumed to be 4.99 kN/mm^2 and 3.81 kN/mm^2 in strong axis and weak axis, respectively.

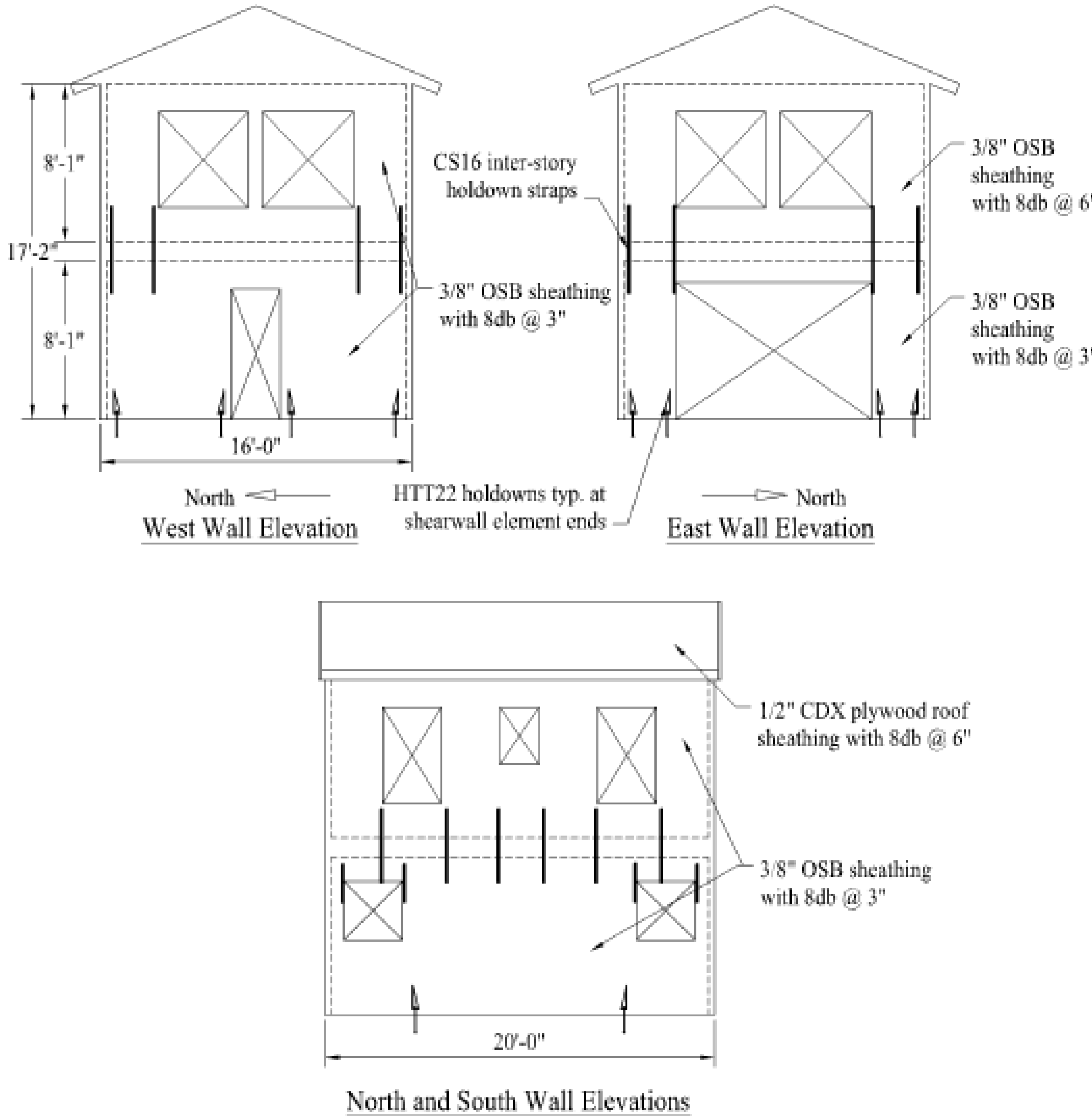

Figure 6.2 Elevations of Phase-9 Test Structure Showing Major Structural Components (Fischer, et al 2001)

6.3.2 Nail Joint Modeling

The nail joints used in this building were 8d box and 3/8-in OSB sheathing panels. The investigators did some monotonic and hysteretic testing on the joints, but the electronic data cannot be found. So the relevant data for the CUREE project completed by Dolan and Carradine (8d box and 19/32-in OSB sheathing panels) were used for the simulation. Figure 6.3 showed the hysteretic loops of this connection and the parameters suitable for the connection tested by Dolan and Carridine.

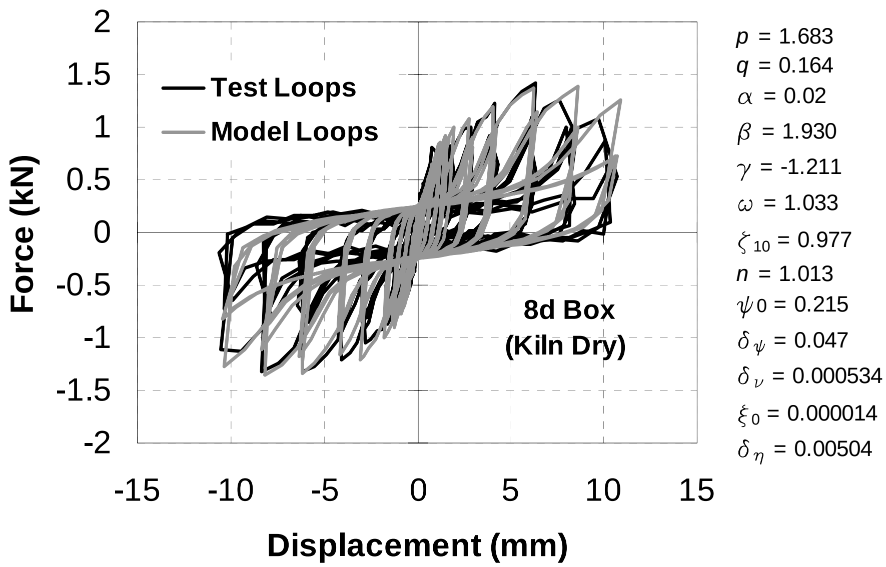

Figure 6.3 Parameter Estimation of the Single Nail Joint

Although there is no electronic data (e.g. spread sheet) available for the nailed connection configuration used in the test, there are some hysteresis figures available in "PDF" format (Figures 6.4 and 6.5). The average ultimate capacity of these tested nailed connections was 0.996 kN (224 lbs). However the ultimate capacity of the available model is 1.38 kN (310 lbs). The ratio between the two is 0.72. To account for the configuration differences, the parameter "ω" was reduced to 0.877.

$$\frac{0.877^2}{1.033^2} = 0.72$$

Since "ω" governs both the joint stiffness and ultimate capacity, it is an approximate but easy and effective adjustment. The other parameters were kept unchanged since the basic hysteretic loop shapes of both connection configurations have to be similar. With this modification, both initial stiffness and the ultimate strength of the joint were reduced by 28%.

The parameters used for this nail joint configuration in this test structure were p =1.683, q=0.164, α=0.02, β=1.93,γ=-1.211, ω= 0.877, ζ_0=0.977, n=1.013, ψ_0=0.215, δ_ψ=0.047, δ_ν=0.000534, ξ_0=0.000014, δ_η=0.00504.

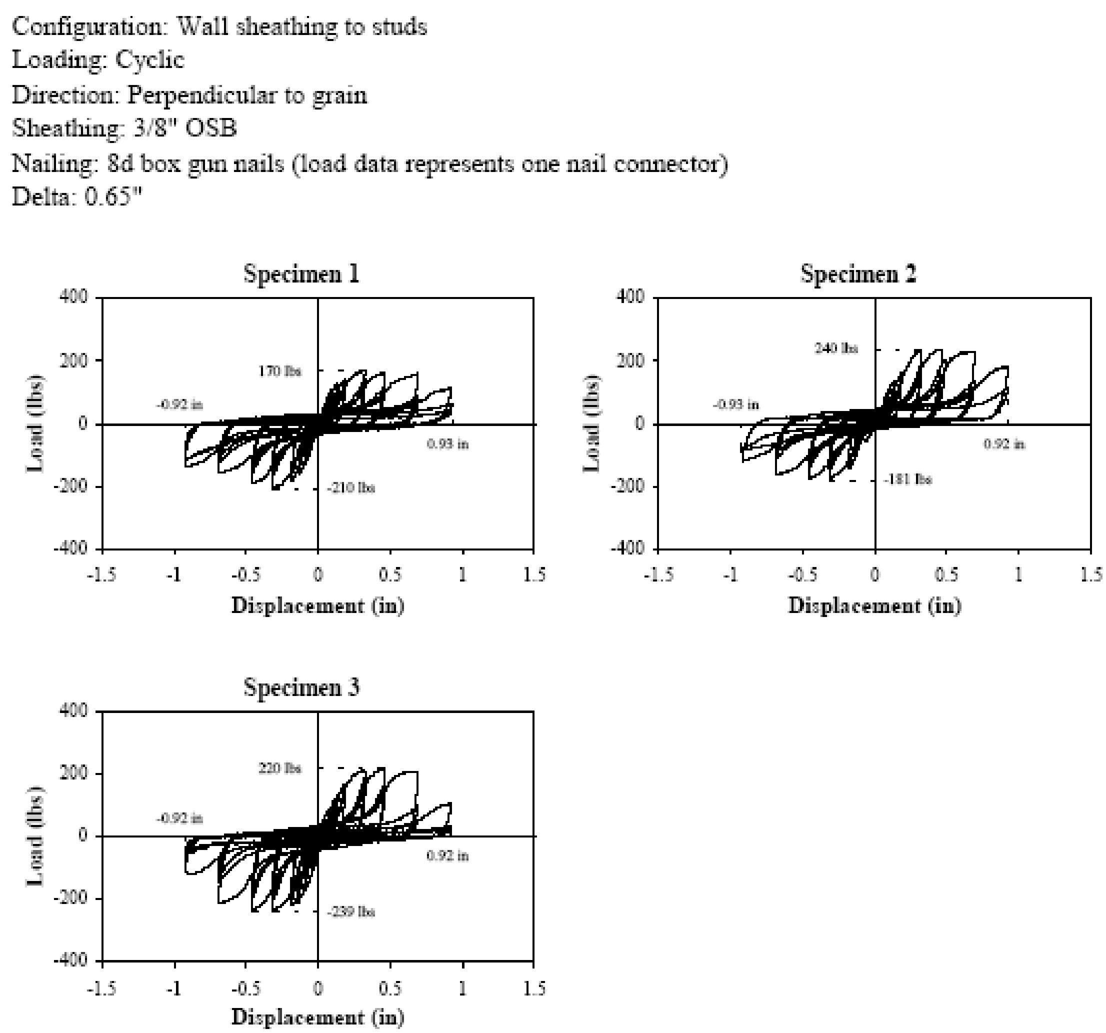

Figure 6.4 Nail Joint Cyclic Test Results from Fischer, et al (2001) (Perpendicular to Grain)

Configuration: Wall sheathing to studs
Loading: Cyclic
Direction: Parallel to grain
Sheathing: 3/8" OSB
Nailing: 8d box gun nails (load data represents one nail connector)
Delta: 0.65"

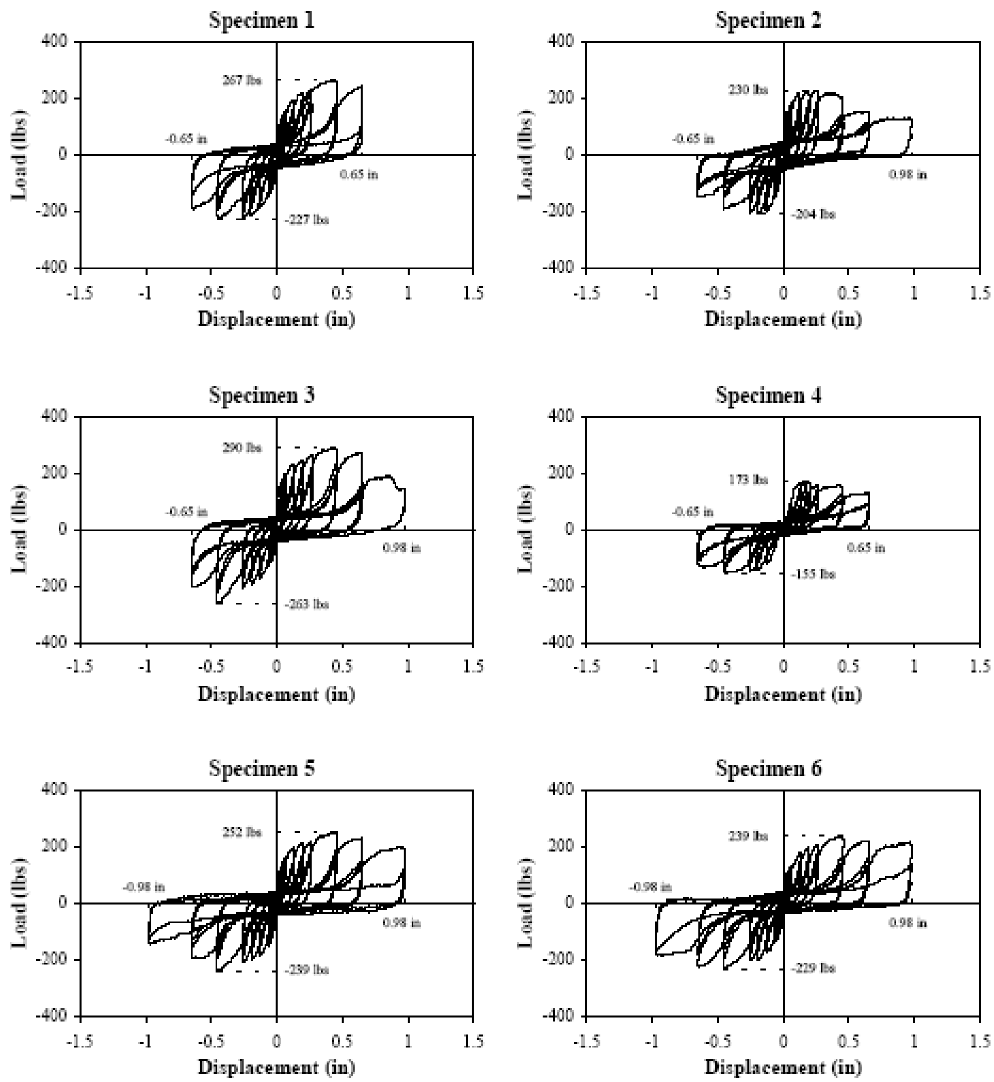

Figure 6.5 Nail Joint Cyclic Test Results from Fischer, et al (2001) (Parallel to Grain)

6.3.3 Detailed Shear Wall Modeling

The detailed layout of the shear walls lying parallel to the loading direction and the relevant detailed shear wall models are shown in Figures 6.6 through 6.8. The small Xs shown in the shear wall models are the positions of the nail joints. To be noted is that, to be simple, only half of the shear walls were modeled. The load values in the vertical ordinate of the hysteretic loops were doubled afterwards.

Figure 6.6 shows the 1^{st}-story east wall. The nailing schedule for this shear wall was 76mm (3 in.) o. c. (2 rows) along the sheathing left, right, and top edges. The nailing along the bottom plate was only one row with 76 mm (3 in.) o. c. The intermediate nailing schedule was 305 mm (12 in.) o. c.

Figure 6.7 shows the 1^{st}-story west wall. The nailing schedule for this shear wall was 152 mm (6 in.) o. c. (2 rows) along the sheathing left, right, and top edges. The nailing along the bottom plate was only one row with 152 mm (6 in.) o. c. The intermediate nailing schedule was 305 mm (12 in.) o. c. There was one extra stud, to which the inter-story strap was connected. It was used to transmit the load from the 2nd floor. There are two separate OSB panels in this half shear wall model. One is 1219×2438 mm (4×8 ft), and the other is 762×2438 mm (2.5×8 ft). Bearing springs were modeled between them, which can prevent overlapping but have no resistance to separation.

Figure 6.8 shows the 2^{nd}-story east and west wall. The nailing schedule for this shear wall was 152 mm (6 in.) o. c. on edges and 305 mm (12 in.) o. c. intermediate. The vertical frame between the two windows was formed by five 2×4 lumbers and a layer of OSB panel on them. It was simply modeled as one frame member with 1/2 the moment of inertia of the 5 pieces of lumber.

(a) Real Wall Configuration

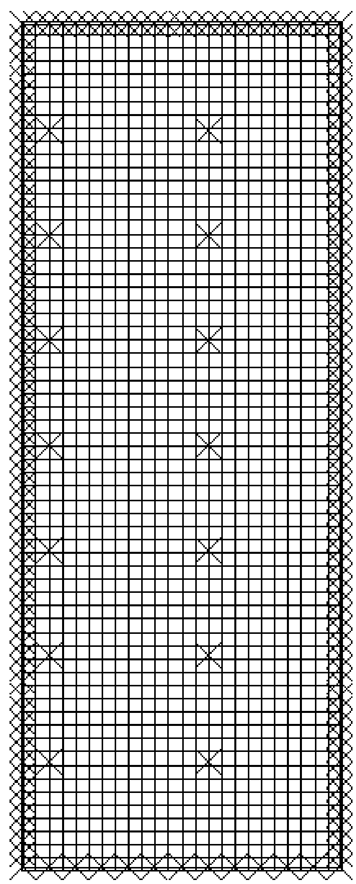

(b) Detailed Model of Half Wall

Figure 6.6 1st-story East Wall Configuration and Detailed Model

(a) Real Wall Configuration

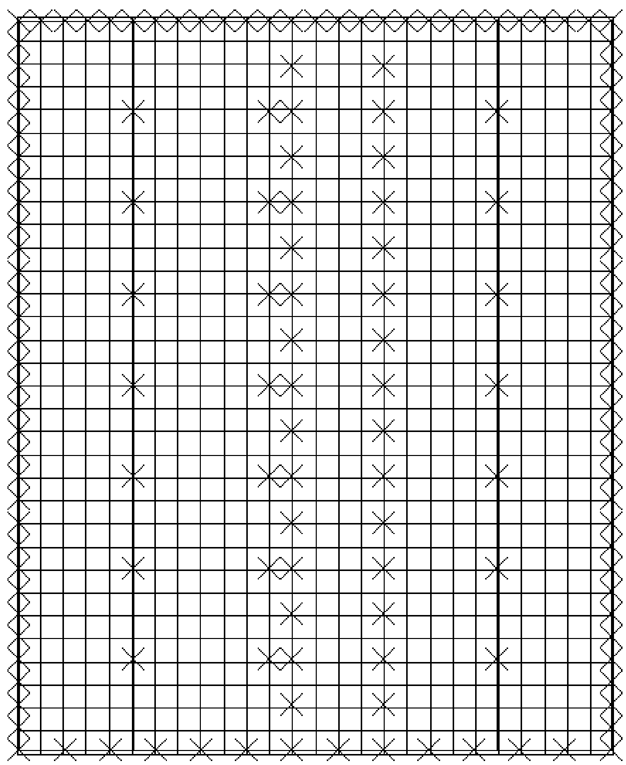

(b) Detailed Model of Half Wall

Figure 6.7 1st-story West Wall Configuration and Detailed Model

(a) Real Wall Configuration

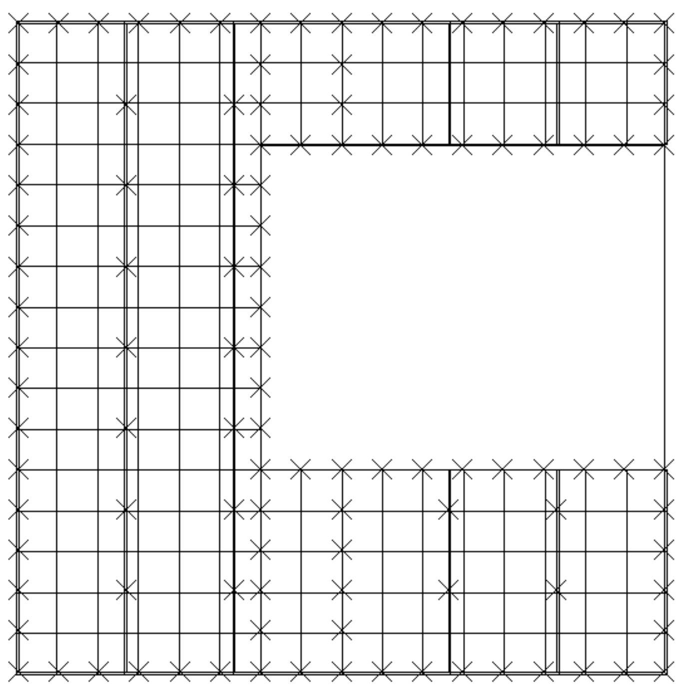

(b) Detailed Model of Half Wall

Figure 6.8 2nd-story East and West Walls Configuration and Detailed Model

It is hard to account for the influence from all the factors, so some unimportant factors were ignored in these detailed shear wall models. Some assumptions were made in the modeling process:

1. Since cracks at the corners between wall segment and header are going to appear and develop rapidly with the loading process, the stiffness and capacity contributions from headers were ignored.
2. Because the configurations of the shear walls in this test were all symmetric, to save the computation time, only half of each wall line was modeled. Vertical displacement was restricted along centerline of the 2nd-story East and West Wall to account for the corresponding boundary conditions. The load values were doubled in the final hysteretic loops.
3. The nails along the edges of the east and the west shear walls of the 1st-floor were staggered in 2 rows, and the distance between the two rows was the thickness of one 2×4 stud, which is only around 1.5 inches. In the detailed model, the nails were assumed to be in one row with 1/2 of the real spacing.
4. The influence of tie-down anchors was considered in the detailed model. Since there is no hysteresis data available for the anchors used in this test, HTT22, and the overturning effect was not significant in this test, the tie-down anchors were regarded as some elastic springs connecting the stud bottom with the bottom plate. The stiffness of the tie-down element was taken as the ratio of the ultimate capacity to the reference displacement, which can be obtained from the product catalog of Simpson Strong Tie. The capacity was 58.38 kN (13125 lbs), and the reference displacement was 2.2 mm (0.087

in.). So the stiffness $K_{tiedown}$ was,

$$K_{tiedown} = \frac{58.38}{2.2} = 26.5kN / mm \qquad (6\text{-}1)$$

5. The shear walls lying in the east-west direction (the south and the north walls) were very stiff and strong compared with the walls lying in North-South direction (the east and the west walls). In this test, the shake table is uniaxial along the North-South direction, so the result will not be sensitive to a few changes in the stiffness and the strength of the south and the north walls. To be simple, four 4×8 ft pieces of solid shear wall were assumed to form the north and the south walls for both the 1st and the 2nd stories (Figure 6.9).

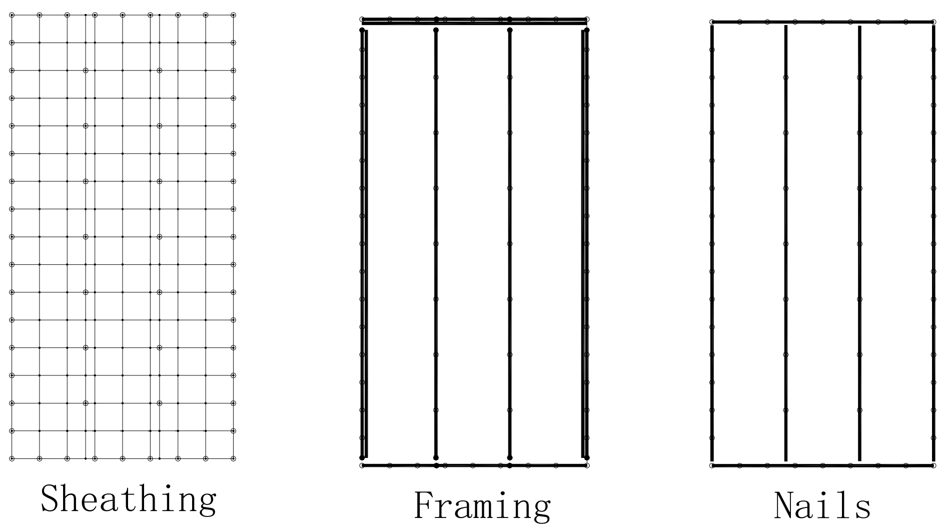

Figure 6.9 1st and 2nd Story North & South Wall Detailed Model

Since only ¼ walls were simulated and analyzed, the load values in the ¼ wall hysteretic results were quadrupled to form the final hysteretic loops.

The detailed shear wall model analysis results (deformed shape, Mises stress contour, and hysteretic loops) were shown in Figures 6.10 to 6.13.

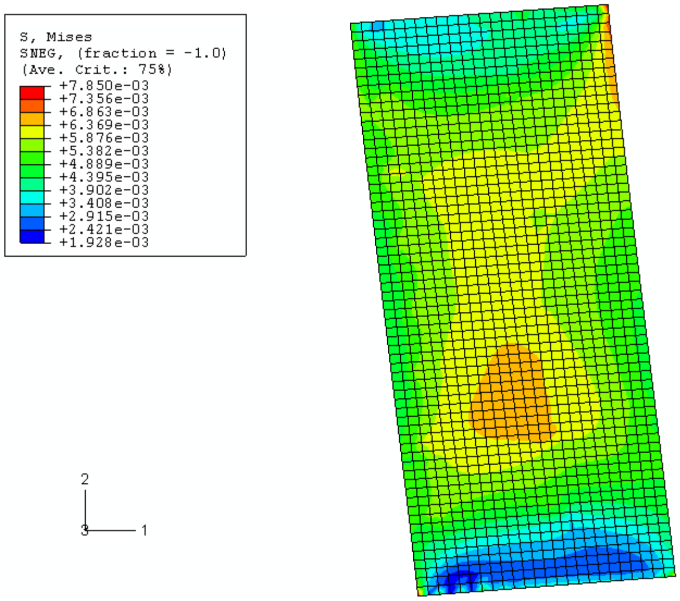

(a) Half Wall Analysis Results

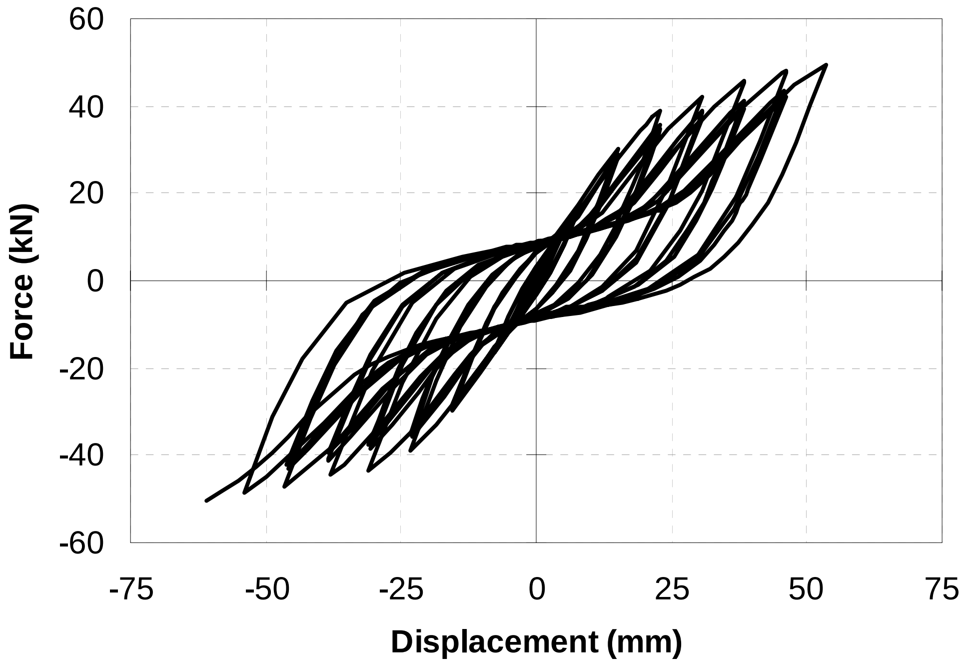

(b) Whole Wall Hysteretic Loops

Figure 6.10 1st-story East Wall Analysis Results

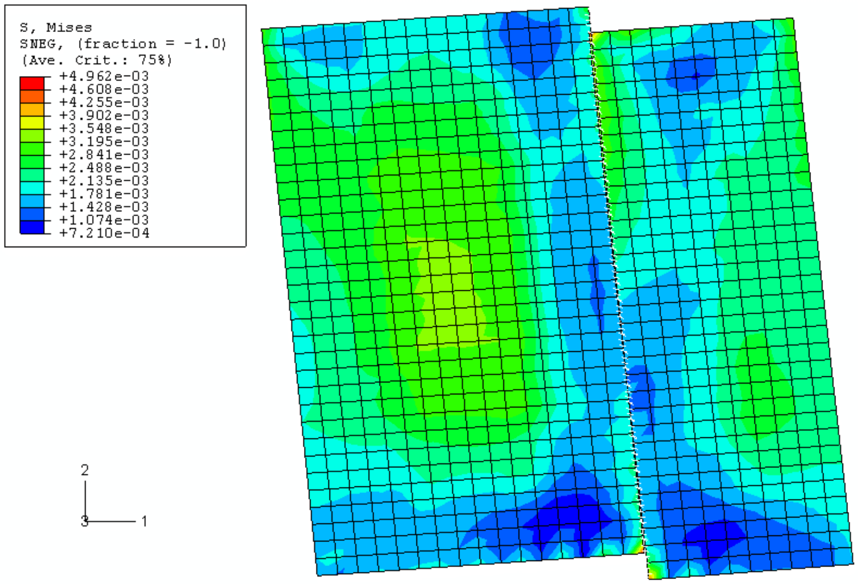

(a) Half Wall Analysis Results

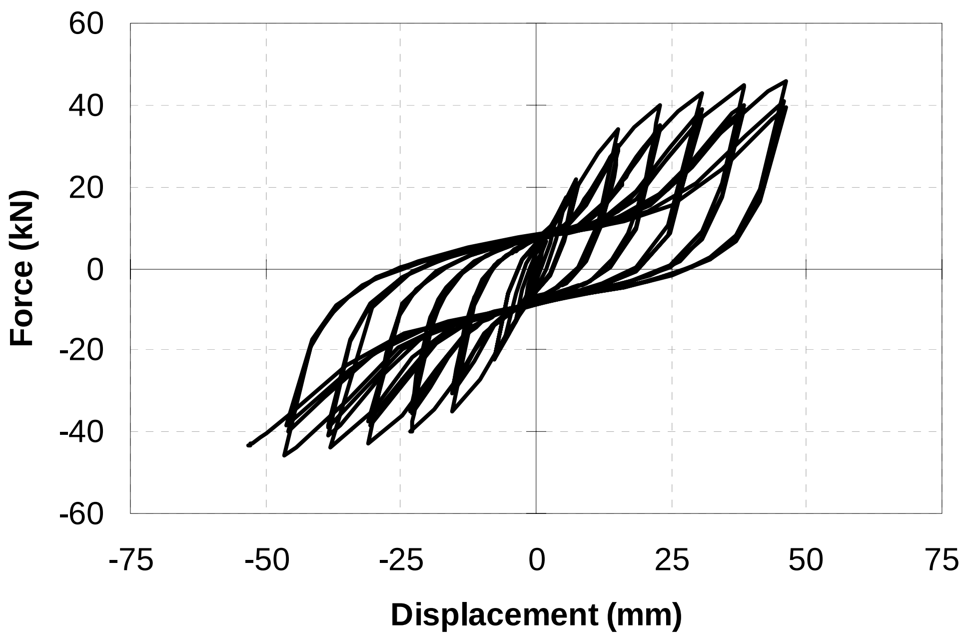

(b) Whole Wall Hysteretic Loops

Figure 6.11 1st-story West Wall Analysis Results

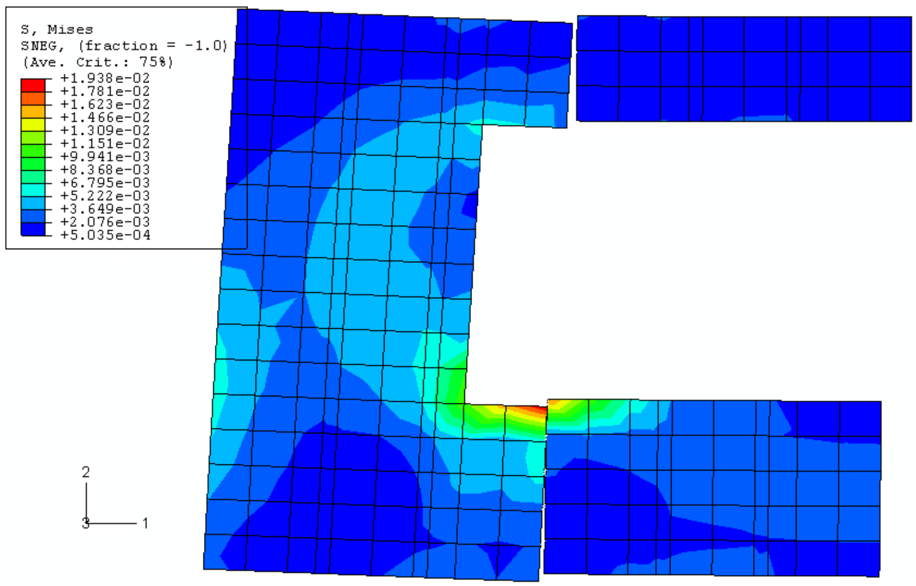

(a) Half Wall Analysis Results

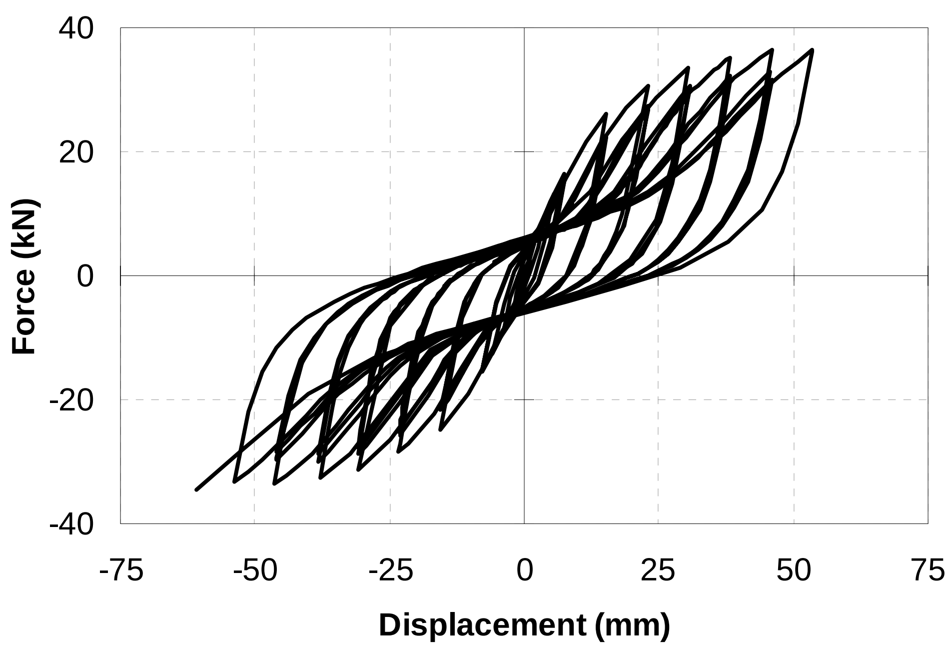

(b) Whole Wall Hysteretic Loops

Figure 6.12 2nd-story East and West Wall Analysis Results

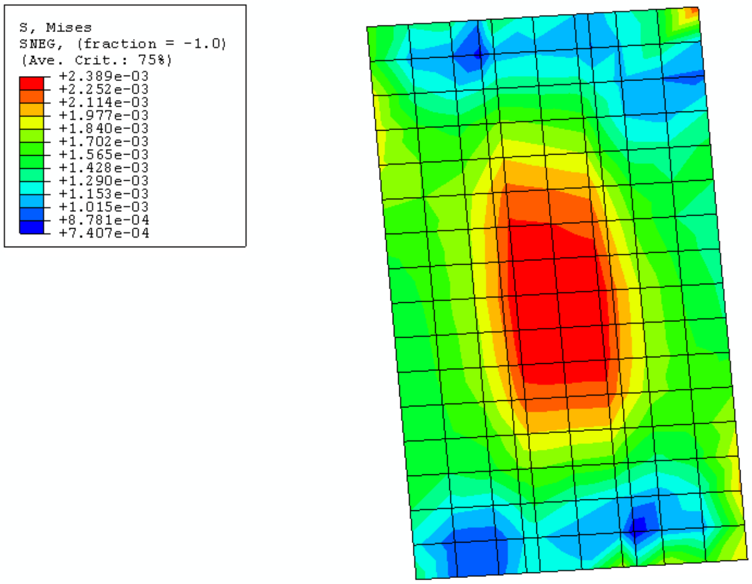

(a) 1/4 Wall Analysis Results

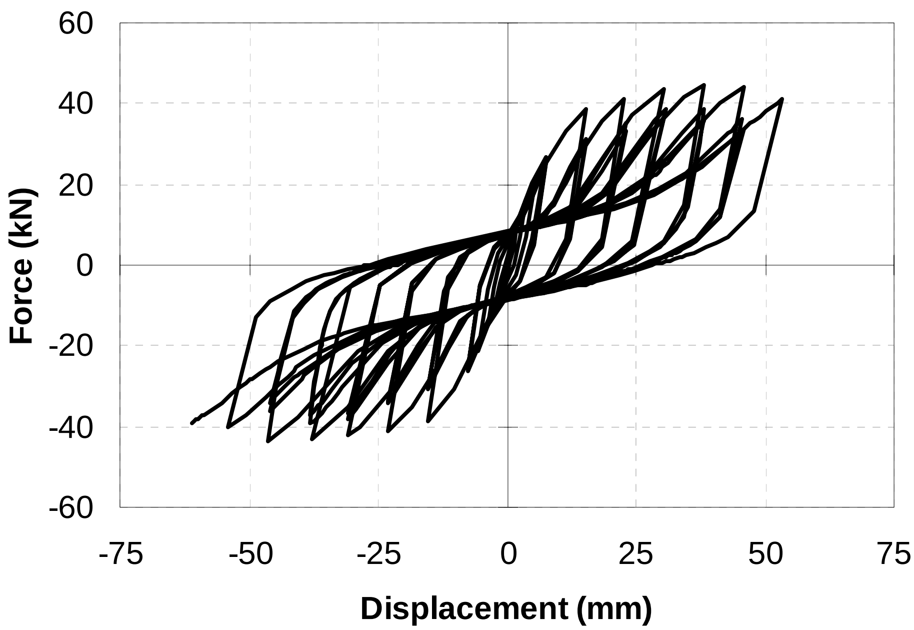

(b) Whole Wall Hysteretic Loops

Figure 6.13 1st and 2nd-story South and North Wall Analysis Results

6.4 Super shear wall model Parameter Estimation

The GA program was applied for each shear wall. The suitable parameters for each super shear wall model were shown in Figures 6.14 through 6.17.

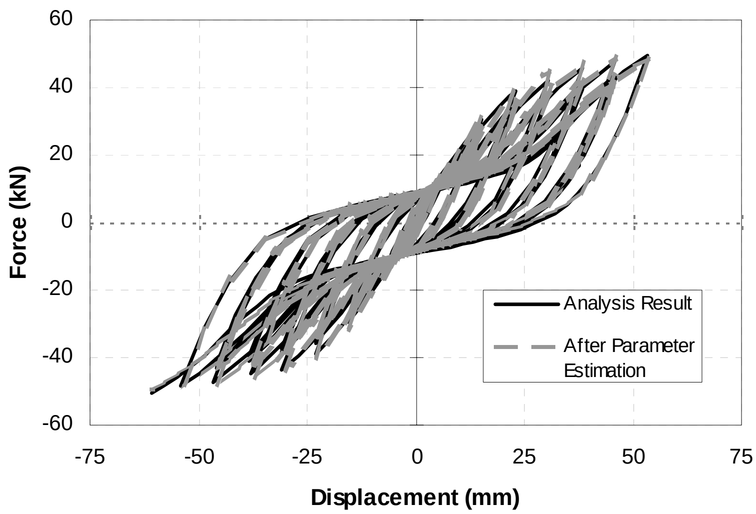

α	=	0.063406
β	=	0.023677
ω	=	1.614844
ζ_0	=	0.896255
n	=	1.17407
Ψ_0	=	0.693759
δ_ψ	=	0.186581
δ_ν	=	0.000008
ξ	=	0.000013
γ	=	-0.00419
δ_η	=	0.000022
p	=	0.113518
q	=	0.120985

Figure 6.14 Super Shear Wall Parameter Estimation of 1st-story East Wall

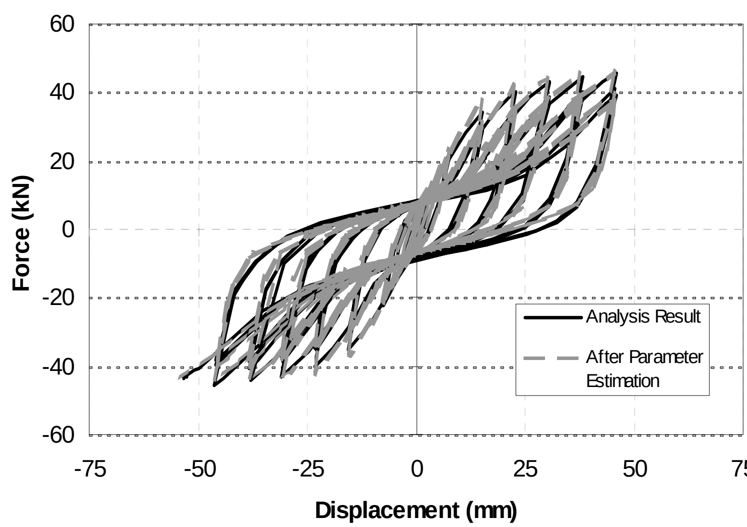

α	=	0.06363
β	=	0.157353
ω	=	1.906539
ζ_0	=	0.928654
n	=	1.012961
Ψ_0	=	0.851558
δ_ψ	=	0.14918
δ_ν	=	0.000013
ξ	=	0.00001
γ	=	-0.10019
δ_η	=	0.000027
p	=	0.161679
q	=	0.111847

Figure 6.15 Super Shear Wall Parameter Estimation of 1st-story West Wall

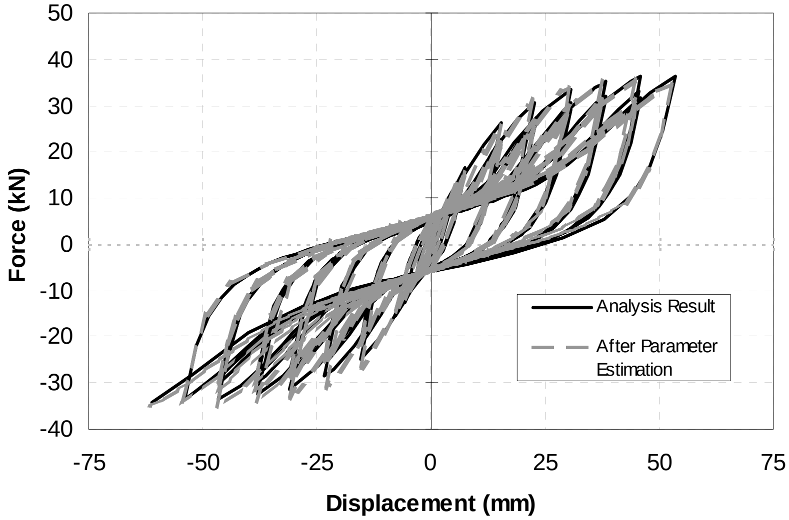

α	=	0.105018
β	=	0.074549
ω	=	1.60374
ζ_0	=	0.928138
n	=	1.204028
Ψ_0	=	0.85429
δ_ψ	=	0.133229
δ_ν	=	0.000018
ξ	=	0.000016
γ	=	-0.04142
δ_η	=	0.000045
p	=	0.182815
q	=	0.146311

Figure 6.16 Super Shear Wall Parameter Estimation of 2nd-story East and West Wall

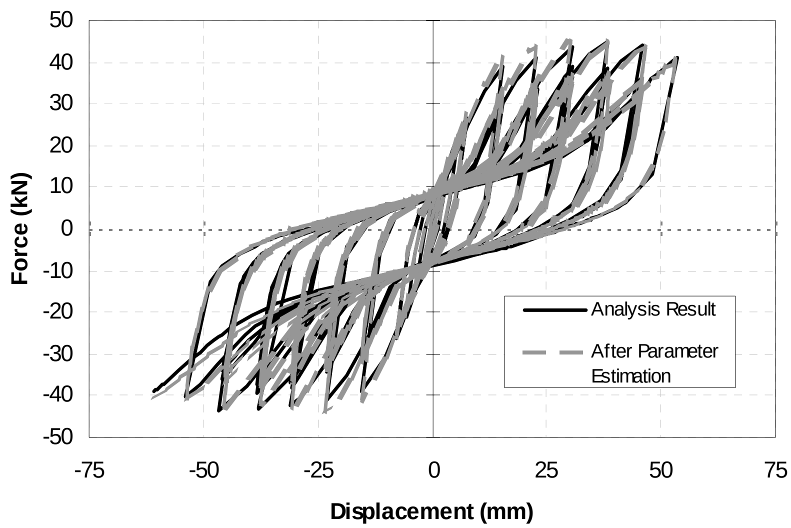

α	=	0.039413
β	=	0.16259
ω	=	2.207585
ζ_0	=	0.942246
n	=	1.046361
Ψ_0	=	0.716038
δ_ψ	=	0.122511
δ_ν	=	0.000007
ξ	=	0.000015
γ	=	-0.08457
δ_η	=	0.000033
p	=	0.191048
q	=	0.145203

Figure 6.17 Super Shear Wall Parameter Estimation of 1st and 2nd-story North and South Wall

6.5 3-D Dynamic Model

6.5.1 Assumptions

Some assumptions were made to simplify the simulation. These assumptions are:

1. The diaphragm acts elastically.
2. The influence from the inter-component elements is negligible. The corner post will be modeled as one frame element that is shared as the common vertical framing element of the crossing shear walls. The shear walls are connected to the diaphragm through horizontal frame members, and the inter-story sliding is negligible.
3. Since the overturning influence has been considered in the detailed model, no springs will be applied between the vertical framing elements and the sill plate elements in the 3D structure model.
4. The mass distributes uniformly in the floor and roof diaphragms.

6.5.2 Description of the 3-D Model

The weight of the structure was from the weight of the framing members, the floor, roof, and wall sheathing panels, the clay roof tiles, and the supplemental weights (Fischer, et al. 2001). The total weight of the structure in Phase 9 was 109.33 kN with 61.52 kN at the floor diaphragm level and 47.82 kN at the roof diaphragm level. The exact weight distribution can be seen in the report prepared by Fischer et al. (2001). In the numerical model, the total floor level weight was assumed to distribute evenly to the nodes of the floor diaphragm, as was the roof weight.

According to the quasi-static test results reported by Fischer et al. (2001), the equivalent stiffness of the floor diaphragm was 38 kN/mm, and the equivalent viscous damping ratio is 8.3%.

The floor diaphragm was modeled with 4 × 6 shell elements. The in-plane stiffness of the floor diaphragm was calibrated using the quasi-static test results given above. The constant elastic modulus of OSB element, 11.72 kN/mm^2, was assigned to these shell elements. The two supporting edges were pinned, and a unit deflection was applied at the mid span. The thickness of the floor diaphragm elements (4.7 mm) was adjusted such that the total reaction at the two supporting edges in the numerical model equaled to 38 kN when the displacement at the middle span is 1 mm. Since the supporting edges were pinned, the flexural deflection of the floor diaphragm was eliminated. All the flexural and shear deflections in the diaphragm were represented as equivalent shear deflection.

The mass of the floor was 0.0063 kN/(mm/s^2). Based on the first vibration mode, the equivalent damping coefficient was $c = \xi \cdot (2m \cdot \omega) = 0.081 kN \cdot s / mm$. The related Rayleigh damping factors α, β were set to be 0.726 and 0.00202 respectively, which make the equation,

$$c = \alpha \cdot m + \beta \cdot k \tag{6-2}$$

The roof diaphragm is very stiff compared to the floor diaphragm because of the contribution of the trusses. It was assumed rigid. In this 3-D model, it was modeled by 4 × 6 shell elements with very high in-plane stiffness.

Vertical and horizontal frame members were simulated with truss elements because all shear wall capacity is assumed from the two diagonal hysteretic springs. Extra capacity from frame behavior would be introduced if the framing members were simulated with beam elements. The axial stiffness of the truss elements was assumed very high to eliminate the stretch and compression in the framing members, which may cause unreal tension or compression in the hysteretic springs. The diaphragm only shared the four corner nodes with the horizontal truss elements. This can eliminate the flexural deformation of the diaphragm, while the shear deformation of the diaphragm was not restrained at all.

The properties of the frames and diaphragms are shown in Table 6.1.

Table 6.1 Properties of Frames and Diaphragms

Component	Section	MOE (kN/mm^2)	X-section Area (mm^2)	Thickness (mm)	Poison's Ratio
Roof Diaphragm	4-node Shell Elements	11.72	N/A	2540	0.3
Floor Diaphragm	4-node Shell Elements	11.72	N/A	4.7	0.3
Frames	Truss Elements	11.72	1×10^6	N/A	N/A

Each of the eight shear walls was represented with a pair of super shear wall hysteretic spring elements. The parameters of each super shear wall hysteretic spring were input through the input file.

A pair of dashpots with a damping ratio of 1% was placed in each shear wall to take the elastic damping effect into account. The total damping coefficient for all the walls in each direction are derived from the equation:

$$c = \xi \cdot (2m \cdot \omega_1) \tag{6-3}$$

Where m is the total mass, ω_1 (different from the stiffness parameter used in the super shear wall model) is the circular frequency of the fundamental vibration mode of the structure, which is 25.12 s^{-1} from the test results, and ξ is the damping ratio, which is set to be 1% here. The total damping coefficient then was distributed to each wall evenly. The damping coefficient was 0.00068 kN/(mm/s) for the east and the west wall. Since there was no data that was able to supply the fundamental vibration mode information in east-west direction, and the walls in east-west direction are very strong and did not influence the results significantly, the same damping coefficient was applied to the shear walls in this direction (North and South walls).

The recorded acceleration time histories of the shake table for test Phase 9 were used as the input ground accelerations for the numerical model. Since the structure was tested under 5 seismic levels (6 if the repeat of Level 3 was counted), and there was no retrofit in the test series, the 5 (or 6) levels of earthquake histories were combined into a train of ground motions for the dynamic time-history analysis. The accumulated earthquake damage can then be considered. The time history train is shown in Figure 6.18.

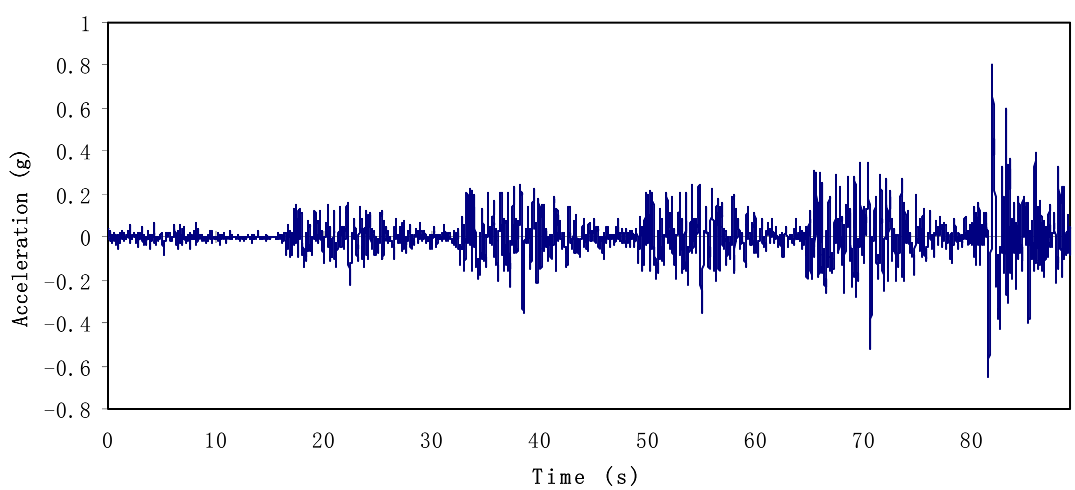

Figure 6.18 Input Ground Acceleration History

6.6 Result Comparisons

The experimental fundamental period is 0.253s, and the numerical result is 0.287s. Therefore, the numerical underestimates the initial structural stiffness. Figure 6.19 shows the comparison of initial experimental and numerical fundamental mode shapes. Since the roof diaphragm was assumed to be rigid and flat, the ridge and eave had the same displacements in the east and west elevations. From the comparison of the mode shapes, the stiffness of the 1st-story west wall was underestimated. The underestimation is partly due to the secant stiffness of the tie-down anchors being taken as the elastic stiffness.

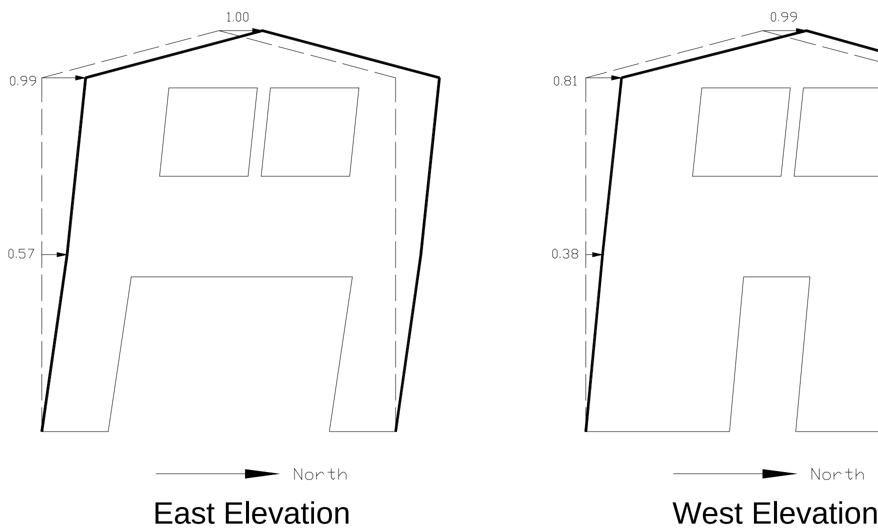

(a) Experimental Mode Shape

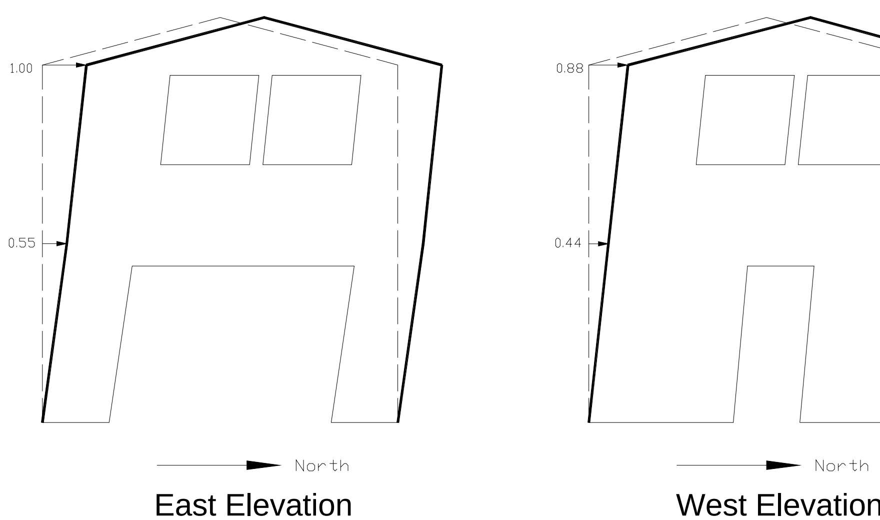

(b) Numerical Mode Shape

Figure 6.19 Comparison of Experimental and Numerical Mode Shapes

After the time history analysis, the relative displacement histories in Level 4 (Design

Level) and Level 5 for the first-story east wall and for the global response (mid span of the roof) were compared with the test results (Figures 6.20 to 6.23). The global hysteretic responses in Level 4 and Level 5 were also compared with the test results (Figures 6.24 and 6.25). These results showed a good agreement between the numerical and the experimental results when the structure was subjected to the high-level amplitude ground motions. The definition and equations of correlation coefficient are shown in Appendix A.

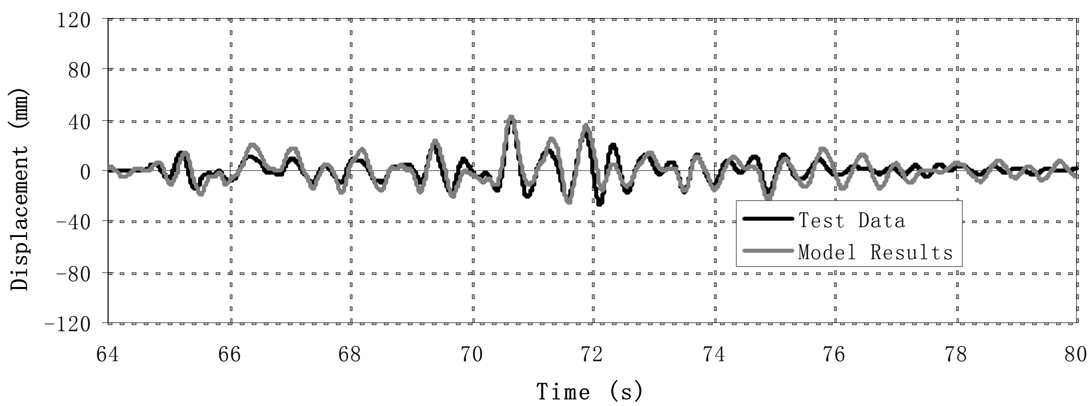

Figure 6.20 1st-story East Wall Relative Displacement History for Level-4 Earthquake Input (Correlation Coefficient = 0.804)

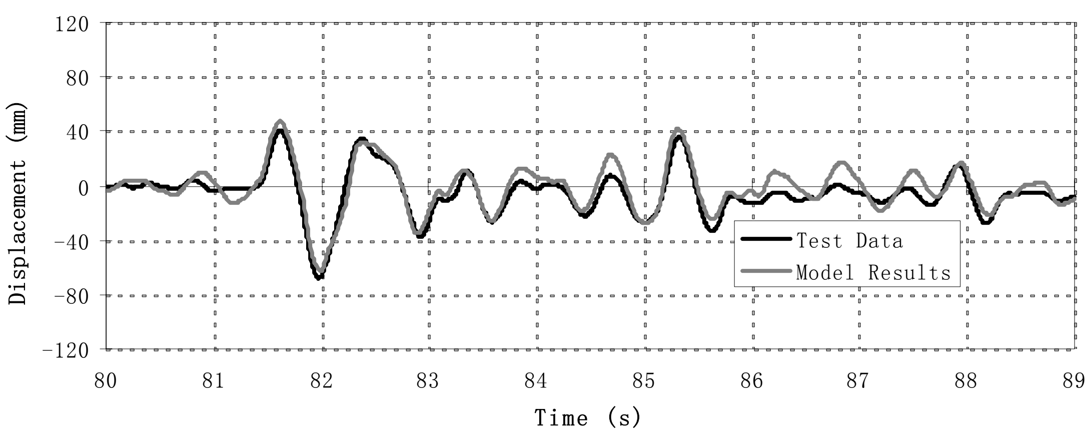

Figure 6.21 1st-story East Wall Relative Displacement History for Level-5 Earthquake Input (Correlation Coefficient = 0.937)

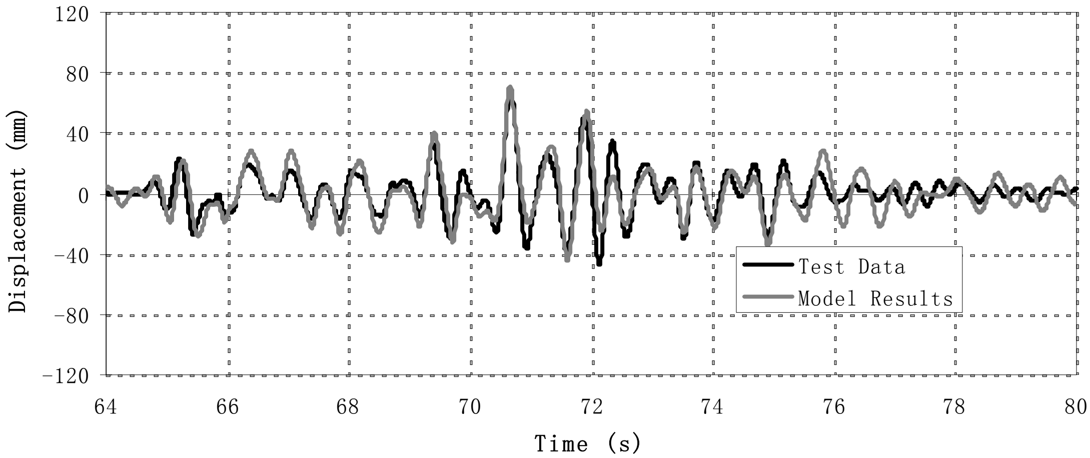

Figure 6.22 Global Relative Displacement History for Level-4 Earthquake Input (Correlation Coefficient = 0.829)

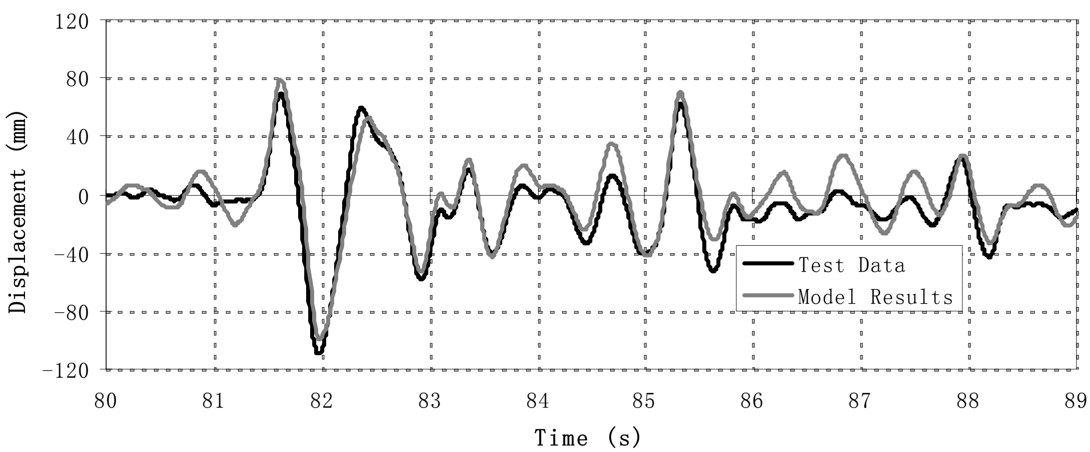

Figure 6.23 Global Relative Displacement History for Level-5 Earthquake Input (Correlation Coefficient = 0.929)

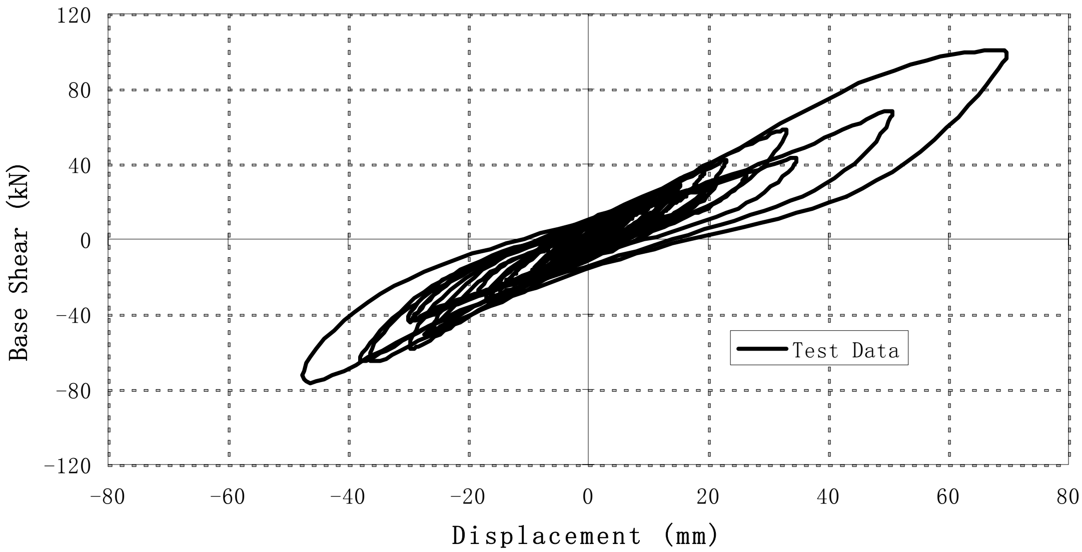

(a) Experimental Results

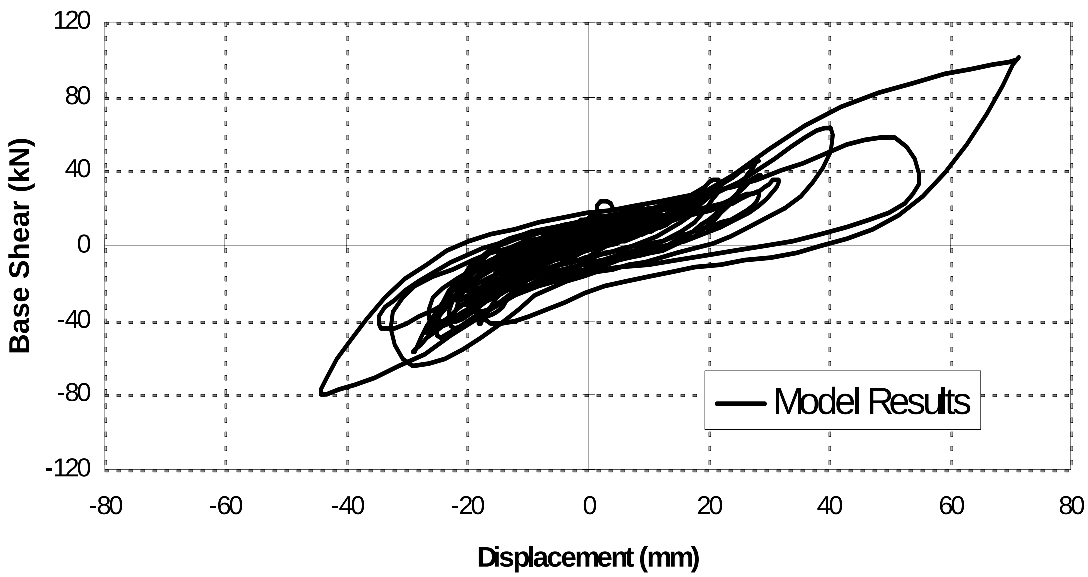

(b) Numerical Results

Figure 6.24 Global Hysteresis Comparison for Level-4 Earthquake Input

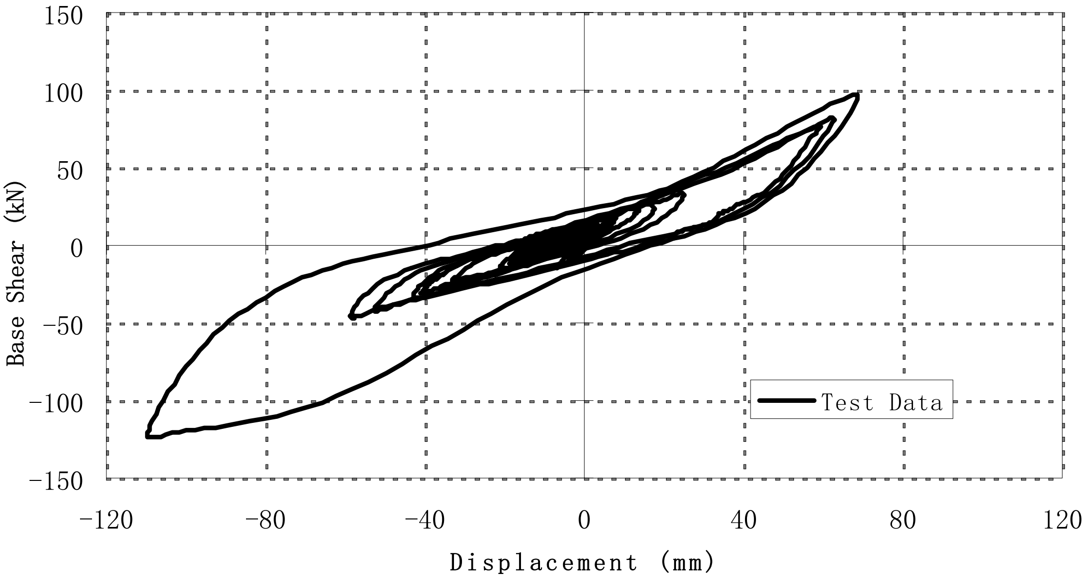

(a) Experimental Results

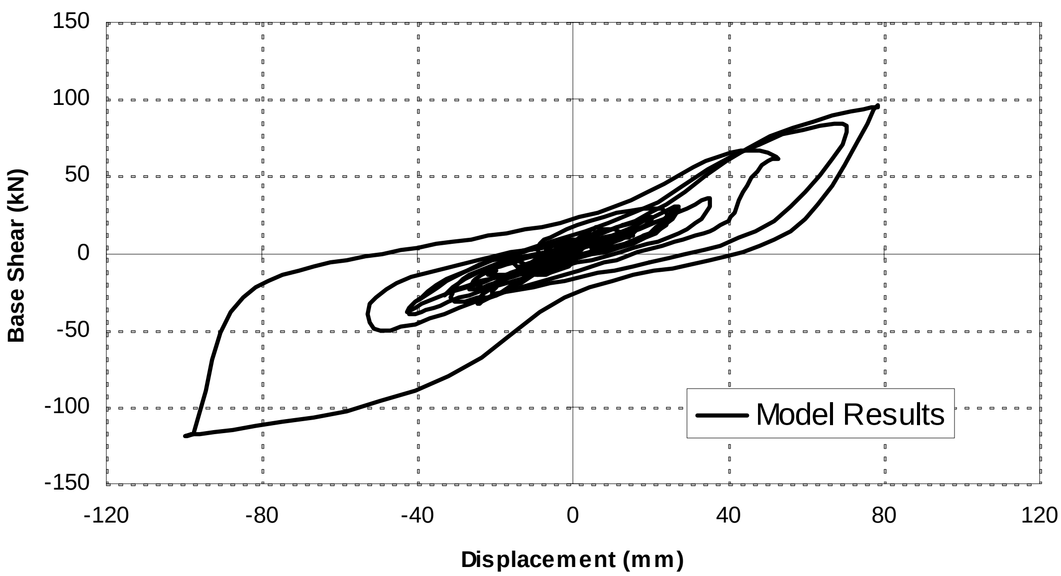

(b) Numerical Results

Figure 6.25 Global Hysteresis Comparison for Level-5 Earthquake Input

The comparison of peak drifts and imposed loads between the numerical and the experimental results are shown in Table 6.2. While some of the error terms for displacement seem high (17% max.), in applied terms the error is only 7 mm (0.27 in.).

Table 6.2 Comparison of Ultimate Drifts and Reactions

Items		Test Results	Model Results	Error (%)
Level 4	Max Global Response (mm)	69.73	71.29	2.2
	Min Global Response (mm)	-47.61	-44.24	-7.1
	Max Base Shear (kN)	97.96	100.52	2.6
	Min Base Shear (kN)	-76.4	-79.92	4.6
	Max 1st-story East Wall Drift (mm)	40.75	43.05	5.6
	Min 1st-story East Wall Drift (mm)	-26.36	-25.67	-2.6
Level 5	Max Global Response (mm)	68.57	78.5	14.5
	Min Global Response (mm)	-109.65	-99.7	-9.1
	Max Base Shear (kN)	97.38	95.53	-1.9
	Min Base Shear (kN)	-122.79	-119.62	-2.6
	Max 1st-story East Wall Drift (mm)	40.33	47.24	17.1
	Min 1st-story East Wall Drift (mm)	-67.91	-62.82	-7.5

6.7 Result Analysis and Conclusions

According to the comparisons, the simple numerical model can predict the nonlinear wood-frame structural response accurately. The errors are acceptable, considering the variations of material and nailing details. The error also proves that the influence of the headers and the out-of-plane action of the wood-frame shear walls are negligible.

In these detailed shear wall models, since the secant stiffness of the tie-down anchors was taken as the elastic stiffness, the initial stiffness of the shear wall was somehow underestimated. However, the results show that the shear walls' ultimate performances were not affected much. The inter-story steel straps were not included in the detailed model of the 2^{nd}-story shear walls. The reasons are: 1. The overturning moment was not that significant for the 2^{nd}-story shear walls; 2. There were many straps used between 1^{st} and 2^{nd} story shear walls, which restricted the overturning; 3. From the geometry point of view, a unit uplift at the inter-story location only causes half a unit global drift. The test results showed that the maximum uplift at the inter-story location was only 0.73 mm and 0.8 mm for the east and west wall, respectively.

6.8 Discussion on the Influence from Shear Wall Out-of-plane Action

The contribution of the shear wall out-of-plane action is from the bending restraint at the two wall ends. The bending restraint mainly comes from three sources: 1. Shear in the sheathing-frame nail joints along the bottom plates; 2. Bottom nail end-grain withdraw; 3. Bending of sheathing panels. Even with the large end-grain frictional stiffness and the relatively large initial shear stiffness of the sheathing-frame nail joints, the influence of the out-of-plane action on the ultimate structure lateral capacity is much less than the effect on the initial frequency. Therefore, out-of-plane action of the walls was ignored in this study.

Chapter 7
Open-front Wood-frame Structure Parametric Study

7.1 Introduction

Paulay (1997) proposed a design method applicable to ductile systems with torsional irregularities. This method is based on the perfect elasto-plastic assumption. For a wood-frame structure, the nonlinearity occurs at very low drift, and the ultimate capacity is normally 2.8 to 3.4 times the allowable design resistance. This means that the torsion moment will develop a lot further after the imposed loads in the shear walls reach the allowable design value. Besides, the assumption of elastic response in the torsion-restraint wall is impossible to guarantee. So the assumptions on which Paulay's formula are based are violated in wood-frame structural design. However this design philosophy represented a good initial trial and may be applied to wood-frame structural design someday after modifications.

Since the configuration and layout of wood-frame residential buildings (houses and apartments) are relatively simple and similar to one another, a parametric study which covers most commonly used structural configurations can supply a significant amount of useful information for open-front wood-frame structural design. In this study, a series of wood-frame structures with different configurations were simulated and investigated using time history analysis under design-level ground motion records. The ground motion record used in this study was a scaled Canoga Park Record (peak acceleration is 0.5 g, same as the Level-4 record used in the shake table test at UCSD (Fischer, et al. 2001)), which is shown in Figure 7.1. Then a parametric study on the torsional behavior of open-front wood-frame structures subjected to seismic loads was performed. The parameters of the study included the open-front percentage, building foot print aspect ratio, and possible inclusion of interior partition walls. These wood-frame structures were 2-stories high and only have front openings in the 1st floor. The shear wall layout on the other stories is assumed to be symmetric. To eliminate the influence from different structural layouts of the 2nd stories, only one-story models were built and analyzed in this study, and the other failure modes (other than the 1st-floor failure) were not considered in this study. The structural performance measures, which were monitored, include structural lateral drifts and imposed loads in the individual shear walls.

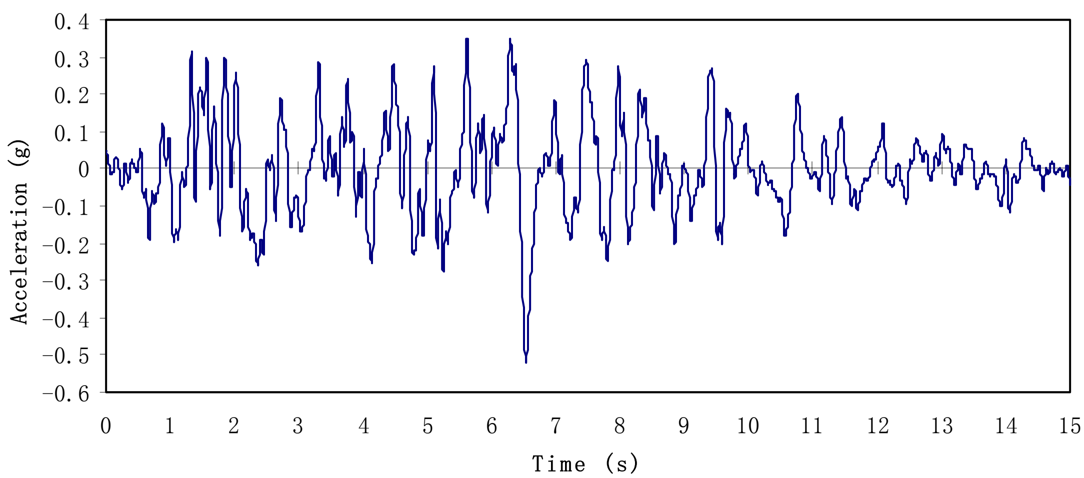

Figure 7.1 Ground Motion History (peak acceleration = 0.5 g)

7.2 Model Configurations

Five different floor plan aspect ratios were considered in this study, the L-to-W ratios of which are 1:1, 1:2, 1:3, 2:1, and 3:1 respectively. For each plan aspect ratio, 5 different front-to-back wall ratios were studied, which were 0:1, 0.25:1, 0.5:1, 0.75:1, 1:1. The 1:1 case is symmetric structurally and serves as the control for each group. The effect of partition walls on the structural seismic performance was also one of variables used in this investigation. Results from separate sets of models with partition walls were used for comparison purposes. In this study, it was assumed that the partition wall was sheathed with gypsum wall board on both sides, and the wall length was taken as 80% of building dimension in the relevant direction. All the studied configurations are shown in Figure 7.2.

The name for each structural model was represented in the format of m_n_k, where m (1 - 5) is the case number, and n (1 or 2) represents without or with partition walls, and k (0 - 100) represents the ratio of front to back wall sheathing length. For instance, 2-1-25 means Case 2 (L : W=1 : 2) without partition walls, and the front-to-back-wall sheathing ratio of 25%.

The unit size of these buildings was assumed to be 6.1 m (20 ft). For instance, the model size of the structure with an aspect ratio of 1:2 is 6.1 × 12.2 m (20 × 40 ft).

7.3 Structural Modeling Techniques

7.3.1 Floor Diaphragm Model

The floor diaphragm model used in the 3D model validation (Chapter 6) was employed in this parametric study. The mass for the 2-story building upper story was assumed to be 30 lbs/ft^2 and distributed uniformly on the floor diaphragm.

7.3.2 Shear Wall Model

The 1219 × 2438 mm (4 × 8 ft) super shear wall model (Figure 5.5) developed based on the tests conducted by Salenikovich (2000) was used as the wall unit for these 3-D building models. The parameters for it are: p = 0.106, q = 0.117, α = 0.0478, β = 0.06, γ = -0.00596, ω = 0.868, ζ_0 = 0.907, n =1.103, ψ_0=0.871, δ_ψ = 0.218, δ_ν = 0.000002, ξ = 0.000015, δ_η=0.00011.

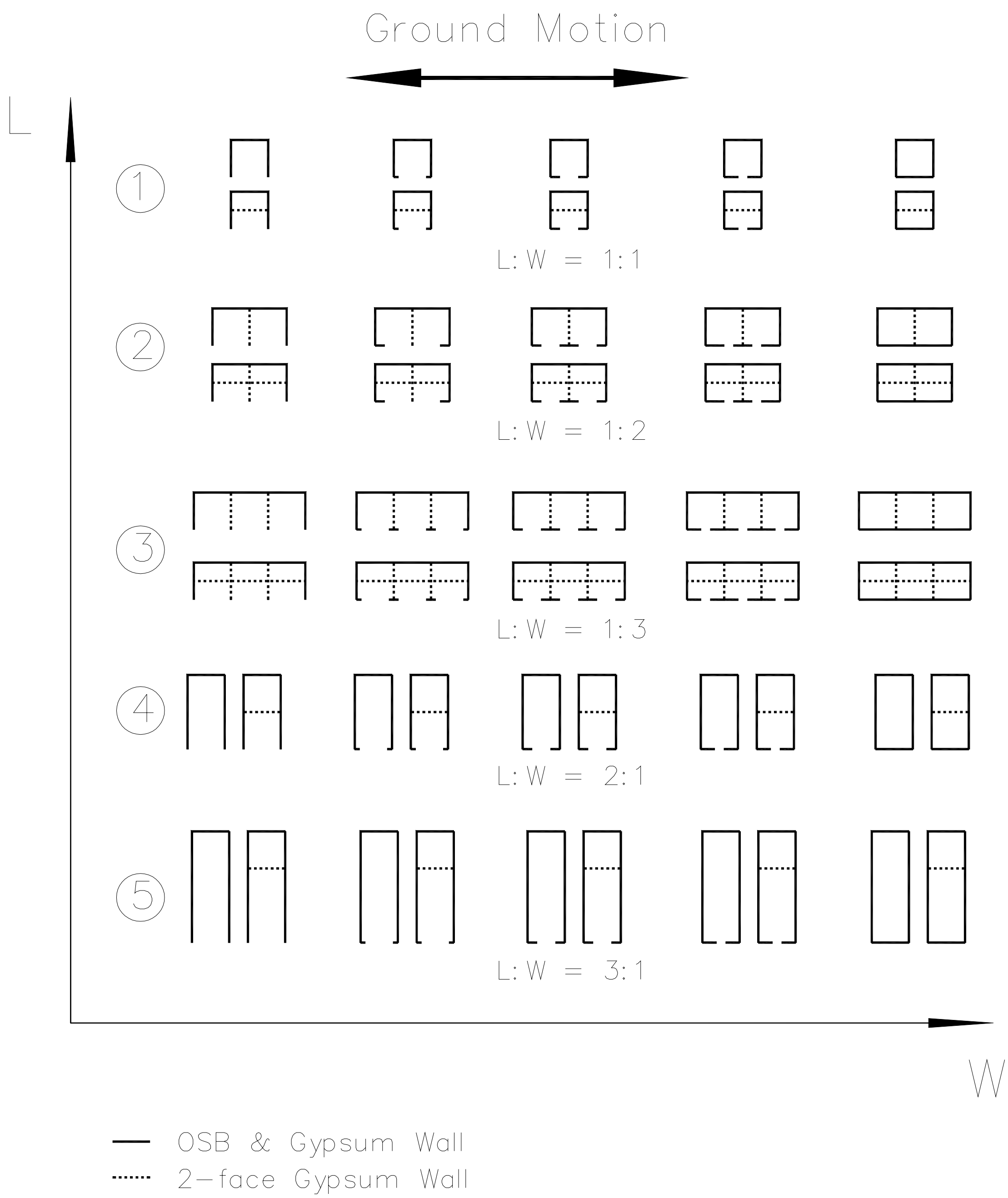

Figure 7.2 Plan Views of The Buildings

The parameter, $\boldsymbol{w}$**,** varies with the variation of wall length in these models because $\boldsymbol{w}^2$ governs both shear wall initial stiffness and ultimate capacity (if no degradation is applied). For instance, the basic $\boldsymbol{w}$ value is 0.868, which is suitable for the wall of 1219 ×2438 mm (4×8 ft). If the size of the wall is 2438×2438 mm (8×8 ft), the relevant $\boldsymbol{w}$ value will be 1.228, which makes:

$$\frac{8}{4} = \frac{\omega_{8\times8\,ft}{}^2}{\omega_{4\times8\,ft}{}^2} = \frac{1.228^2}{0.868^2} \tag{7-1}$$

Besides $\boldsymbol{w}$, the stiffness and strength degradation parameters, $\boldsymbol{d_h}$ and $\boldsymbol{d_n}$ need to be modified for the walls with lengths different than 4 feet. That is because all other properties of the hysteretic loops are proportional to the displacement, and only the degradation is governed by the dissipated energy, which is related to the both displacement and force (Refer to Equations 3-7, 3-8, 3-9, 3-10, and 3-11 in Chapter 3). For instance, if a series of parameters derived for a 1219×2438 mm (4×8 ft) shear wall are to be used for a 2438×2438 mm (8×8 ft) shear wall after modifications, besides changing $\boldsymbol{w}$, the parameters $\boldsymbol{d_h}$ and $\boldsymbol{d_n}$ need to be multiplied by 0.5 for the 1219×2438 mm (4×8 ft) shear wall. In accordance with Equations 3-7, 3-8, 3-9, 3-10, and 3-11 in Chapter 3, the stiffness and strength degradation factors for the 1219×2438 mm (4×8 ft) shear wall are:

$$\eta = 1 + \delta_\eta \cdot \varepsilon_{4\times8} \tag{7-2}$$

and

$$\nu = 1 + \delta_\nu \cdot \varepsilon_{4\times8} \tag{7-3}$$

respectively.

If the same values are used for an 8 × 8 ft shear wall, the stiffness and strength degradation factors for an 8 × 8 ft shear wall are:

$$\eta = 1 + \delta_{\eta} \cdot \varepsilon_{8\times 8} \tag{7-4}$$

and

$$\nu = 1 + \delta_{\nu} \cdot \varepsilon_{8\times 8} \tag{7-5}$$

respectively. Since the energy dissipation of an 8 × 8 ft shear wall is twice that which a 4 × 8 ft wall dissipates,

$$\varepsilon_{8\times 8} = 2 \cdot \varepsilon_{4\times 8} \tag{7-6}$$

using the same degradation shear would overestimate the degradation of the 8 × 8 ft shear wall. Using half the values solves this problem. For a wall with the length of “L”, the degradation parameters would be:

$$\delta_{\eta,LX8} = \delta_{\eta,4X8} \cdot \frac{4}{L} \tag{7-7}$$

$$\delta_{\nu,LX8} = \delta_{\nu,4X8} \cdot \frac{4}{L} \tag{7-8}$$

The elastic viscous damping ratio of 1% ($\xi_0 = 1\%$) was applied in all of these models. The diagonal dashpot elements with the equivalent damping ratio were placed in the super wall elements. Viscous damping coefficients, c, were evaluated based on the equation:

$$c = \xi_0 \cdot (2 \cdot m \cdot \omega_1) \tag{7-9}$$

Where m is the mass of the structure, ω_1 is the circular frequency of the fundamental vibration mode, which is different from the stiffness parameter used in the super shear wall model. ω_1 can be calculated using the equation:

$$\omega_1 = \sqrt{\frac{K_0}{m}} \tag{7-10}$$

Where K_0 is the initial stiffness of the structure in each orthogonal direction. It can be calculated according to the equations:

$$K_{x0} = \sum \omega_{x_i}{}^2 \tag{7-11}$$

$$K_{y0} = \sum \omega_{y_i}{}^2 \tag{7-12}$$

Where ω_{xi} *and* ω_{yi} are the stiffness parameter, ω, of the i[th] shear wall in the directions parallel and perpendicular to the earthquake direction, respectively. For instance, in the case where the plan aspect ratio is 1:1 and no front wall is available, if ω values of the back shear wall and the two perpendicular shear walls are 2, 1.414, and 1.414, respectively, the stiffness in the two orthogonal directions are:

$$K_{x0} = 2^2 = 4kN/mm \tag{7-13}$$

$$K_{y0} = 1.414^2 + 1.414^2 = 4kN/mm \tag{7-14}$$

If the structural mass is 0.0061 kN/(mm/s^2) (weight is 60 kN),

$$\omega_{1x} = \omega_{1y} = \sqrt{\frac{K_{x0}}{m}} = 25.6s^{-1} \tag{7-15}$$

$$c_x = c_y = \xi_0 \cdot (2 \cdot m \cdot \omega_{1x}) = 0.003kN/(mm/s) \tag{7-16}$$

So for the parallel direction (to earthquake direction), the damping coefficient is 0.003 kN/(mm/s) for the back wall, and therefore 0.0015 kN/(mm/s) for each diagonal dashpot element in it (two diagonal dashpot elements in each shear wall). For the perpendicular direction, the damping coefficient of each wall is 0.0015 kN/(mm/s), and therefore 0.00075 for each diagonal dashpot element. It should be noted that since the influence from the 1% damping dashpot is relatively small, for those structures with both front and back shear walls, this damping was distributed evenly to front and back walls even their length are different. This was done to simplify the application to all the different configurations, and this application had little effect on the error of the analysis.

7.3.3 Simulation of Gypsum Wall

It was assumed that the partition walls and the interior face of all structural wood panel walls were constructed with gypsum wall board. The parameters for gypsum walls were taken from one of the two 4 × 8 ft gypsum sheathed walls that were tested by Toothman (2003). In this specimen, thickness of the gypsum board was 12 mm (1/2 in.), and the gypsum was connected to the framing with 3mm × 38mm long × 9.5mm head, 11gauge Galvanized roofing nails. The perimeter spacing was 178mm (7in.), and the field spacing was 406mm (16in.). The comparison of the hysteretic loops and parameter estimation is shown in Figure 7.3. The hysteretic energy comparison between the experimental and numerical results is shown in Figure 7.4.

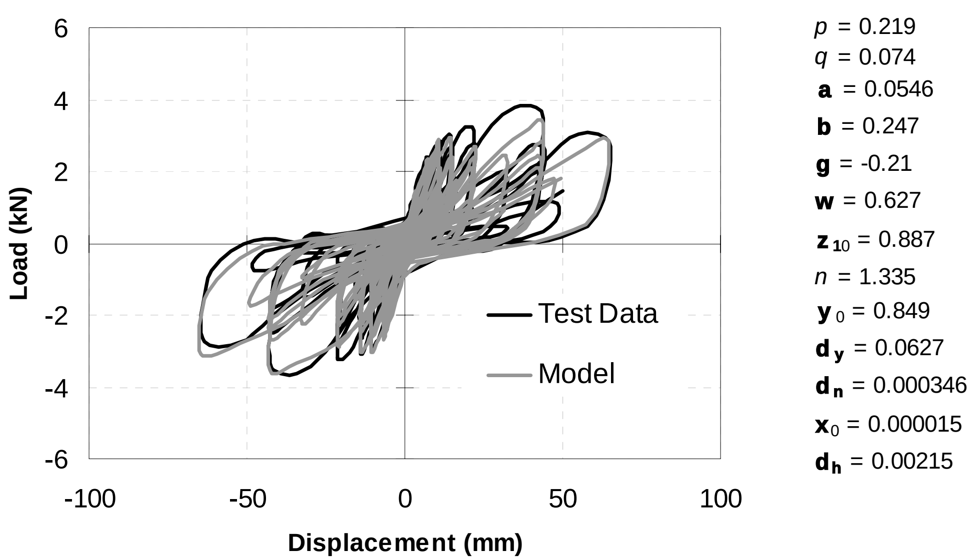

Figure 7.3 4×8 ft Gypsum Wall Parameter Estimation

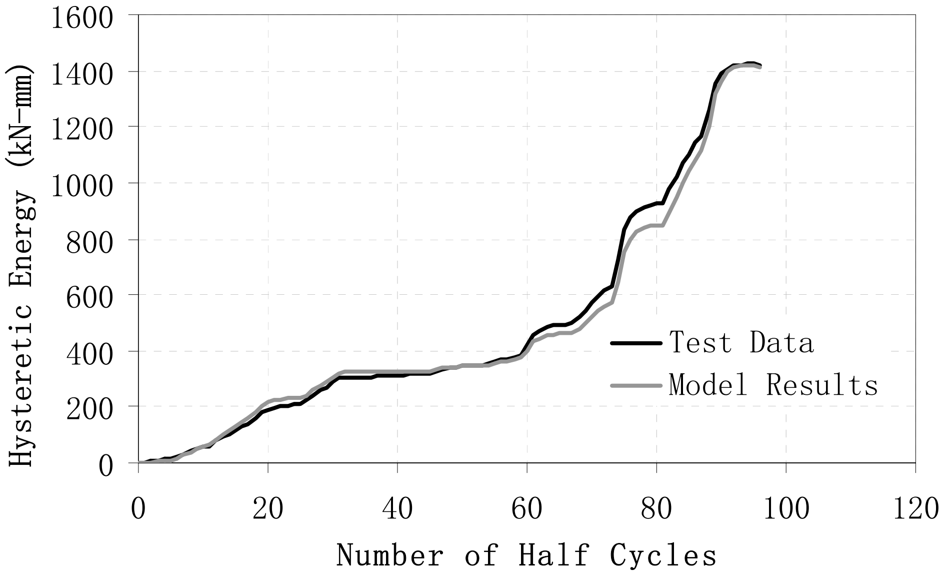

Figure 7.4 Gypsum Wall Hysteretic Energy Comparison

Each exterior shear wall was simulated with 2 sets of diagonal hysteretic springs, one of which represents OSB panel attachment and the other represents gypsum board attachment.

7.4 Structural Design

From the Maps of Maximum Considered Earthquake Ground Motion given in the IBC (2003), design accelerations for the San Francisco Bay California Area were taken as

$$S_s = 150\% \cdot g \tag{7-17}$$

$$S_1 = 100\% \cdot g \tag{7-18}$$

and the Site Type (soil classification) was assumed to be "D". From Table 1615.1.2(1) and 1615.1.2(2) of the IBC,

$$F_a = 1.0 \tag{7-19}$$

$$F_v = 1.5 \tag{7-20}$$

Therefore,

$$S_{Ds} = \frac{2}{3} \cdot F_a \cdot S_s = 1.0g \tag{7-21}$$

$$S_{D1} = \frac{2}{3} \cdot F_v \cdot S_1 = 1.0g \tag{7-22}$$

From IBC (2003) the structural system response factor for wood light-frame bearing walls is:

$$R = 6.5 \tag{7-23}$$

Comparison between the design response spectrum according the IBC design criteria above and the spectrum of the scaled Canoga Park earthquake record can be seen in Figure 7.5. From the comparison, it is obvious that the scaled Canoga Park earthquake record can trigger higher structural response in periods of 0.2 to 1 second, which covers the most common natural periods of wood-frame buildings.

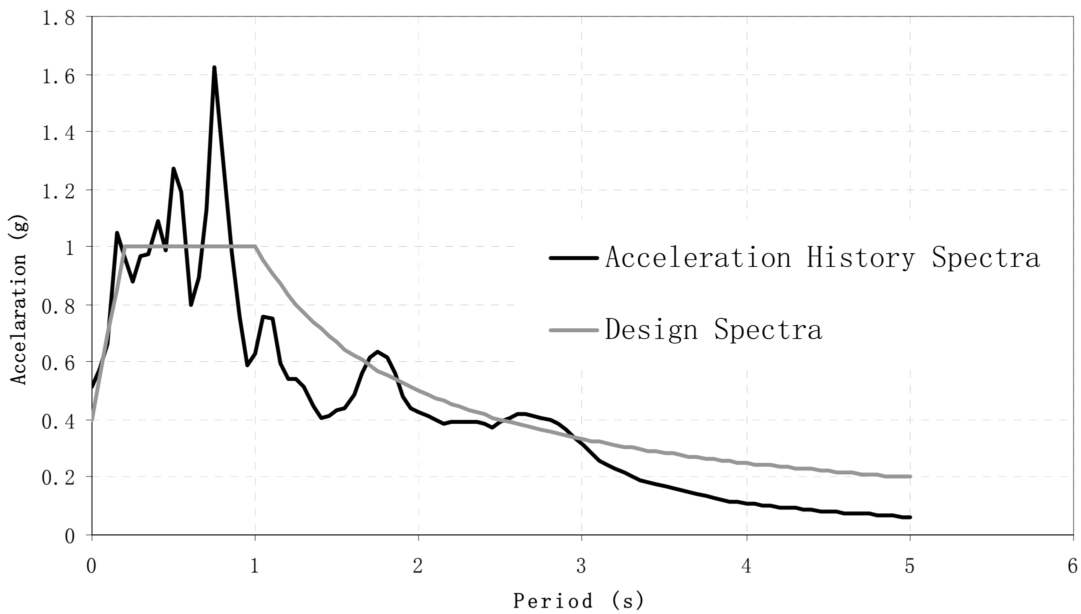

Figure 7.5 Response Spectra Comparison

According to Special Design Provisions for Wind and Seismic (2001 Edition Supplement, ASD/LRFD), the nominal unit shear capacity of the shear wall constructed with 11-mm (7/16-in) wood structural panels and 8d nails at 152 mm (6 in.) o. c. (edge), 305 mm (12 in.) o. c. (field) is 7.44 kN/m (510 lbs/ft) for seismic design (This assumes the wall is fully restrained). The LRFD factored unit resistance is determined by multiplying the nominal unit shear capacity by a resistance factor of 0.65. So the design resistance capacity is 4.84 kN/m (331 lbs/ft).

For Case 1 (L:W = 1:1), the building weight is 53.4 kN (12 kips), and the seismic demand is:

$$EQ = \frac{1.2 \cdot S_{Ds} \cdot W}{R} = 2215 \ lbs = 9.85kN \tag{7-24}$$

The required total length of shear wall in each orthogonal direction is:

$$L = \frac{2215}{331} = 6.7\,ft = 2.04m \tag{7-25}$$

Considering the structural response triggered by the ground motion history is higher than that of design demand, 3.05 m (10 ft) long shear walls were used in the design (an amplifier factor of 1.49 was applied).

The shear wall lengths and corresponding parameters of **w**, **d_n**, and **d_h** for different opening ratios are listed in Tables 7.1 through 7.3. It should be noted that the front and back walls are parallel to the direction of the design ground motion, and the perpendicular walls are those oriented perpendicular to the direction of the design ground motion.

Table 7.1 Front Wall Design (L:W = 1:1)

Case		Total Length (ft)	Front/Back Ratio	Front Wall (east wall)							
				OSB Wall				Gypsum Wall			
				Length	w	d_n	d_h	Length	w	d_n	d_h
1	1_1_0	10	0	0.00	**0.000**	**N/A**	**N/A**	0.00	**0.000**	**N/A**	**N/A**
	1_1_25	10	0.25	2.00	**0.614**	**4.00E-06**	**2.12E-04**	2.00	**0.443**	**6.92E-04**	**4.29E-03**
	1_1_50	10	0.5	3.33	**0.792**	**2.40E-06**	**1.27E-04**	3.33	**0.572**	**4.15E-04**	**2.58E-03**
	1_1_75	10	0.75	4.29	**0.898**	**1.87E-06**	**9.89E-05**	4.29	**0.649**	**3.23E-04**	**2.00E-03**
	1_1_100	10	1	5.00	**0.970**	**1.60E-06**	**8.48E-05**	5.00	**0.701**	**2.77E-04**	**1.72E-03**

Table 7.2 Back Wall Design (L:W = 1:1)

Case		Total Length (ft)	Front/Back Ratio	Back Wall (west wall)							
				OSB Wall				Gypsum Wall			
				Length	w	d_n	d_h	Length	w	d_n	d_h
1	1_1_0	10	0	10.00	**1.372**	**8.00E-07**	**4.24E-05**	10.00	**0.991**	**1.38E-04**	**8.59E-04**
	1_1_25	10	0.25	8.00	**1.228**	**1.00E-06**	**5.30E-05**	8.00	**0.887**	**1.73E-04**	**1.07E-03**
	1_1_50	10	0.5	6.67	**1.121**	**1.20E-06**	**6.36E-05**	6.67	**0.809**	**2.08E-04**	**1.29E-03**
	1_1_75	10	0.75	5.71	**1.037**	**1.40E-06**	**7.42E-05**	5.71	**0.749**	**2.42E-04**	**1.50E-03**
	1_1_100	10	1	5.00	**0.970**	**1.60E-06**	**8.48E-05**	5.00	**0.701**	**2.77E-04**	**1.72E-03**

Table 7.3 Perpendicular Wall Design (L:W = 1:1)

Case		Total Length (ft)	Front/Back Ratio	Perpendicular Wall							
				OSB Wall				Gypsum Wall			
				Length	w	d_n	d_h	Length	w	d_n	d_h
1	1_1_0	10	0	5.00	**0.970**	**1.60E-06**	**8.48E-05**	5.00	**0.701**	**2.77E-04**	**1.72E-03**
	1_1_25	10	0.25	5.00	**0.970**	**1.60E-06**	**8.48E-05**	5.00	**0.701**	**2.77E-04**	**1.72E-03**
	1_1_50	10	0.5	5.00	**0.970**	**1.60E-06**	**8.48E-05**	5.00	**0.701**	**2.77E-04**	**1.72E-03**
	1_1_75	10	0.75	5.00	**0.970**	**1.60E-06**	**8.48E-05**	5.00	**0.701**	**2.77E-04**	**1.72E-03**
	1_1_100	10	1	5.00	**0.970**	**1.60E-06**	**8.48E-05**	5.00	**0.701**	**2.77E-04**	**1.72E-03**

The cases with partition walls in the parallel direction (parallel to the design ground motion direction) have the same exterior shear wall layout as the cases without partition walls. The partition was assumed to be “non-structural” for the design, but the gypsum was attached as if it was “structural” and was included in the time-step analysis. Essentially, this means the length of regular wood structural panel shear wall was determined assuming the partition was not present. The gypsum partition wall’s length in the configurations with an aspect ratio of 1:1 is 16 ft (80% of the relevant building dimension). The relevant parameters of $\mathbf{w}$, $\mathbf{d_n}$, and $\mathbf{d_h}$ are 1.773, 4.33E-5, and 2.68E-4 respectively. It should be noted that since these walls were assumed to be sheathed in both sides, these parameters were derived based on the length of 32 ft.

The 1% equivalent viscous damping coefficients are 0.00203 kN/(mm/s) in the two orthogonal directions.

The design tables for all of the other cases with different aspect ratios are presented in the Appendix B.

A 2.5% story height (ASCE7-05) drift was regarded as the drift failure criteria since this is the code allowable drift. The analysis results presented later show that the without-partition-wall cases (1_1_0, 1_1_25, 4_1_0, 4_1_25, 4_1_50, 4_1_75, 6_1_0, 6_1_25, 6_1_50, 6_1_75) all fail because the front wall drift is beyond the drift criteria (in Case 2_1_0, the front wall drift is only 5% beyond the criteria, so it could be regarded OK). Normally, the torsional design in wood-frame structures is neglected. In this study, a check of the feasibility of elastic torsion design philosophy for wood-frame structures is completed. The structures that do not have partition walls and suffer potential failure (front wall drift was larger than 2.5% story height) have been redesigned based on the elastic torsional design philosophy. Only the structures without partition walls were redesigned because the partition walls are regarded as non-structural and their contributions are often ignored in real design. To be conservative, if the structure without partition walls cannot satisfy the design criteria, the structure will be regarded as failed, even when the structure that has the same configuration but has partition walls could survive.

The redesign of the failed structures was based on the following equations:

$$T = V_{//} \cdot e_r \tag{7-26}$$

$$V_{\perp} = \frac{T}{W} \tag{7-27}$$

where, T is torsion moment, $V_{//}$ is the total parallel design resistance, e_r is the eccentricity between mass center and stiffness center, $V_{\perp}$ is the imposed loads in perpendicular walls, and W is the distance between exterior perpendicular walls.

The redesign results are shown in Table 7.4.

Table 7.4 Torsion Design Results

Cases	$V_{//}$	e_r	T	W	V	$L_{\perp\, extra}$	$L_{\perp\, original}$	$L_{\perp\, total}$
	kips	ft	kip-ft	ft	kips	ft	ft	ft
1_1_0	3.31	10	33.1	20	1.655	5	5	10
1_1_25	3.31	6	19.86	20	0.993	3	5	8
4_1_0	6.62	20	132.4	20	6.62	20	10	30
4_1_25	6.62	12	79.44	20	3.972	12	10	22
4_1_50	6.62	6.67	44.1554	20	2.20777	6.67	10	16.67
4_1_75	6.62	2.88	19.0656	20	0.95328	2.88	10	12.88
5_1_0	9.93	30	297.9	20	14.895	45	15	60
5_1_25	9.93	18	178.74	20	8.937	27	15	42
5_1_50	9.93	10	99.3	20	4.965	15	15	30
5_1_75	9.93	4.32	42.8976	20	2.14488	6.48	15	21.48

7.5 Analysis Results

The analysis results are shown in Figures 7.6 through 7.101. It should be noted that the redesigned analysis results are the analysis results of those cases that have been redesigned to account for torsional response.

Group1_1 (L:W=1:1, w/o partition wall)

The shear wall drift time traces in each case are shown in Figures 7.6 through 7.19.

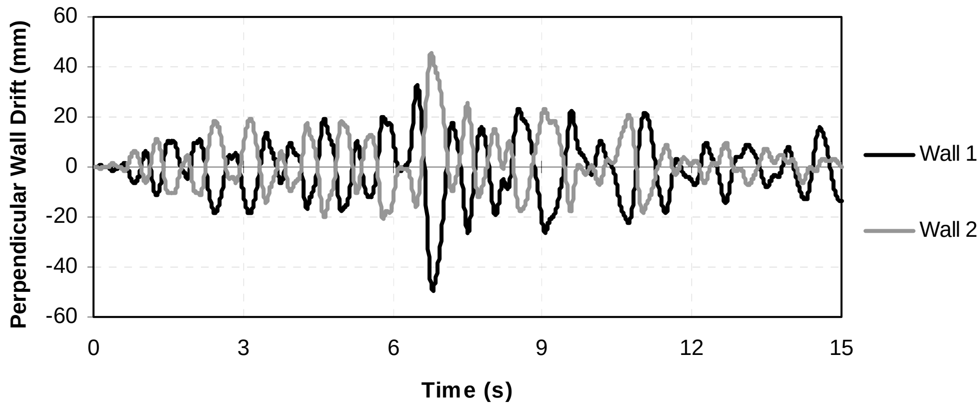

Figure 7.6 Drifts of Perpendicular Walls (Case 1_1_0)

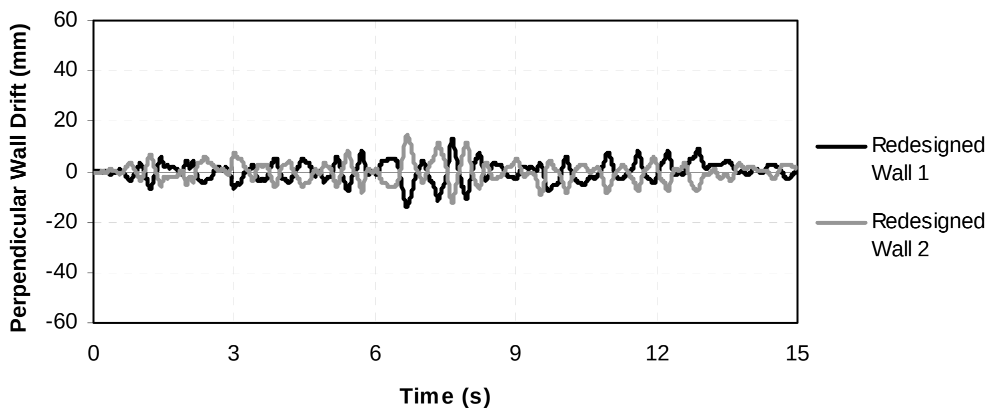

Figure 7.7 Drifts of Perpendicular Walls (Redesigned Case 1_1_0)

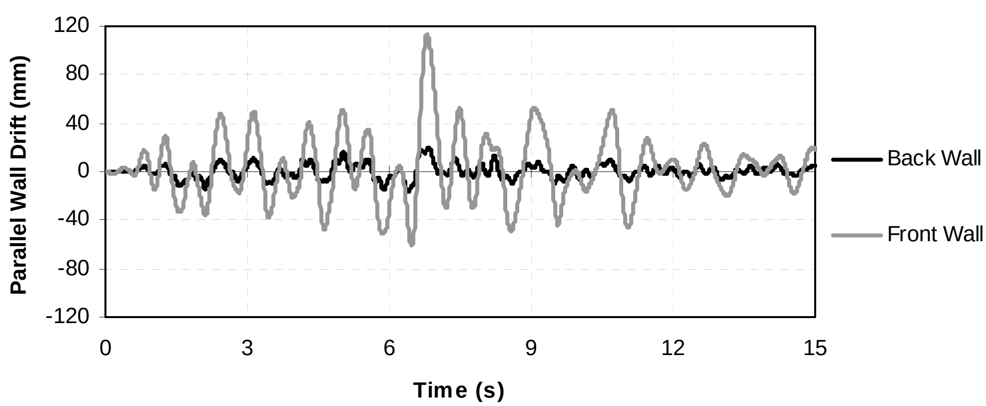

Figure 7.8 Drifts of Parallel Walls (Case 1_1_0)

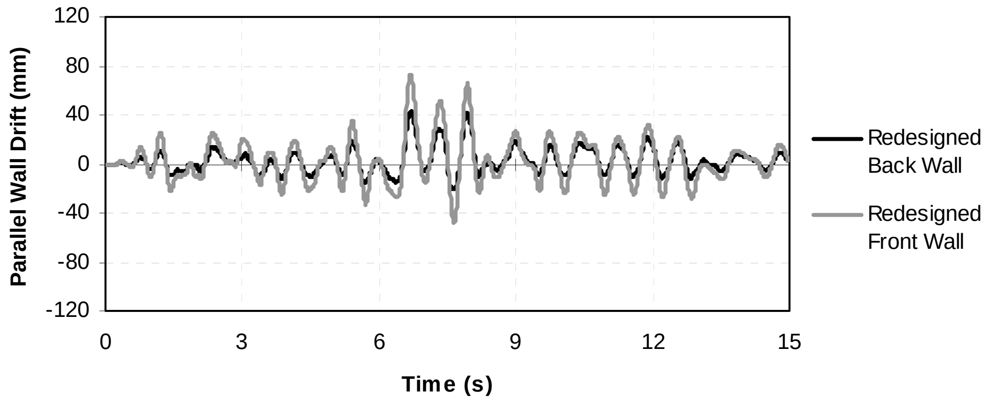

Figure 7.9 Drifts of Parallel Walls (Redesigned Case 1_1_0)

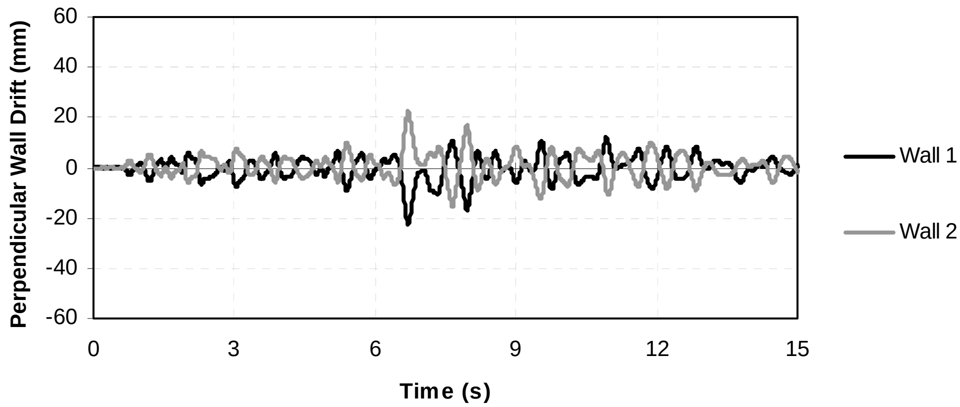

Figure 7.10 Drifts of Perpendicular Walls (Case 1_1_25)

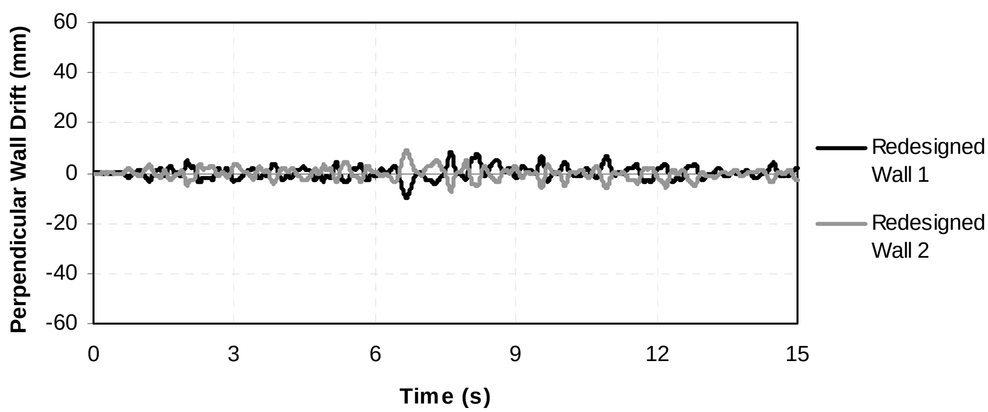

Figure 7.11 Drifts of Perpendicular Walls (Redesigned Case 1_1_25)

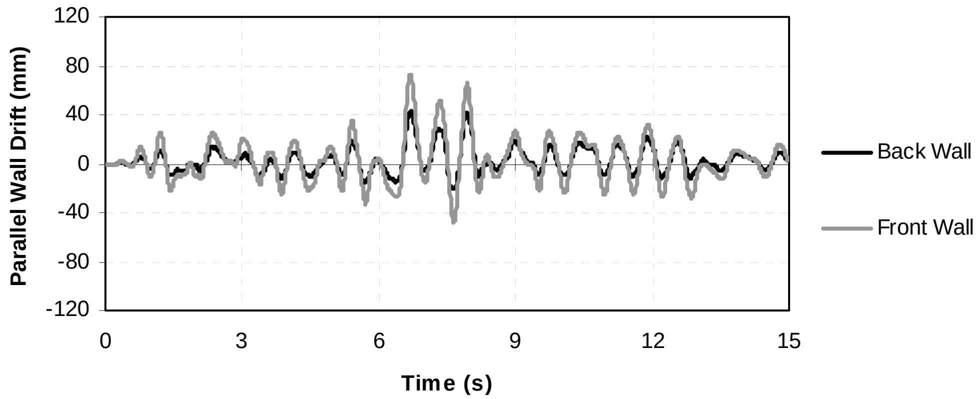

Figure 7.12 Drifts of Parallel Walls (Case 1_1_25)

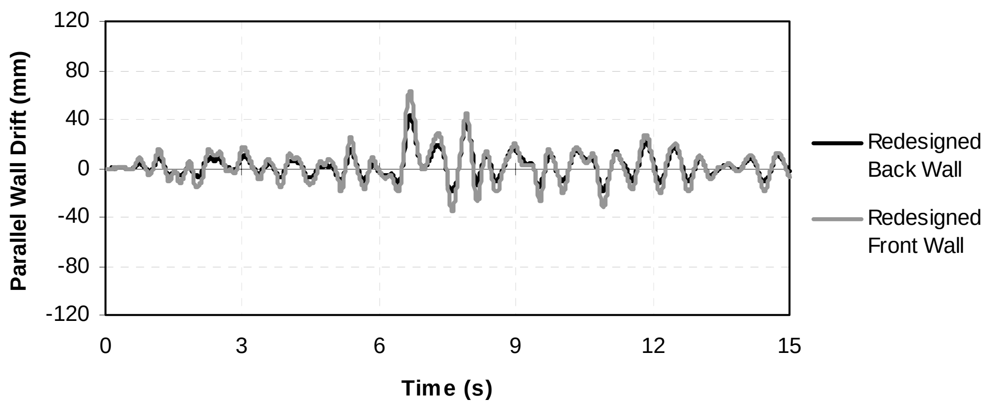

Figure 7.13 Drifts of Parallel Walls (Redesigned Case 1_1_25)

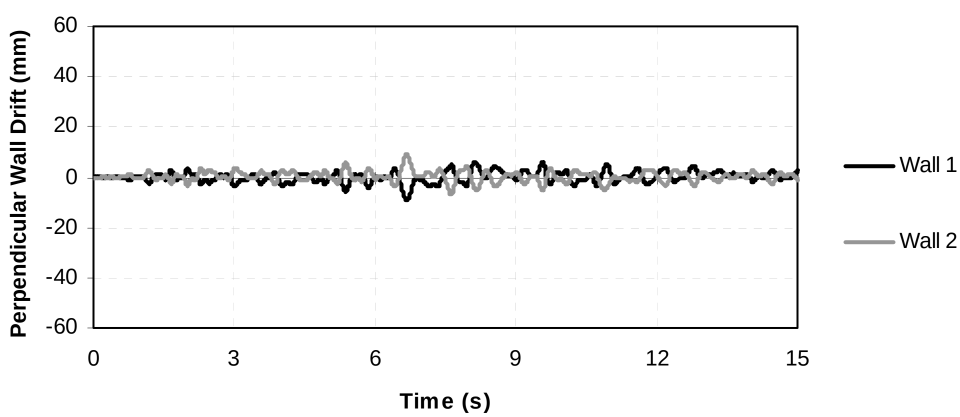

Figure 7.14 Drifts of Perpendicular Walls (Case 1_1_50)

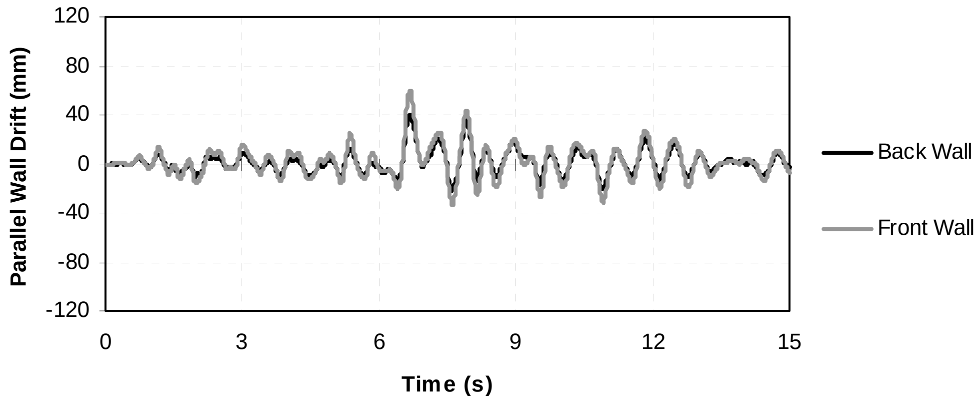

Figure 7.15 Drifts of Parallel Walls (Case 1_1_50)

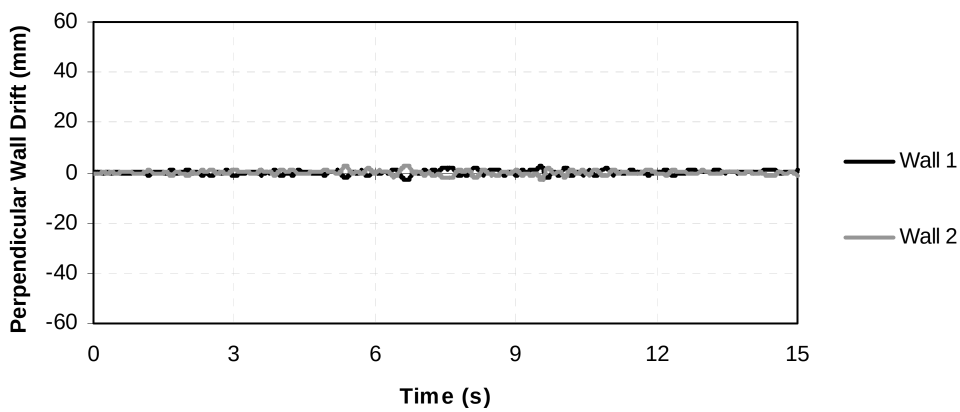

Figure 7.16 Drifts of Perpendicular Walls (Case 1_1_75)

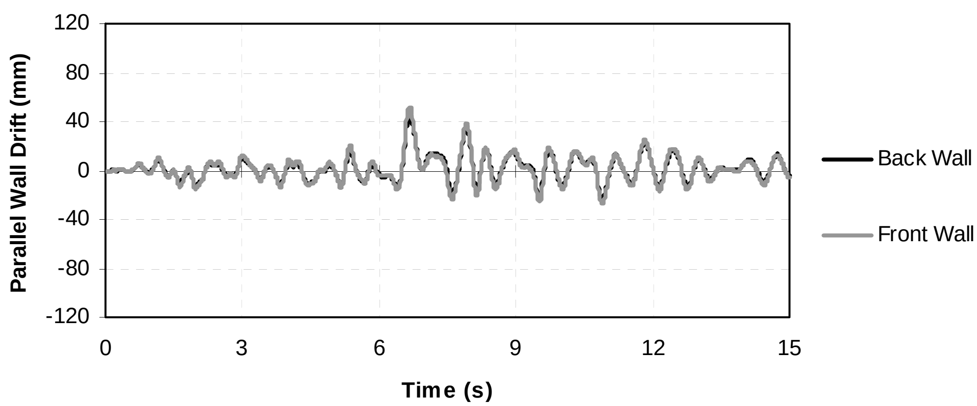

Figure 7.17 Drifts of Parallel Walls (Case 1_1_75)

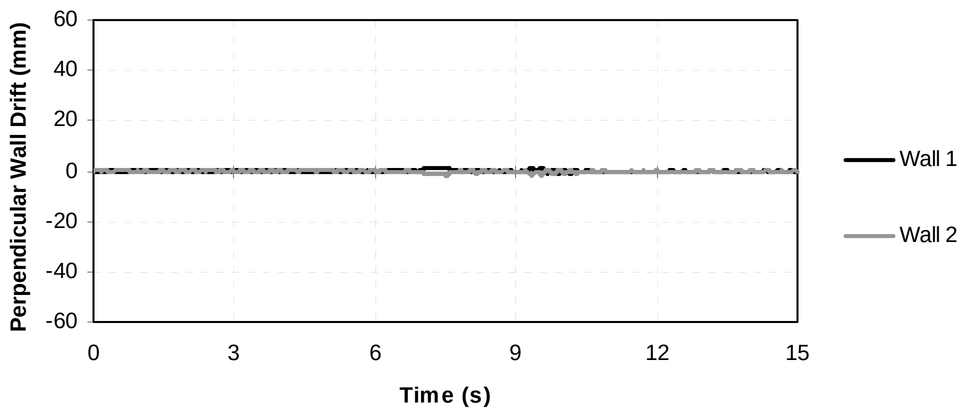

Figure 7.18 Drifts of Perpendicular Walls (Case 1_1_100)

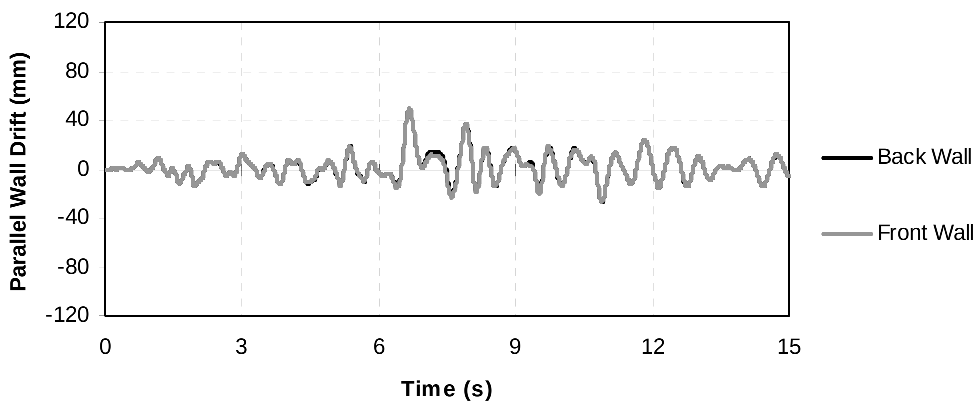

Figure 7.19 Drifts of Parallel Walls (Case 1_1_100)

Peak drifts in the perpendicular walls are shown in Figure 7.20. The drifts in the perpendicular walls were almost symmetric when the structure was subjected to the earthquake in the parallel direction. No failure occurred in the perpendicular walls from the drift point of view. The maximum perpendicular wall drift decreases from 49.23 mm to 1.72 mm when the front-to-back wall ratio increases from 0% (completely open front) to 100% (symmetric). Theoretically, the perpendicular wall drifts should be zero when the structure is symmetric, and the small drift values from the analysis were caused by numerical errors developed in the analysis. The updated configuration based on elastic torsional design philosophy reduced the peak drifts in perpendicular walls by over 50%.

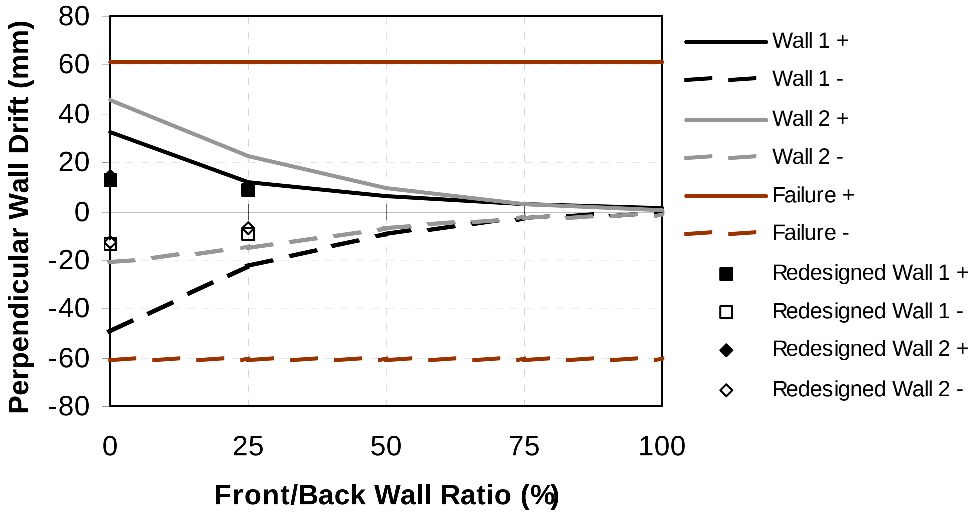

Figure 7.20 Peak Perpendicular Wall Drift (L:W=1:1, w/o partition wall)

Peak drifts in the parallel walls are shown in Figure 7.21. The maximum back wall drift increases from 20.12 mm to 48.96 mm and the maximum front wall drift decreased from 113.05 mm to 49.12 mm when the front-to-back wall ratio increases from 0% (completely open front) to 100% (symmetric). The reason is that when the degree of non-symmetry reduces, the torsional behavior weakens, and the drifts in parallel walls tend to be symmetric. The back wall is the strongest when the front wall is completely open because it was designed to resist the entire base shear for this case. So the front wall drift reduces and the back wall drift increases as the opening in the front wall is reduced. Theoretically, the drift in the back and the front walls should be same when the structure is symmetric and the small difference was caused by the numerical errors developed in the analysis. The structures with the front-to-back wall ratios of 0 and 25% failed due to excessive drift. The updated configuration based on elastic torsional design philosophy reduced the peak drifts in the parallel walls for these two cases. However, the peak values were still higher than the failure criteria.

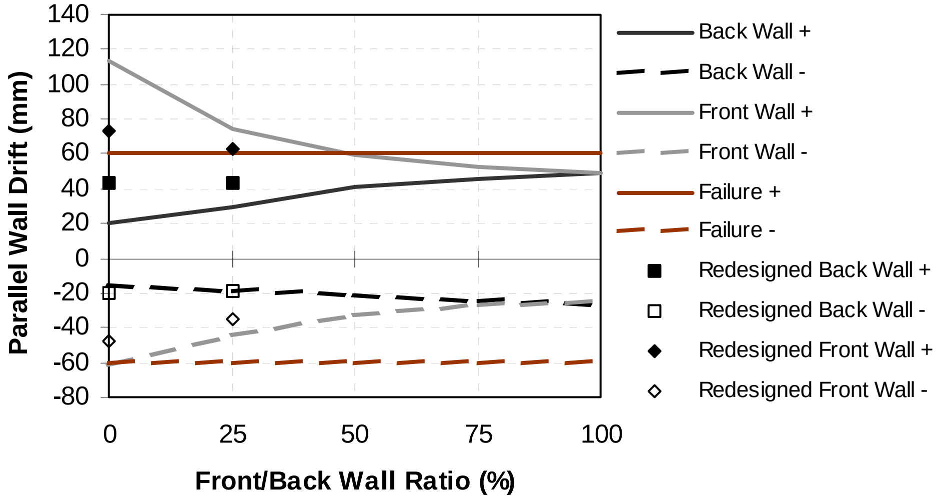

Figure 7.21 Peak Parallel Wall Drift (L:W=1:1, w/o partition wall)

Figure 7.22 shows the peak imposed loads in the perpendicular walls. It should be noted that the inclusion of figures of peak imposed loads is for the sake of completeness of the results plotting. Since the wall length is variable for the buildings with different opening ratios or plan aspect ratios. The absolute load values cannot be the basis of any judgement.

Figure 7.23 shows ratio of the peak imposed load to allowable design resistance (a normalized load and will be called “load ratio”) in the perpendicular walls. It is generally assumed that the ultimate wood-frame shear wall strength capacity is 2.8 to 3.4 times the allowable design value, and 3.0 is assumed to be the value in this study. As shown in Figure 7.23, the perpendicular walls did not reach ultimate capacity, and the load ratio in the perpendicular walls dropped from 2.568 (completely open front) to 0.286 (symmetric).

Theoretically, the load ratio in perpendicular walls should be zero when the structure is symmetric and the small value was caused by the numerical errors developed in the analysis. For Cases 1_1_0 and 1_1_25, the load ratio dropped in the perpendicular walls after the perpendicular walls were strengthened based on the torsional design.

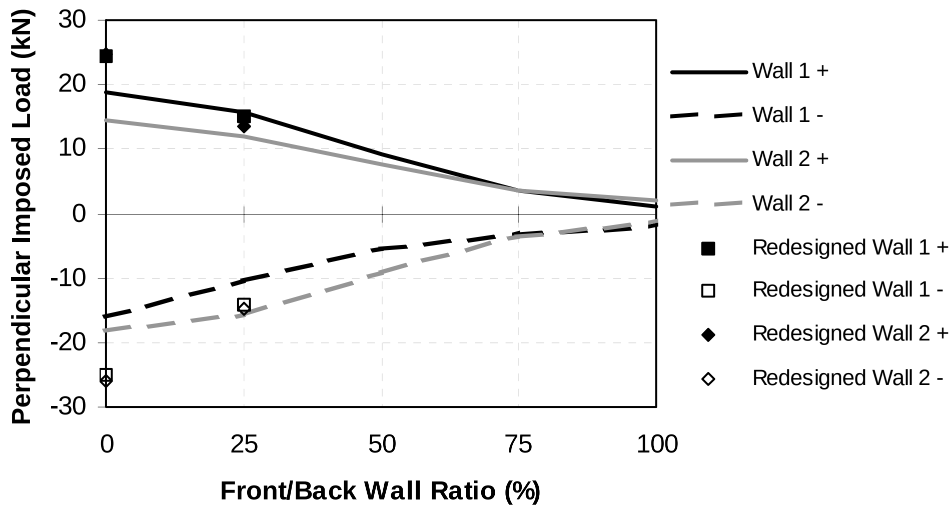

Figure 7.22 Peak Perpendicular Impose Load (L:W=1:1, w/o partition wall)

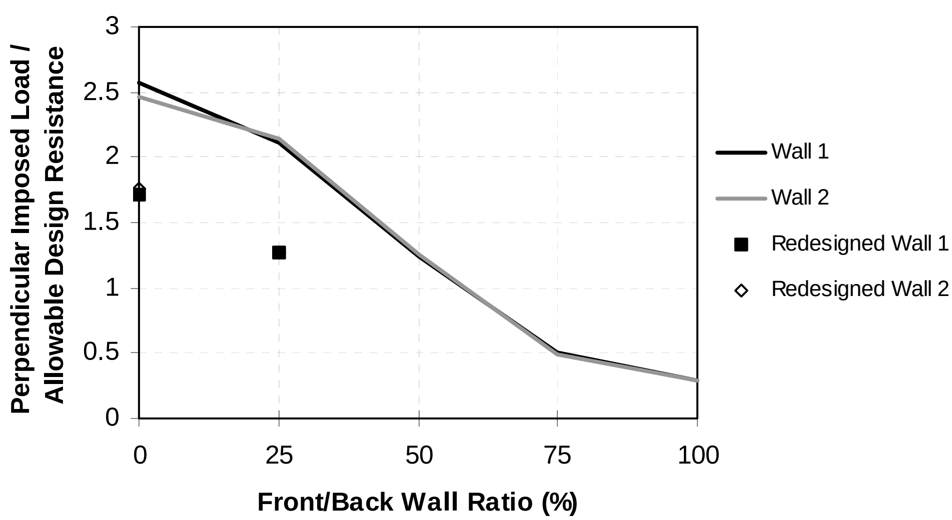

Figure 7.23 Peak Perpendicular Imposed Load / Design Resistance (L:W=1:1, w/o partition wall)

Peak loads and load ratios in the parallel walls are shown in Figures 7.24 and 7.25, respectively. As shown in Figure 7.25, the load ratio increased in the back wall from 1.81 (completely open front) to 2.57 (symmetric) and decreased in the front wall from 2.72 (front-to-back wall ratio 25%) to 2.58 (symmetric) when the front-to-back wall ratio increased. Load ratio is proportional to wall drift. The higher wall drift is, the higher load ratio is, though the relationship is nonlinear. The torsional response was resisted harder because the perpendicular walls were strengthened based on the torsional design, so the load ratios in the back and front walls became closer with each other.

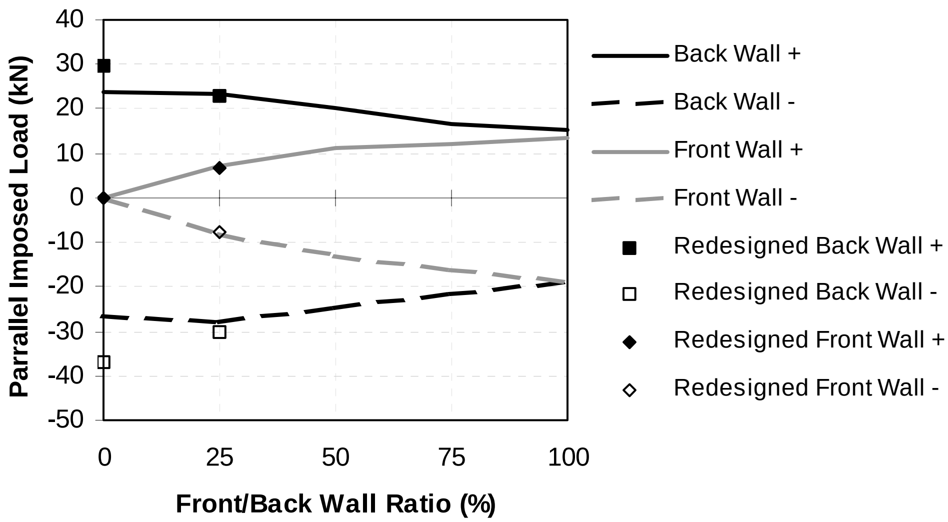

Figure 7.24 Peak Parallel Impose Load (L:W=1:1, w/o partition wall)

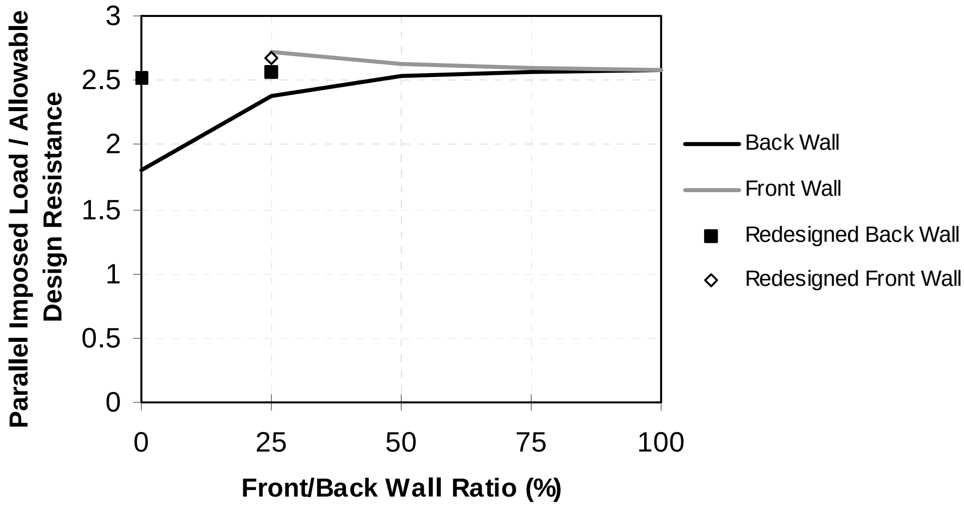

Figure 7.25 Peak Parallel Imposed Load / Design resistance (L:W=1:1, w/o partition wall)

The peak drifts, imposed loads and load ratios are also listed in Tables 7.5 and 7.6.

Table 7.5 Peak Drifts of the Shear Walls (Group 1_1)

Front/Back Wall ratio (%)	Peak Perpendicular Wall Drift (mm)						Peak Parallel Wall Drift (mm)					
	Wall 1			Wall 2			Back Wall			Front Wall		
	+	-	MAX	+	-	MAX	+	-	MAX	+	-	MAX
0	32.66	-49.23	**49.23**	45.47	-20.82	**45.47**	20.12	-15.91	**20.12**	113.05	-61.17	**113.05**
25	11.94	-22.60	**22.60**	22.58	-15.30	**22.58**	29.89	-18.62	**29.89**	74.82	-44.07	**74.82**
50	6.26	-9.29	**9.29**	9.08	-6.83	**9.08**	40.67	-21.28	**40.67**	59.86	-32.69	**59.86**
75	2.59	-3.09	**3.09**	3.09	-2.83	**3.09**	45.66	-24.24	**45.66**	52.17	-27.44	**52.17**
100	1.56	-0.90	**1.56**	0.66	-1.72	**1.72**	48.96	-26.48	**48.96**	49.12	-26.17	**49.12**
0 (Redesigned)	12.96	-13.89	**13.89**	14.58	-12.58	**14.58**	43.06	-20.56	**43.06**	73.13	-48.22	**73.13**
25 (Redesigned)	8.59	-9.68	**9.68**	8.98	-7.30	**8.98**	43.51	-19.17	**43.51**	62.98	-35.48	**62.98**

Table 7.6 Peak Imposed Loads and Load Ratios in the Shear Walls (Group 1_1)

Front/Back Wall ratio (%)	Peak Perpendicular Imposed Loads (kN)								Peak Parallel Imposed Loads (kN)							
	Wall 1				Wall 2				Back Wall				Front Wall			
	+	-	MAX	Load Ratio	+	-	MAX	Load Ratio	+	-	MAX	Load Ratio	+	-	MAX	Load Ratio
0	18.90	-16.02	**18.90**	2.57	14.44	-18.16	**18.16**	2.47	23.91	-26.60	**26.60**	1.81	0.00	0.00	**0.00**	N/A
25	15.59	-10.31	**15.59**	2.12	12.02	-15.80	**15.80**	2.15	23.55	-27.93	**27.93**	2.37	7.21	-8.00	**8.00**	2.72
50	9.10	-5.59	**9.10**	1.24	7.56	-9.20	**9.20**	1.25	20.31	-24.90	**24.90**	2.54	11.06	-12.89	**12.89**	2.63
75	3.72	-3.37	**3.72**	0.51	3.59	-3.58	**3.59**	0.49	16.57	-21.56	**21.56**	2.56	12.22	-16.34	**16.34**	2.59
100	1.18	-2.10	**2.10**	0.29	2.14	-1.34	**2.14**	0.29	15.04	-18.95	**18.95**	2.57	13.67	-19.01	**19.01**	2.58
0 (Redesigned)	24.39	-25.16	**25.16**	1.71	24.86	-25.87	**25.87**	1.76	29.66	-37.16	**37.16**	2.52	0.00	0.00	**0.00**	N/A
25 (Redesigned)	14.94	-14.24	**14.94**	1.27	13.51	-14.90	**14.90**	1.26	22.94	-30.20	**30.20**	2.56	6.90	-7.87	**7.87**	2.67

Group 1_2 (L:W = 1:1, w/ partition gypsum wall)

The time traces of the shear wall drifts in each case are shown in Figures 7.26 through 7.40.

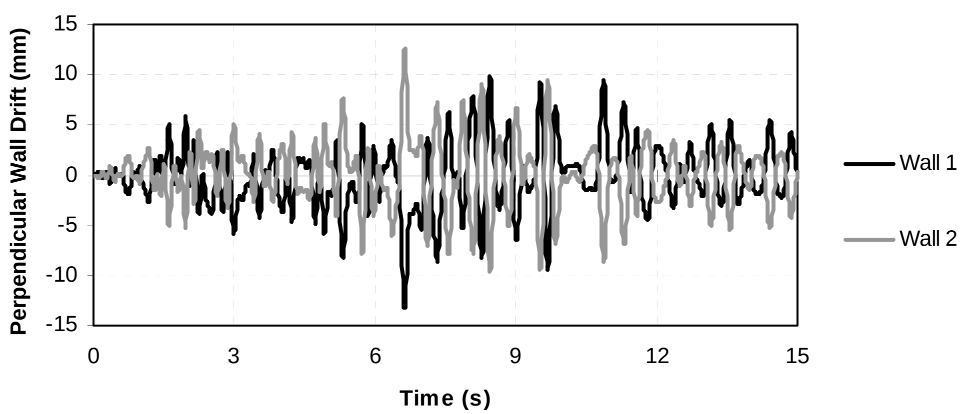

Figure 7.26 Drifts of Perpendicular Walls (Case 1_2_0)

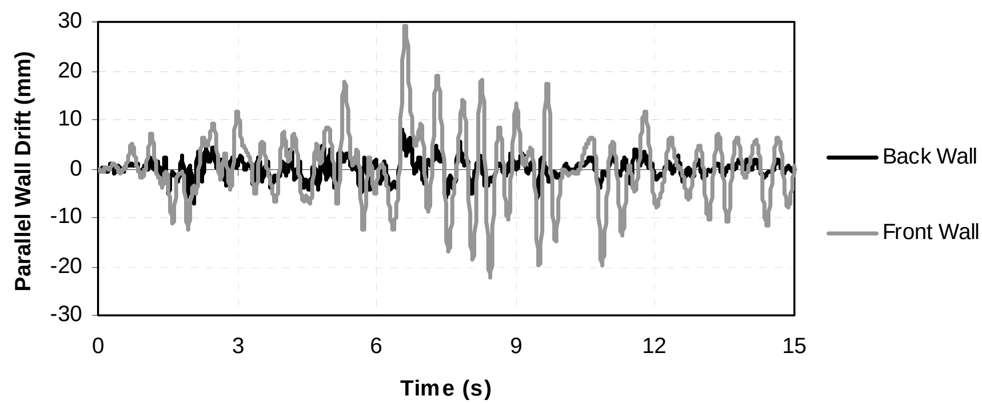

Figure 7.27 Drifts of Parallel Walls (Case 1_2_0)

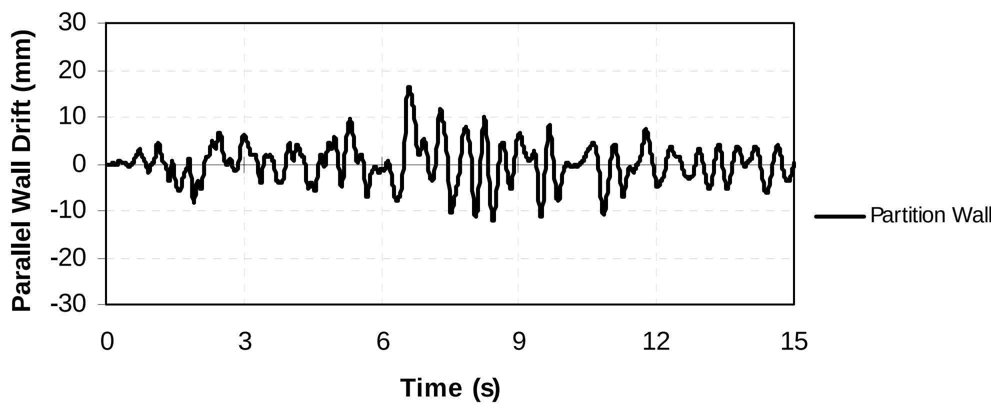

Figure 7.28 Drifts of Partition Wall (Case 1_2_0)

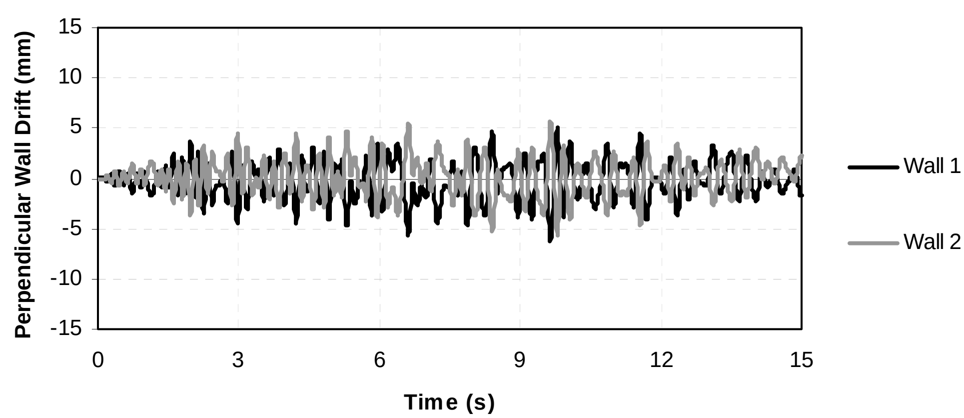

Figure 7.29 Drifts of Perpendicular Walls (Case 1_2_25)

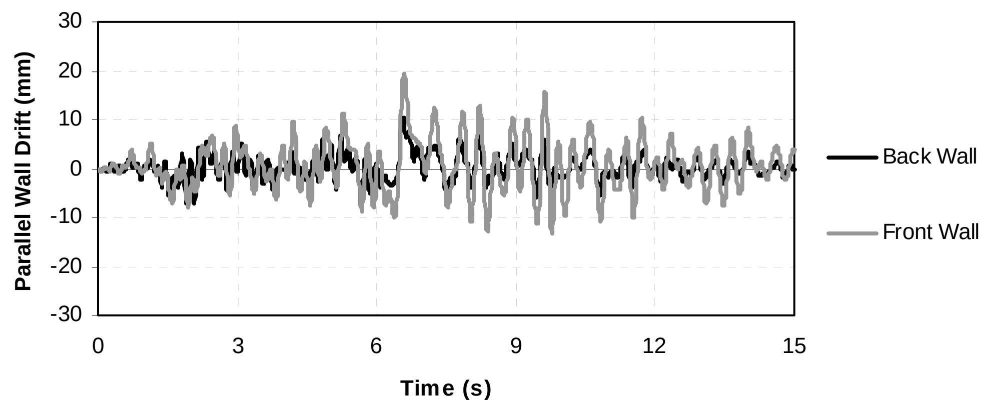

Figure 7.30 Drifts of Parallel Walls (Case 1_2_25)

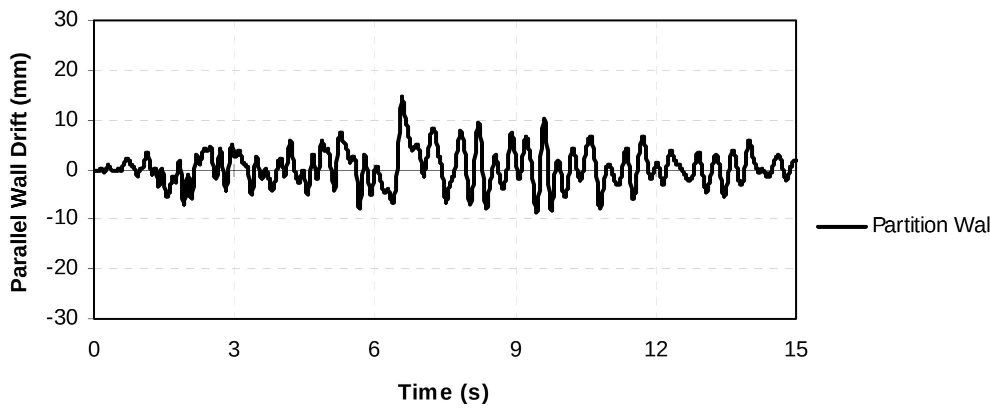

Figure 7.31 Drifts of Partition Wall (Case 1_2_25)

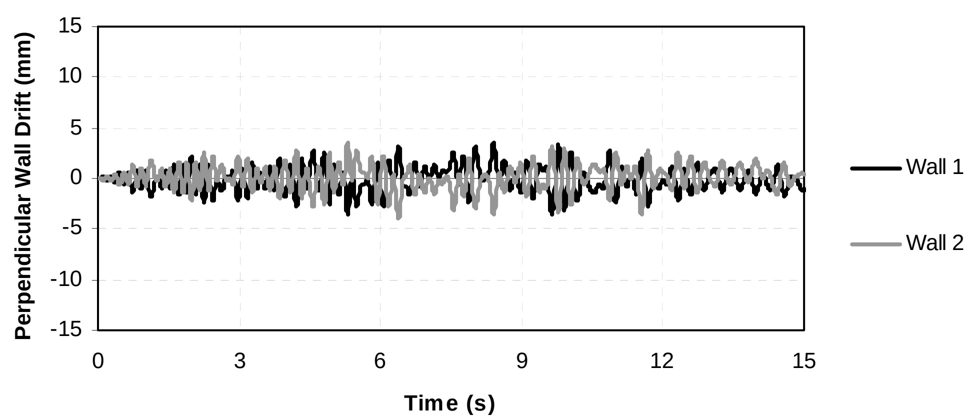

Figure 7.32 Drifts of Perpendicular Walls (Case 1_2_50)

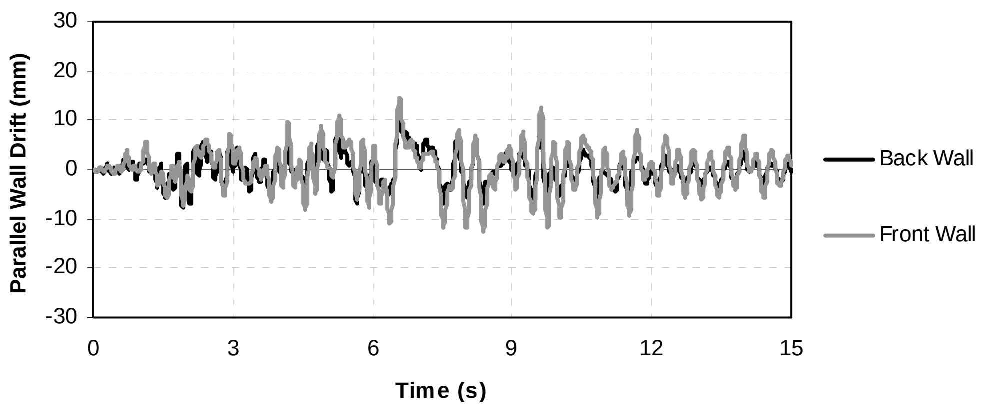

Figure 7.33 Drifts of Parallel Walls (Case 1_2_50)

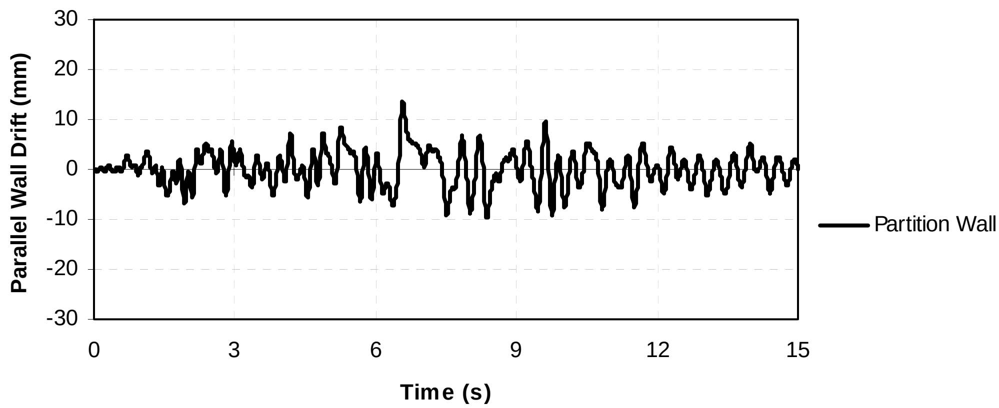

Figure 7.34 Drifts of Partition Wall (Case 1_2_50)

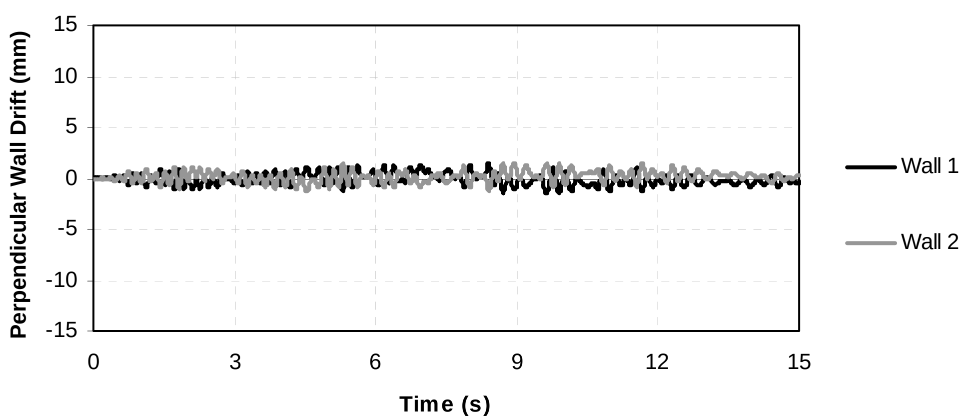

Figure 7.35 Drifts of Perpendicular Walls (Case 1_2_75)

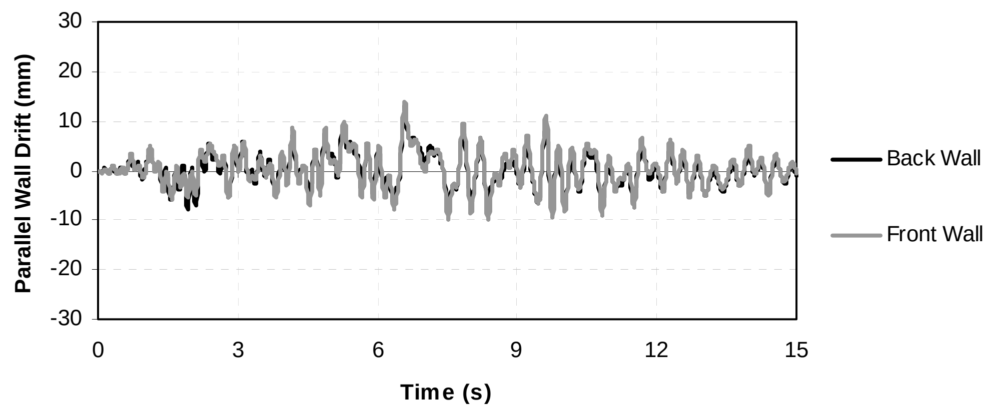

Figure 7.36 Drifts of Parallel Walls (Case 1_2_75)

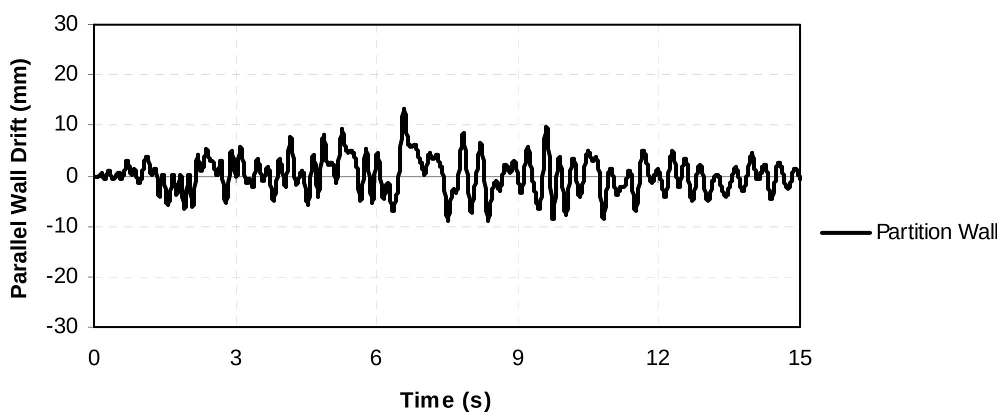

Figure 7.37 Drifts of Partition Wall (Case 1_2_75)

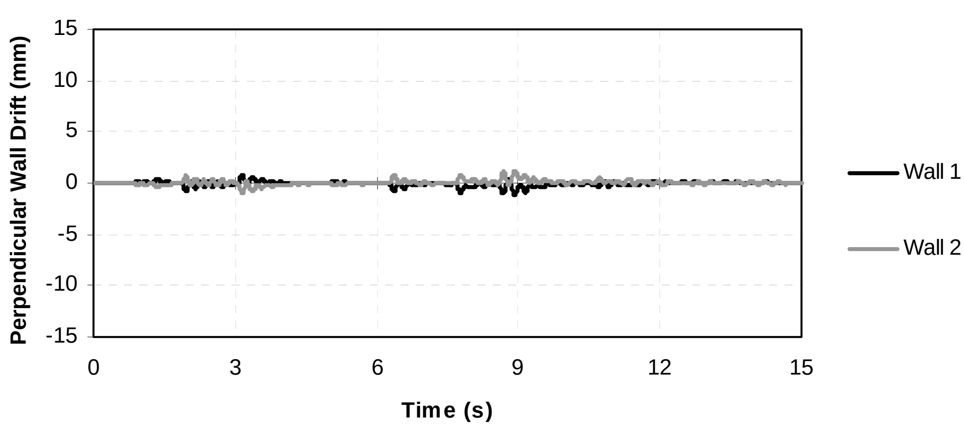

Figure 7.38 Drifts of Perpendicular Walls (Case 1_2_100)

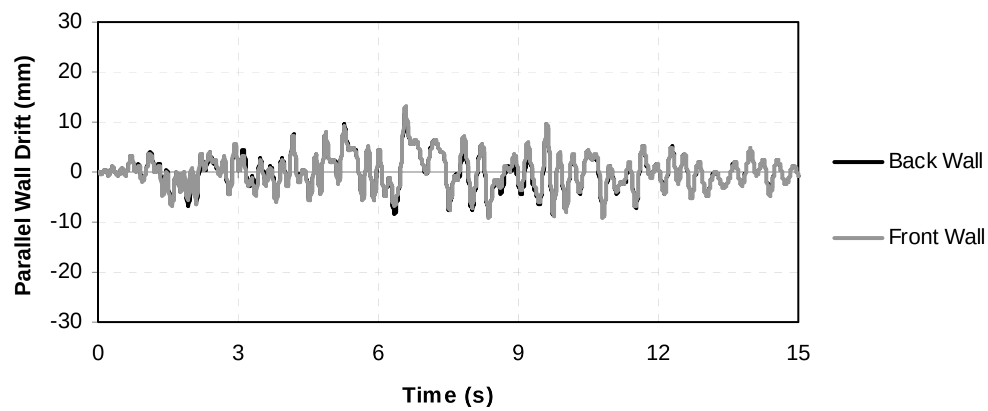

Figure 7.39 Drifts of Parallel Walls (Case 1_2_100)

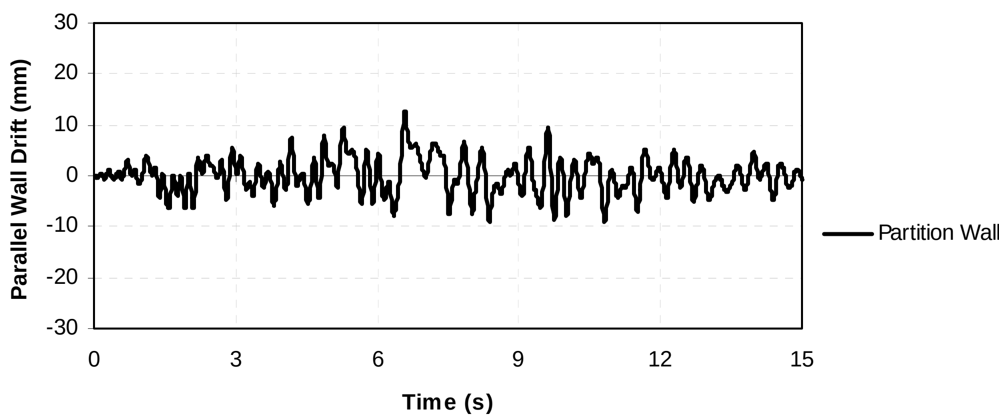

Figure 7.40 Drifts of Partition Wall (Case 1_2_100)

The hysteresis of the back wall and the partition wall in Case 1_1_0 are shown in Figures 7.41 and 7.42, respectively. The peak imposed load is 17.6 kN and 27.7 kN in the back wall and the partition wall, respectively. It seems unreasonable that the imposed load in the partition wall is even greater than the structural wall. However, if considering that the partition wall length is 16 ft (doubly sheathed) while the back wall length is 10 ft, and the maximum drift of the partition wall is 16.6 mm while the maximum drift of the back wall is only 7.9 mm, the large imposed load in the partition wall can be understood. As shown in Figure 7.42, the degradation of the gypsum partition has not been so significant in such a drift range, which is also an important reason why the contribution from the partition wall is so significant. The situations in all the other buildings which have partition walls are similar with this building case.

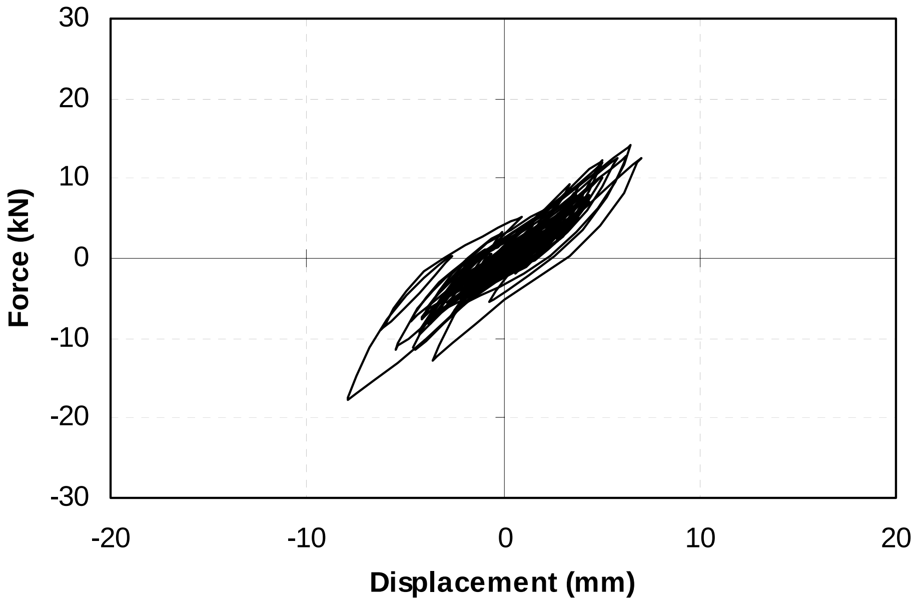

Figure 7.41 Back Wall Hysteresis

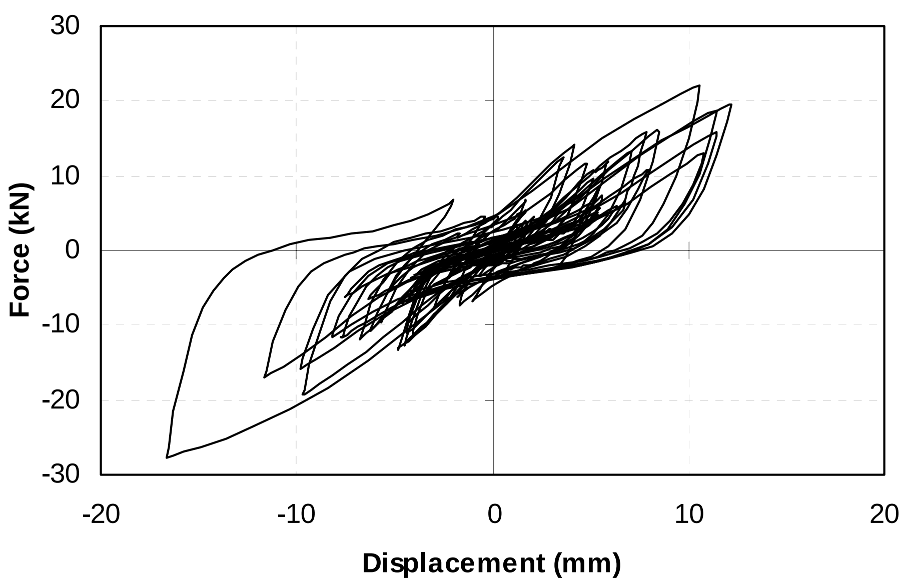

Figure 7.42 Partition Wall Hysteresis

The peak structural responses of the buildings in Group 1_2 (L:W=1:1, with parallel partition walls) are shown in Figures 7.43 through 7.48. From these figures, it can be concluded that the same design rules for the structure without partition walls can apply to the buildings with partition walls except that the maximum responses (drifts and imposed loads) in the structural walls were significantly reduced because of the contribution from the partition walls. Compared to the analysis results without partition walls, the peak drifts in perpendicular walls was reduced by 50% (front-to-back wall ratio 75%) to 73% (completely open front), the peak drift in the back wall was reduced by 61% (completely open front) to 75% (symmetric), and the peak drift in the front wall was reduced by 73% (symmetric) to 76% (front-to-back wall ratio 50%). The peak imposed loads in the perpendicular walls was reduced by 35% to 57%, and the imposed base shear in the parallel walls was reduced by 34% to 41%. These results show that while the partition wall did not eliminate the probable damage in the structures, it did prevent failures (drift or strength) from occurring in the buildings with a 1:1 plan aspect ratio.

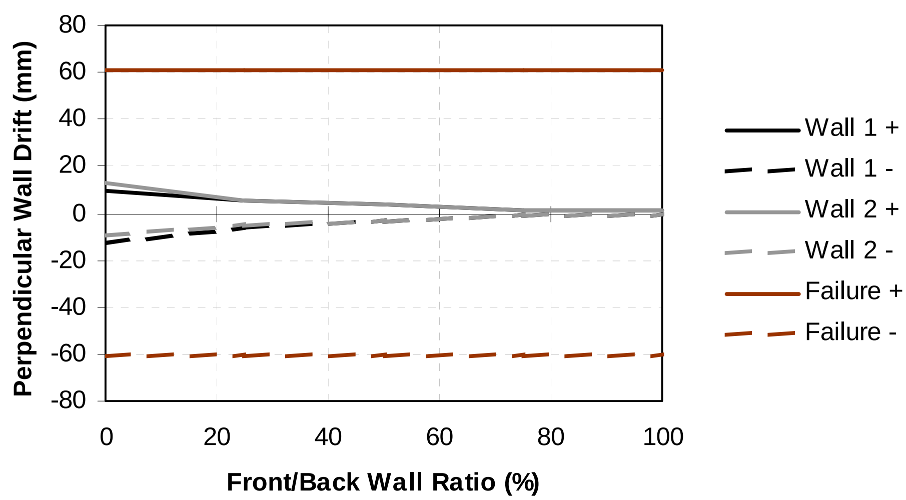

Figure 7.43 Peak Perpendicular Wall Drift (L:W=1:1, w/ partition wall)

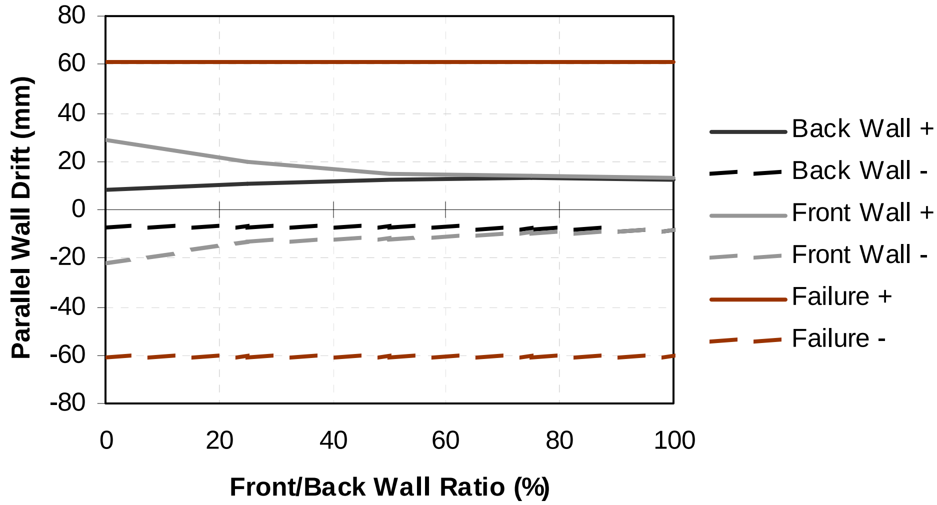

Figure 7.44 Peak Parallel Wall Drift (L:W=1:1, w/ partition wall)

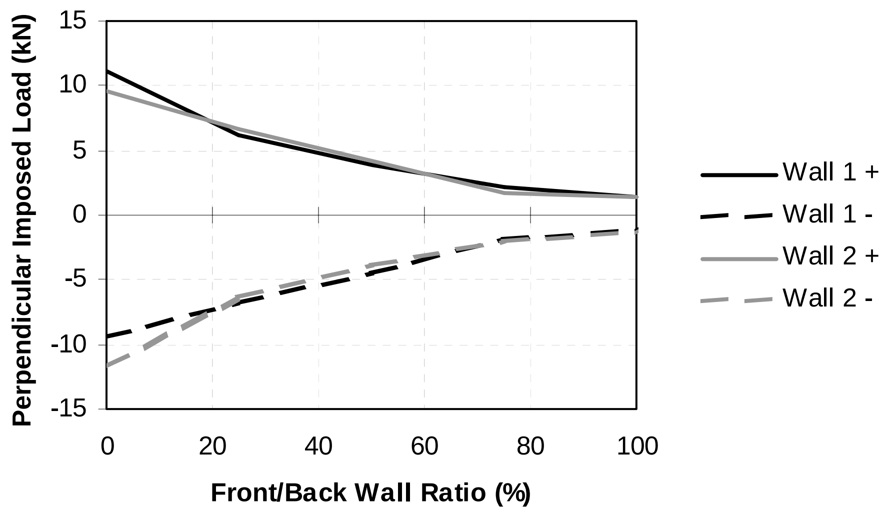

Figure 7.45 Peak Perpendicular Impose Load (L:W=1:1, w/ partition wall)

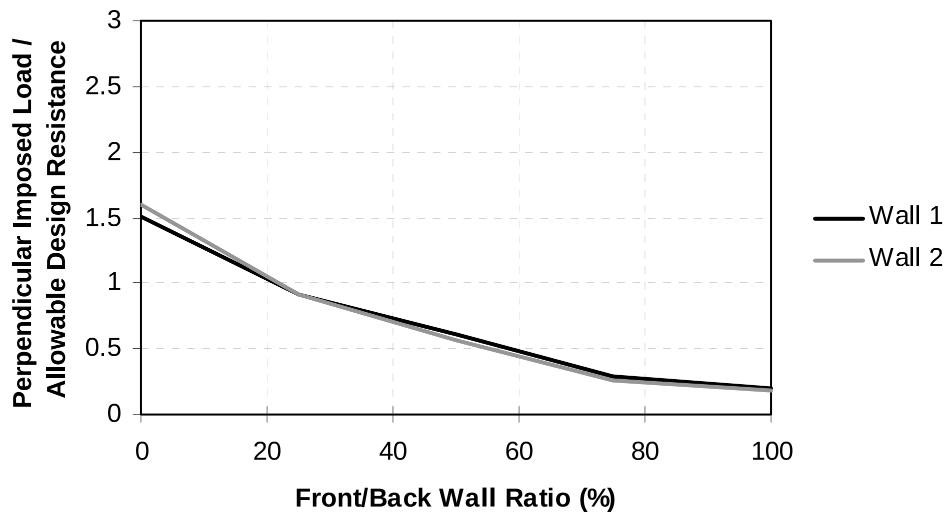

Figure 7.46 Peak Perpendicular Imposed Load / Design resistance (L:W=1:1, w/ partition wall)

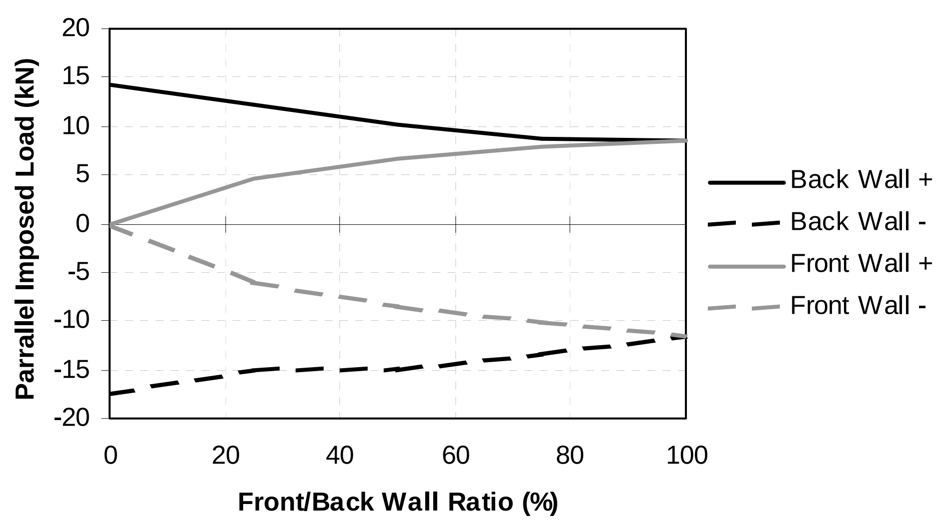

Figure 7.47 Peak Parallel Impose Load (L:W=1:1, w/ partition wall)

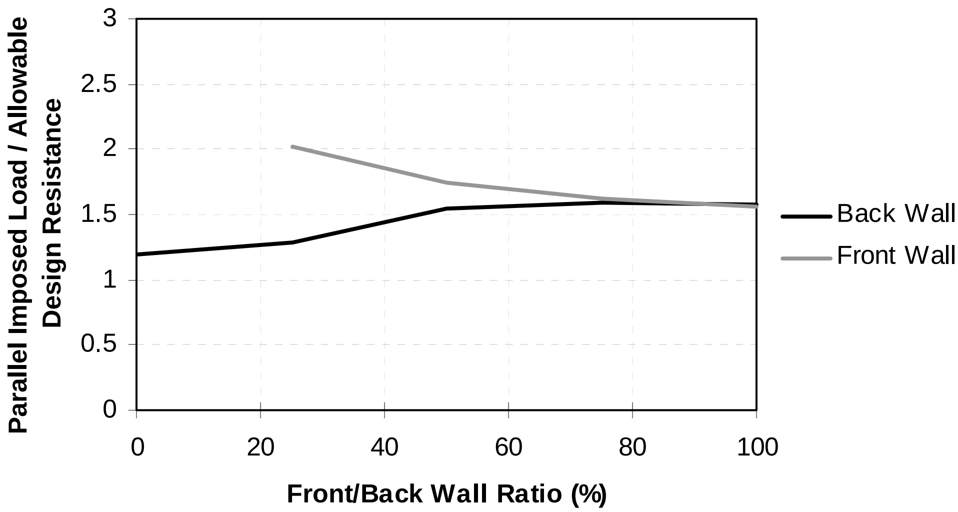

Figure 7.48 Peak Parallel Imposed Load / Design resistance (L:W=1:1, w/ partition wall)

The peak drifts, imposed loads and load ratios are listed in Tables 7.7 and 7.8.

Table 7.7 Peak Drifts of the Shear Walls (Group 1_2)

Front/Back Wall ratio (%)	Perpendicular Wall Drift (mm)						Parallel Wall Drift (mm)					
	Wall 1			Wall 2			Back Wall			Front Wall		
	+	-	MAX	+	-	MAX	+	-	MAX	+	-	MAX
0	9.81	-13.22	**13.22**	12.52	-9.66	**12.52**	7.91	-7.01	**7.91**	29.28	-22.05	**29.28**
25	5.05	-6.21	**6.21**	5.63	-5.67	**5.67**	10.56	-7.29	**10.56**	19.54	-13.10	**19.54**
50	3.51	-3.51	**3.51**	3.49	-4.00	**4.00**	12.37	-7.58	**12.37**	14.53	-12.68	**14.53**
75	1.44	-1.54	**1.54**	1.49	-1.32	**1.49**	12.97	-8.42	**12.97**	13.69	-10.04	**13.69**
100	0.84	-1.16	**1.16**	1.16	-0.96	**1.16**	12.24	-8.93	**12.24**	13.19	-9.11	**13.19**

Table 7.8 Peak Imposed Loads and Load Ratios in the Shear Walls (Group 1_2)

Front/Back Wall ratio (%)	Perpendicular Imposed Loads (kN)								Parallel Imposed Loads (kN)							
	Wall 1				Wall 2				Back Wall				Front Wall			
	+	-	MAX	Load Ratio	+	-	MAX	Load Ratio	+	-	MAX	Load Ratio	+	-	MAX	Load Ratio
0	11.07	-9.43	**11.07**	1.50	9.52	-11.76	**11.76**	1.60	14.18	-17.60	**17.60**	1.20	0.00	0.00	**0.00**	N/A
25	6.19	-6.78	**6.78**	0.92	6.73	-6.33	**6.73**	0.91	12.30	-15.15	**15.15**	1.29	4.55	-5.97	**5.97**	2.03
50	3.87	-4.48	**4.48**	0.61	4.20	-3.94	**4.20**	0.57	10.06	-15.17	**15.17**	1.55	6.76	-8.56	**8.56**	1.74
75	2.13	-1.79	**2.13**	0.29	1.66	-1.95	**1.95**	0.26	8.74	-13.41	**13.41**	1.59	7.89	-10.21	**10.21**	1.62
100	1.41	-1.31	**1.41**	0.19	1.35	-1.38	**1.38**	0.19	8.54	-11.60	**11.60**	1.58	8.51	-11.54	**11.54**	1.57

The peak parallel base shear for each analysis case in group 1_1 and 1_2 is shown in Figure 7.49. The base shear demands are lower in the buildings with the front/back wall ratios of 0% and 25%. The reason is that rotational vibration mode is more significant in the buildings with bigger front opening. The demands become more consistent for the redesigned buildings because the strengthened perpendicular walls offer a better torsional resistant capacity.

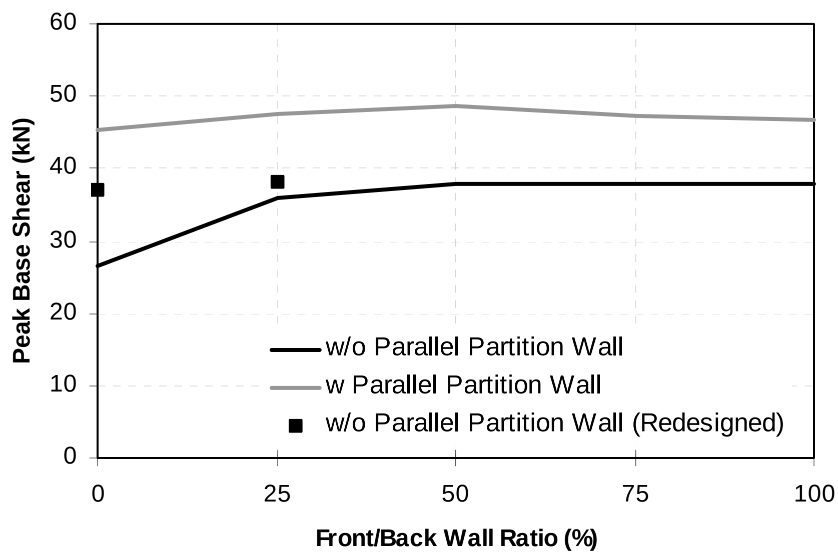

Figure 7.49 Peak Parallel Base Shear (L:W=1:1)

Group 2_1 (L:W=1:2, w/o parallel partition walls)

The shear wall drift time traces and the peak value tables for this and all the following groups of building configurations are shown in the Appendix C.

The same set of figures as used for Group 1_1 is presented for this group. Compared with the results of Group 1_1, the same design rules apply to Group 2_1, while the torsional behavior of the buildings in Group 2_1 declined significantly because the torsion was well resisted in the configurations with a L:W ratio of 1:2.

From Figure 7.50, the maximum perpendicular wall drift decreases from 16.49 mm to 0.44 mm when the front-to-back wall ratio increases from 0% (completely open front) to 100% (symmetric). The drift level was much less than that in Group 1_1.

It is shown in Figure 7.51 that the maximum back wall drift increases from 44.7 mm to 50.23 mm and the maximum front wall drift decreased from 64.04 mm to 50.3 mm when the front-to-back wall ratio increases from 0% (completely open front) to 100% (symmetric). The structure with the front-to-back wall ratios of 0 failed due to excessive drift, but the peak drift was only 5% higher than the drift criteria. So it might be regarded OK from the drift point of view.

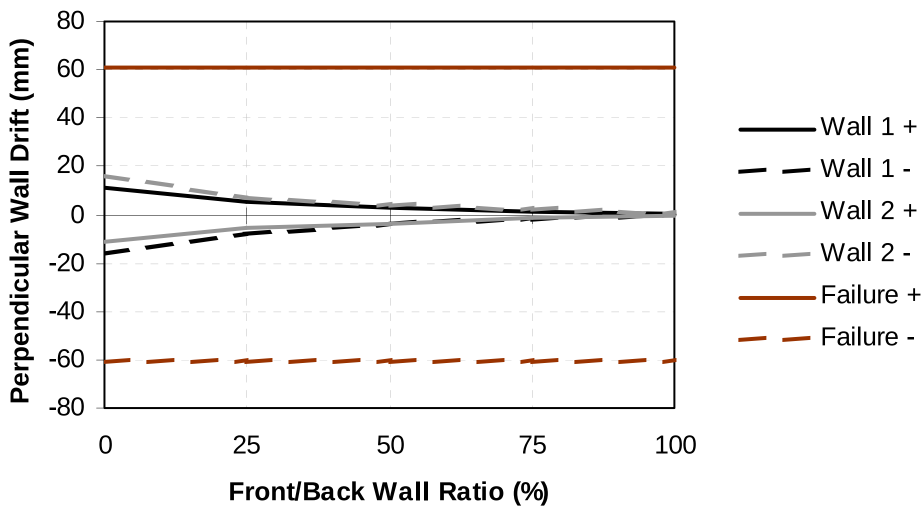

Figure 7.50 Peak Perpendicular Wall Drift (L:W=1:2, w/o parallel partition wall)

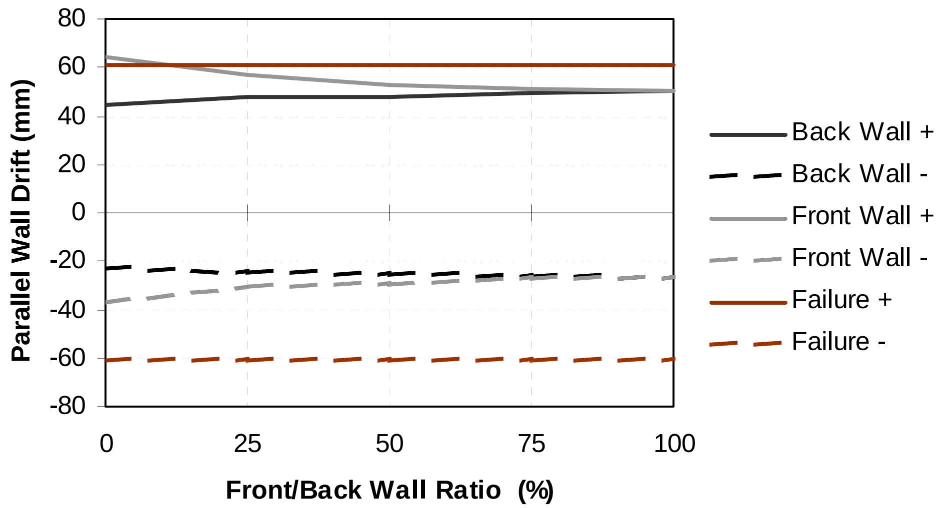

Figure 7.51 Peak Parallel Wall Drift (L:W=1:2, w/o parallel partition wall)

In Figure 7.52, the peak perpendicular imposed loads are shown to be higher than those in Group 1_1. However, it is not fair to say the torsional behavior is more significant in Group 2_1 because the perpendicular wall length in Group 2_1 is 10 ft, while 5 ft in Group 1_1. Therefore one should make the comparison based on the result shown in Figure 7.53. As shown in Figure 7.53, the load ratios in the two perpendicular walls dropped from 1.807 (completely open front) to 0.081 (symmetric, should be zero theoretically), which is much lower than those shown for Group 1_1 in Figure 7.23.

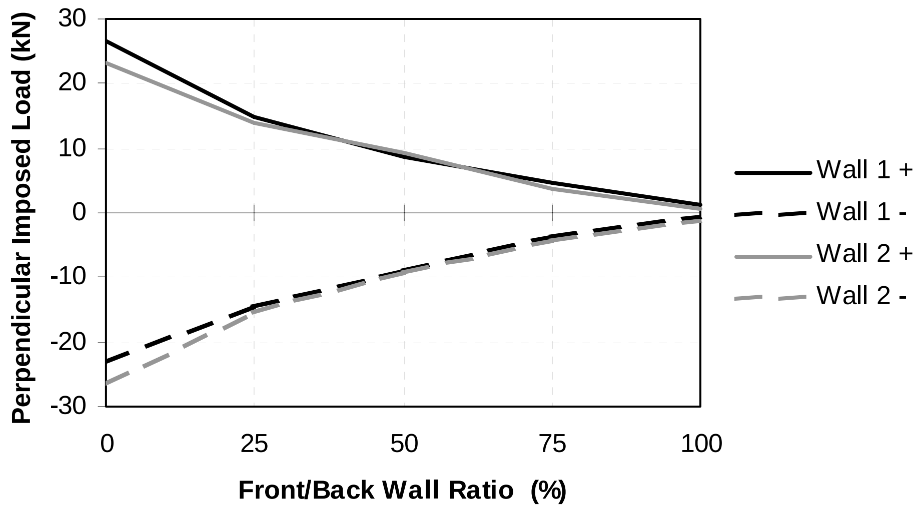

Figure 7.52 Peak Perpendicular Imposed Load (L:W=1:2, w/o parallel partition wall)

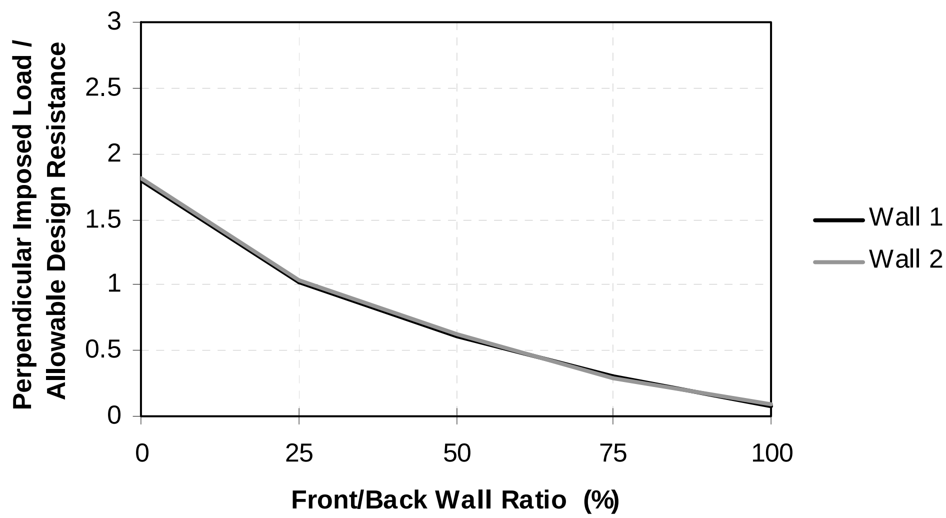

Figure 7.53 Peak Perpendicular Imposed Load / Design resistance (L:W=1:2, w/o parallel partition wall)

The peak imposed loads in parallel walls are plotted in Figure 7.54, and are much higher than those shown for Group 1_1 in Figure 7.24. This is also caused by the wall length changes. The parallel wall lengths in the buildings in Group 2_1 are double of those in Group 1_1.

In Figure 7.55, the ratio of maximum imposed load to design load is shown to increase in the back wall from 2.56 (completely open front) to 2.59 (symmetric) and decreased in front wall from 2.65 (front-to-back wall ratio 25%) to 2.59 (symmetric) when the front-to-back wall ratio increases. However, in practical terms the ratios remain constant for this plan aspect ratio.

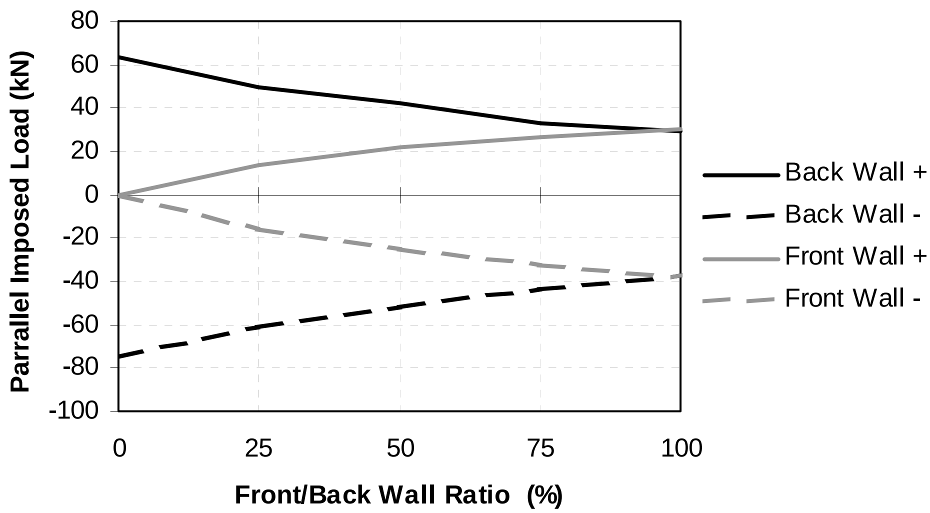

Figure 7.54 Peak Parallel Imposed Load (L:W=1:2, w/o parallel partition wall)

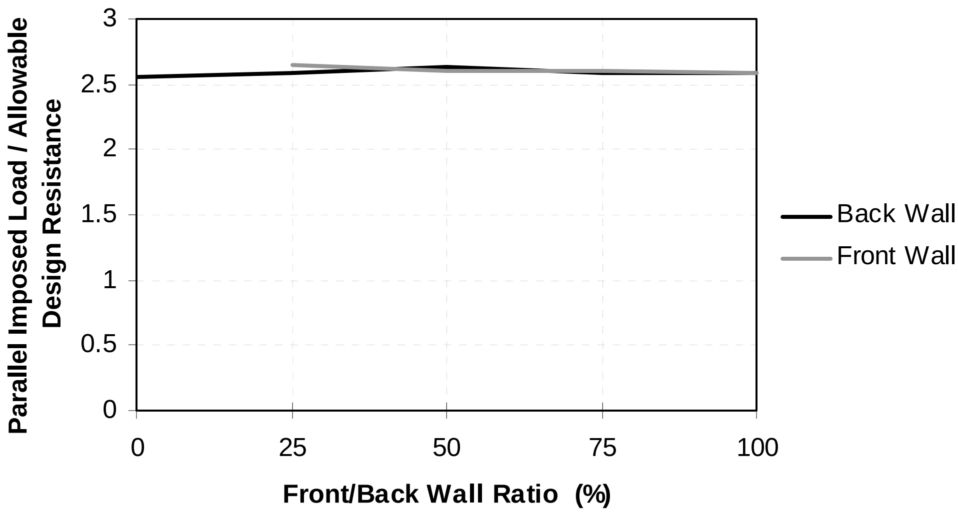

Figure 7.55 Peak Parallel Imposed Load / Design resistance (L:W=1:2, w/o parallel partition wall)

Group 2_2 (L:W=1:2, w/ parallel partition wall)

The structural responses of the buildings in Group 2_2 (L:W=1:2, with parallel partition wall) are presented in Figures 7.56 through 7.61. Compared with the analysis results without parallel partition walls, the peak drifts in perpendicular walls was reduced by 26% (front-to-back wall ratio 75%) to 50% (completely open front), the peak drifts in the back walls was reduced by 73% (symmetric) to 74% (completely open front), and the peak drift in the front wall was reduced by 68% (completely open front) to 74% (symmetric). The peak imposed loads in the perpendicular walls was reduced by 18% to 41%. The imposed load in the parallel walls was reduced by 39% to 44%.

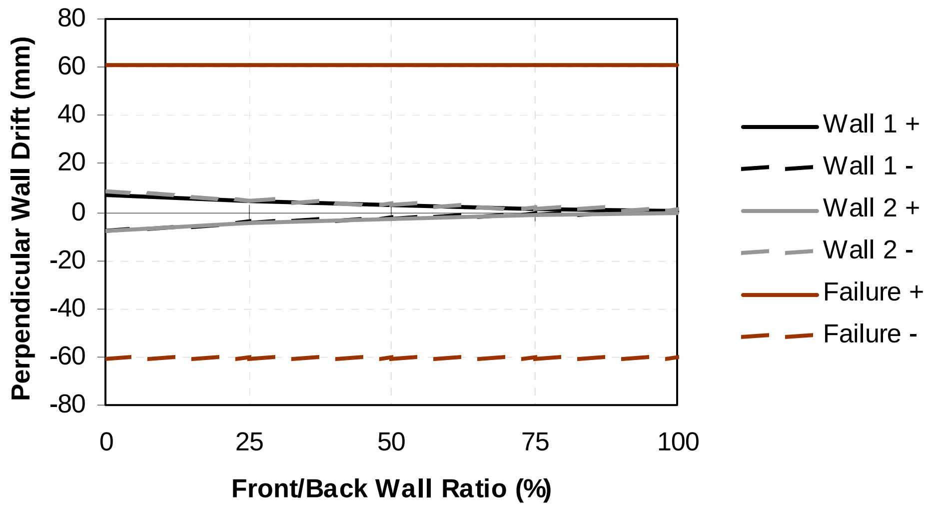

Figure 7.56 Peak Perpendicular Wall Drift (L:W=1:2, w/ parallel partition wall)

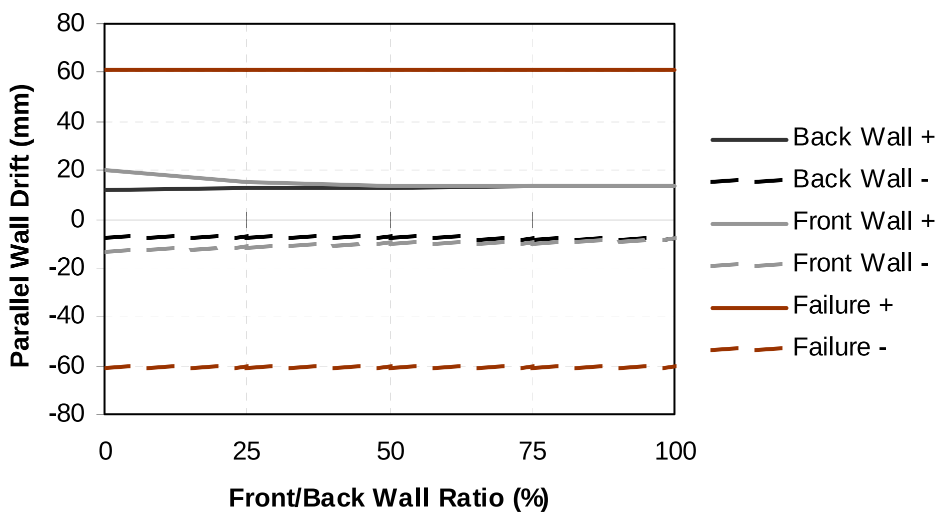

Figure 7.57 Peak Parallel Wall Drift (L:W=1:2, w/ parallel partition wall)

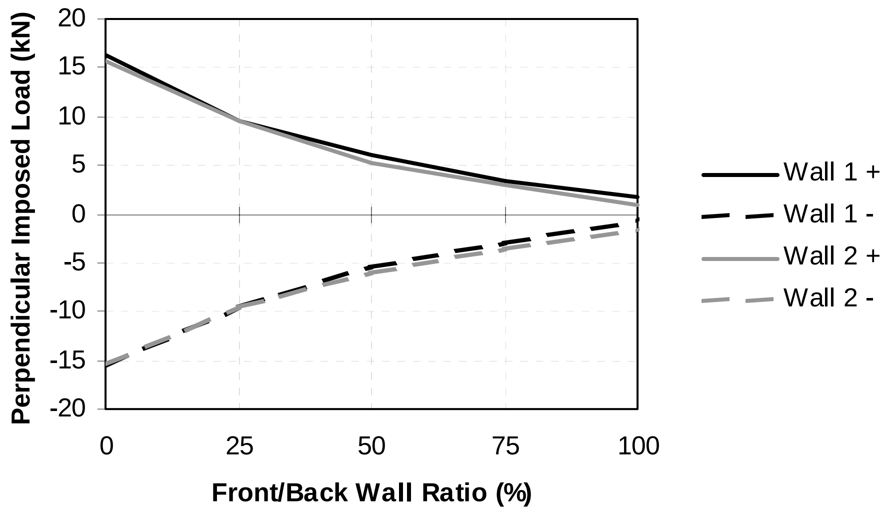

Figure 7.58 Peak Perpendicular Imposed Load (L:W=1:2, w/ parallel partition wall)

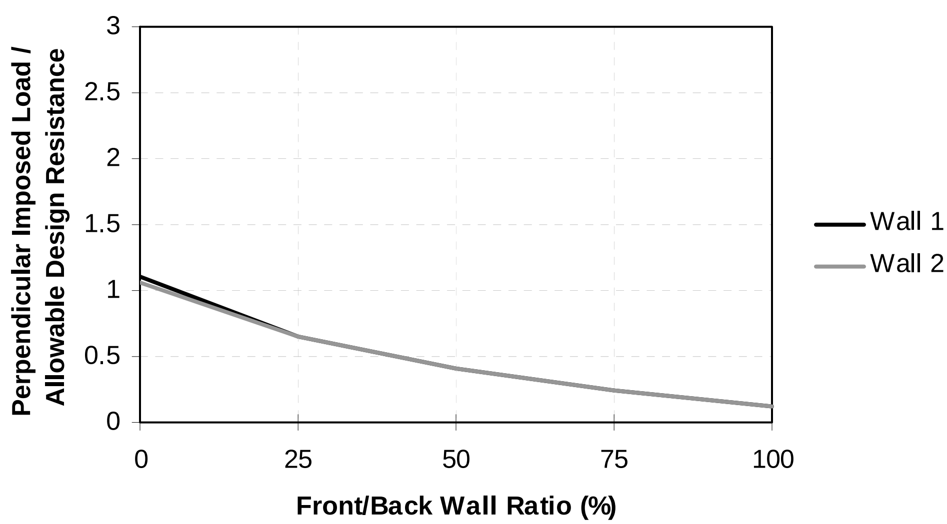

Figure 7.59 Peak Perpendicular Imposed Load / Design resistance (L:W=1:2, w/ parallel partition wall)

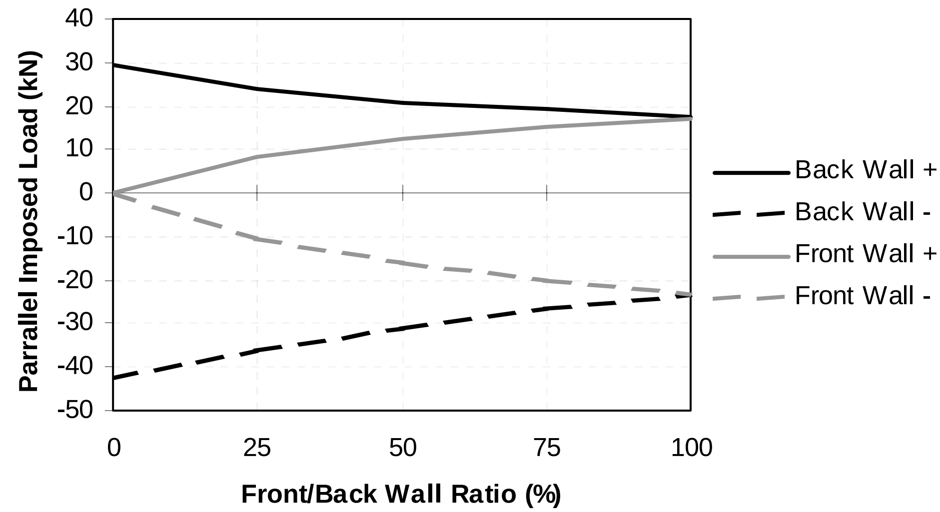

Figure 7.60 Peak Parallel Imposed Load (L:W=1:2, w/ parallel partition wall)

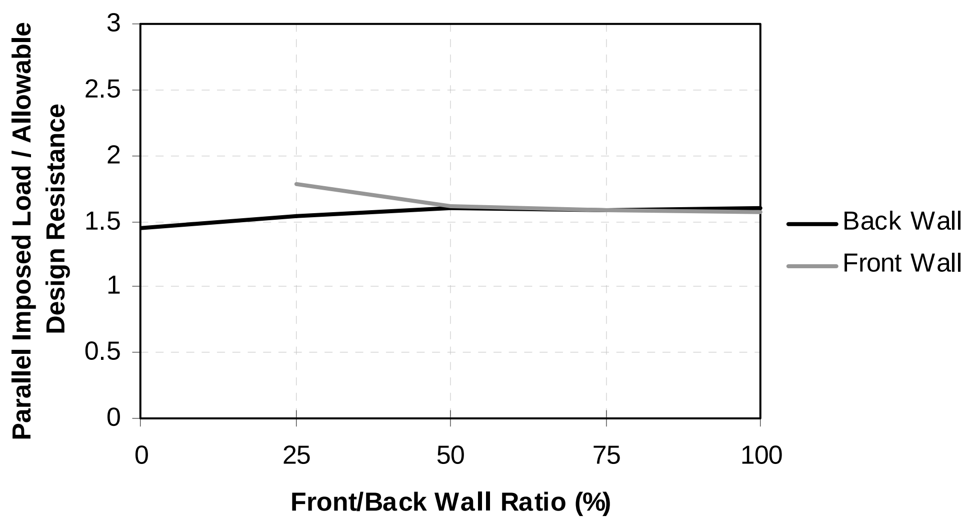

Figure 7.61 Peak Parallel Imposed Load / Design resistance (L:W=1:2, w/ parallel partition wall)

The peak parallel base shear for each analysis case in group 2_1 and 2_2 is shown in Figure 7.62. Because the buildings with a L:W ratio of 1:2 can resist torsional behavior better compared to the buildings with a L:W of 1:1, rotational vibration mode is almost prevented. As a result, the base shear demands are almost constant in the buildings with different front/back wall ratios.

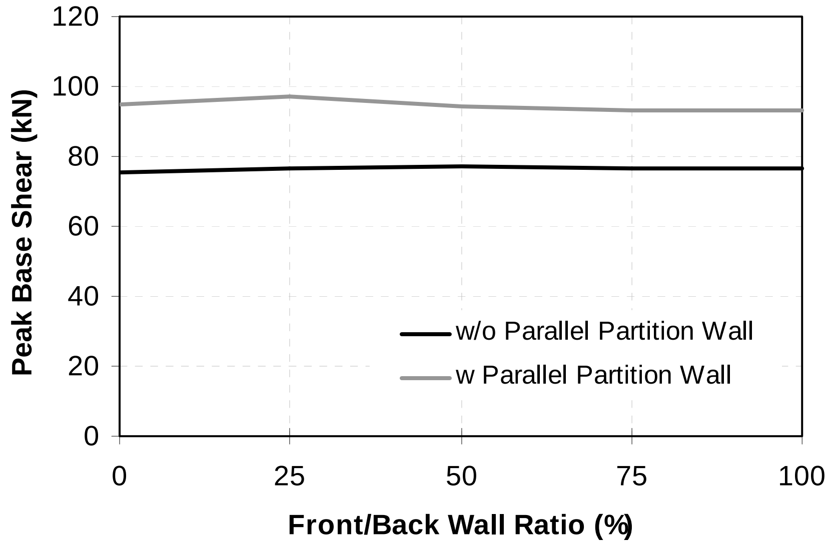

Figure 7.62 Peak Parallel Base Shear (L:W=1:2)

Group 3_1 (L:W=1:3, w/o parallel partition wall)

The same set of figures as used to present the analysis results for the previous groups is used for this group. Compared to the results for Groups 1_1 and 2_1, the same design rules apply to Group 3_1, while the torsional behavior of the buildings in Group 3_1 declined significantly because the torsion was better resisted in the configurations with a L:W ratio of 1:3. It should be noted that the better performance was also partly due to the contribution from the two partition walls in perpendicular direction.

In Figure 7.63, the peak perpendicular wall drift is shown to decrease from 8.02 mm to 0.4 mm when the front-to-back wall ratio increases from 0% (complete open front) to 100% (symmetric).

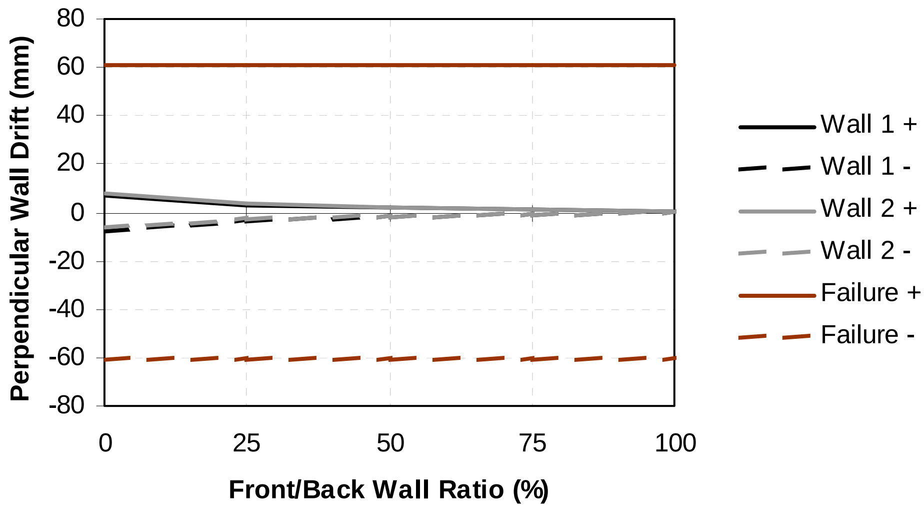

Figure 7.63 Peak Perpendicular wall Drift (L:W=1:3, w/o parallel partition wall)

The peak drift, shown in Figure 7.64, in the back wall is shown to increase from 48.34 mm to 50.77 mm and the peak drift in the front wall is shown to decrease from 58.17 mm to 50.8 mm, when the front-to-back wall ratio increases from 0% (complete open front) to 100% (symmetric). No structural failure due to excessive drift occurred in the buildings in this group.

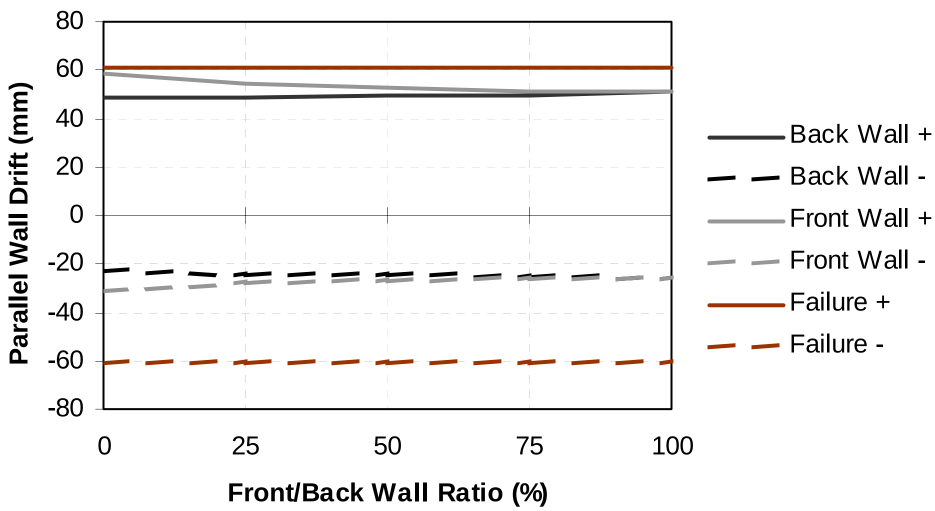

Figure 7.64 Peak Parallel wall Drift (L:W=1:3, w/o parallel partition wall)

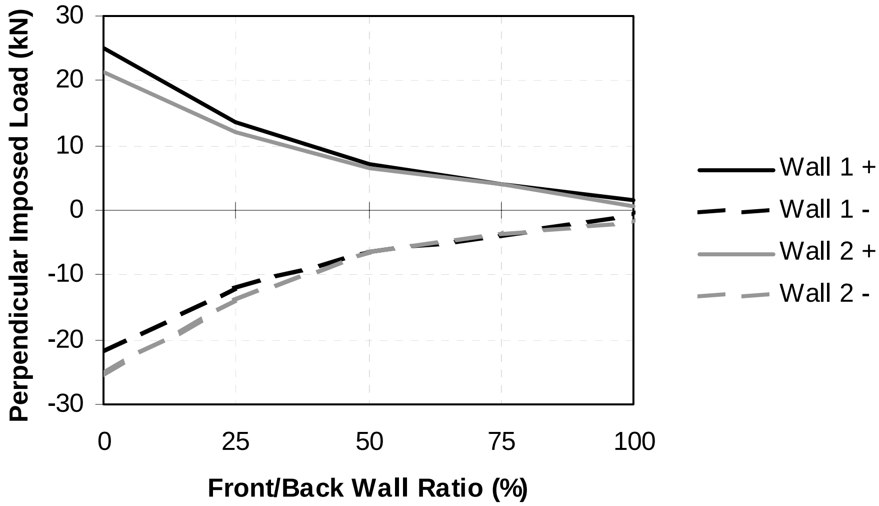

Figure 7.65 Peak Perpendicular Imposed Load (L:W=1:3, w/o parallel partition wall)

From Figure 7.66, it can be seen that the ratio of maximum imposed load to design load in the two perpendicular walls dropped from 1.146 (completely open front) to 0.076 (symmetric, should be zero theoretically).

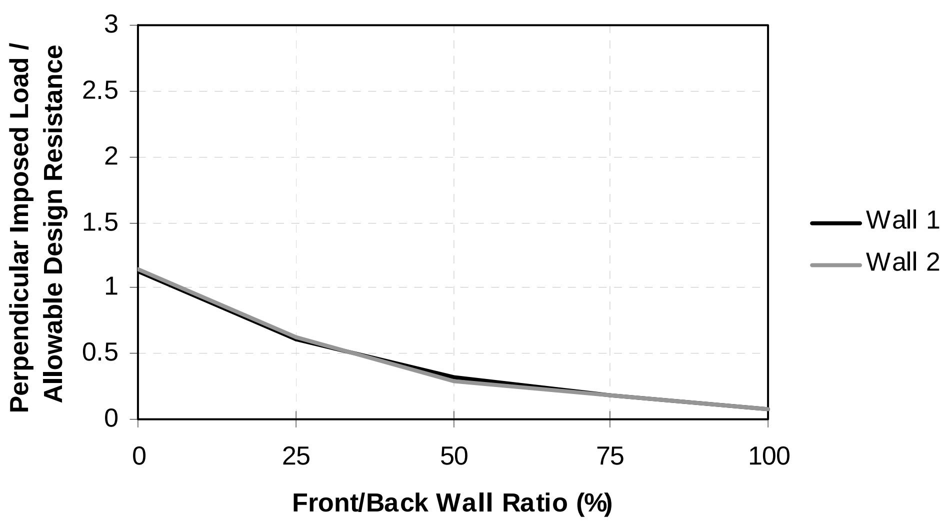

Figure 7.66 Peak Perpendicular Imposed Load / Design resistance (L:W=1:3, w/o parallel partition wall)

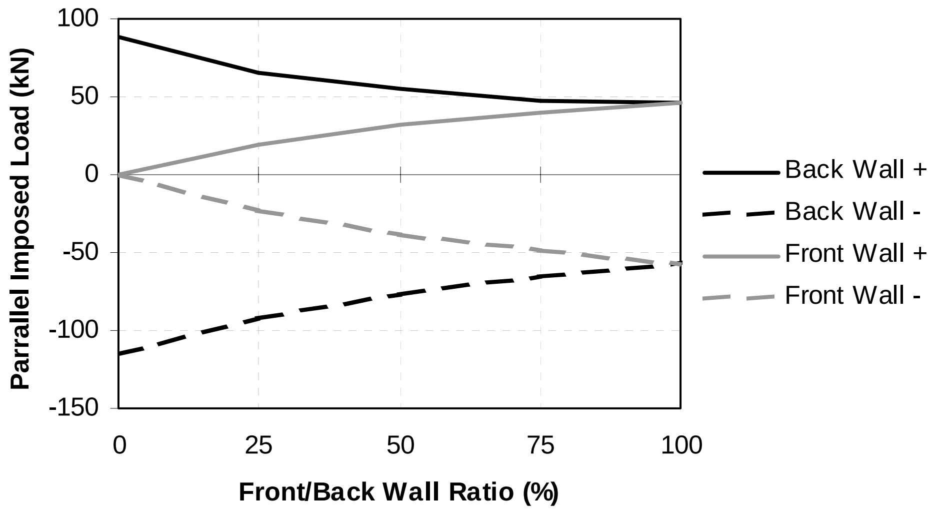

Figure 7.67 Peak Parallel Imposed Load (L:W=1:3, w/o parallel partition wall)

As shown in Figure 7.68, due to the strong torsion resistance supplied by the perpendicular walls, the ratio of maximum imposed load to design load varied in a small range, it increased from 2.595 to 2.614 in the back wall and decreased from 2.67 to 2.6 in the front wall when the front-to-back wall ratio increased. However, from a practical point of view, the load ratio was constant.

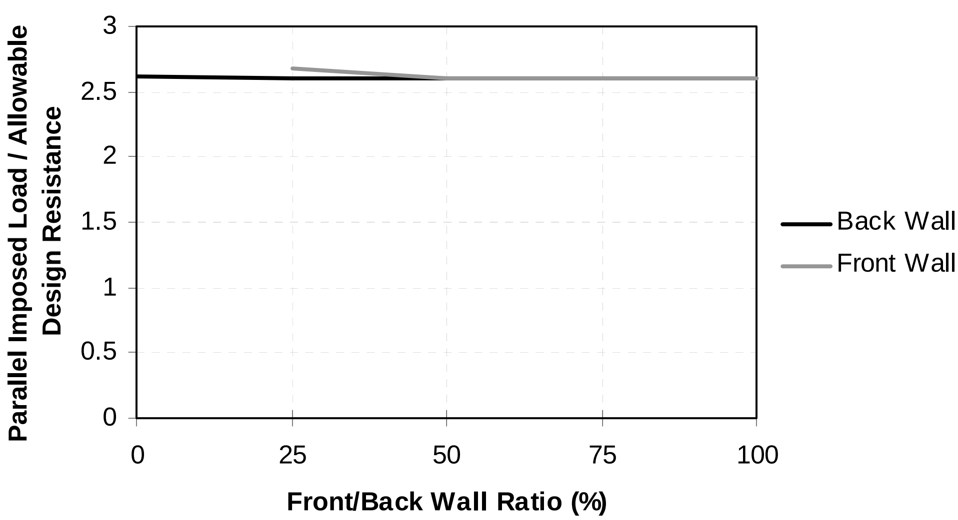

Figure 7.68 Peak Parallel Imposed Load / Design resistance (L:W=1:3, w/o parallel partition wall)

Group 3_2 (L:W=1:3, w/ parallel partition wall)

The structural responses of the buildings in Group 3_2 (L:W=1:3, with parallel partition wall) are shown in Figures 7.69 through 7.74. Compared to the analysis results for the configuration without a parallel partition wall, the peak drift in perpendicular walls was reduced by 12% (front-to-back wall ratio 75%) to 49% (completely open front), the peak drift in the back wall was reduced by 75% (symmetric) to 76% (completely open front), and the peak drift in the front wall was reduced by 72% (completely open front) to 75% (symmetric). The peak imposed loads in the perpendicular walls was reduced by 4% to 44%. The imposed load in the parallel walls was reduced by 40% to 43%. None of the models analyzed for this plan aspect ratio resulted in either a drift or strength failure.

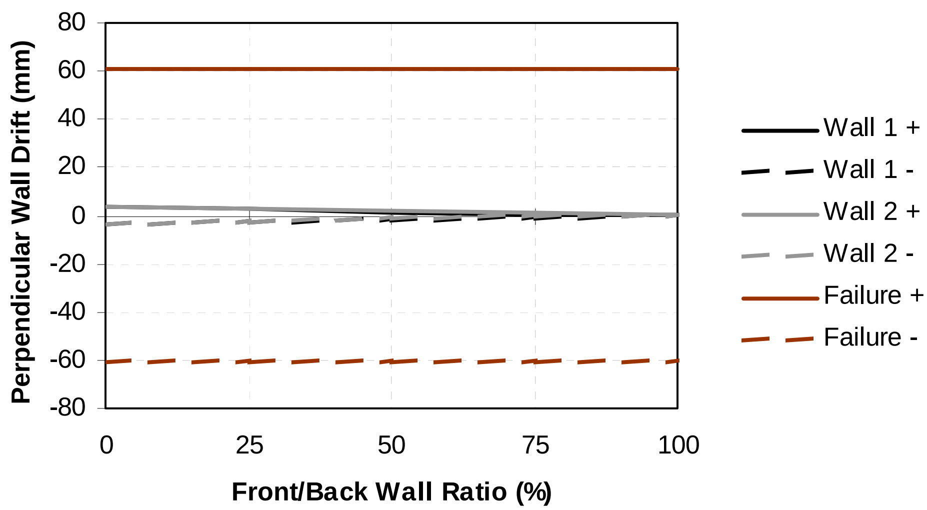

Figure 7.69 Peak Perpendicular Wall Drift (L:W=1:3, w/ parallel partition wall)

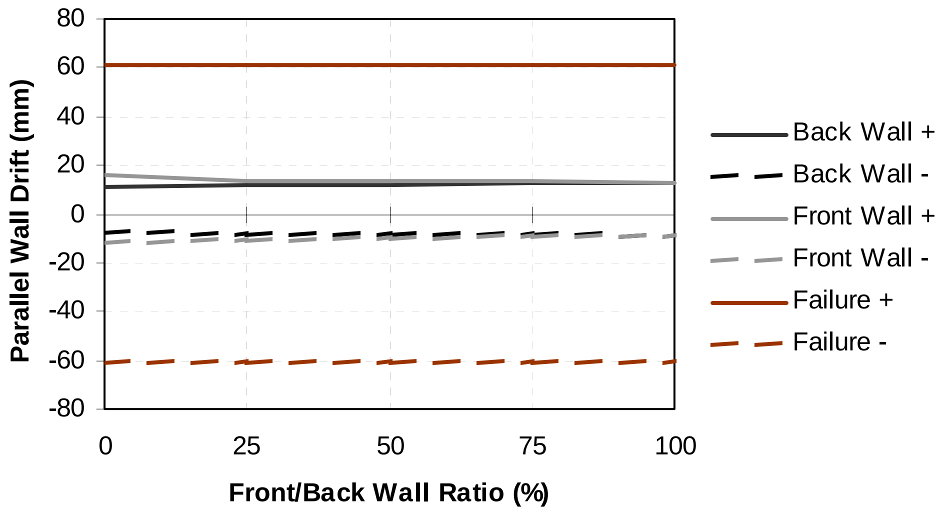

Figure 7.70 Peak Parallel Wall Drift (L:W=1:3, w/ parallel partition wall)

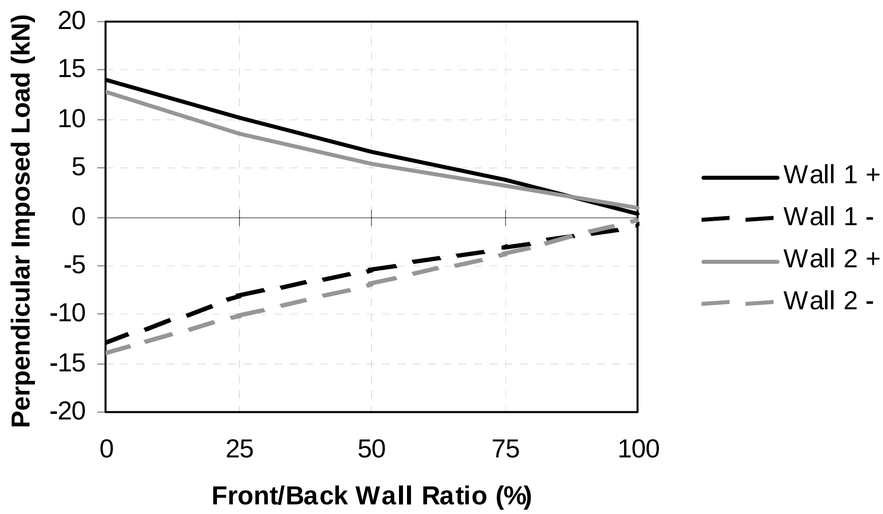

Figure 7.71 Peak Perpendicular Imposed Load (L:W=1:3, w/ parallel partition wall)

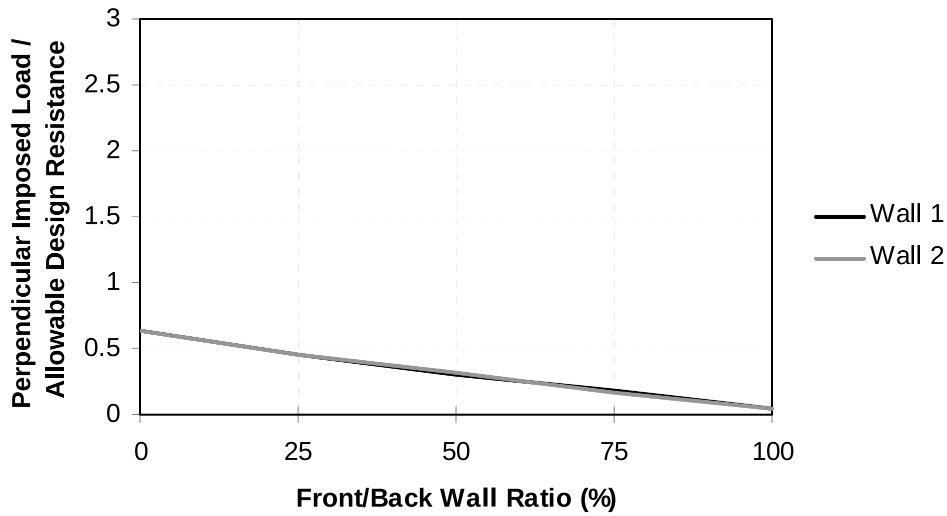

Figure 7.72 Peak Perpendicular Imposed Load / Design resistance (L:W=1:3, w/ parallel partition wall)

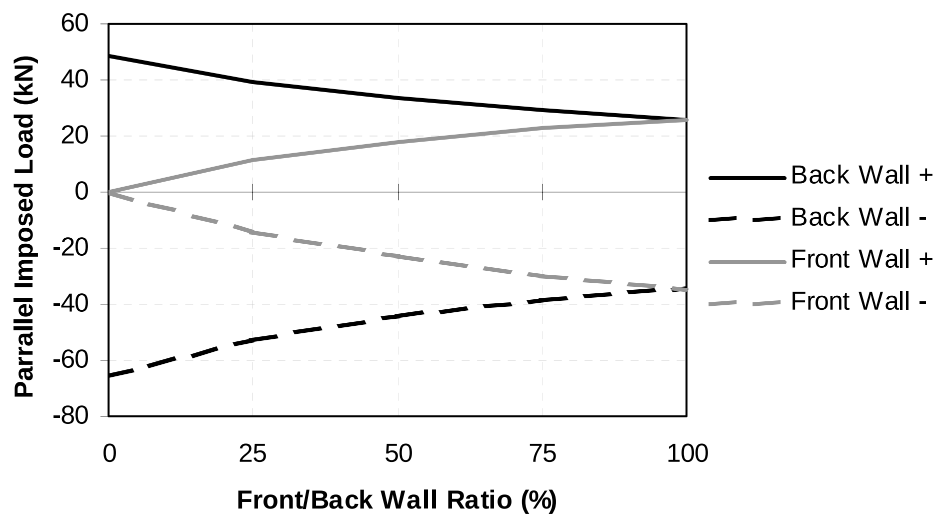

Figure 7.73 Peak Parallel Imposed Load (L:W=1:3, w/ parallel partition wall)

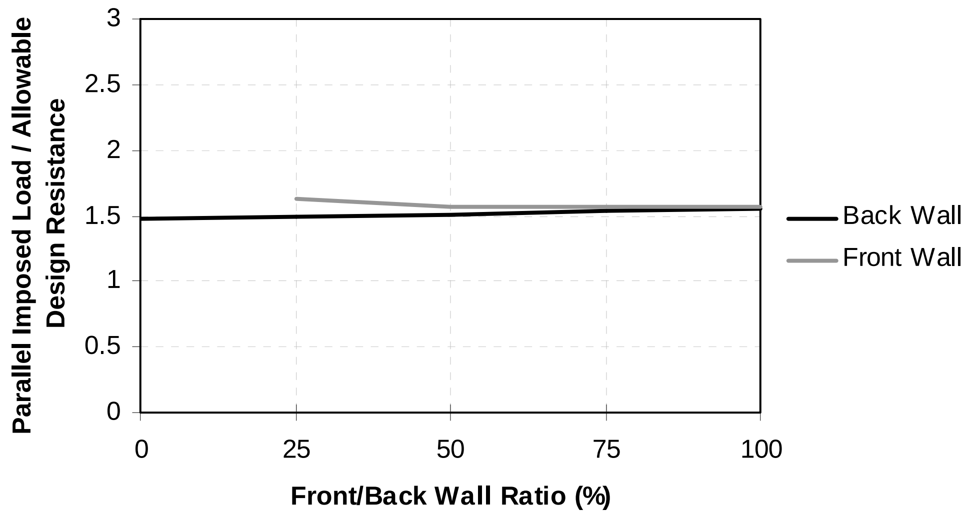

Figure 7.74 Peak Parallel Imposed Load / Design resistance (L:W=1:3, w/ parallel partition wall)

The peak parallel base shear for each analysis case in group 3_1 and 3_2 is shown in Figure 7.75. Because the buildings with a L:W ratio of 1:3 can resist torsional behavior much better compared to the buildings with a L:W of 1:1, rotational vibration mode is almost prevented. As a result, the base shear demands are almost constant in the buildings with different front/back wall ratios.

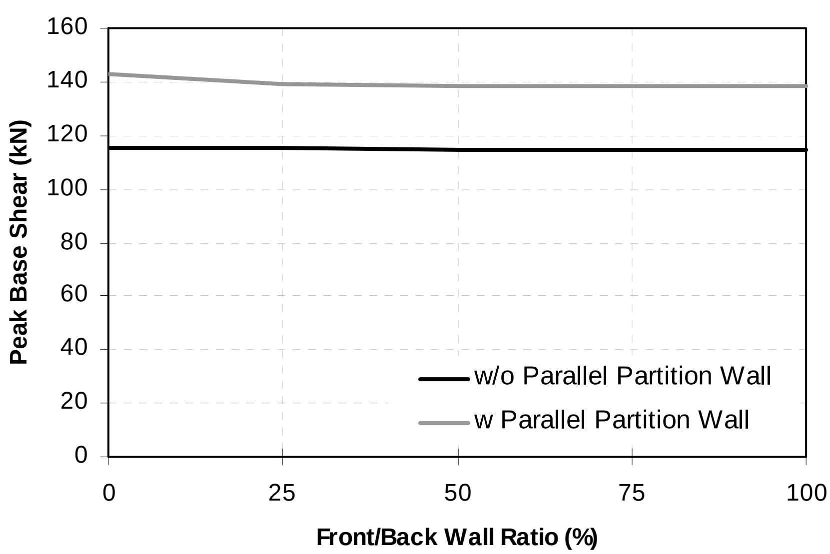

Figure 7.75 Peak Parallel Base Shear (L:W=1:3)

Group 4_1 (L:W=2:1, w/o partition wall)

The same set of figures as used to present the results of the previous groups is used to present the results for this group. Compared to the results of Groups 1_1, 2_1, and 3_1, the same design rules apply to Group 4_1. The torsional behavior of the buildings in Group 4_1 increased significantly because the torsion was inefficiently resisted in the configurations with a L:W ratio of 2:1.

From Figure 7.76, it can be seen that he maximum perpendicular wall drift decreases from 45.18 mm to 1.82 mm when the front-to-back wall ratio increases from 0% (complete open front) to 100% (symmetric). The updated configuration based on elastic torsional design philosophy reduced the peak drifts in perpendicular walls by up to 50%.

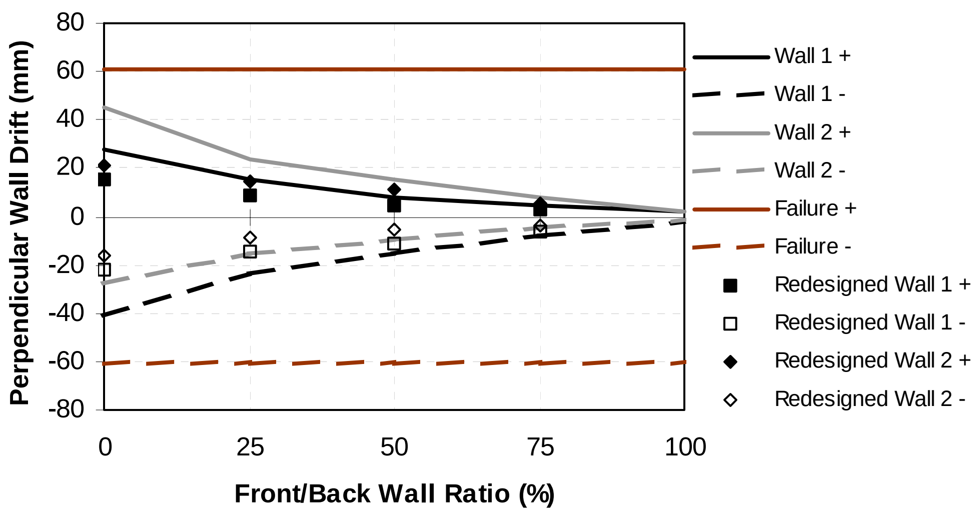

Figure 7.76 Peak Perpendicular Wall Drift (L:W=2:1, w/o partition wall)

As shown in Figure 7.77, the maximum back wall drift increases from 12.59 mm to 49.39 mm and the maximum front wall drift decreased from 185.93 mm to 49.71 mm when the front-to-back wall ratio increases from 0% (completely open front) to 100%

(symmetric). All the structures in this group failed due to excessive drift and load ratio except for the one with symmetric structural layout. The redesigned configurations based on elastic torsional design philosophy reduced the peak drifts in parallel walls. However, the peak drift and load ratio values were still higher than the failure criteria.

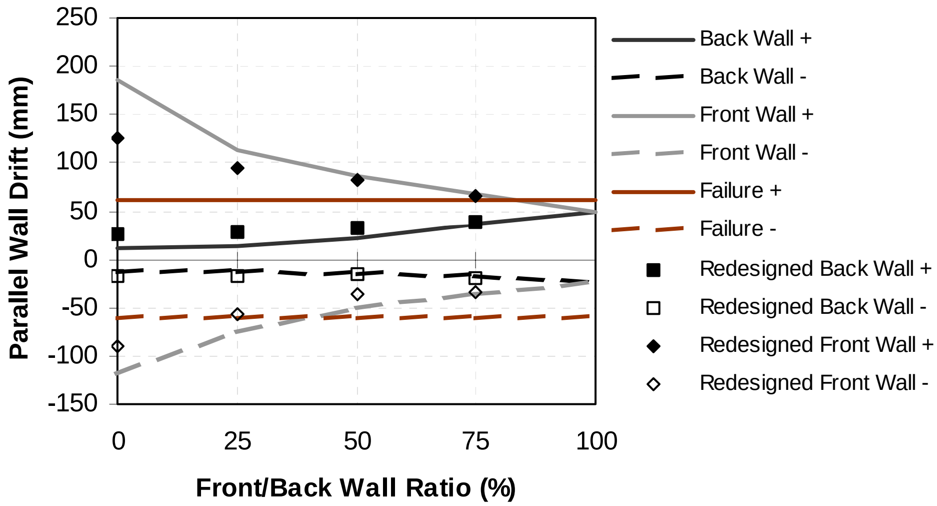

Figure 7.77 Peak Parallel Wall Drift (L:W=2:1, w/o partition wall)

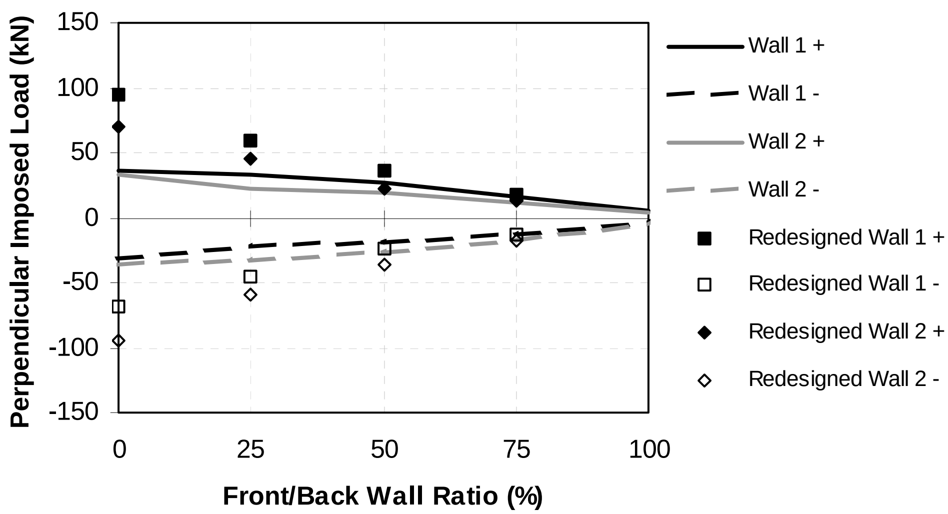

Figure 7.78 Peak Perpendicular Imposed Load (L:W=2:1, w/o partition wall)

As shown in Figure 7.79, maximum imposed load to design load ratio in the two perpendicular walls dropped from 2.477 (completely open front) to 0.323 (symmetric, should be zero theoretically). Since the perpendicular walls were strengthened based on the redesign, the load ratios dropped in them. As shown in Figure 7.80, the imposed load in the back wall increased from 0% front-to-back wall ratio to 50% and decreased from 50% to 100%. The reason is that the large L-to-W ratio caused a significant torsional vibration mode for the configurations with low front-to-back wall ratios, and it was shown in the animation that the building moved more like rotating about the back wall, which ended up with a huge drift in the front wall while a relatively small drift in the back wall. As that we can imagine, the imposed load in the shear wall is proportional to the drift though the relationship is nonlinear. The low drift in the back wall resulted in low imposed load. This can explain the similar phenomena in Figures 7.86, 7.93, and 7.99.

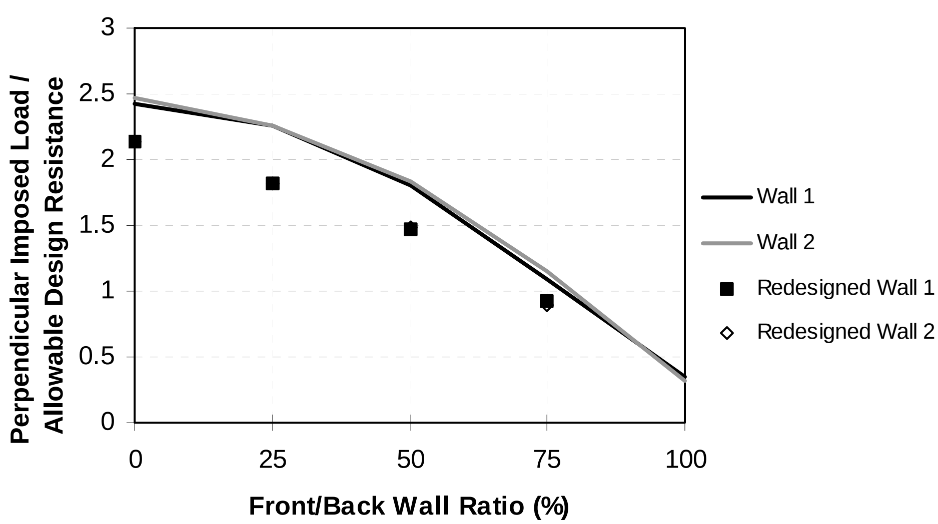

Figure 7.79 Peak Perpendicular Imposed Load / Design resistance (L:W=2:1, w/o partition wall)

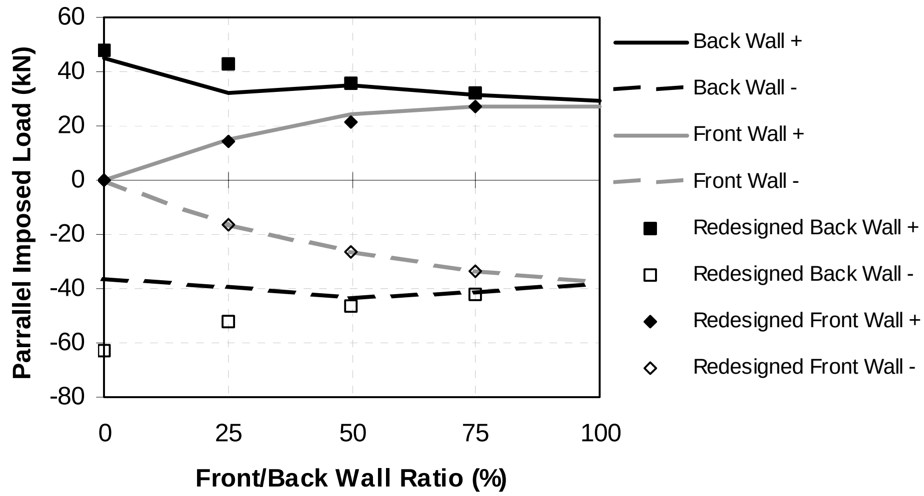

Figure 7.80 Peak Parallel Imposed Load (L:W=2:1, w/o partition wall)

As shown in Figure 7.81, the ratio of maximum imposed load to design load increased in the back wall from 1.53 (completely open front) to 2.58 (symmetric) and decreased in front wall from 2.77 (front-to-back wall ratio 25%) to 2.58 (symmetric) when the front-to-back wall ratio increased. The torsional behavior was resisted more effectively because the perpendicular walls were strengthened based on the redesign, so the load ratio values for the back and the front walls became closer.

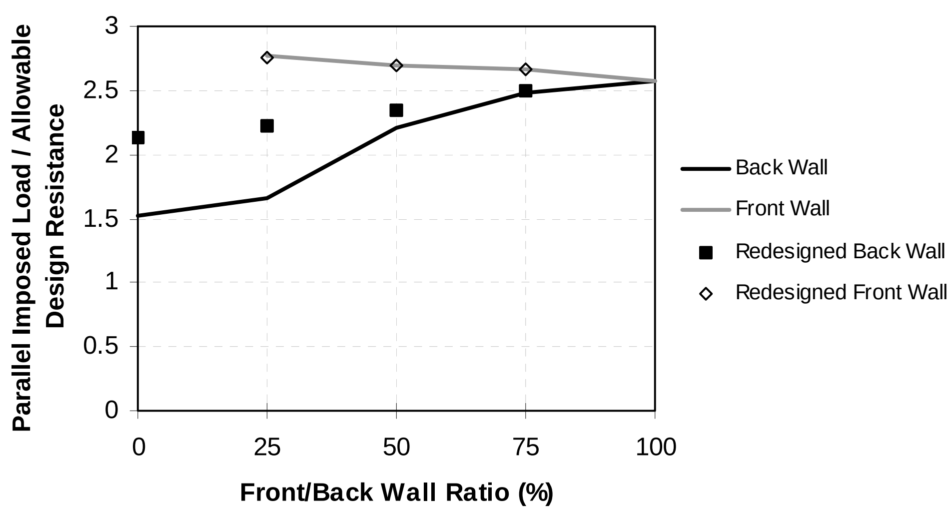

Figure 7.81 Peak Parallel Imposed Load / Design resistance (L:W=2:1, w/o partition wall)

Group 4_2 (L:W=2:1, w/ partition wall)

The structural responses of the buildings in Group 4_2 (L:W=2:1, with partition wall) are shown in Figures 7.82 through 7.87. Compared with the analysis results for the configuration without partition walls, the peak drift in perpendicular walls was reduced by 37% (completely open front) to 62% (front-to-back wall ratio 75%), peak drift in the back wall was reduced by 32% (front-to-back wall ratio 25%) to 52% (symmetric), and peak drift in the front wall was reduced by 38% (completely open front) to 58% (front-to-back wall ratio 75%). The peak imposed loads in the perpendicular walls were reduced by 5% to 61%, and the imposed base shear in the parallel walls was reduced by 8% to 42%. However, the drift in the front wall was still greater than the allowable drift for the completely open front condition.

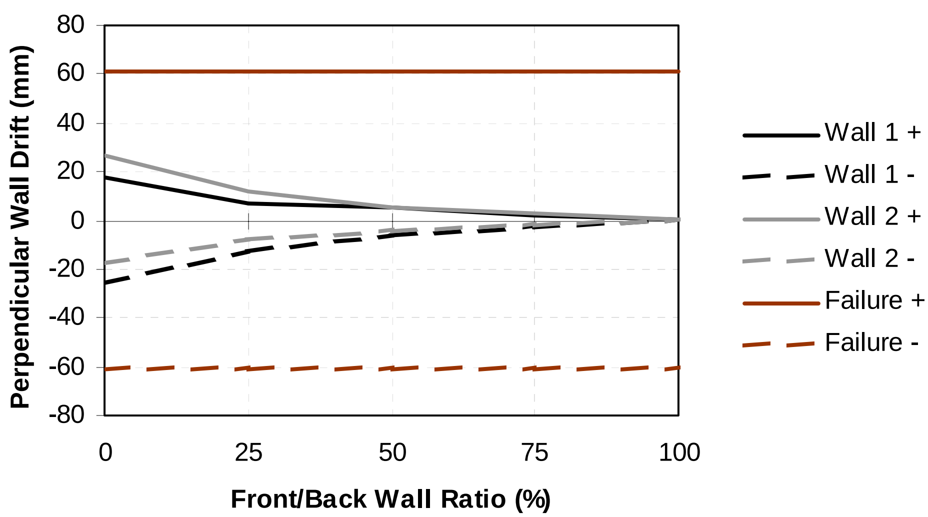

Figure 7.82 Peak Perpendicular Wall Drift (L:W=2:1, w/ partition wall)

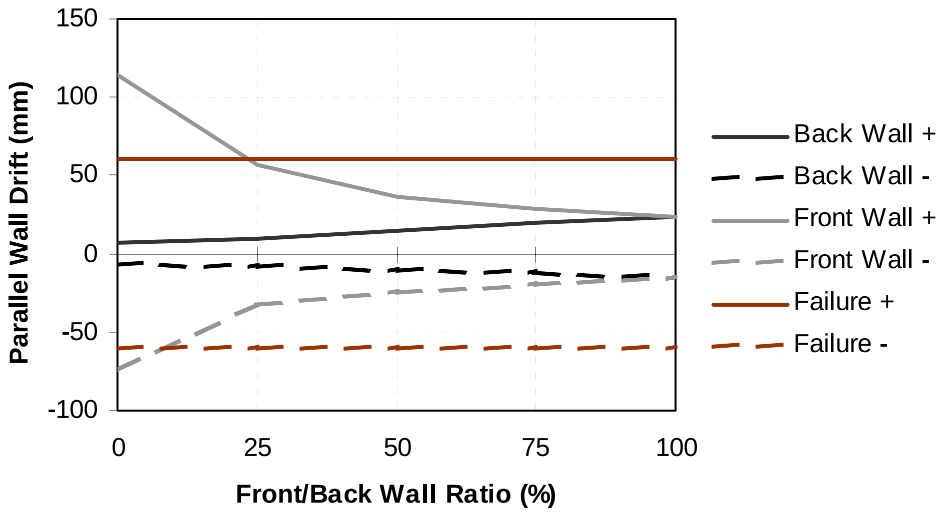

Figure 7.83 Peak Parallel Wall Drift (L:W=2:1, w/ partition wall)

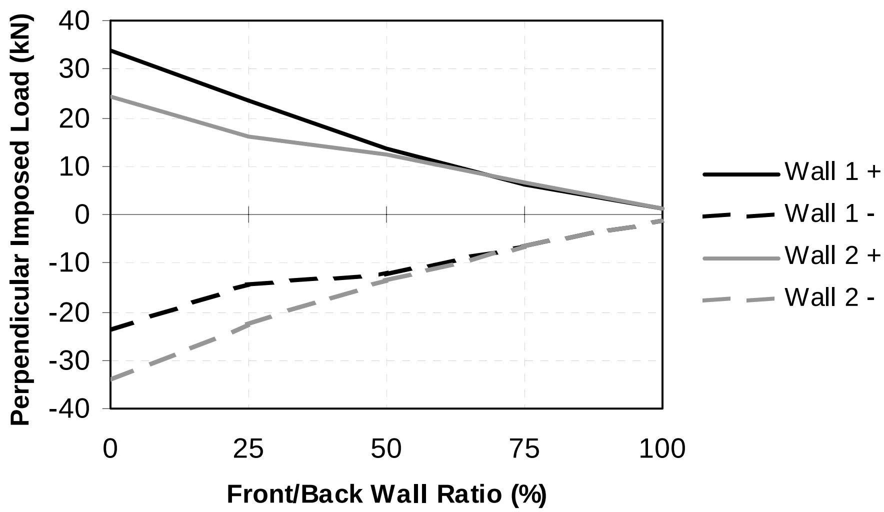

Figure 7.84 Peak Perpendicular Imposed Load (L:W=2:1, w/ partition wall)

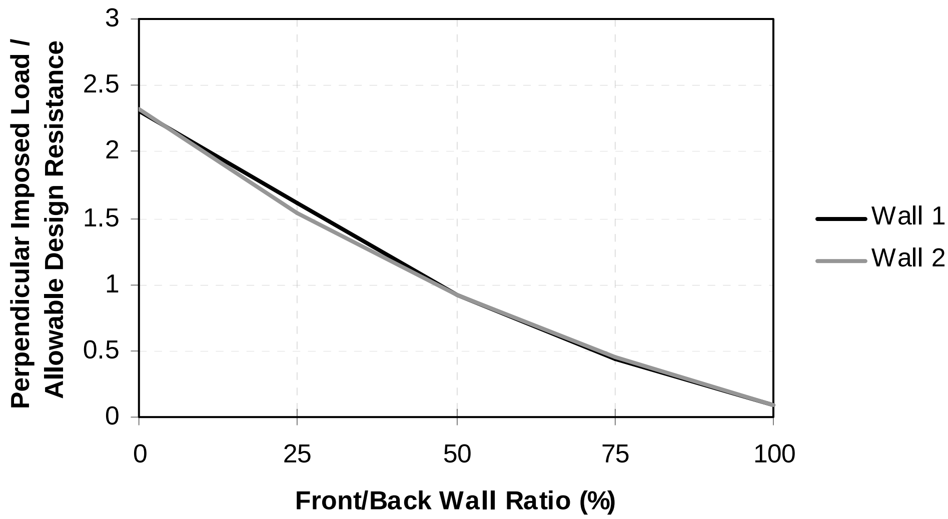

Figure 7.85 Peak Perpendicular Imposed Load / Design resistance (L:W=2:1, w/ partition wall)

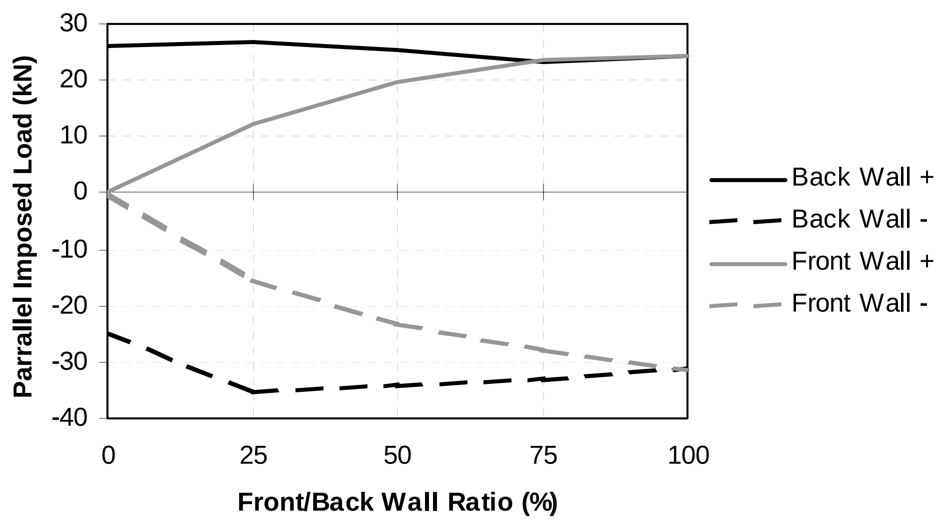

Figure 7.86 Peak Parallel Imposed Load (L:W=2:1, w/ partition wall)

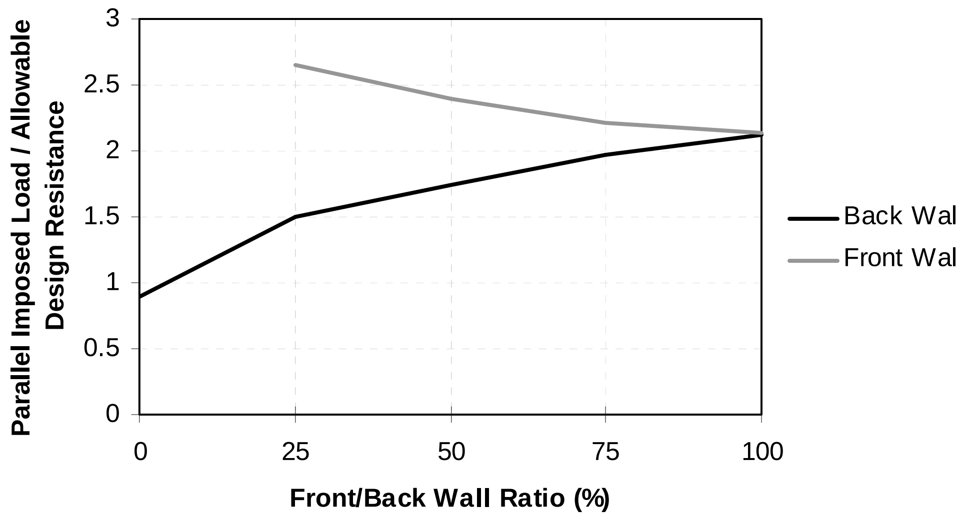

Figure 7.87 Peak Parallel Imposed Load / Design resistance (L:W=2:1, w/ partition wall)

The peak parallel base shear for each analysis case in group 4_1 and 4_2 is shown in Figure 7.88. The base shear demand increases as the front/back wall ratio increases. Because the buildings with a L:W ratio of 2:1 have a worse torsional resistant capacity compared to the buildings with a L:W of 1:1, rotational vibration mode is significant when the front/back wall ratio is low. The demands become more consistent for the redesigned buildings because the strengthened perpendicular walls offer a better torsional resistant capacity.

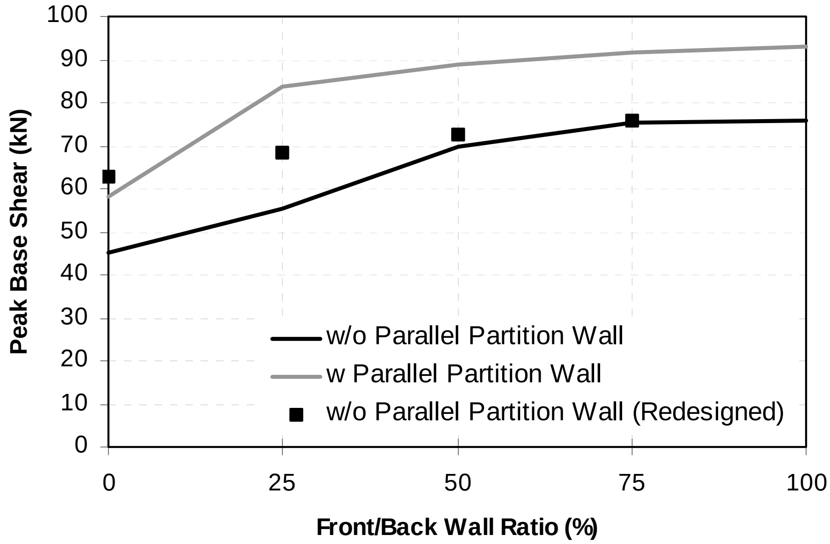

Figure 7.88 Peak Parallel Base Shear (L:W=2:1)

Group 5_1 (L:W=3:1, w/o partition wall)

The same set of figures as used to present the analysis results for the previous groups is used for this group. Compared to the results for Group 4_1, the same design rules apply to Group 5_1, while the torsional behavior of the buildings in Group 5_1 increased more because the torsion was the most inefficiently resisted in the configurations with a L:W ratio of 3:1.

Figure 7.89 shows that the peak perpendicular wall drift decreases from 50.14 mm to 0.37 mm when the front-to-back wall ratio increases from 0% (completely open front) to 100% (symmetric). The redesigned configuration based on elastic torsional design philosophy reduced the peak drifts in perpendicular walls for the completely open front condition.

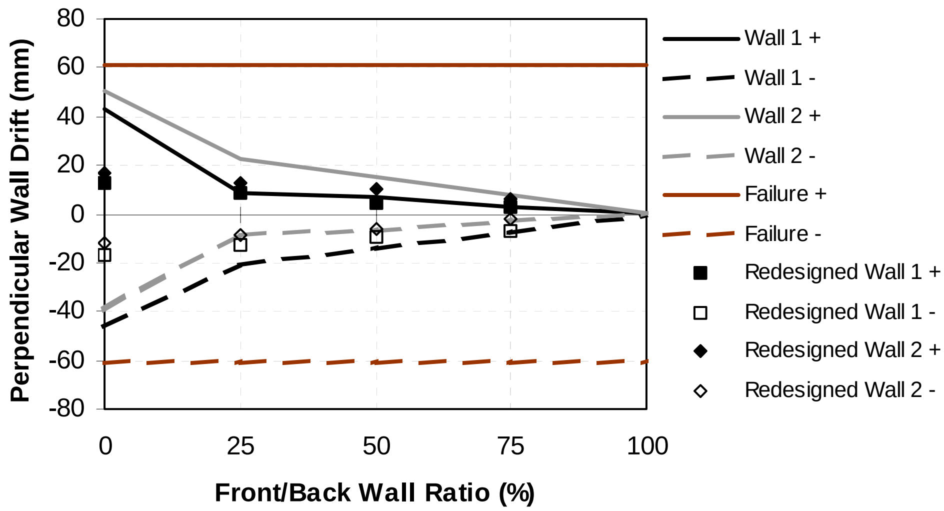

Figure 7.89 Peak Perpendicular Wall Drift (L:W=3:1, w/o partition wall)

As shown in Figure 7.90, the peak drift in the back wall increases from 12.67 mm to 52.14 mm and the peak drift in the front wall decreased from 306.99 mm to 52.45 mm when the front-to-back wall ratio increased from 0% (completely open front) to 100% (symmetric). All the buildings in this group failed except for the symmetric configuration. The redesigned configuration based on elastic torsional design philosophy reduced the peak drifts in the parallel walls. However, the peak values were still higher than the failure criteria.

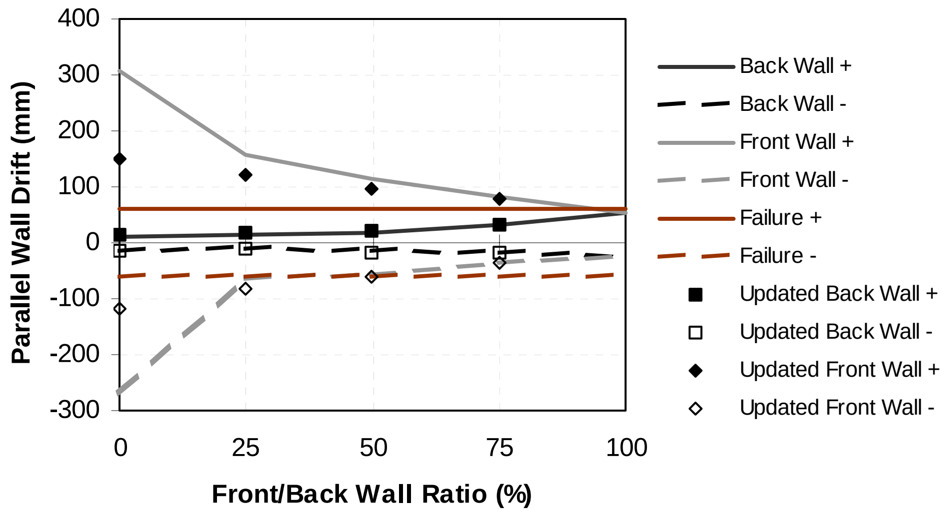

Figure 7.90 Peak Parallel Wall Drift (L:W=3:1, w/o partition wall)

As shown in Figure 7.92, the peak load ratio in the two perpendicular walls dropped from 2.586 (completely open front) to 0.077 (symmetric, should be zero theoretically). Although the maximum imposed loads in the perpendicular walls increased after the redesign (Figure 7.91), the load ratios dropped (Figure 7.92).

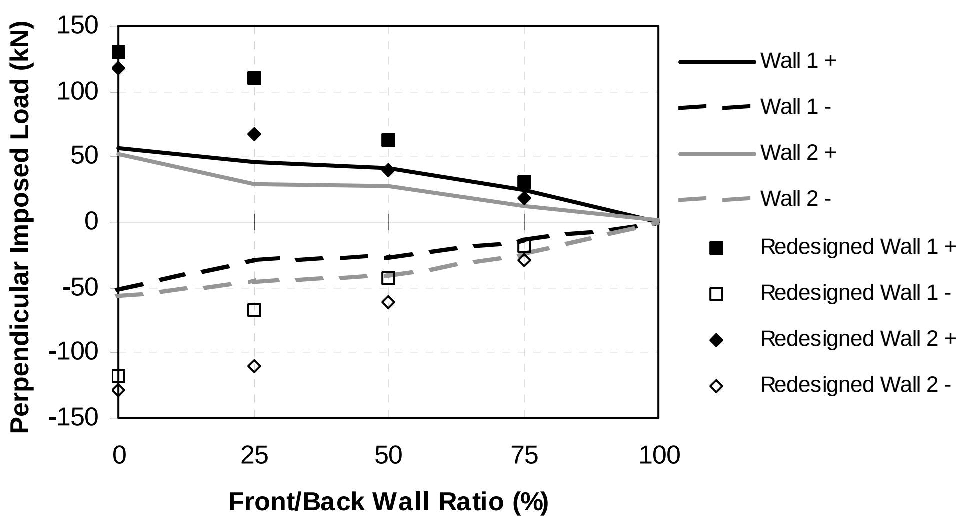

Figure 7.91 Peak Perpendicular Imposed Load (L:W=3:1, w/o partition wall)

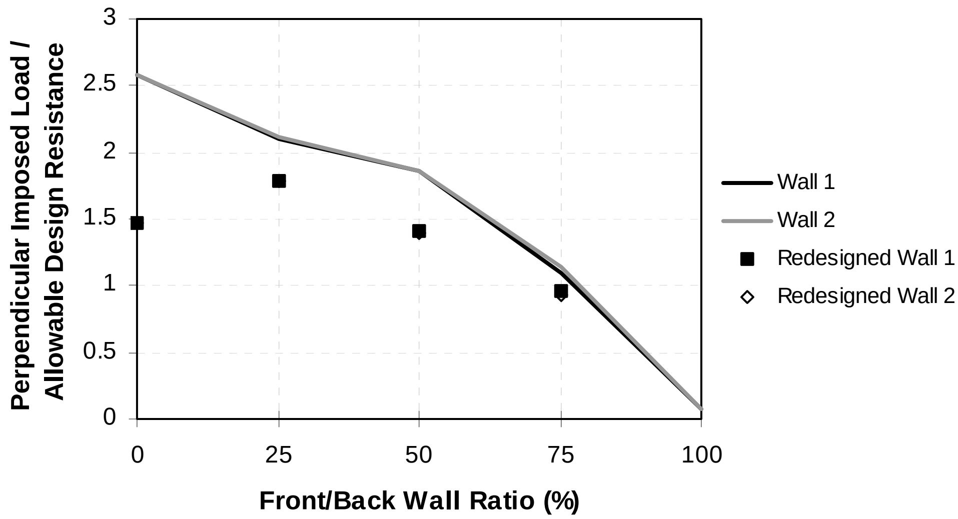

Figure 7.92 Peak Perpendicular Imposed Load / Design resistance (L:W=3:1, w/o partition wall)

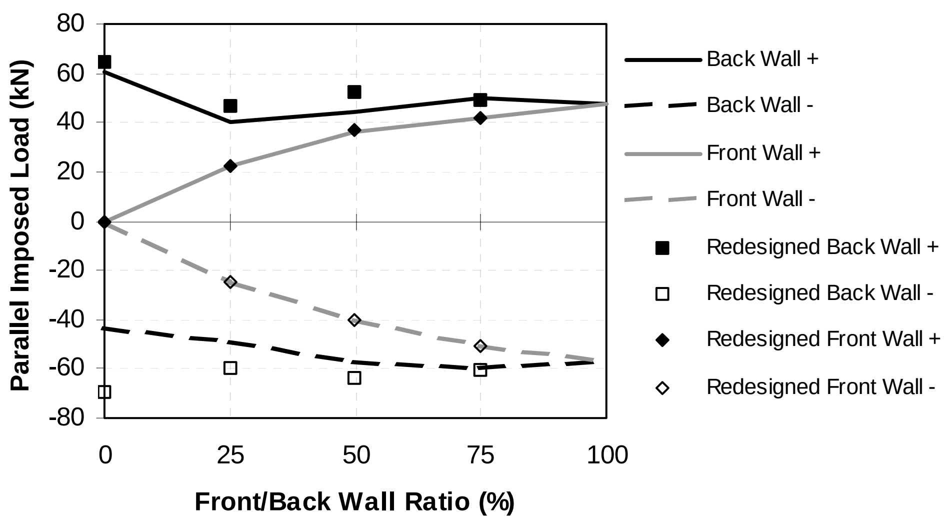

Figure 7.93 Peak Parallel Imposed Load (L:W=3:1, w/o partition wall)

As shown in Figure 7.94, the load ratios increased in the back wall from 1.38 (completely open front) to 2.61 (symmetric) and decreased in the front wall from 2.76 (front-to-back wall ratio 25%) to 2.61 (symmetric) when the front-to-back wall ratio increased. The torsional behavior was resisted more effectively because of the strengthening of the perpendicular walls based on the torsion redesign, so the load ratio values for the back and the front walls became closer.

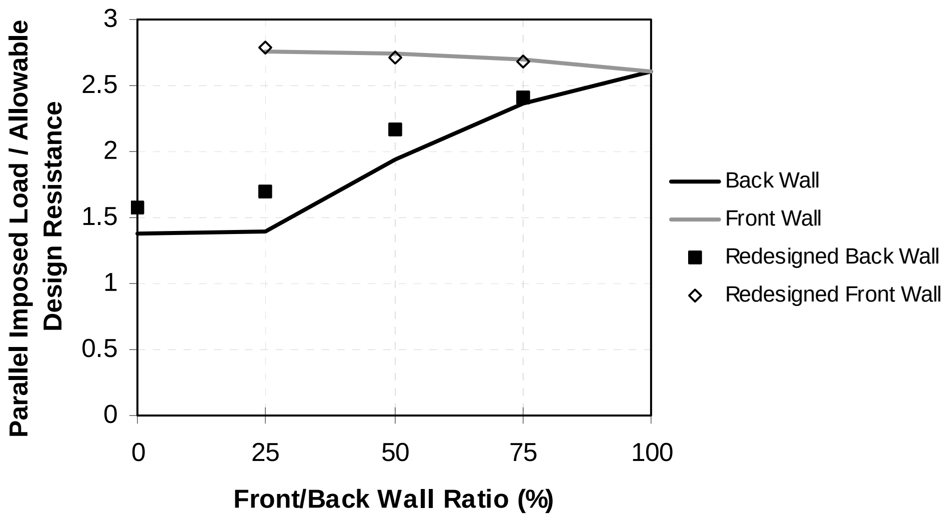

Figure 7.94 Peak Parallel Imposed Load / Design resistance (L:W=3:1, w/o partition wall)

Group 5_2 (L:W=3:1, w/ partition walls)

The structural responses of the buildings in Group 5_2 (L:W=3:1, with partition wall) are shown in Figures 7.95 through 7.100.

Compared with the analysis results for the configuration without partition walls, the peak drift in perpendicular walls was reduced by 24% (front-to-back wall ratio 25%) to 50% (completely open front), the peak drift in the back wall was reduced by 36% (front-to-back wall ratio 50%) to 59% (symmetric), and the peak drift in the front wall was reduced by 27% (front-to-back wall ratio 25%) to 45% (completely open front). It should be noted that the partition wall location is at the 1/3 structural span instead of half way, so the analysis results were asymmetric in the two parallel walls even when the front-to-back wall ratio was 100%. The peak imposed loads in the perpendicular walls was reduced by 7% to 29%. The imposed load in the parallel walls was reduced by 10% to 33%.

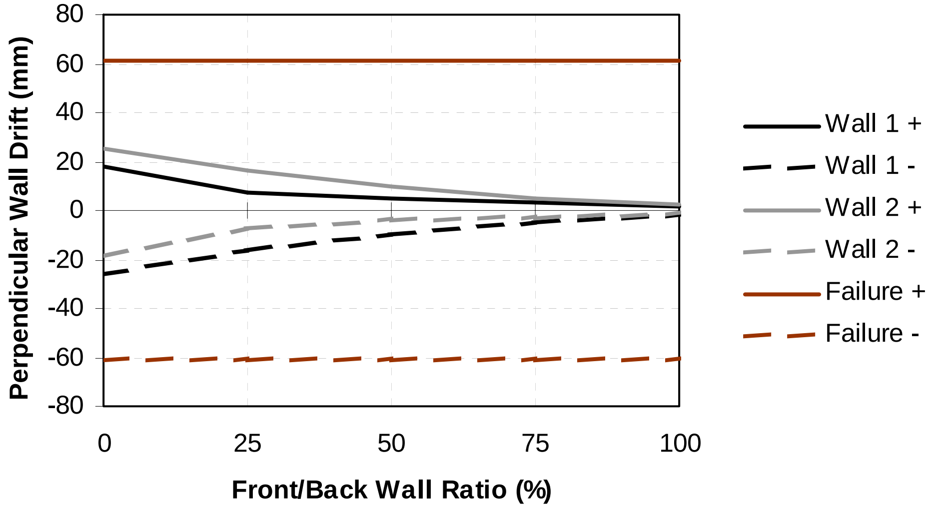

Figure 7.95 Peak Perpendicular Wall Drift (L:W=3:1, w/ partition wall)

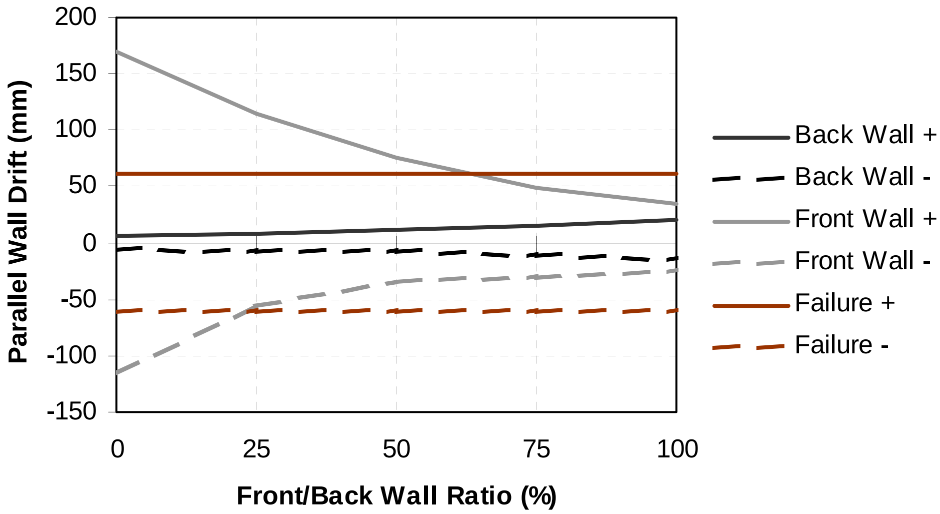

Figure 7.96 Peak Parallel Wall Drift (L:W=3:1, w/ partition wall)

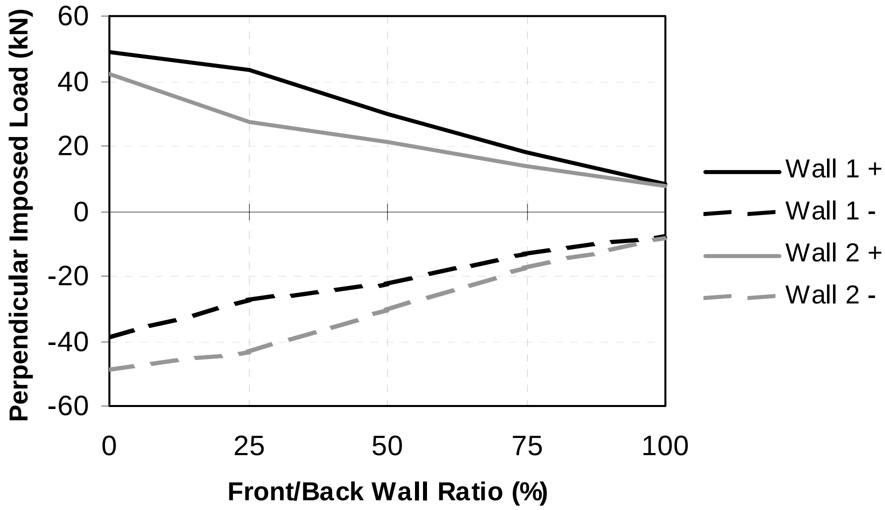

Figure 7.97 Peak Perpendicular Imposed Load (L:W=3:1, w/ partition wall)

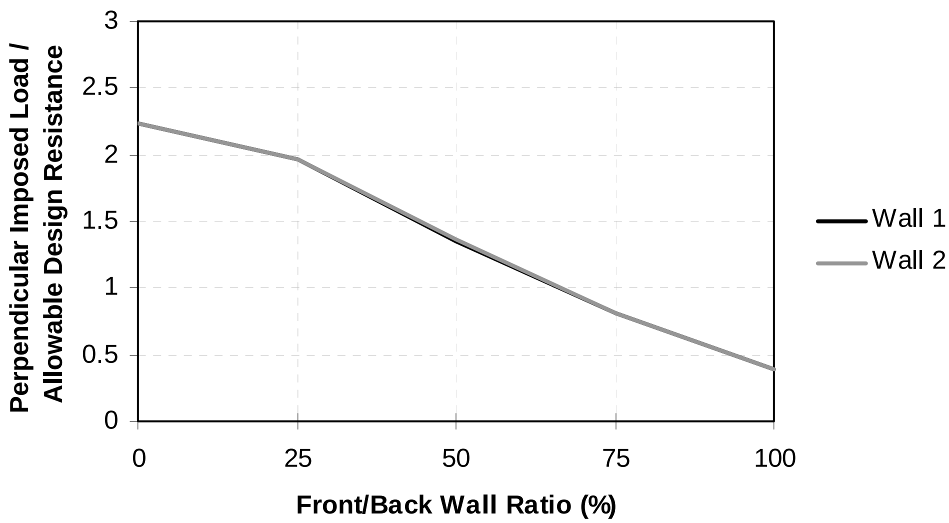

Figure 7.98 Peak Perpendicular Imposed Load / Design resistance (L:W=3:1, w/ partition wall)

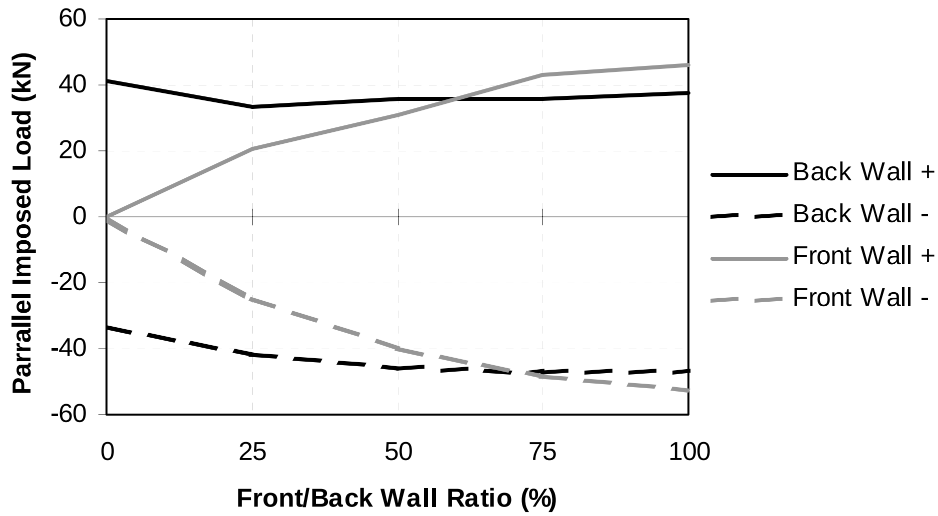

Figure 7.99 Peak Parallel Imposed Load (L:W=3:1, w/ partition wall)

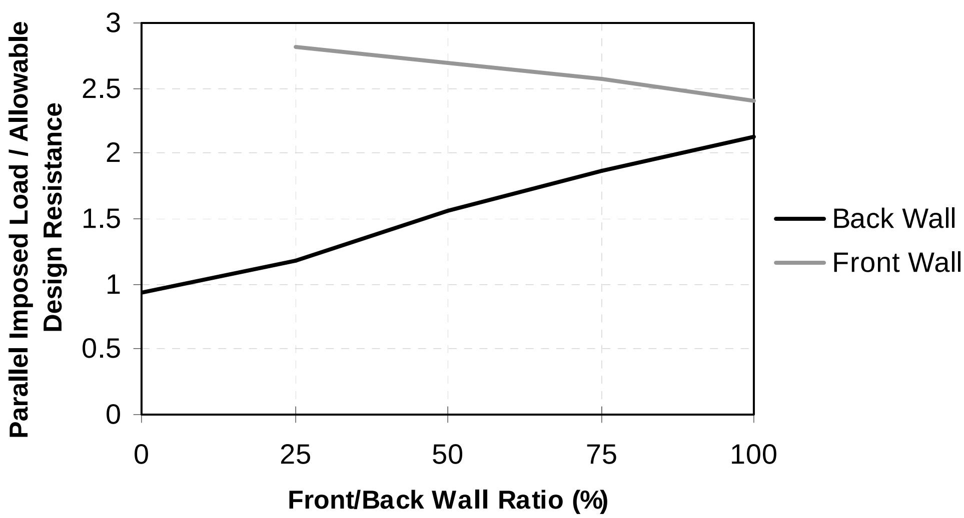

Figure 7.100 Peak Parallel Imposed Load / Design resistance (L:W=3:1, w/ partition wall)

The peak parallel base shear for each analysis case in Group 5_1 and 5_2 is shown in Figure 7.101. Similar to Group 4_1 and 4_2, the base shear demand increases as the front/back wall ratio increases. Because the buildings with a L:W ratio of 3:1 have the worst torsional resistant capacity in all the studied L:W ratios, rotational vibration mode is very significant when the front/back wall ratio is low. The demands become more consistent for the redesigned buildings because the strengthened perpendicular walls offer a better torsional resistant capacity.

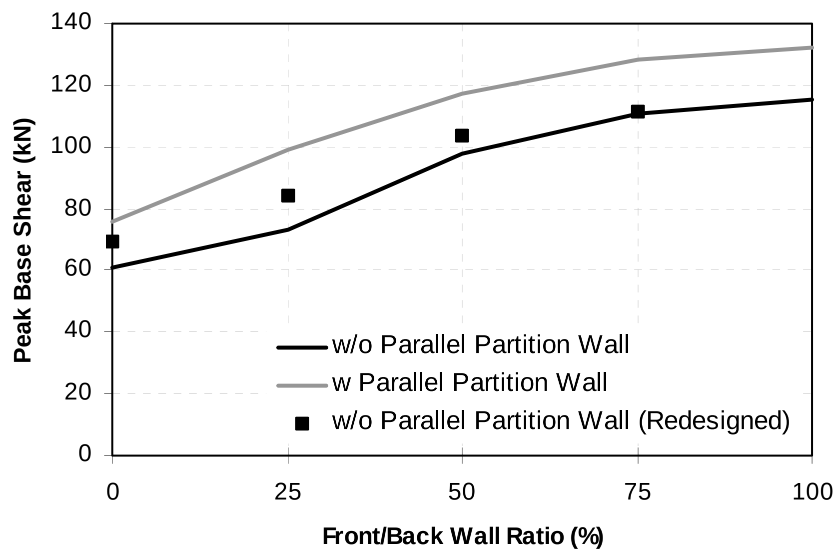

Figure 7.101 Peak Parallel Base Shear (L:W=3:1)

To prove that the effect of structural size and mass is negligible to the analysis results, two extra open-front structure models with L-to-W ratio of 3:1 were analyzed, one of which has the configuration of 30 × 90 ft and the same mass distribution of the models above (30 lbs/ft^2), and the other with the configuration of 20 × 60 ft (same as Case 5) but with twice the mass of Case-5 models (60 lbs/ft^2). Both models had a completely open front wall and no partition walls. The design criteria and procedure applied to these two structures were exactly same as the models above. The analysis results show that the wall drifts of these two structures are almost the same as those of Case 5_1_0 (20 × 60 ft, 30 lbs/ft^2, with complete open front wall, without partition walls). The ratio of imposed wall load to the allowable value of each wall is also almost the same as that of Case 5_1_0.

From the comparison, the conclusion can be drawn that the analysis results above can apply to the structures with different sizes or mass if they have the same L-to-W ratios. It should be noted that the contribution of partition walls depends on the stiffness and strength ratios of partition walls to structural walls. So structural size may affect the contribution from partition walls, and the structural responses as a result.

7.6 Summary

From the analysis results, numerous findings can be pointed out.

First of all, since nonlinear time history analysis was used, all the results are in the sense of non-linearity.

Since the simplified seismic design procedure was employed in this study, the seismic demand was amplified by a factor of 1.2. Furthermore, in the Special Design Provisions for Wind and Seismic (2005 Edition Supplement, ASD/LRFD), the shear resistance factor for LRFD design procedure was changed from 0.65 (2001 Edition) to 0.80. In addition, an amplifier factor of 1.49 was applied in the shear wall design (Chapter 7.4). The accumulative effect of these three items gives a 2.2 increase in capacity. As a result, a structural system response factor (R-Factor) of about 3 instead of 6.5 should be used for wood light-frame bearing walls.

For structures with the same plan aspect ratio, the drift and imposed load on perpendicular walls decrease when front-to-back wall ratio increases from 0% to 100%, and the values become almost zero (they are not exactly zeros because of numerical error) when the structure becomes symmetric (front-to-back wall ratio equals 100%). This is because the drift and load in the perpendicular walls are caused by the torsional behavior of structures. Without the torsional irregularity, there will not be any drift and load imposed on these perpendicular walls.

For the structures with the same plan aspect ratio, with the increase of front-to-back wall ratio from 0% to 100%, the drift of the back wall increases, while the drift of front wall decreases until both reach to almost the same value (there is a little difference because of numerical error) when the structures become symmetric (front-to-back wall ratio equals 100%). The reason is that the stiffness and strength of the back wall decreases, while those for the front wall increase as front-to-back wall ratio increases.

For the structures with the same plan aspect ratio, with the increase of front-to-back wall ratio from 0% to 100%, the ratio of imposed load to allowable load in the back wall increases, while that in the front wall decreases. The reason is that when the structure is asymmetric, the frequency of torsional vibration mode is much lower than that of the translatory vibration mode. Therefore, back and front walls do not respond in the same phase in the ground motion direction because of the structural torsional behavior and diaphragm shear and flexural deflections (Figure C.70). This behavior is called out-of-phase effect here. The closer the front-to-back wall ratio is to 0% and the larger the L-to-W ratio is, the more significant this effect is. For the structures with a front-to-back wall ratio close to 0% and a large L-to-W ratio, the out-of-phase effect is so significant that makes the structures behavior more like they are rotating around the back wall, and the front wall's drift is much larger than that of back wall. This is due to the significant difference of stiffness and long distance between back and front walls causing a large effective eccentricity. Therefore, in the structures with large openings in the front wall and large L-to-W ratio, the back wall's capacity cannot be utilized fully to resist lateral seismic loads associated with the whole floor mass. In the symmetric structures, the capacity of parallel walls can be utilized completely.

The partition wall can resist 24% to 61% of the base shear and effectively decrease the structural global drift by 28% to 76%. The effect depends on the structural geometry and partition wall location. For structures with larger L-to-W ratios, the benefit from partition wall is lower than in the structures with smaller L-to-W ratios. This is because the length of the partition wall parallel to the supposed ground vibration direction is relatively short when compared to the exterior structural walls. Generally, in buildings of larger size, the benefit from a partition wall is less than in smaller ones. For instance, a building with the plan of 9.1×9.1 m (30×30 ft) required 4 times more structural wall length than a building with the plan of 6.1×6.1 m (20×20 ft) because the total mass of the former structure is 4 times that of the latter, while the partition wall length can only increase by a factor of 1.5 from the geometry point of view. Also, the stiffness ratio of the partition wall to exterior structural wall in the larger building dropped significantly compared with that in the smaller building. Partition walls can also significantly reduce the structural torsion behavior by reducing the torsional irregularity. For the buildings with completely open fronts (Front-to-back wall ratio equals 0%), the partition walls can decrease the torsion angle by 38% to 73%.

The extreme front wall drift in the buildings (without partition walls) with a completely open fronts and a L-to-W ratio of 1/3 is 58 mm, while it is 64 mm, 113 mm, 186 mm, and more than 300 mm for the structures with the L-to-W ratios of 1/2, 1, 2, and 3, respectively. The first reason to explain the significant drift increase is that the eccentricity between center of stiffness and mass center becomes larger and the restraint arm between perpendicular walls becomes shorter relative to the eccentricity when L-to-W ratio becomes larger, so they will suffer more from torsional irregularity. Furthermore, the geometry makes the situation worse, since a small rotation angle results in a large drift in front wall of the structures with large L-to-W ratios. Besides, the perpendicular two gypsum partition walls in the structure with L-to-W ratio of 1/3 also contributed in torsion resistance.

For the structures (without partition walls) with completely open fronts, the ratio of maximum perpendicular wall imposed load to design load and the extreme perpendicular wall drifts (proportional with torsion angle) increase rapidly from the L-to-W ratio of 1/3 to 1, but they do not change much from 1 to 3. The possible reason is that from 1/3 to 1 the torsional vibration modal frequency is relatively high, while from 1 to 3 the frequency is low. From the displacement spectrum point of view, the peak torsion angle may change a lot in the high frequency zone when the frequency drops, and may not change significantly in the low frequency range.

For the buildings in Group 5, when Front-to-back wall ratio equals 1, there is still significant load and displacement imposed on perpendicular walls, and the loads imposed on front and back wall do not match each other. The reason is that the partition wall has been put in at the 1/3-L position (not in the half way), and the structure was asymmetric even though the Front-to-back wall ratio is 1.

The assumed failure criteria for this study was when the drift reaches 2.5% of the structural height (ASCE7-05), which is 61 mm (2.4 in.). From the results, perpendicular walls don’t fail for any of the cases with or without partition walls.

When the parallel wall drift is studied, the structures with L-to-W ratios of 1/2 and

1/3 perform much better than the other structures with larger L-to-W ratios. They do not fail even when the front wall is 100% open. The structure with a L-to-W ratio of 1 does not fail when the front-to-back wall ratio equals or is larger than 50% if no partition wall is available, and does not fail if partition wall is present. The structure with a L-to-W ratio of 2 fails when the front-to-back wall ratio equals to or is less than 75% if no partition wall is present and when the front wall is 100% open if partition wall is present. The structure with a L-to-W ratio of 3 fails when there is any opening in the front wall if no partition wall is present and when the front-to-back wall ratio is less than 75% if partition wall is present.

By considering torsion in the design process, the perpendicular walls were lengthened. But the results show that the increase in perpendicular wall length according to the elastic design method reduces the front wall drifts, but still cannot make it lower than the design failure criteria (2.5% structural height). The required extra perpendicular length is 2 and 3 times that required in the original design (required to resist translatory seismic load only) for the 100% front open structures with L-to-W ratios of 2 and 3, respectively. After lengthening the perpendicular walls based on the special torsion design, the front wall drift was reduced by 33% and 51% for these two cases respectively. However, both cases still have drifts more than 2 times the design criteria. The analysis results showed that the strengthening of the perpendicular walls reduced the torsion by 53% and 66% for these two cases respectively. However, because of the large L-to-W ratio, a small torsional response can cause a huge front wall drift. At the same time, because strengthening causes more load to be imposed on the perpendicular walls, it also triggered more shear deflection in diaphragm. Based on the above discussion, the torsional design method based on elastic assumptions is not satisfactory in the design of open-front wood-frame structures when L-to-W ratio is greater than 1, and it is not necessary when L-to-W ratio is less than or equal to 1/2.

According to the parametric study and the analysis of results, some recommendations can be made for real open-front wood-frame structure design. When wood shear wall buildings are loaded in the transverse direction, as shown in Figure 7.102, it is recommended that resisting shear walls be placed symmetrically in the front and back walls.

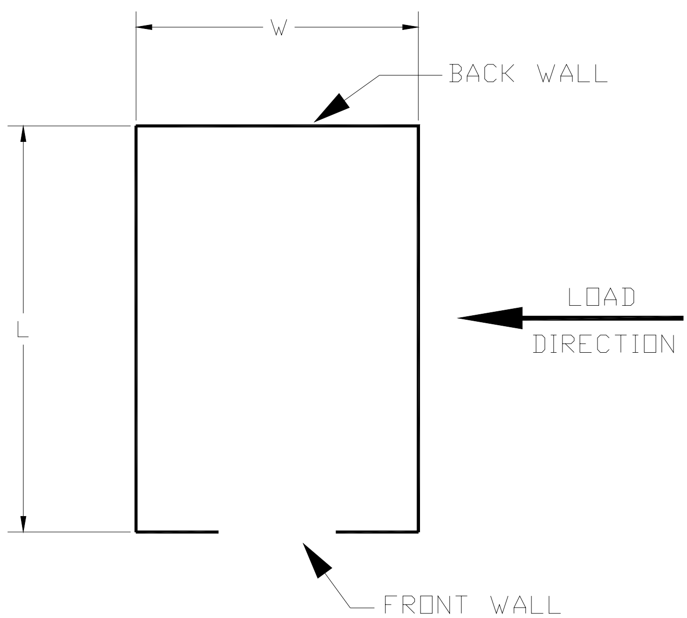

Figure 7.102 Open-front Building under Transverse Loading

Where it is not possible to put 50% of the required transverse shear wall strength in the front wall, the following are recommended:

- For buildings with a diaphragm L:W ratio of 1:1, it is acceptable to place 33% of the required transverse shear wall in the front wall and 67% in the back wall.

- For buildings with a diaphragm L:W between 1:1 and 2:1, it is acceptable to linearly interpolate between 33% and 50% of the required shear wall strength at the front wall.
- For buildings with a diaphragm L:W ratio of 2:1 and greater, providing less than 50% of the required shear wall in the front wall should not be permitted, except where a detailed analytical study indicates that acceptable performance will result.
- For buildings with a diaphragm L:W ratio of 1:2 to 1:3, no limits on distribution of shear wall strength to the front and back walls is needed.

The recommendations were summarized in Table 7.9.

Table 7.9 Summary of the Design Recommendations

Geometry	L : W	Limits on shear wall distribution
	1 : 3	None
	1 : 2	None
	1 : 1	33% minimum of required shear wall strength in front wall
	2 : 1	50% of required shear wall strength in front wall
	3 : 1	50% of required shear wall strength in front wall

In all cases where the distribution is other than 50% of required length to the front wall, required perpendicular shear wall length should be determined considering 100% of the base shear in the longitudinal direction acting concurrently with 100% of the base shear acting in the transverse direction. All of the above recommendations apply equally to a back or side wall if less than 50% of the required shear wall length were to be placed in those walls.

7.7 Structural Response under Two-directional Ground Motion

7.7.1 Introduction

From the single-directional loading analysis that was run previously, part of capacity of the “perpendicular” walls was consumed when structural non-symmetry existed in the “parallel” direction. Therefore, the degree of safety in “perpendicular” direction will be below the code margin if one considered an earthquake which has components in two orthogonal directions. However, this is the case for all real earthquakes. To investigate the effect of two-directional loading, the same buildings were analyzed using both traces of the Canoga Park record.

To make the comparison easier, the wall notations were kept the same as previously used though there are no walls that are only “parallel” or “perpendicular” to ground motions.

7.7.2 Two-directional Time History Analysis

The ground motion history was the scaled the same as before, only both horizontal traces of the Canoga Park Record were used. To be comparable with the results under single-directional ground motion, the major motion record applied in the “parallel” direction was the same as that used in the previous analysis (peak acceleration is 0.5 g). The minor motion record (peak acceleration is 0.43g) was applied in the “perpendicular” direction (the acceleration record is shown in Figure 7.103).

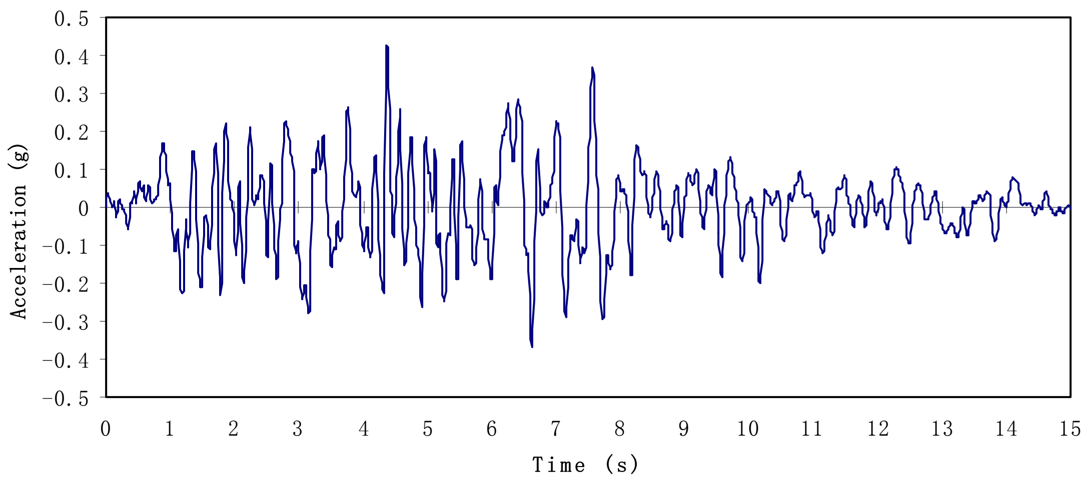

Figure 7.103 Ground Motion History in Minor Direction (peak acceleration = 0.43 g)

From the previous analysis, the structures with aspect ratios greater than 2 (Cases 4 and 5) failed if any non-symmetry exists, only Cases 1, 2, and 3 are included in this study with a two-directional earthquake attack. The lowest acceptable Front-to-back wall ratio in the single-direction analysis was 50%, 0%, and 0% for Cases 1, 2, and 3 respectively (without “parallel partition walls”). In this study, only the structural configurations with the lowest acceptable Front-to-back wall ratios (Cases 1_1_50, 2_1_0, and 3_1_0) Case 1_1_100 (symmetric in both direction, used as the control) were studied. The plan views of these configurations are shown in Figure 7.104. Both the uni-directional and two-directional analysis results for these cases were shown in Table 7.10 for comparison purposes.

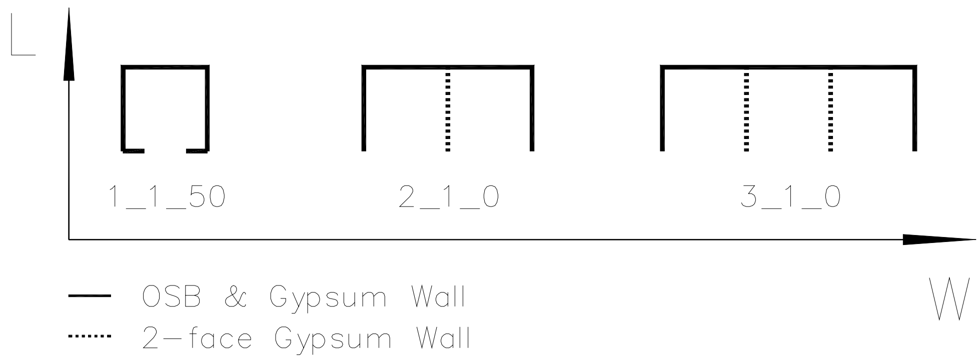

Figure 7.104 Plan Views of Buildings 1_1_50, 2_1_0, and 3_1_0

Table 7.10 Single-directional & Two-directional Earthquake Time History Analysis Results

Case		Peak Perpendicular Wall Drift (mm)		Peak Parallel Wall Drift (mm)		Peak Perpendicular Imposed Load Ratio		Peak Parallel Imposed Load Ratio	
		Wall 1	Wall 2	Back Wall	Front Wall	Wall 1	Wall 2	Back Wall	Front Wall
Single - directional	1_1_100	1.56	1.72	48.96	49.12	0.29	0.29	2.57	2.58
	1_1_50	9.29	9.08	40.67	59.86	1.24	1.25	2.54	2.63
	2_1_0	16.40	16.49	44.70	64.04	1.80	1.81	2.56	N/A
	3_1_0	8.02	7.66	48.34	58.17	1.13	1.15	2.61	N/A
Two - directional	1_1_100	33.38	32.61	49.12	51.10	2.04	2.16	2.58	2.60
	1_1_50	22.05	59.98	31.26	70.85	1.96	2.48	2.39	2.67
	2_1_0	16.74	49.78	35.14	65.83	1.86	2.57	2.45	N/A
	3_1_0	10.18	31.28	44.93	59.37	1.36	2.33	2.59	N/A

The results show that, for Case 1_1_100, since the structure is symmetric in both orthogonal directions, the influence of the earthquake components in the two orthogonal directions were not coupled. The maximum parallel wall drifts and imposed loads are almost the same as those obtained from the single-directional earthquake time history analysis. The maximum drifts and imposed loads in the two perpendicular walls are very close with each other (the small difference was caused by numerical error). The maximum perpendicular drift and load ratio in the “perpendicular” walls were both less than those in the “parallel” walls. That is because the intensity of the “perpendicular” ground motion component is lower than the “parallel” component.

For the other cases, compared to the single-directional analysis results, the maximum drifts and imposed loads in the two “perpendicular” walls increased significantly and were not consistent anymore. The drift increase was due to the extra earthquake input in the “perpendicular” direction. The inconsistent drifts were due to the combined effect of the two ground motion components. The phenomenon also appeared in the experimental results observed by Mosalam, et al (2002).

For Cases 1_1_50, 2_1_0, and 3_1_0, the back wall drift decreased, while the front wall drift increased when subjected to two-directional earthquake. The reason is that the extra earthquake input in the “perpendicular” direction increased the drifts and degradation of the “perpendicular” walls, and as a result, the structural torsional resistance was weakened. So the torsional behavior of the buildings is more significant when subjected to two-directional earthquake.

Front wall failure due to excessive drift occurs in Cases 1_1_50 (70.85 mm) and 2_1_0 (65.83 mm) while not in Case 3_1_0 (59.37). However, the drift in Case 3_1_0 was only 1.63 mm short of failing the drift requirement. In the cases with non-symmetric resistance, the “perpendicular” walls were used to resist the ground motion in “perpendicular” direction and the torsion caused by the ground motion in “parallel” direction as well. So the torsional resistance was weakened compared to the analysis for single-directional ground motion response as a result. This caused the failure of Case 1_1_50 and 2_1_0. Of these three cases, the performance of Case 3_1_0 was the best, Case 2_1_0 second, and Case 1_1_50 the worst. The first reason is that Case 3 and 2 have better torsion resistant structural configurations due to the non-symmetry which occurs in the long sides of the building. The second reason is the added contribution of the “perpendicular” gypsum partition walls in Cases 2_1_0 and 3_1_0.

It is generally assumed that the ultimate wood-frame shear wall strength capacity is 2.8 to 3.4 times the allowable design value. To maintain the same safety margin when subjected to two-directional earthquakes, it is recommended that the portion of resistance consumed by the structural torsional behavior be replaced by requiring extra wall length or strength. For instance, if the maximum imposed load in “perpendicular” wall is 1.5 times the allowable design value when the structure is only analyzed for the earthquake loading in “parallel” direction, which means the torsional behavior consumed half of the wall’s capacity, the wall length should be increased by 50% or the affected wall’s strength should be increased by 50% by adding additional nailing or other strengthening measures.

Based on the recommendation to increase the strength, the “perpendicular” walls were lengthen by 41.7%, 60.2%, and 38.2% for Cases 1_1_50, 2_1_0, and 3_1_0 respectively using the single-directional time history analysis results to determine the required extra strength. The parameters of the “perpendicular” walls were updated correspondingly (Table 7.11). The updated models were analyzed using the two-directional ground motion history again, and the results were shown in Table 7.12.

The results show that the maximum drifts in the “parallel” walls were reduced to 63.66 mm and 63.15 mm for Cases 1_1_50 and 2_1_0 respectively, which are close to the failure criteria of 61 mm, and can be regarded as satisfactory from a drift criteria point of view. For Case 3_1_0, the maximum drift was reduced to 58.04 mm.

If one considers the distribution of imposed load on the revised building, the loading ratios in the perpendicular walls both were reduced as expected. In fact, the ratios for the perpendicular walls are in line with the analysis with no openings. The load ratios for the back wall of the parallel direction increased when the perpendicular walls were strengthened. This is surprising until one realizes that the strengthening of the perpendicular walls reduces the torsional responses and therefore some of the load in the parallel direction that was transferred to the perpendicular walls from the front wall is now being transferred by the diaphragm to the back wall. However, the parallel direction load ratios are in the same range as those for the configuration with no openings.

Table 7.11 Perpendicular Shear Wall Parameter Update

Case	Total Length (ft)	Front / Back Ratio	Perpendicular Wall							
			OSB Wall				Gypsum Wall			
			Length (ft)	w	d_n	d_h	Length (ft)	w	d_n	d_h
1_1_50	10	0	7.08	1.155	1.13E-06	5.99E-05	7.08	0.834	1.95E-04	1.21E-03
2_1_0	20	0	16.02	1.737	4.99E-07	2.65E-05	16.02	1.255	8.64E-05	5.36E-04
3_1_0	30	0	20.73	1.976	3.86E-07	2.05E-05	20.73	1.427	6.68E-05	4.14E-04

Table 7.12 Updated Two-directional Earthquake Time History Analysis Results

Front/Back ratio	Max Perpendicular Wall Drift (mm)		Max Parallel Wall Drift (mm)		Max Perpendicular Imposed Load / Design Load		Max Parallel Imposed Load / Design Load	
	Wall 1	Wall 2	Back Wall	Front Wall	Wall 1	Wall 2	Back Wall	Front Wall
1_1_100	33.38	32.61	49.12	51.10	2.04	2.16	2.58	2.60
1_1_50	18.73	33.37	39.13	63.66	1.65	2.33	2.49	2.64
2_1_0	15.12	29.68	49.03	63.15	1.20	2.28	2.59	N/A
3_1_0	9.57	23.06	48.30	58.04	1.22	2.11	2.63	N/A

7.7.3 Summary

As shown in the two-directional loading analysis, the structures that can survive the single-directional earthquake attack may not survive when subjected to two-directional earthquakes. A method to add sufficient strength to replace the consumed capacity caused by torsional behavior is a proposed solution, and the numerical tests on 3 structural configurations showed it is acceptable. More detailed solutions can only be accomplished by relevant nonlinear time history analysis.

Chapter 8
Summary, Conclusions, and Future Research

8.1 Summary

A general numerical hysteretic model, BWBN, was improved and applied to describe the hysteretic behavior of nailed wood joints in which the hysteretic constitutive law was characterized by a series of ordinary differential equations including 13 parameters. These parameters are estimated using cyclic test results. This model is capable of producing versatile and smoothly varying hysteretic curves and is nonlinear, history-dependent, including stiffness and strength degradation and pinching. It also can describe the partial loop response accurately after the improvement. This model has been embedded into ABAQUS/Standard (2005) as a user-defined element. The coupled property of nailed wood joints can be achieved in the model by using an oriented spring pair model. The accuracy of the model was verified through two shear wall examples with different configurations (with and without openings) and boundary conditions (with and without tie-down anchors).

Based on this joint model, a super shear wall model was developed which is capable of representing the hysteretic behavior of whole wood-frame shear wall lines with a pair of diagonal hysteretic spring elements. In accordance with the configuration of the two-story 3-D wood-frame structure tested in UC San Diego (Fischer et al, 2001), a 3D wood-frame structural model was developed in ABAQUS/Standard (2005). In this model, the super shear wall model was utilized to simulate the shear walls. Floor and roof diaphragms were assumed to perform elastically, and the hysteretic characteristics of diaphragms were represented as equivalent viscous damping. The same ground acceleration history used in the test was used as the input loading history for the model. Through comparison of the fundamental period and mode shapes, global and first-story displacement histories, and the global hysteresis of the test and numerical model results, the super shear wall model was validated.

To evaluate the influence of the open-front torsional irregularity on the structural behavior of wood-frame buildings under a design-level earthquake (hazard level of 10% / 50 years), a parametric study was conducted using the super shear wall model. The parameters considered in this study included plan aspect ratio, open-front ratio, and inclusion of gypsum partition walls or not. 5 groups of open-front wood-frame structural models were developed. The models had plan aspect ratios of 1:1, 1:2, 1:3, 2:1, and 3:1, respectively. Each group included 5 different open-front ratios, which were 0, 25%, 50%, 75%, and 100%. The relevant models with gypsum partition walls were also developed for the purposes of studying the influence of partition walls on structural behavior. The Canoga Park ground acceleration history from the 1992 Northridge, CA earthquake (with an amplitude scaling factor of 1.2) was used in this study. The peak ground acceleration of this record is 0.5g after being scaled.

8.2 Conclusions

The results from the above study led to the following conclusions and recommendations:

1. **Comparison of the detailed shear wall model and super shear wall model:**

   In the detailed shear wall model, each sheathing-to-frame connector was simulated with a hysteretic spring element, the 13 parameters of which were estimated through “GA” program based on the connector cyclic test results. This detailed model was able to accurately predict the load-to-drift relationship of the shear wall subjected to static monotonic, static cyclic, and dynamic loadings. Since it is inefficient to simulate every connector in a 3-D building system, the detailed model was only used to develop the cyclic load hysteresis of a wall, which can then be the data basis for the super shear wall model’s parameter estimation. In another words, the detailed shear wall model was usually employed as a virtual test.

There are only two diagonal hysteretic springs in the super shear wall model, so the computational time and storage can be significantly reduced during the analysis process. The parameters for the super model can be calibrated based on real test results or the detailed shear wall analysis results. The super shear wall model can simulate the nonlinear behavior of 3D light-frame structures accurately and efficiently.

2. Conclusions on the parametric study on open-front wood-frame structures:

a) A structural system response factor (R-Factor) of about 3 instead of 6.5 should be used for wood light-frame bearing walls.

b) For structures with the same plan aspect ratio, when front-to-back wall ratio increases from 0% to 100%, the drift and imposed load on perpendicular walls decreases and the values become almost zero (they are not exactly zeros because of numerical error) when the structure becomes symmetric (front-to-back wall ratio equals 100%). The drift and the load ratio of the back wall increases, while the drift and the load ratio of the front wall decreases until both reach almost the same value (there is a little difference because of numerical error) when structures become symmetric (front-to-back wall ratio equals 100%).

c) The partition walls can share 24% to 61% of the base shear, decreasing the building drift by 28% to 76%, and reducing the torsion angle by 38% to 73%. The beneficial effect depends on structural size, diaphragm aspect ratio, and partition wall location. So, in real designs, the benefits from partition walls should usually only be regarded as extra safety resources.

d) For the structures with the complete open fronts without partition walls, the extreme front wall drift increases significantly when the diaphragm aspect ratio (L-to-W ratio) changes from 1/3 to 3. The extreme torsion angle increases rapidly when the diaphragm aspect ratio changes from 1/3 to 1 but does not change much when the diaphragm aspect ratio changes from 1 to 3.

e) The torsional response of the building should be considered in all designs if a uniform safety margin is to be maintained for all building configurations. However, from Figure 7.23, if a 50% overload in the perpendicular walls was to be considered acceptable, then a 25% opening ratio for buildings with 1:1 aspect ratio diaphragms would be acceptable before special design considerations would be required. If "non-structural" partition walls are present the opening ratio could be increased to about 50%. Similar triggers can be set using this analysis for other diaphragm aspect ratios.

f) If the potential earthquake in perpendicular wall direction is not considered, perpendicular walls don't fail for any of the cases with or without partition walls.

g) The performance of the buildings with the same open-front ratio can be significantly different if the buildings have different diaphragm aspect ratios. The structures with L-to-W ratios of 1/2 and 1/3 perform much better than the other structures with larger L-to-W ratios. In other words, openings should be located in the long dimension of the building for the best response.

h) For the cases in which the ultimate front wall drifts exceed the design criteria (2.5% structural height), the results show that strengthening perpendicular walls according to the elastic design methods can reduce the front wall drifts, but cannot reduce it below the design failure criteria.

i) It is recommended that resisting shear walls be placed symmetrically in the front and back walls. Where it is not possible to place shear walls symmetrically, the following are recommended:

  - For buildings with a diaphragm L:W ratio of 1:1, 33% minimum required shear wall strength should be placed in the front wall.
  - For buildings with a diaphragm L:W between 1:1 and 2:1, it is acceptable to linearly interpolate between 33% and 50% of the required shear wall strength at the front wall.
  - For buildings with a diaphragm L:W ratio of 2:1 and greater, any structural non-symmetry in W direction is not acceptable, except where a detailed analytical study indicates that acceptable performance will result.

- For buildings with a diaphragm L:W ratio of 1:2 to 1:3, no limits on distribution of shear wall strength to the front and back walls is needed.

The recommendations have been summarized in Table 7.9.

j) Conclusions and recommendations are applicable to structures with different sizes and masses as long as the aspect ratios and partition wall to structural wall ratios are the same.

k) Part of the perpendicular wall capacity is consumed to resist the load imposed by torsional behavior. The degree of safety was reduced when the possibility of ground motion in the perpendicular wall direction was considered. It is recommended that the consumed portion of resistance in the perpendicular direction be replaced by adding a corresponding length to the perpendicular walls or strengthening the existing walls. The more reliable and accurate estimation of structural behavior when subjected to a two-directional earthquake can only be accomplished by relevant nonlinear time history analysis.

8.3 Future Research

Some future research is needed to extend this study:

1. The BWBN model can simulate structural stiffness and strength degradation. However, degradation may increase after the displacement reaches some maximum value. Since the interest of this study was structural behavior before and close to the failure point (2.5% drift, the structure is regarded as

failure after this point), the post failure stage has not been studied much. Post failure performance is a stage in which the structural collapse happens. It would be helpful to understand structural collapse mechanisms better if the structural post failure stage can be modeled more accurately.

2. In the modifications of the BWBN model, some empirical expressions were utilized to describe the partial loop behavior of nailed wood joints and super shear wall hysteresis. The results proved that they are accurate enough for wood-frame structures. However, these expressions are probably not suitable for other light-frame structures and may need to be modified.
3. In the parametric study, only one ground motion record was used, which corresponded to the design-level event in the San Francisco Bay area. Therefore more time history analysis with additional ground motion records would be needed to make the analysis results more comprehensive.
4. Additional nonlinear time history analysis with two-directional ground motion inputs are needed for a better understanding of the nonlinear response of open-front wood-frame structures under two-directional ground motions.

REFERENCE

ABAQUS (2005). “ABAQUS Analysis User’s Manual (Version 6.5)”, Hibbitt, Karlsson, and Sorenson, Inc., Pawtucket, RI.

Baber, T. T. and Y-K. Wen. 1981. “Random Vibration of Hysteretic Degrading Systems”. Journal of Engineering Mechanics Division ASCE, 107(EM6). pp. 1069-1087.

Baber, T. T. and M. N. Noori. 1985. “Random Vibration of Degrading, Pining Systems”. Journal of Engineering Mechanics ASCE, 111(8). pp. 1010-1026.

Bouc, R. 1967. “Force Vibration of Mechanical Systems with Hysteresis”, Abstract. Proc. Fourth Conference on Nonlinear Oscillation, Praque, Czechoslovakia.

Casciati, F. 1987. “Nonlinear Stochastic Dynamics of Large Structural Systems by Equivalent Linearization.” In Reliability and Risk Analysis in Civil Engineering 2, N.C. Lind, ed., University of Waterloo, Canada. pp. 1165-1172.

Ceccotti, A. and A. Vignoli. 1990. “Engineered Timber Structures: An Evaluation of Their Seismic Behavior”. Proc. 1990 International Timber Engineering Conference, Tokyo, Japan, pp. 946-953.

Chui, Y. H. and C. Ni. 1997. “Load-Embedment Response of Timber to Reversed Cyclic Load”. Wood and Fiber Science, 29(2), pp. 148-160.

Chui, Y. H., C. Ni, and L. Jiang. 1998. “Finite-Element Model for Nailed Wood Joints under Reversed Cyclic Load”. Journal of Structural Engineering ASCE, 124(1), pp. 96-103.

Collins, M., B. Kasal, P. Paevere, and G. C. Foliente. 2005. “Three-Dimensional Model of

Light-frame Wood Buildings. I: Model Description”. Journal of Structural Engineering ASCE, 131(4), pp. 676-683

Collins, M., B. Kasal, P. Paevere, and G. C. Foliente. 2005. “Three-Dimensional Model of Light-frame Wood Buildings. II: Experimental Investigation and Validation of Analytical Model”. Journal of Structural Engineering ASCE, 131(4), pp. 684-692

Dinehart, D. W. and H. W. Shenton III. 1998. “Comparison of Static and Dynamic Response of Timber Shear Walls”. Journal of Structural Engineering ASCE, 124(6), pp. 686-695

Dolan, J.D. 1989. “The dynamic response of timber shear walls”. Ph. D Dissertation, Dept. of Civil Engineering. University of British Columbia, Vancouver, BC, Canada.

Dolan, J. D. and D. M. Carradine. 2003. “CUREE Nail Fastener Connections Report”, Washington State University, USA.

Du, Y. 2003. “The Development and Use of a Novel Finite Element for the Evaluation of Embedded Fluid Dampers within Light-Frame Timber Structures with Seismic Loading”. Ph. D Dissertation, Department of Civil and Environmental Engineering. Washington State University, Pullman, Washington, USA.

Durham, J., F. Lam, and H. G. L. Prion. 2001. “Seismic Resistance of Wood Shear Walls with Large OSB Panels.” Journal of Structural Engineering ASCE, 127(12), pp. 1460-1466

Fischer, D., A. Filiatrault, B. Folz, C.-M. Uang, and F. Seible. 2001. “Shake Table Tests of a Two-Story House.” CUREE Publication No. W-06, Richnomd, Calif. USA

Foliente, G. C. 1993. “Stochastic Dynamic Response of Wood Structural Systems”. Ph. D Dissertation, Dept. of Wood Science and Forest Products. Virginia Polytechnic Institute and State University, Blacksburg, Virginia, USA.

Foliente, G. C. 1995. “Hysteresis Modeling of Wood Joints and Structural Systems”. Journal of Structural Engineering ASCE, 121(6), pp. 1013-1022.

Folz, B. and A. Filiatrault. 2001. “Cyclic Analysis of Wood Shear Walls”. Journal of Structural Engineering ASCE, 127(4), pp. 433-441

Folz, B. and A. Filiatrault. 2004. “Seismic Analysis of Woodframe Strucures I: Model Formulation”. Journal of Structural Engineering ASCE, 130(9), pp. 1353-1360

Folz, B. and A. Filiatrault. 2004. “Seismic Analysis of Woodframe Strucures II: Model Implementation and Verification”. Journal of Structural Engineering ASCE, 130(9), pp. 1361-1370

Fonseca, F. and J. Judd. 2004. “Analytical Modeling of Nailed Sheathing Connections in Wood Shear Walls”. IX ENCONTRO BRASILEIRO EM MADEIRAS E EM ESTRUTURAS DE MADEIRA CUIABA-JULHO DE, Universidade de Brigham Young, Faculdade de Engenharia Civil e Ambiental.

Foschi, R. O. 1977a. “Analysis of Wood Diaphragms and Trusses. Part I: Diaphragms”. Canadian Journal of Civil Engineering, 4, pp. 345-352.

Foschi, R. O. 1977b. “Analysis of Wood Diaphragms and Trusses. Part II: Truss-plate connections”. Canadian Journal of Civil Engineering, 4, pp. 353-362.

Foschi, R. O. 2000. “Modeling the Hysteretic Response of Mechanical Connections for Wood Structures”. Proc., World Conf. On Timber Eng., Dept. of Wood Science, ed. UBC, Vancouver, Canada.

Foschi, R. O., F. Yao., and D. Rogerson. 2000. “Determining Embedment Response Parameters from Connector Tests”. Proc., World Conf. On Timber Eng., Dept. of Wood Science, ed. UBC, Vancouver, Canada.

He, M., M. Henrik, F. Lam, and H. G. L. Prion. 1999. “Cyclic Performance of Perforated Wood Shear Walls with Oversize OSB panels”. Journal of Structural Engineering ASCE, 125(1), pp. 10-18.

He, M., F. Lam, and R. O. Foschi. 2001. “Modeling Three-Dimensional Timber Light-Frame Buildings”. Journal of Structural Engineering ASCE, 127(8), pp. 901-912.

Heine, C. P. 1997. “Effect of Overturning Restraint on the Performance of Fully Sheathed and Perforated Timber Framed Shear Walls”. Master Thesis, Dept. of Wood Science and Forest Products. Virginia Polytechnic Institute and State University, Blacksburg, Virginia, USA

Heine, C. P. 2001. “Simulated Response of Degrading Hysteretic Joints With Slack Behavior”. Ph. D Dissertation, Dept. of Wood Science and Forest Products. Virginia Polytechnic Institute and State University, Blacksburg, Virginia, USA.

Kasal, B. 1992. “A Nonlinear Three-Dimensional Finite-Element Model of A Light-Frame Wood Structure”. Ph. D Dissertation, Dept. of Civil Engineering. Oregon State University, USA.

Kasal, B. and R. J. Leichti. 1992. “Nonlinear Finite-Element Model for Light-Frame Stud Walls”. Journal of Structural Engineering ASCE, 118(11), pp. 3122-3135.

Kasal, B. and R. J. Leichti. 1992. “Incorporating Load Sharing in Shear Wall Design of Light-Frame Structures”. Journal of Structural Engineering ASCE, 118(12), pp.

3350-3361.

Kasal, B., R. J. Leichti, and R. Y. Itani. 1994. “Nonlinear Finite-Element Model of Complete Light-Frame Wood Structures”. Journal of Structural Engineering ASCE, 120(1), pp. 100-119.

Kasal, B., and H. Xu. 1997. “A mathematical model of connections with nonlinear nonconservative hysteretic behavior.” Earthquake performance and safety of timber structures, G. C. Foliente, ed., Forest Products Society, Madison, Wis., 105–107.

Kasal, B., M. S. Collins, P. Paevere, and G. C. Foliente. 2005. “Design Models of Light-frame Wood Buildings under Lateral Loads”. Journal of Structural Engineering ASCE, 130(8), pp. 1263-1271

Kivell, B. T., P. J. Moss and A. J. Carr. 1981. “Hysteretic Modeling of Moment Resisting Nailed Timber Joints”. Bulletin of New Zealand Nat. Soc. For Earthquake Eng. 14(4), pp. 233-245

Kochkin, V., S. McKee, J. Crandell, E. Jenkins, A. Osborne, and K. Jackson. 2001. “Wood Shear Walls with Corners”. Report prepared for The U.S. Department of Housing and Urban Development Office of Policy Development and Research Washington, DC, National Association of Home Builders Washington, DC (Contract H-21172CA), NAHB Research Center, Inc. Upper Marlboro, MD.

Lam, F., H. G. L. Prion, and M. He. 1997. “Lateral Resistance of Wood Shear Walls with Large Sheathing Panels”. Journal of Structural Engineering ASCE, 123(12), pp. 1666-1673

van de Lindt, J. W. 2004. “Evolution of Wood Shear Wall Testing, Modeling, and Reliability Analysis: Bibliography”. Practice Periodical on Structural Design and Construction ASCE, 9(1), pp. 44-53

Loh, C. and R. Ho. 1990. “Seismic Damage Assessment Based on Different Hysteretic Rules”. Earthquake Engineering and Structural Dynamics 19, pp. 753-771

Lybanon, M. and K.C. Messa. 1999. Genetic algorithm model fitting. In: Practical Handbook of Genetic Algorithms. Complex Coding Systems. Volume III. Edited by L. D. Chambers. CRC Press, New York.

McKee, S., J. Crandell, R. Hicks, and L. Marchman. 1998. “The Performance of Perforated Shear Walls with Narrow Wall Segments, Reduced Base Restraint, and Alternative Framing Methods”. Report prepared for The U.S. Department of Housing and Urban Development Office of Policy Development and Research Washington, DC, National Association of Home Builders Housing Affordability Through Design Efficiency Program Washington, DC (Contract H-21065CA), NAHB Research Center, Inc. Upper Marlboro, MD.

Mosalam, K. M., C. Machado, K. Gliniorz, C. Naito, E. Kunkel, and S. A. Mahin. 2002. “Seismic Evaluation of an Asymmetric Three-Story Woodframe Building”. CUREE Publication No. W-19

Ni, C., E. Karacabeyli, and A. Ceccotti. 1998. “Design of Shear Walls with Openings under Lateral and Vertical Loads”. Paper prepared for PTEC`99, Draft v. 4, December 2

Ni, C., and E. Karacabeyli. 2000. “Effect of overturning restraint of performance of shear walls”. Proceedings of the world Conference on Timber Engineering. Whistler Resort, British Columbia, Canada.

Paevere, P. J., G. C. Foliente, and B. Kasal. 2003. “Load-sharing and Redistribution in a One-Story Woodframe Building”. Journal of Structural Engineering ASCE, 129(9), pp. 1275-1284

Paulay, T. 1997. “Displacement-based Design Approach to Earthquake-induced Torsion in Ductile Buildings”. Engineering Structures, 19(9), pp. 699-707

Polensek, A. and H. I. Laursen. 1984. “Seismic Behavior of Bending Components and Intercomponent Connections of Light-framed Wood Buildings”. Final Report to the National Science Foundation (Grant CEE-8104626), Dept. of Forest Products, Oregon State Univ., Corvallis, OR.

Salenikovich, A. J. 2000. “The Racking Performance of Light-Frame Shear Walls”. Ph. D Dissertation, Department of Wood Science and Forest Products. Virginia Polytechnic Institute and State University, Blacksburg, VA, USA

Smart, J. V. 2002. “Capacity Resistance and Performance of Single-Shear Bolted and Nailed Connections: An Experimental Investigation”. M.S Thesis, Dept. of Civil Engineering. Virginia Polytechnic Institute and State University, Blacksburg, Virginia, USA.

Sugiyama, H. and T. Matsumoto. 1994, Empirical Equations for the Estimation of Racking Strength of a Plywood Sheathed Shear Wall with Openings, Summary of Technical Papers Annul Meetings, Trans. Of A.I.J.

Tarabia, A. M. and R. Y. Itani. 1997. “Static and Dynamic Modeling of Light-Frame Wood Buildings”. Computers & Structures, 63(2), pp. 319-334

Tarabia, A. M. and R. Y. Itani. 1997. “Seismic Response of Light-Frame Wood Buildings”. Journal of Structural Engineering ASCE, 123(11), pp. 1470-1477

Tarabia, A. M. 1994. “Response of Light-frame Buildings due to earthquake loadings”. PhD Dissertation, Department of Civil and Environmental Engineering. Washington State

University, Pullman, Washington, USA

Toothman, A. J. 2003. “Monotonic and Cyclic Performance of Light-Frame Shear Walls with Various Sheathing Materials”. Master Thesis, Dept. of Wood Science and Forest Products. Virginia Polytechnic Institute and State University, Blacksburg, Virginia, USA

Wen, Y-K. 1976. “Method for Random Vibration of Hysteretic Systems”. Journal of the Engineering Mechanics Division ASCE 102(EM2). pp. 249-263

Wen, Y-K. 1980. “Equivalent Linearization for Hysteretic Systems under Random Excitation.” Journal of Applied Mechanics ASME. 47 pp. 150-154

APPENDIX A
Correlation Coefficient

The correlation coefficient, a concept from statistics, is a measure of how well trends in the predicted values follow trends in past actual values. It is a measure of how well the predicted values from a forecast model "fit" with the real-life data.

The correlation coefficient is a number between 0 and 1. If there is no relationship between the predicted values and the actual values the correlation coefficient is 0 or very low (the predicted values are no better than random numbers). As the strength of the relationship between the predicted values and actual values increases, so does the correlation coefficient. A perfect fit gives a coefficient of 1.0. Thus the higher the correlation coefficient the better.

Assume X and Y are a real-life data array and the corresponding predicted value array, respectively. The size of them is n.

The variances (ss_{xx}, ss_{yy}) and covariance (ss_{xy}) of X and Y are:

$$ss_{xx} = \sum_{i=1}^{n} (x_i - \bar{x})^2 \tag{A-1}$$

$$ss_{yy} = \sum_{i=1}^{n} (y_i - \bar{y})^2 \tag{A-2}$$

$$ss_{xy} = \sum_{i=1}^{n} (x_i - \bar{x})(y_i - \bar{y}) \tag{A-3}$$

For linear lease squares fitting, the coefficient b in

$$y = a + bx \tag{A-4}$$

is given by

$$b = \frac{ss_{xy}}{ss_{xx}} \tag{A-5}$$

and the coefficient *b’* in

$$x = a' + b' y \tag{A-6}$$

$$b' = \frac{ss_{xy}}{ss_{yy}} \tag{A-7}$$

The correlation coefficient *r* is then defined by

$$r = \sqrt{b \cdot b'} \tag{A-8}$$

APPENDIX B
Shear Wall Design for the Parametric Study

Group 2_1 (L:W=1:2, w/ perpendicular partition wall, w/o parallel partition wall)

Table B.1 Front Wall Design (Group 2_1)

Case		Total Length (ft)	Front/Back Ratio	Front Wall (east wall)							
				OSB Wall				Gypsum Wall			
				Length	w	dn	dh	Length	w	dn	dh
2	2_1_0	20	0	0.00	**0.000**	**N/A**	**N/A**	0.00	**0.000**	**N/A**	**N/A**
	2_1_25	20	0.25	4.00	**0.868**	**2.00E-06**	**1.06E-04**	4.00	**0.627**	**3.46E-04**	**2.15E-03**
	2_1_50	20	0.5	6.67	**1.121**	**1.20E-06**	**6.36E-05**	6.67	**0.809**	**2.08E-04**	**1.29E-03**
	2_1_75	20	0.75	8.57	**1.271**	**9.33E-07**	**4.95E-05**	8.57	**0.918**	**1.61E-04**	**1.00E-03**
	2_1_100	20	1	10.00	**1.372**	**8.00E-07**	**4.24E-05**	10.00	**0.991**	**1.38E-04**	**8.59E-04**

Table B.2 Back Wall Design (Group 2_1)

Case		Total Length (ft)	Front/Back Ratio	Back Wall (west wall)							
				OSB Wall				Gypsum Wall			
				Length	w	dn	dh	Length	w	dn	dh
2	2_1_0	20	0	20.00	**1.941**	**4.00E-07**	**2.12E-05**	20.00	**1.402**	**6.92E-05**	**4.29E-04**
	2_1_25	20	0.25	16.00	**1.736**	**5.00E-07**	**2.65E-05**	16.00	**1.254**	**8.65E-05**	**5.37E-04**
	2_1_50	20	0.5	13.33	**1.585**	**6.00E-07**	**3.18E-05**	13.33	**1.145**	**1.04E-04**	**6.44E-04**
	2_1_75	20	0.75	11.43	**1.467**	**7.00E-07**	**3.71E-05**	11.43	**1.060**	**1.21E-04**	**7.51E-04**
	2_1_100	20	1	10.00	**1.372**	**8.00E-07**	**4.24E-05**	10.00	**0.991**	**1.38E-04**	**8.59E-04**

Table B.3 Perpendicular Wall Design (Group 2_1)

Case		Total Length (ft)	Front/Back Ratio	Perpendicular Wall							
				OSB Wall				Gypsum Wall			
				Length	w	dn	dh	Length	w	dn	dh
1	2_1_0	20	0	10.00	**1.372**	**8.00E-07**	**4.24E-05**	10.00	**0.991**	**1.38E-04**	**8.59E-04**
	2_1_25	20	0.25	10.00	**1.372**	**8.00E-07**	**4.24E-05**	10.00	**0.991**	**1.38E-04**	**8.59E-04**
	2_1_50	20	0.5	10.00	**1.372**	**8.00E-07**	**4.24E-05**	10.00	**0.991**	**1.38E-04**	**8.59E-04**
	2_1_75	20	0.75	10.00	**1.372**	**8.00E-07**	**4.24E-05**	10.00	**0.991**	**1.38E-04**	**8.59E-04**
	2_1_100	20	1	10.00	**1.372**	**8.00E-07**	**4.24E-05**	10.00	**0.991**	**1.38E-04**	**8.59E-04**

Length of the perpendicular partition wall is 16 ft. The corresponding values of **w**, **dn**, **dh** are 1.773, 4.33E-5, and 2.68E-4 respectively.

Group 2_2 (L:W=1:2, w/ perpendicular partition wall, w/ parallel partition wall)

Length of the additional parallel partition wall is 32 ft. The corresponding values of **w**, **dn**, **dh** are 2.508, 2.16E-5, and 1.34E-4 respectively.

Group 3_1 (L:W=1:3, w/ perpendicular partition wall, w/o parallel partition wall)

Table B.4 Front Wall Design (Group 3_1)

Case		Total Length (ft)	Front/Back Ratio	Front Wall (east wall)							
				OSB Wall				Gypsum Wall			
				Length	**w**	**dn**	**dh**	Length	**w**	**dn**	**dh**
3	3_1_0	30	0	0.00	**0.000**	**N/A**	**N/A**	0.00	**0.000**	**N/A**	**N/A**
	3_1_25	30	0.25	6.00	**1.063**	**1.33E-06**	**7.07E-05**	6.00	**0.768**	**2.31E-04**	**1.43E-03**
	3_1_50	30	0.5	10.00	**1.372**	**8.00E-07**	**4.24E-05**	10.00	**0.991**	**1.38E-04**	**8.59E-04**
	3_1_75	30	0.75	12.86	**1.556**	**6.22E-07**	**3.30E-05**	12.86	**1.124**	**1.08E-04**	**6.68E-04**
	3_1_100	30	1	15.00	**1.681**	**5.33E-07**	**2.83E-05**	15.00	**1.214**	**9.23E-05**	**5.73E-04**

Table B.5 Back Wall Design (Group 3_1)

Case		Total Length (ft)	Front/Back Ratio	Back Wall (west wall)							
				OSB Wall				Gypsum Wall			
				Length	**w**	**dn**	**dh**	Length	**w**	**dn**	**dh**
3	3_1_0	30	0	30.00	**2.377**	**2.67E-07**	**1.41E-05**	30.00	**1.717**	**4.61E-05**	**2.86E-04**
	3_1_25	30	0.25	24.00	**2.126**	**3.33E-07**	**1.77E-05**	24.00	**1.536**	**5.77E-05**	**3.58E-04**
	3_1_50	30	0.5	20.00	**1.941**	**4.00E-07**	**2.12E-05**	20.00	**1.402**	**6.92E-05**	**4.29E-04**
	3_1_75	30	0.75	17.14	**1.797**	**4.67E-07**	**2.47E-05**	17.14	**1.298**	**8.07E-05**	**5.01E-04**
	3_1_100	30	1	15.00	**1.681**	**5.33E-07**	**2.83E-05**	15.00	**1.214**	**9.23E-05**	**5.73E-04**

Table B.6 Perpendicular Wall Design (Group 3_1)

Case		Total Length (ft)	Front/Back Ratio	Perpendicular Wall							
				OSB Wall				Gypsum Wall			
				Length	**w**	**dn**	**dh**	Length	**w**	**dn**	**dh**
3	3_1_0	30	0	15.00	**1.681**	**5.33E-07**	**2.83E-05**	15.00	**1.214**	**9.23E-05**	**5.73E-04**
	3_1_25	30	0.25	15.00	**1.681**	**5.33E-07**	**2.83E-05**	15.00	**1.214**	**9.23E-05**	**5.73E-04**
	3_1_50	30	0.5	15.00	**1.681**	**5.33E-07**	**2.83E-05**	15.00	**1.214**	**9.23E-05**	**5.73E-04**
	3_1_75	30	0.75	15.00	**1.681**	**5.33E-07**	**2.83E-05**	15.00	**1.214**	**9.23E-05**	**5.73E-04**
	3_1_100	30	1	15.00	**1.681**	**5.33E-07**	**2.83E-05**	15.00	**1.214**	**9.23E-05**	**5.73E-04**

Length of the perpendicular partition wall is 16 ft. The corresponding values of **w, dn, dh** are 1.773, 4.33E-5, and 2.68E-4 respectively.

Group 3_2 (L:W=1:3, w/ perpendicular partition wall, w/ parallel partition wall)

Length of the additional parallel partition wall is 48 ft. The corresponding values of **w, dn, dh** are 3.072, 1.44E-5, and 8.95E-5 respectively.

Group 4_1 (L:W=2:1, w/o partition wall)

Table B.7 Front Wall Design (Group 4_1)

Case		Total Length (ft)	Front/Back Ratio	Front Wall (east wall)							
				OSB Wall				Gypsum Wall			
				Length	**w**	**dn**	**dh**	Length	**w**	**dn**	**dh**
4	4_1_0	20	0	0.00	**0.000**	**N/A**	**N/A**	0.00	**0.000**	**N/A**	**N/A**
	4_1_25	20	0.25	4.00	**0.868**	**2.00E-06**	**1.06E-04**	4.00	**0.627**	**3.46E-04**	**2.15E-03**
	4_1_50	20	0.5	6.67	**1.121**	**1.20E-06**	**6.36E-05**	6.67	**0.809**	**2.08E-04**	**1.29E-03**
	4_1_75	20	0.75	8.57	**1.271**	**9.33E-07**	**4.95E-05**	8.57	**0.918**	**1.61E-04**	**1.00E-03**
	4_1_100	20	1	10.00	**1.372**	**8.00E-07**	**4.24E-05**	10.00	**0.991**	**1.38E-04**	**8.59E-04**

Table B.8 Back Wall Design (Group 4_1)

Case		Total Length (ft)	Front/Back Ratio	Back Wall (west wall)							
				OSB Wall				Gypsum Wall			
				Length	w	dn	dh	Length	w	dn	dh
4	4_1_0	20	0	20.00	**1.941**	**4.00E-07**	**2.12E-05**	20.00	**1.402**	**6.92E-05**	**4.29E-04**
	4_1_25	20	0.25	16.00	**1.736**	**5.00E-07**	**2.65E-05**	16.00	**1.254**	**8.65E-05**	**5.37E-04**
	4_1_50	20	0.5	13.33	**1.585**	**6.00E-07**	**3.18E-05**	13.33	**1.145**	**1.04E-04**	**6.44E-04**
	4_1_75	20	0.75	11.43	**1.467**	**7.00E-07**	**3.71E-05**	11.43	**1.060**	**1.21E-04**	**7.51E-04**
	4_1_100	20	1	10.00	**1.372**	**8.00E-07**	**4.24E-05**	10.00	**0.991**	**1.38E-04**	**8.59E-04**

Table B.9 Perpendicular Wall Design (Group 4_1)

Case		Total Length (ft)	Front/Back Ratio	Perpendicular Wall							
				OSB Wall				Gypsum Wall			
				Length	w	dn	dh	Length	w	dn	dh
4	4_1_0	20	0	10.00	**1.372**	**8.00E-07**	**4.24E-05**	10.00	**0.991**	**1.38E-04**	**8.59E-04**
	4_1_25	20	0.25	10.00	**1.372**	**8.00E-07**	**4.24E-05**	10.00	**0.991**	**1.38E-04**	**8.59E-04**
	4_1_50	20	0.5	10.00	**1.372**	**8.00E-07**	**4.24E-05**	10.00	**0.991**	**1.38E-04**	**8.59E-04**
	4_1_75	20	0.75	10.00	**1.372**	**8.00E-07**	**4.24E-05**	10.00	**0.991**	**1.38E-04**	**8.59E-04**
	4_1_100	20	1	10.00	**1.372**	**8.00E-07**	**4.24E-05**	10.00	**0.991**	**1.38E-04**	**8.59E-04**

Group 4_2 (L:W=2:1, w/ parallel partition wall)

Length of the additional parallel partition wall is 16 ft. The corresponding values of **w, dn, dh** are 1.773, 4.33E-5, and 2.68E-4 respectively.

Group 5_1 (L:W=3:1, w/o partition wall)

Table B.10 Front Wall Design (Group 5_1)

Case		Total Length (ft)	Front/Back Ratio	Front Wall (east wall)							
				OSB Wall				Gypsum Wall			
				Length	w	dn	dh	Length	w	dn	dh
5	5_1_0	30	0	0.00	**0.000**	**N/A**	**N/A**	0.00	**0.000**	**N/A**	**N/A**
	5_1_25	30	0.25	6.00	**1.063**	**1.33E-06**	**7.07E-05**	6.00	**0.768**	**2.31E-04**	**1.43E-03**
	5_1_50	30	0.5	10.00	**1.372**	**8.00E-07**	**4.24E-05**	10.00	**0.991**	**1.38E-04**	**8.59E-04**
	5_1_75	30	0.75	12.86	**1.556**	**6.22E-07**	**3.30E-05**	12.86	**1.124**	**1.08E-04**	**6.68E-04**
	5_1_100	30	1	15.00	**1.681**	**5.33E-07**	**2.83E-05**	15.00	**1.214**	**9.23E-05**	**5.73E-04**

Table B.11 Back Wall Design (Group 5_1)

Case		Total Length (ft)	Front/Back Ratio	Back Wall (west wall)							
				OSB Wall				Gypsum Wall			
				Length	w	dn	dh	Length	w	dn	dh
5	5_1_0	30	0	30.00	**2.377**	**2.67E-07**	**1.41E-05**	30.00	**1.717**	**4.61E-05**	**2.86E-04**
	5_1_25	30	0.25	24.00	**2.126**	**3.33E-07**	**1.77E-05**	24.00	**1.536**	**5.77E-05**	**3.58E-04**
	5_1_50	30	0.5	20.00	**1.941**	**4.00E-07**	**2.12E-05**	20.00	**1.402**	**6.92E-05**	**4.29E-04**
	5_1_75	30	0.75	17.14	**1.797**	**4.67E-07**	**2.47E-05**	17.14	**1.298**	**8.07E-05**	**5.01E-04**
	5_1_100	30	1	15.00	**1.681**	**5.33E-07**	**2.83E-05**	15.00	**1.214**	**9.23E-05**	**5.73E-04**

Table B.12 Perpendicular Wall Design (Group 5_1)

Case		Total Length (ft)	Front/Back Ratio	Perpendicular Wall							
				OSB Wall				Gypsum Wall			
				Length	w	dn	dh	Length	w	dn	dh
5	5_1_0	30	0	15.00	**1.681**	**5.33E-07**	**2.83E-05**	15.00	**1.214**	**9.23E-05**	**5.73E-04**
	5_1_25	30	0.25	15.00	**1.681**	**5.33E-07**	**2.83E-05**	15.00	**1.214**	**9.23E-05**	**5.73E-04**
	5_1_50	30	0.5	15.00	**1.681**	**5.33E-07**	**2.83E-05**	15.00	**1.214**	**9.23E-05**	**5.73E-04**
	5_1_75	30	0.75	15.00	**1.681**	**5.33E-07**	**2.83E-05**	15.00	**1.214**	**9.23E-05**	**5.73E-04**
	5_1_100	30	1	15.00	**1.681**	**5.33E-07**	**2.83E-05**	15.00	**1.214**	**9.23E-05**	**5.73E-04**

Group 5_2 (L:W=3:1, w/ parallel partition wall)

Length of the additional parallel partition wall is 16 ft. The corresponding values of **w, dn, dh** are 1.773, 4.33E-5, and 2.68E-4 respectively.

APPENDIX C
Results of the Parametric Study

Group 2_1 (L:W=1:2, w/ perpendicular partition wall, w/o parallel partition wall)

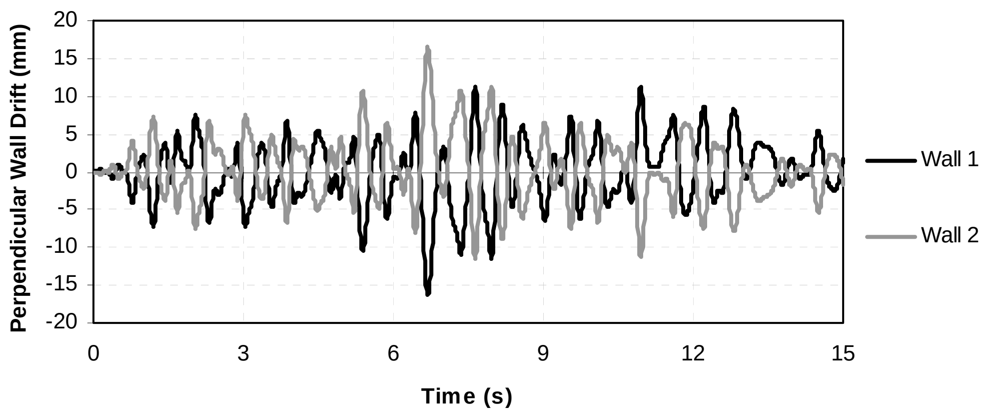

Figure C.1 Drifts of Perpendicular Walls (Case 2_1_0)

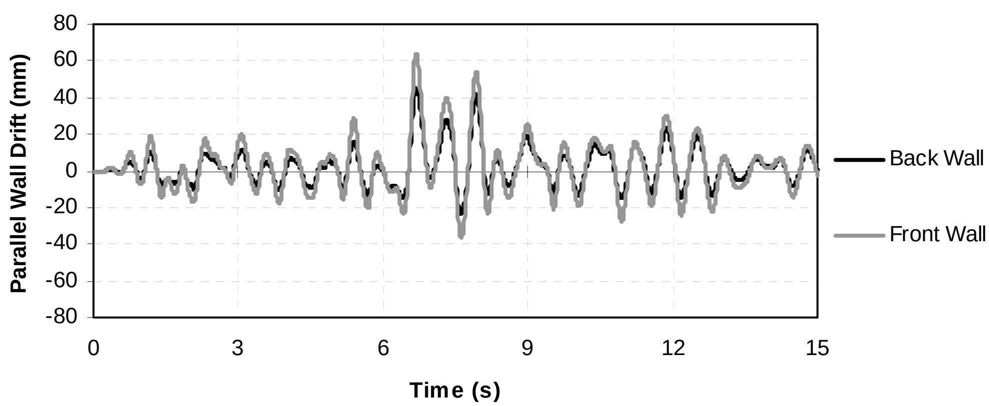

Figure C.2 Drifts of Parallel Walls (Case 2_1_0)

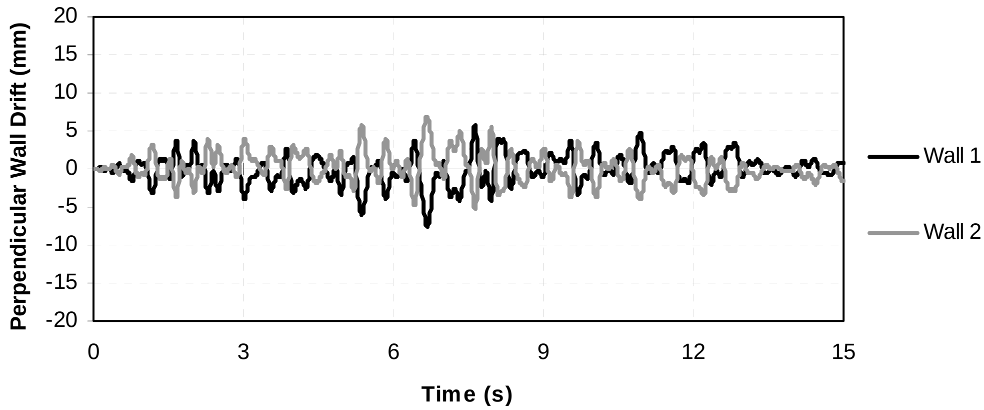

Figure C.3 Drifts of Perpendicular Walls (Case 2_1_25)

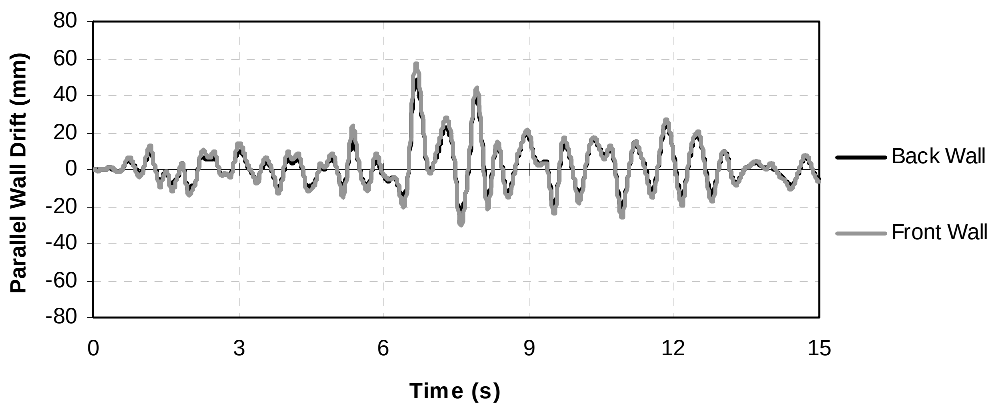

Figure C.4 Drifts of Parallel Walls (Case 2_1_25)

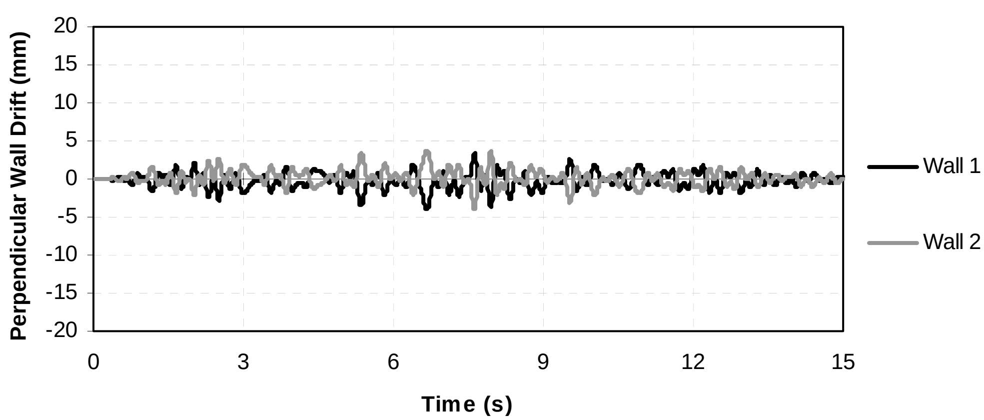

Figure C.5 Drifts of Perpendicular Walls (Case 2_1_50)

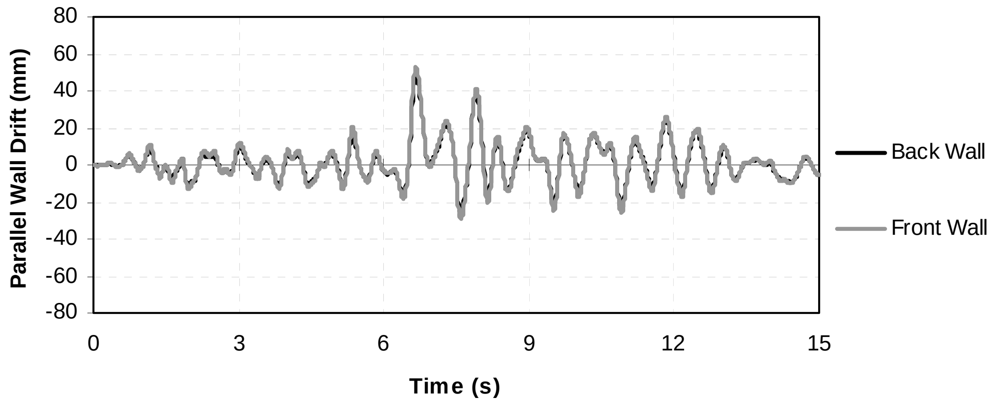

Figure C.6 Drifts of Parallel Walls (Case 2_1_50)

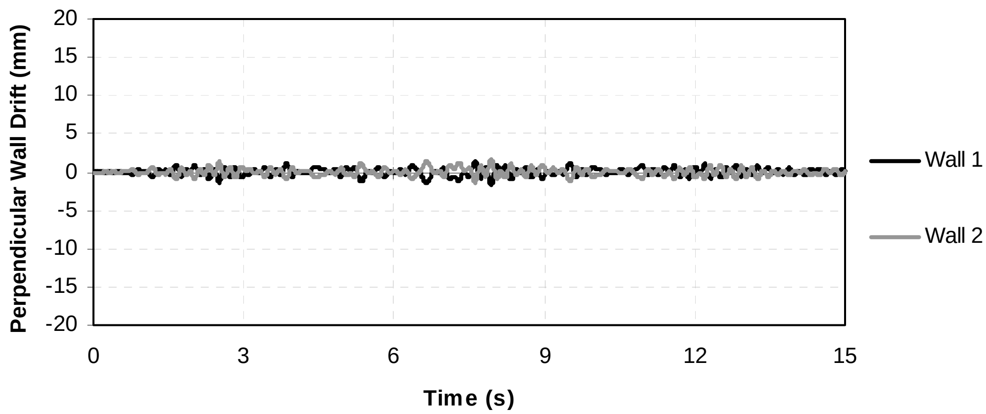

Figure C.7 Drifts of Perpendicular Walls (Case 2_1_75)

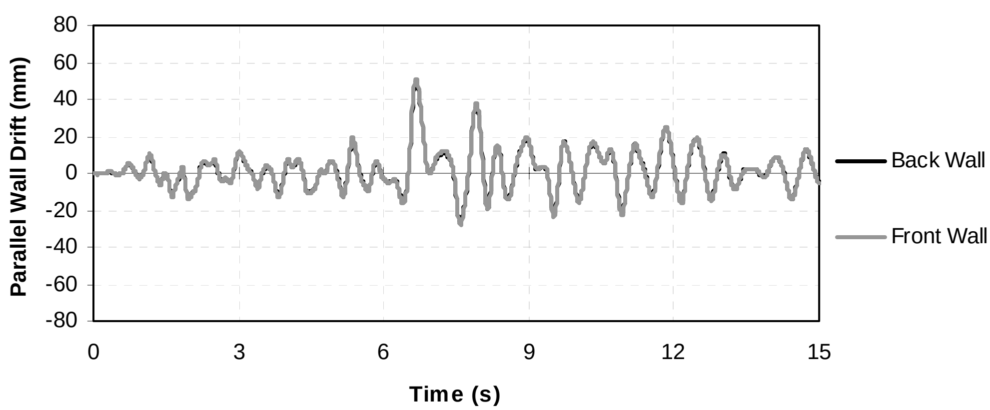

Figure C.8 Drifts of Parallel Walls (Case 2_1_75)

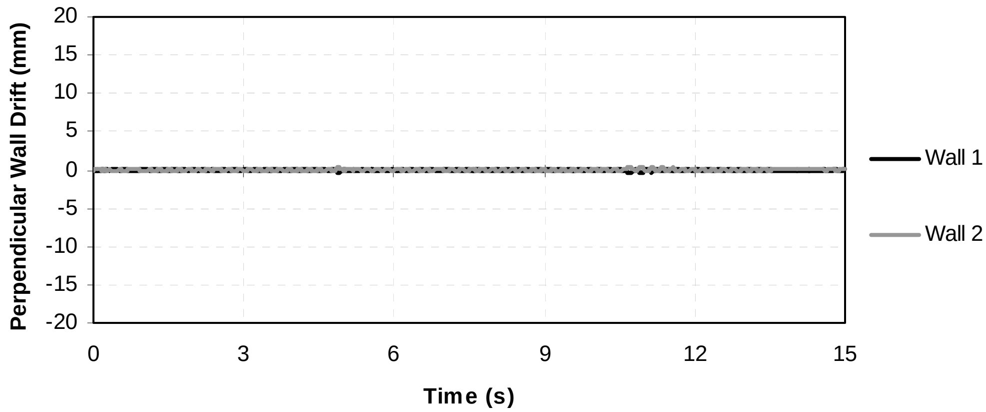

Figure C.9 Drifts of Perpendicular Walls (Case 2_1_100)

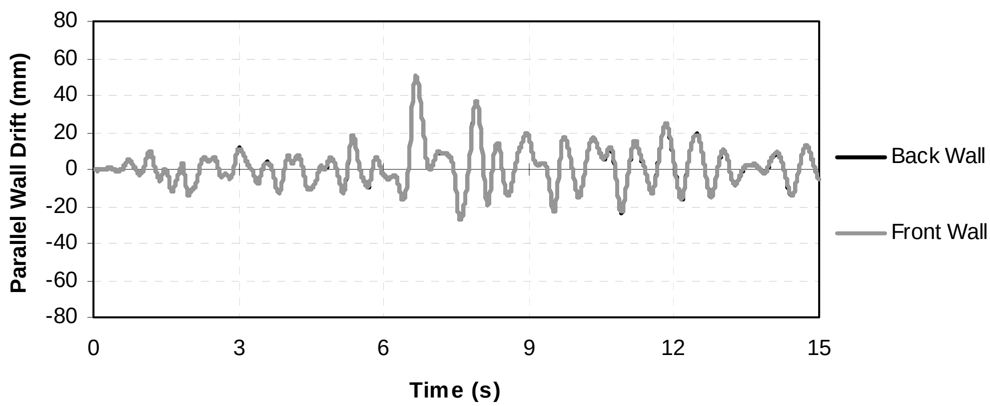

Figure C.10 Drifts of Parallel Walls (Case 2_1_100)

Table C.1 Peak Drifts of the Shear Walls (Group 2_1)

Front/Back Wall ratio (%)	Peak Perpendicular Wall Drift (mm)						Peak Parallel Wall Drift (mm)					
	Wall 1			Wall 2			Back Wall			Front Wall		
	+	-	MAX	+	-	MAX	+	-	MAX	+	-	MAX
0	11.31	-16.40	**16.40**	16.49	-11.46	**16.49**	44.70	-23.25	**44.70**	64.04	-36.73	**64.04**
25	5.69	-7.61	**7.61**	6.87	-5.28	**6.87**	48.12	-24.36	**48.12**	57.00	-30.63	**57.00**
50	3.31	-3.92	**3.92**	3.81	-3.92	**3.92**	47.57	-25.39	**47.57**	52.44	-29.44	**52.44**
75	1.48	-1.69	**1.69**	1.67	-1.35	**1.67**	49.24	-26.17	**49.24**	50.98	-27.59	**50.98**
100	0.19	-0.44	**0.44**	0.46	-0.22	**0.46**	50.23	-27.50	**50.23**	50.30	-27.38	**50.30**

Table C.2 Peak Imposed Loads and Load Ratios in the Shear Walls (Group 2_1)

Front/Back Wall ratio (%)	Peak Perpendicular Imposed Loads (kN)								Peak Parallel Imposed Loads (kN)							
	Wall 1				Wall 2				Back Wall				Front Wall			
	+	-	MAX	Load Ratio	+	-	MAX	Load Ratio	+	-	MAX	Load Ratio	+	-	MAX	Load Ratio
0	26.48	-23.20	**26.48**	**1.80**	23.11	-26.61	**26.61**	**1.81**	63.23	-75.46	**75.46**	**2.56**	0.00	0.00	**0.00**	**N/A**
25	14.97	-14.56	**14.97**	**1.02**	14.01	-15.33	**15.33**	**1.04**	49.93	-61.07	**61.07**	**2.59**	13.20	-15.59	**15.59**	**2.65**
50	8.80	-9.07	**9.07**	**0.62**	9.29	-9.28	**9.29**	**0.63**	42.21	-51.72	**51.72**	**2.63**	21.74	-25.59	**25.59**	**2.61**
75	4.49	-3.75	**4.49**	**0.30**	3.63	-4.27	**4.27**	**0.29**	32.62	-43.53	**43.53**	**2.59**	26.55	-32.77	**32.77**	**2.6**
100	1.20	-0.63	**1.20**	**0.08**	0.69	-1.26	**1.26**	**0.09**	29.60	-38.16	**38.16**	**2.59**	29.77	-38.17	**38.17**	**2.59**

Group 2_2 (L:W=1:2, w/ perpendicular partition wall, w/ parallel partition wall)

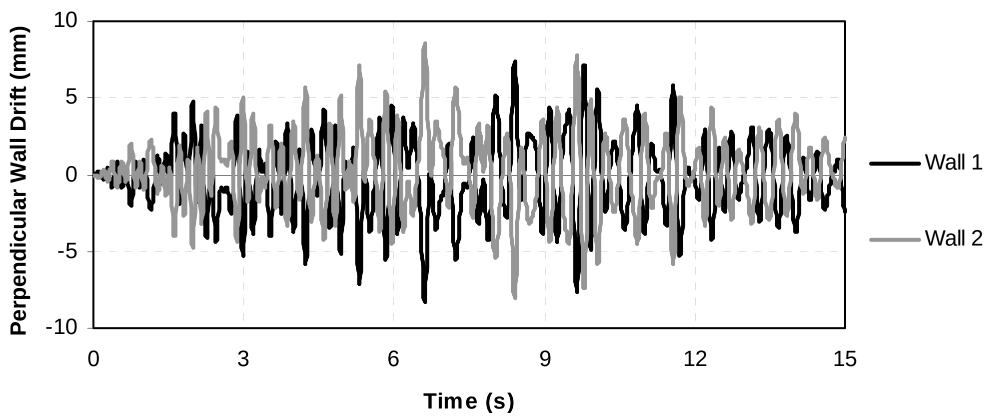

Figure C.11 Drifts of Perpendicular Walls (Case 2_2_0)

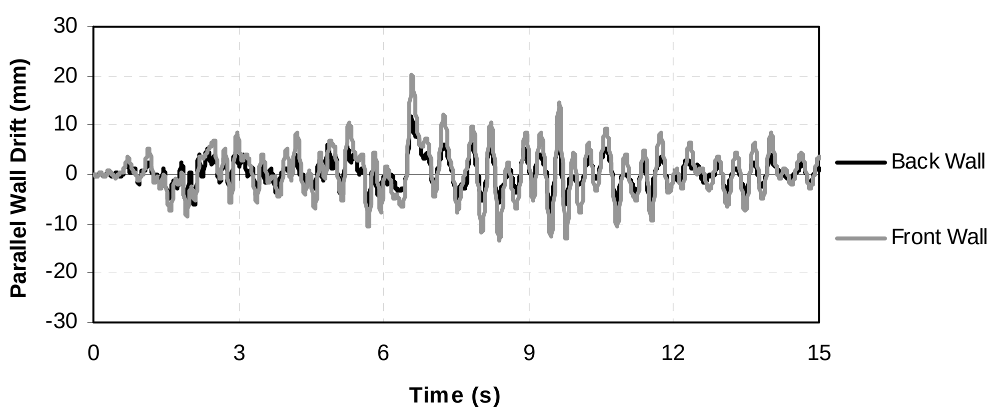

Figure C.12 Drifts of Parallel Walls (Case 2_2_0)

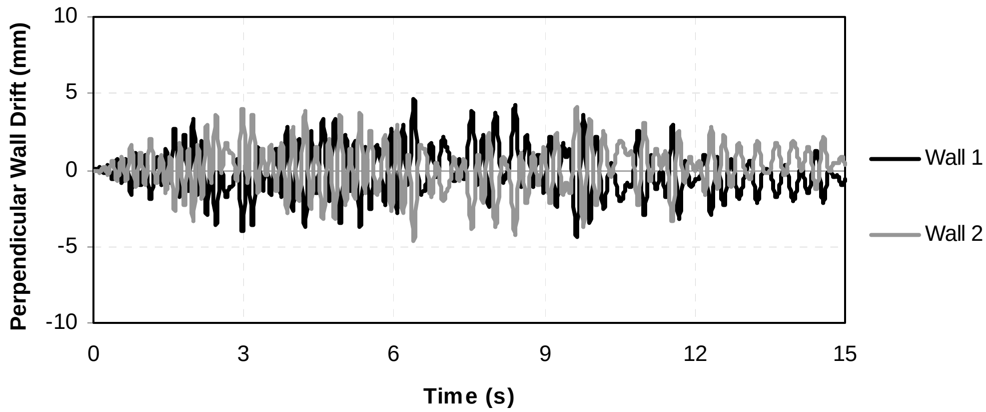

Figure C.13 Drifts of Perpendicular Walls (Case 2_2_25)

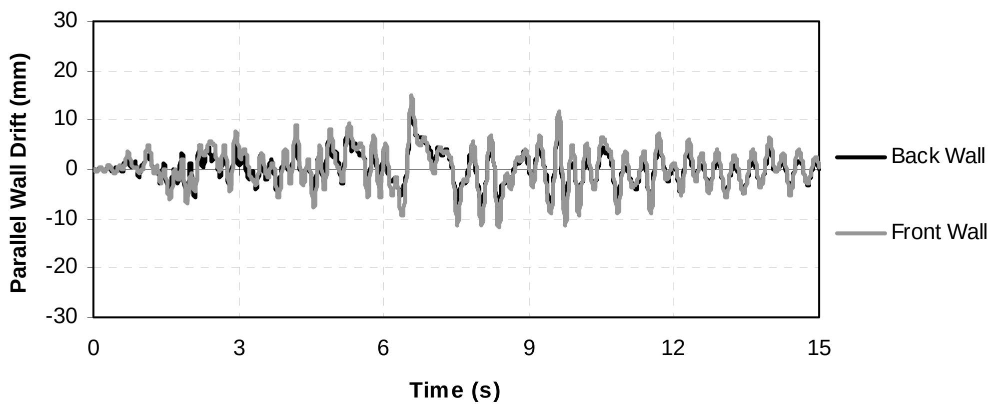

Figure C.14 Drifts of Parallel Walls (Case 2_2_25)

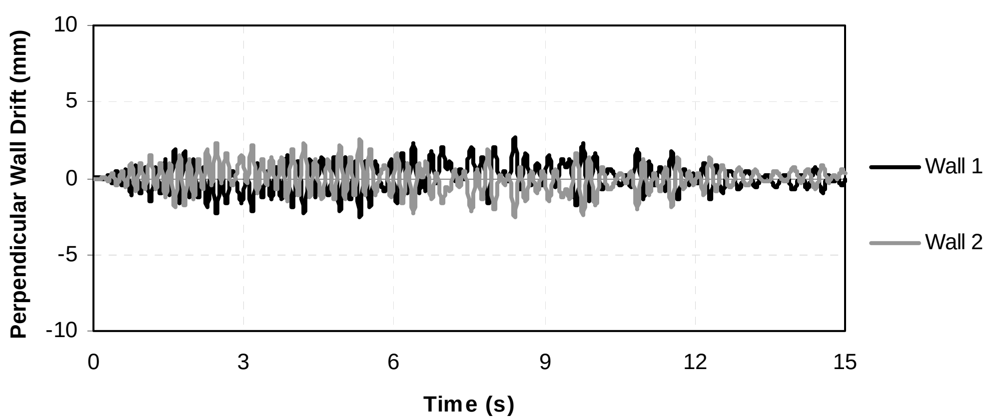

Figure C.15 Drifts of Perpendicular Walls (Case 2_2_50)

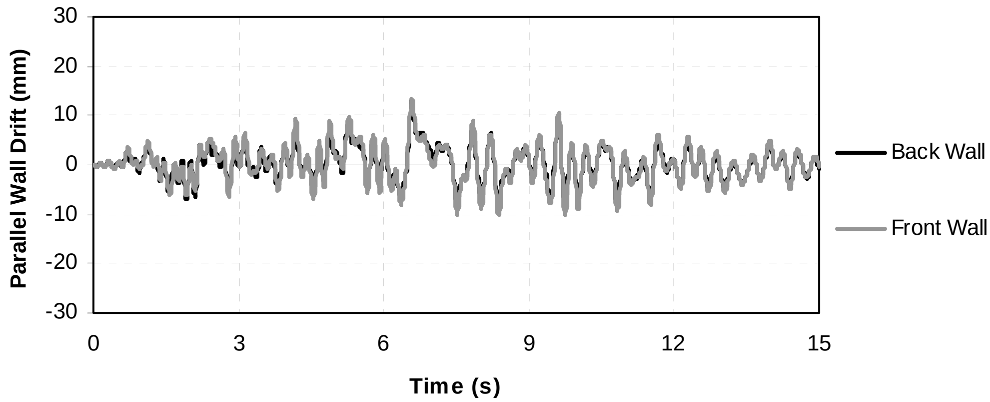

Figure C.16 Drifts of Parallel Walls (Case 2_2_50)

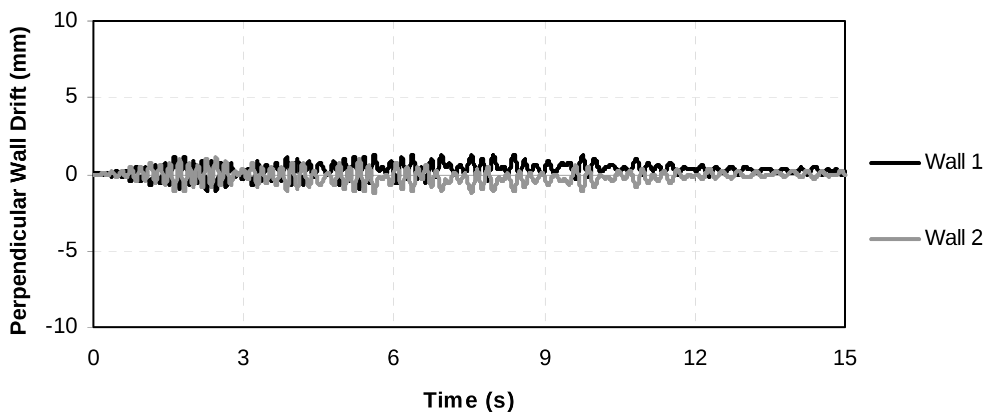

Figure C.17 Drifts of Perpendicular Walls (Case 2_2_75)

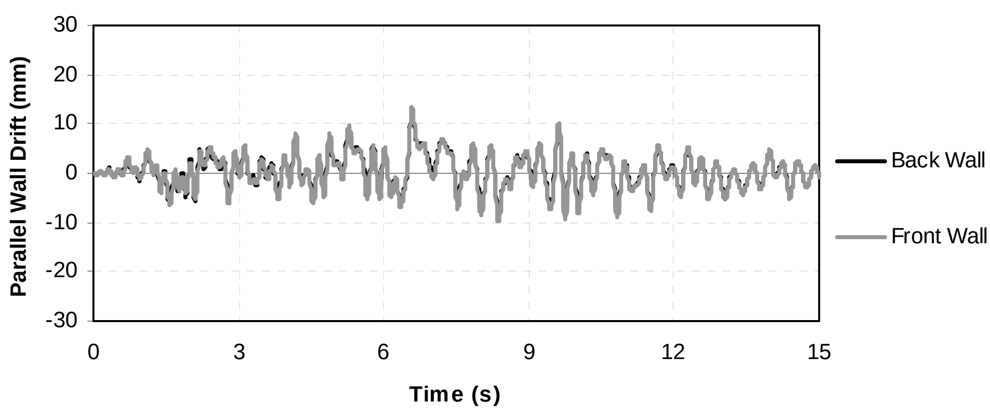

Figure C.18 Drifts of Parallel Walls (Case 2_2_75)

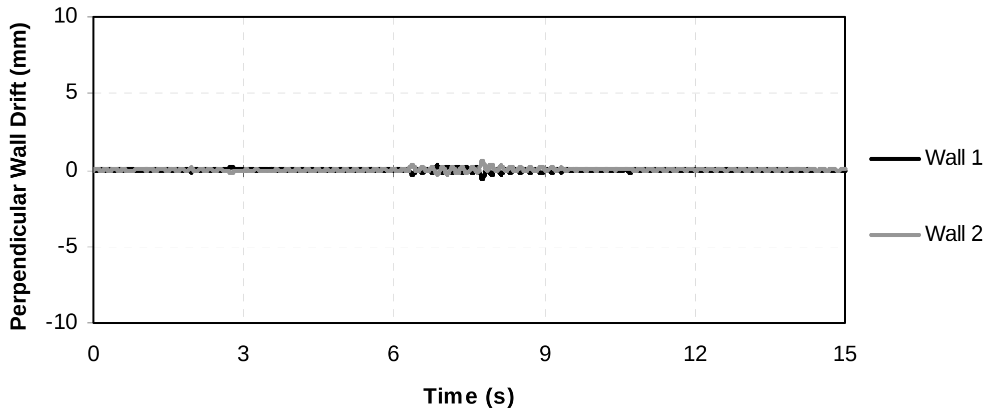

Figure C.19 Drifts of Perpendicular Walls (Case 2_2_100)

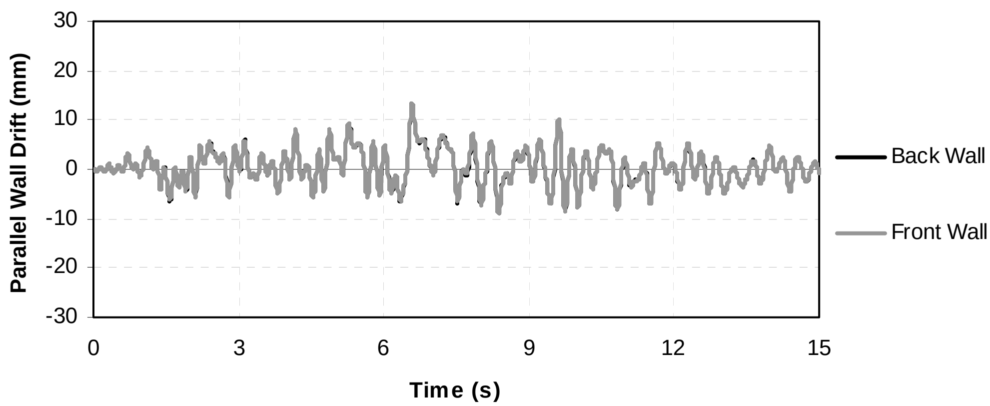

Figure C.20 Drifts of Parallel Walls (Case 2_2_100)

Table C.3 Peak Drifts of the Shear Walls (Group 2_2)

Front/Back Wall ratio (%)	Peak Perpendicular Wall Drift (mm)						Peak Parallel Wall Drift (mm)					
	Wall 1			Wall 2			Back Wall			Front Wall		
	+	-	MAX	+	-	MAX	+	-	MAX	+	-	MAX
0	7.35	-8.27	**8.27**	8.55	-8.06	**8.55**	11.70	-7.68	**11.70**	20.28	-13.44	**20.28**
25	4.67	-4.38	**4.67**	4.09	-4.66	**4.66**	12.57	-8.07	**12.57**	14.92	-11.87	**14.92**
50	2.64	-2.60	**2.64**	2.60	-2.50	**2.60**	12.81	-7.93	**12.81**	13.55	-10.29	**13.55**
75	1.25	-1.11	**1.25**	1.10	-1.22	**1.22**	13.21	-8.64	**13.21**	13.33	-9.90	**13.33**
100	0.28	-0.62	**0.62**	0.60	-0.29	**0.60**	13.32	-8.81	**13.32**	13.54	-8.74	**13.54**

Table C.4 Peak Imposed Loads and Load Ratios in the Shear Walls (Group 2_2)

Front/Back Wall ratio (%)	Peak Perpendicular Imposed Loads (kN)								Peak Parallel Imposed Loads (kN)							
	Wall 1				Wall 2				Back Wall				Front Wall			
	+	-	MAX	Load Ratio	+	-	MAX	Load Ratio	+	-	MAX	Load Ratio	+	-	MAX	Load Ratio
0	16.25	-15.79	**16.25**	**1.10**	15.71	-15.50	**15.71**	**1.07**	29.56	-42.56	**42.56**	**1.45**	0.00	0.00	**0.00**	**N/A**
25	9.50	-9.62	**9.62**	**0.65**	9.51	-9.48	**9.51**	**0.65**	23.91	-36.13	**36.13**	**1.53**	8.15	-10.48	**10.48**	**1.78**
50	6.00	-5.38	**6.00**	**0.41**	5.30	-6.03	**6.03**	**0.41**	20.87	-31.32	**31.32**	**1.6**	12.52	-15.87	**15.87**	**1.62**
75	3.48	-2.98	**3.48**	**0.24**	2.98	-3.49	**3.49**	**0.24**	19.35	-26.55	**26.55**	**1.58**	15.41	-19.99	**19.99**	**1.58**
100	1.75	-0.81	**1.75**	**0.12**	0.85	-1.69	**1.69**	**0.11**	17.34	-23.46	**23.46**	**1.59**	17.19	-23.17	**23.17**	**1.57**

Group 3_1 (L:W=1:3, w/ perpendicular partition wall, w/o parallel partition wall)

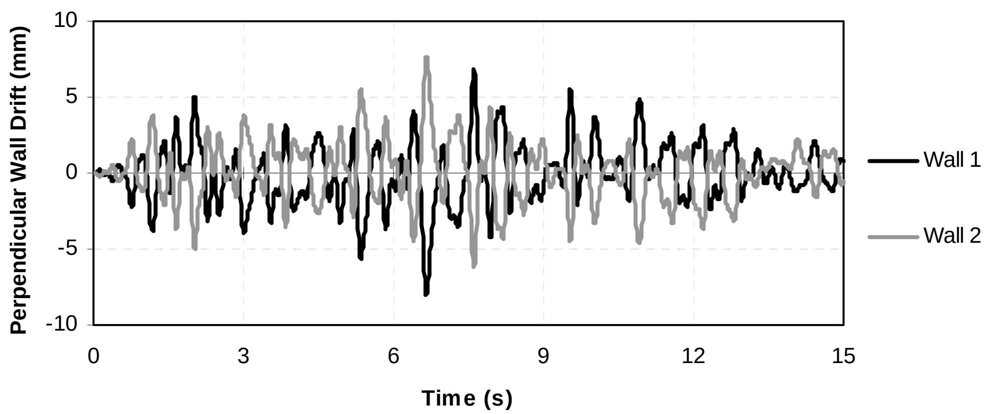

Figure C.21 Drifts of Perpendicular Walls (Case 3_1_0)

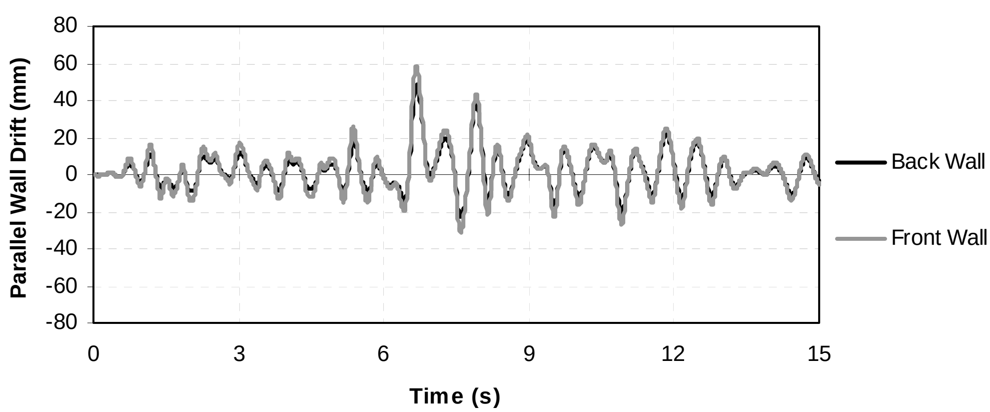

Figure C.22 Drifts of Parallel Walls (Case 3_1_0)

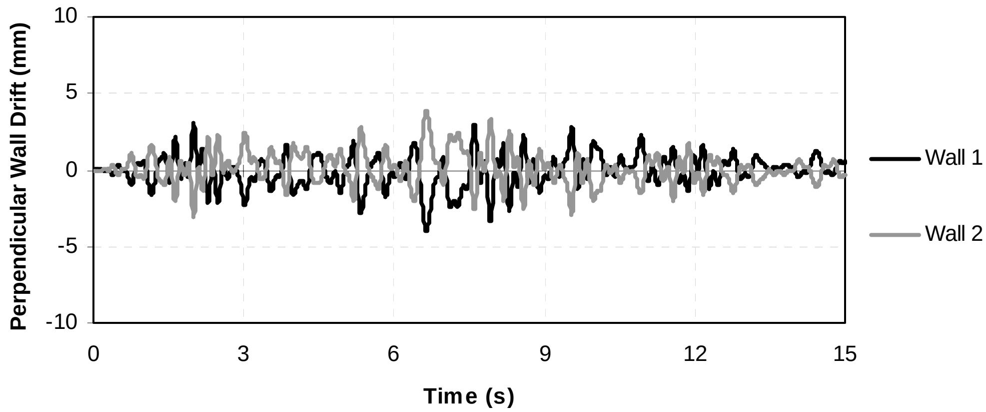

Figure C.23 Drifts of Perpendicular Walls (Case 3_1_25)

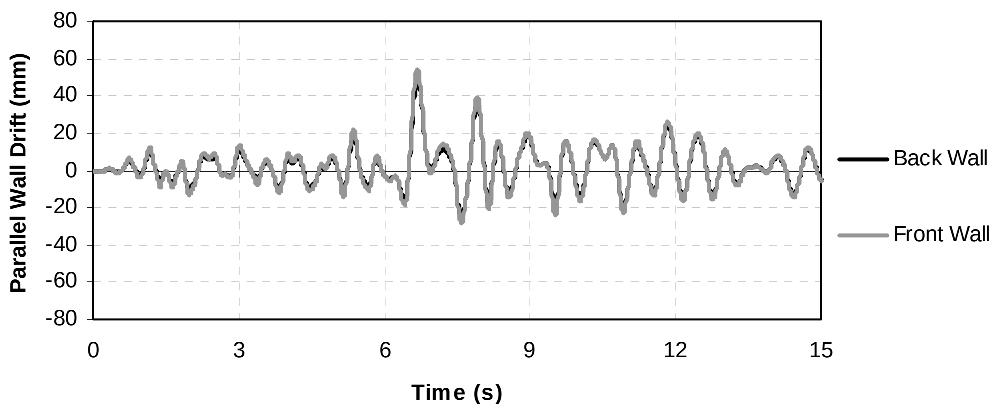

Figure C.24 Drifts of Parallel Walls (Case 3_1_25)

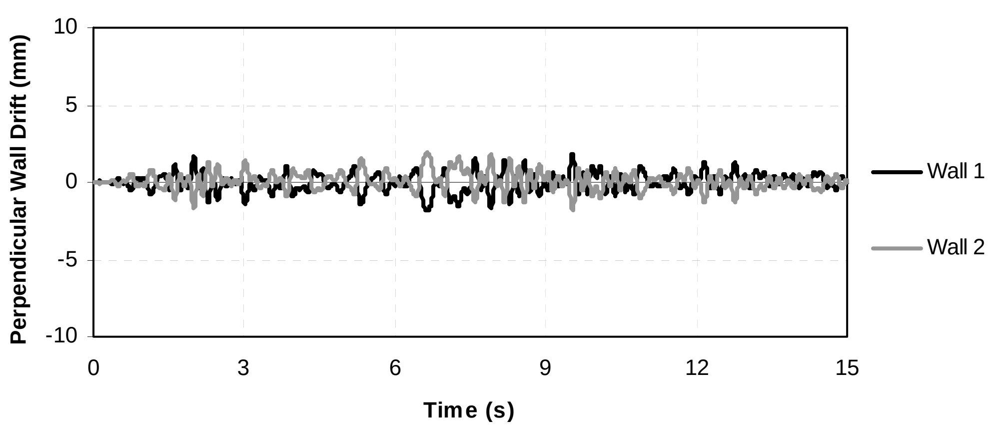

Figure C.25 Drifts of Perpendicular Walls (Case 3_1_50)

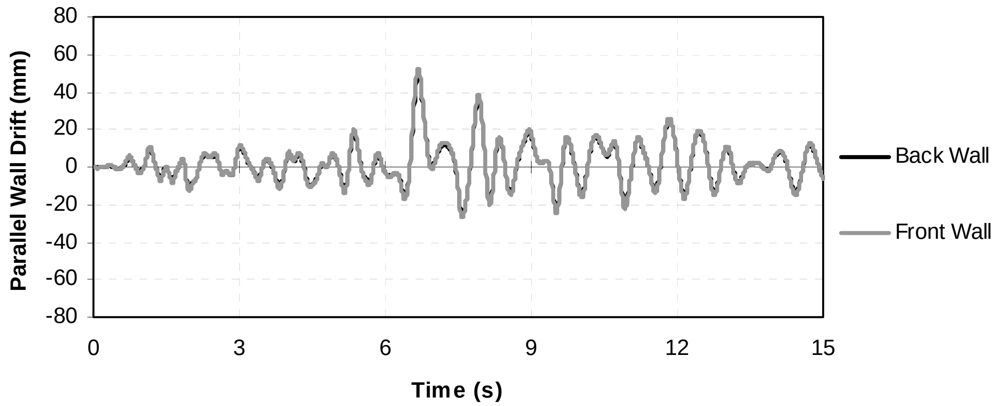

Figure C.26 Drifts of Parallel Walls (Case 3_1_50)

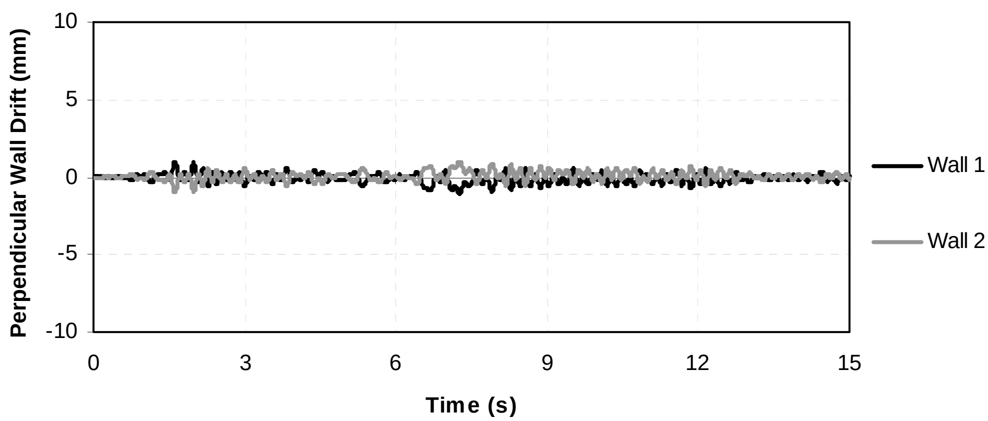

Figure C.27 Drifts of Perpendicular Walls (Case 3_1_75)

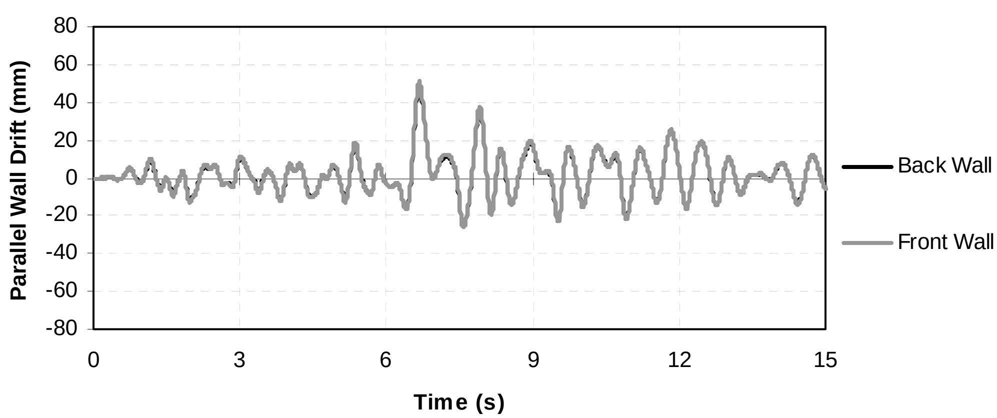

Figure C.28 Drifts of Parallel Walls (Case 3_1_75)

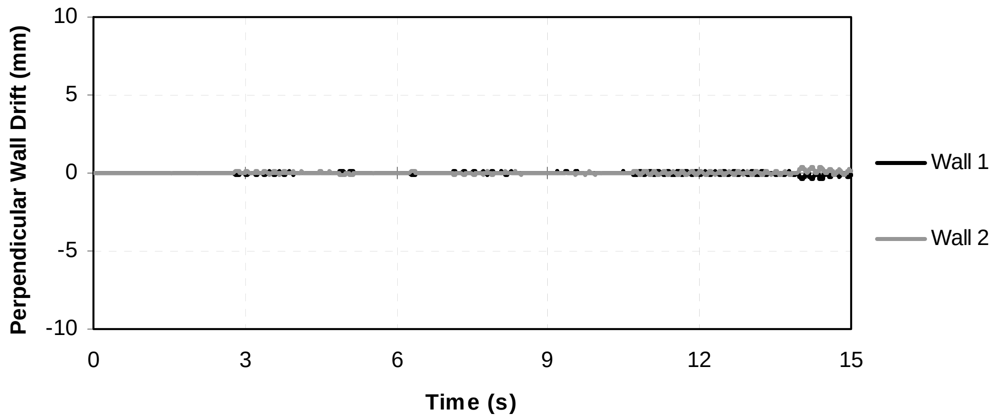

Figure C.29 Drifts of Perpendicular Walls (Case 3_1_100)

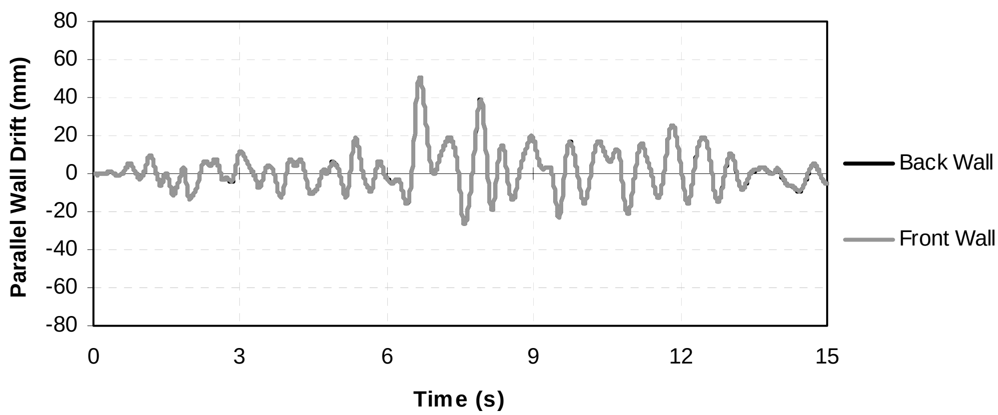

Figure C.30 Drifts of Parallel Walls (Case 3_1_100)

Table C.5 Peak Drifts of the Shear Walls (Group 3_1)

Front/Back Wall ratio (%)	Peak Perpendicular Wall Drift (mm)						Peak Parallel Wall Drift (mm)					
	Wall 1			Wall 2			Back Wall			Front Wall		
	+	-	MAX	+	-	MAX	+	-	MAX	+	-	MAX
0	6.85	-8.02	**8.02**	7.66	-6.22	**7.66**	48.34	-22.95	**48.34**	58.17	-31.15	**58.17**
25	3.08	-4.03	**4.03**	3.89	-3.05	**3.89**	48.95	-24.52	**48.95**	54.36	-28.36	**54.36**
50	1.86	-1.88	**1.88**	1.89	-1.80	**1.89**	49.52	-24.96	**49.52**	52.40	-26.92	**52.40**
75	0.99	-1.07	**1.07**	1.02	-0.99	**1.02**	49.78	-25.68	**49.78**	51.02	-26.26	**51.02**
100	0.17	-0.40	**0.40**	0.40	-0.17	**0.40**	50.77	-26.41	**50.77**	50.80	-26.41	**50.80**

Table C.6 Peak Imposed Loads and Load Ratios in the Shear Walls (Group 3_1)

Front/Back Wall ratio (%)	Peak Perpendicular Imposed Loads (kN)								Peak Parallel Imposed Loads (kN)							
	Wall 1				Wall 2				Back Wall				Front Wall			
	+	-	MAX	Load Ratio	+	-	MAX	Load Ratio	+	-	MAX	Load Ratio	+	-	MAX	Load Ratio
0	25.05	-21.82	**25.05**	**1.13**	21.32	-25.30	**25.30**	**1.15**	89.10	-115.47	**115.47**	**2.61**	0.00	0.00	**0.00**	**N/A**
25	13.46	-12.17	**13.46**	**0.61**	12.13	-13.81	**13.81**	**0.63**	65.60	-91.71	**91.71**	**2.60**	19.45	-23.63	**23.63**	**2.67**
50	7.02	-6.58	**7.02**	**0.32**	6.54	-6.50	**6.54**	**0.30**	54.98	-76.47	**76.47**	**2.60**	31.78	-38.39	**38.39**	**2.61**
75	3.92	-4.00	**4.00**	**0.18**	3.97	-3.83	**3.97**	**0.18**	47.10	-65.51	**65.51**	**2.60**	40.21	-49.22	**49.22**	**2.6**
100	1.67	-0.74	**1.67**	**0.08**	0.75	-1.71	**1.71**	**0.08**	46.56	-57.38	**57.38**	**2.60**	46.24	-57.36	**57.36**	**2.6**

Group 3_2 (L:W=1:3, w/ perpendicular partition wall, w/ parallel partition wall)

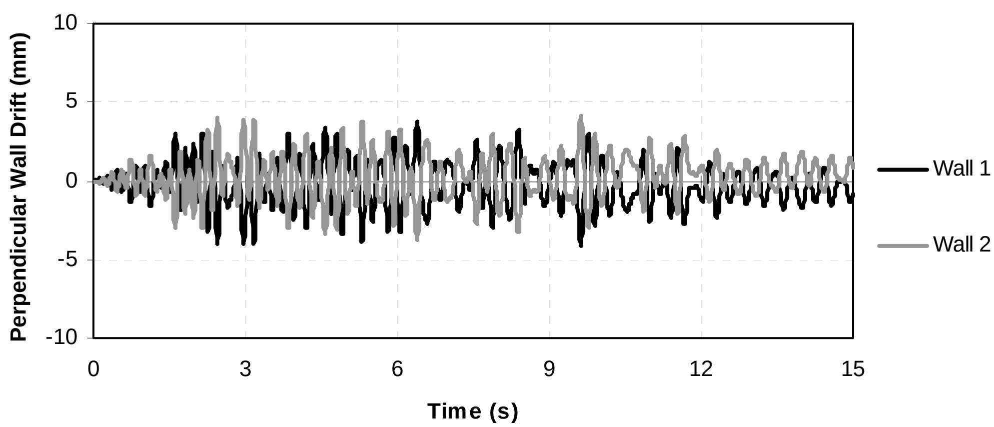

Figure C.31 Drifts of Perpendicular Walls (Case 3_2_0)

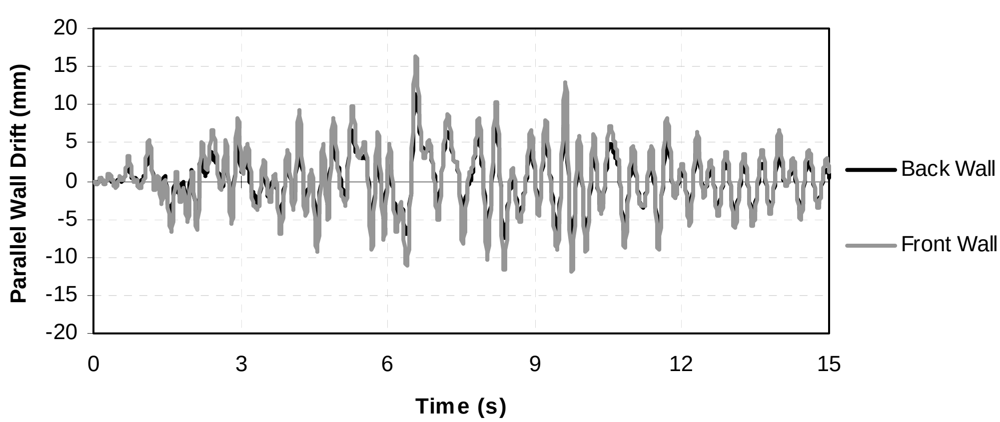

Figure C.32 Drifts of Parallel Walls (Case 3_2_0)

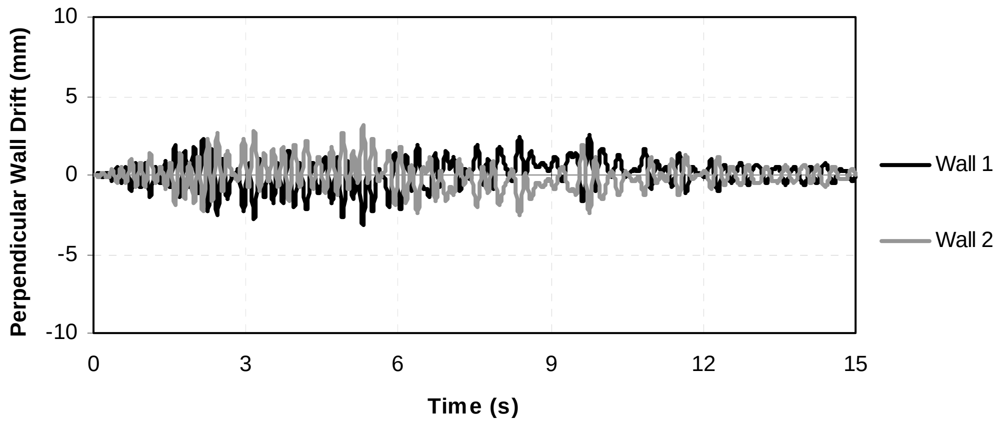

Figure C.33 Drifts of Perpendicular Walls (Case 3_2_25)

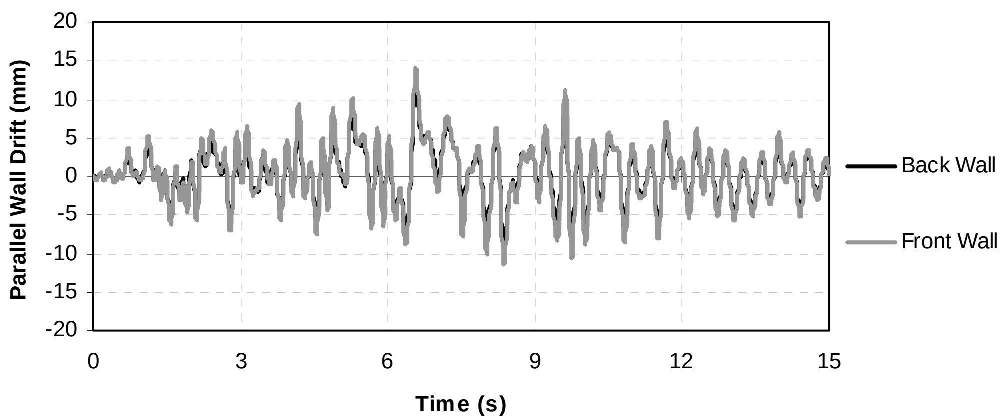

Figure C.34 Drifts of Parallel Walls (Case 3_2_25)

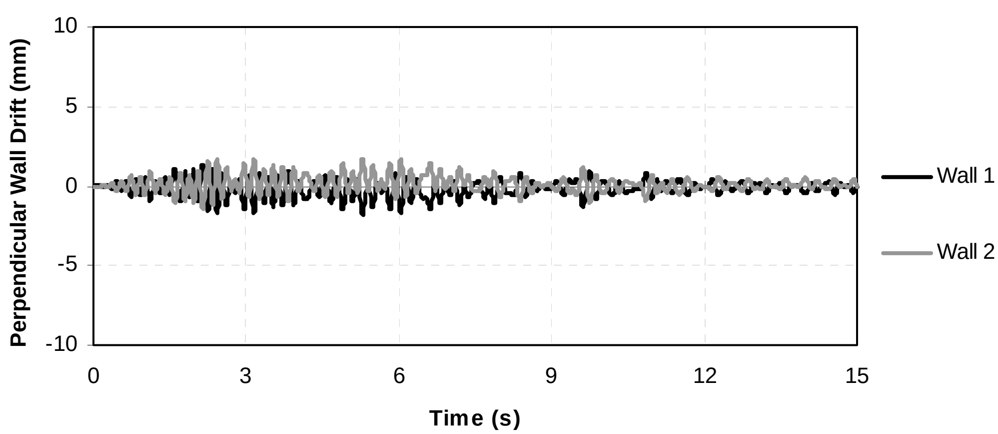

Figure C.35 Drifts of Perpendicular Walls (Case 3_2_50)

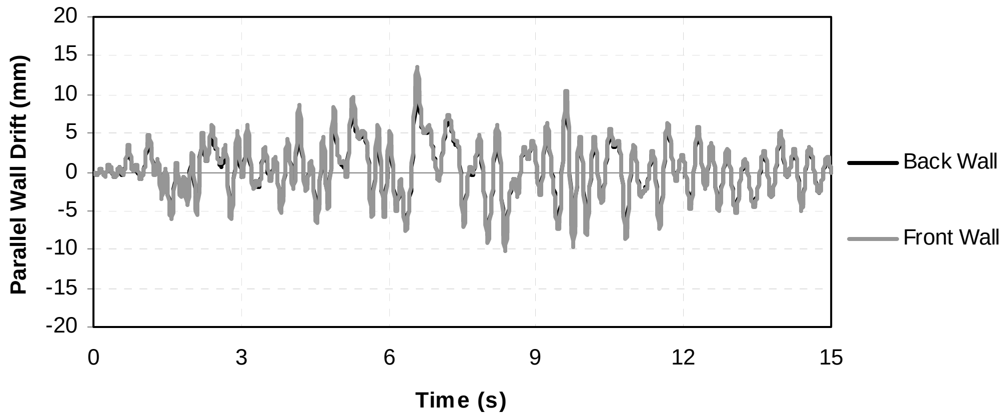

Figure C.36 Drifts of Parallel Walls (Case 3_2_50)

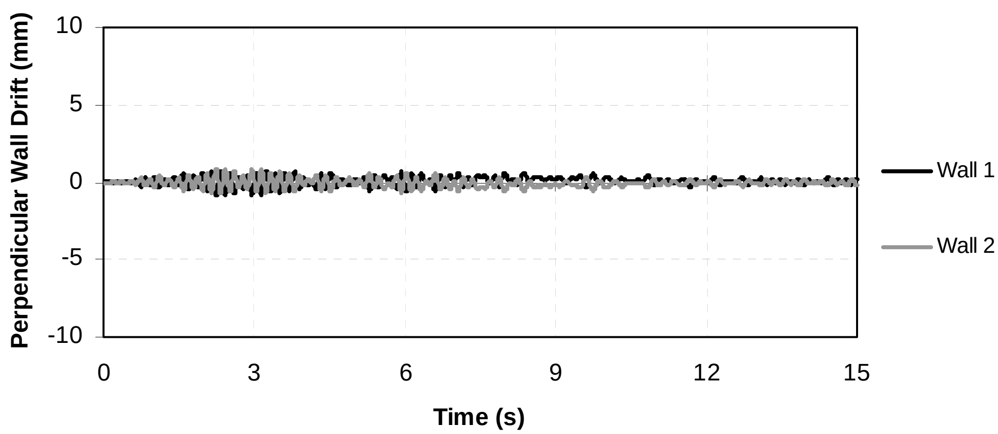

Figure C.37 Drifts of Perpendicular Walls (Case 3_2_75)

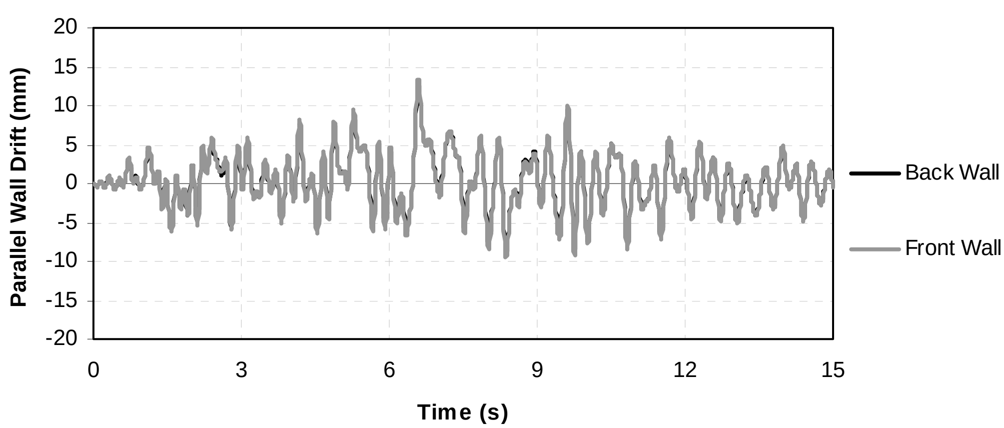

Figure C.38 Drifts of Parallel Walls (Case 3_2_75)

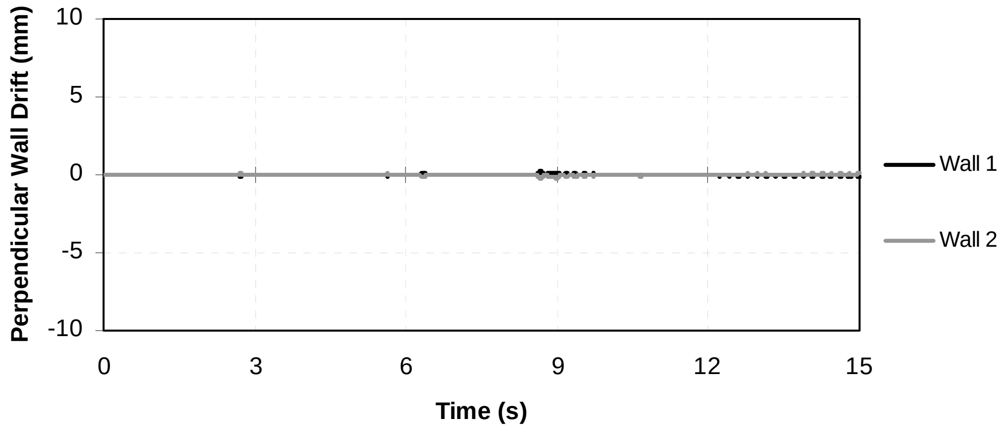

Figure C.39 Drifts of Perpendicular Walls (Case 3_2_100)

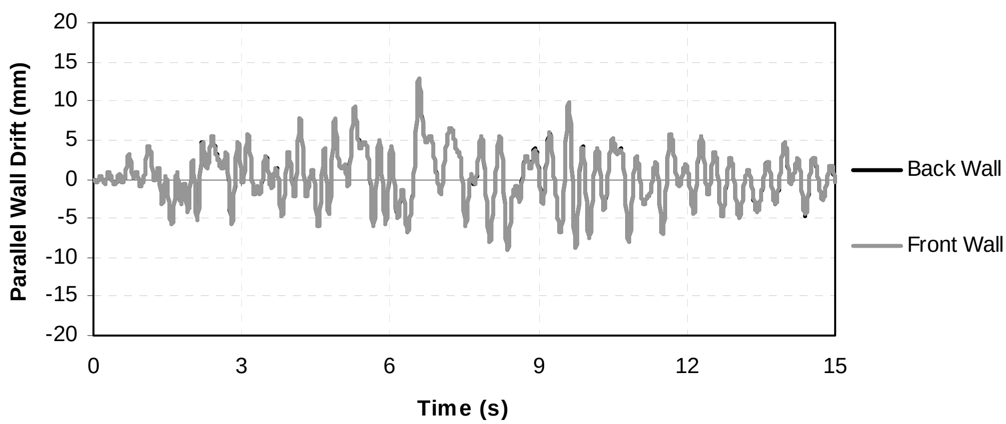

Figure C.40 Drifts of Parallel Walls (Case 3_2_100)

Table C.7 Peak Drifts of the Shear Walls (Group 3_2)

Front/Back Wall ratio (%)	Peak Perpendicular Wall Drift (mm)						Peak Parallel Wall Drift (mm)					
	Wall 1			Wall 2			Back Wall			Front Wall		
	+	-	MAX	+	-	MAX	+	-	MAX	+	-	MAX
0	3.71	-4.08	**4.08**	4.13	-3.73	**4.13**	11.40	-7.85	**11.40**	16.21	-11.93	**16.21**
25	2.55	-3.11	**3.11**	3.10	-2.53	**3.10**	11.62	-8.65	**11.62**	13.94	-11.36	**13.94**
50	1.36	-1.81	**1.81**	1.75	-1.40	**1.75**	11.75	-8.94	**11.75**	13.53	-10.13	**13.53**
75	0.75	-0.88	**0.88**	0.90	-0.72	**0.90**	12.66	-8.76	**12.66**	13.38	-9.41	**13.38**
100	0.21	-0.09	**0.21**	0.08	-0.22	**0.22**	12.94	-9.16	**12.94**	12.90	-9.16	**12.90**

Table C.8 Peak Imposed Loads and Load Ratios in the Shear Walls (Group 3_2)

Front/Back Wall ratio (%)	Peak Perpendicular Imposed Loads (kN)								Peak Parallel Imposed Loads (kN)							
	Wall 1				Wall 2				Back Wall				Front Wall			
	+	-	MAX	Load Ratio	+	-	MAX	Load Ratio	+	-	MAX	Load Ratio	+	-	MAX	Load Ratio
0	14.06	-13.11	**14.06**	**0.64**	12.74	-14.04	**14.04**	**0.64**	48.41	-65.56	**65.56**	**1.48**	0.00	0.00	**0.00**	**N/A**
25	10.11	-8.15	**10.11**	**0.46**	8.59	-10.09	**10.09**	**0.46**	39.19	-52.96	**52.96**	**1.50**	11.40	-14.38	**14.38**	**1.63**
50	6.74	-5.40	**6.74**	**0.31**	5.42	-6.87	**6.87**	**0.31**	33.40	-44.60	**44.60**	**1.51**	18.10	-23.20	**23.20**	**1.58**
75	3.86	-3.15	**3.86**	**0.17**	3.10	-3.75	**3.75**	**0.17**	29.31	-38.85	**38.85**	**1.54**	22.70	-29.81	**29.81**	**1.57**
100	0.32	-0.93	**0.93**	**0.04**	0.90	-0.32	**0.90**	**0.04**	25.99	-34.34	**34.34**	**1.55**	25.95	-34.80	**34.80**	**1.58**

Group 4_1 (L:W=2:1, w/o parallel partition wall)

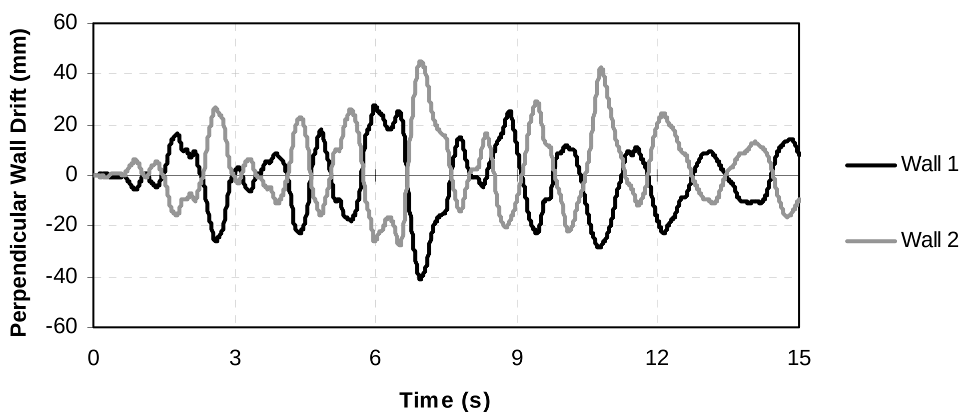

Figure C.41 Drifts of Perpendicular Walls (Case 4_1_0)

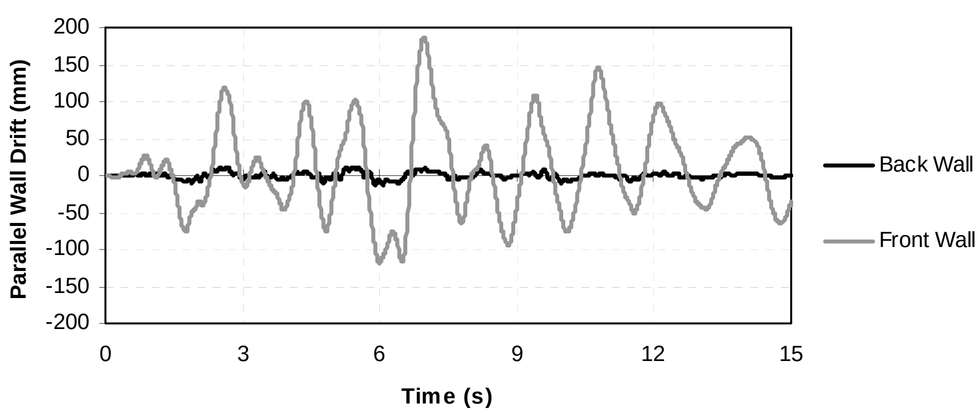

Figure C.42 Drifts of Parallel Walls (Case 4_1_0)

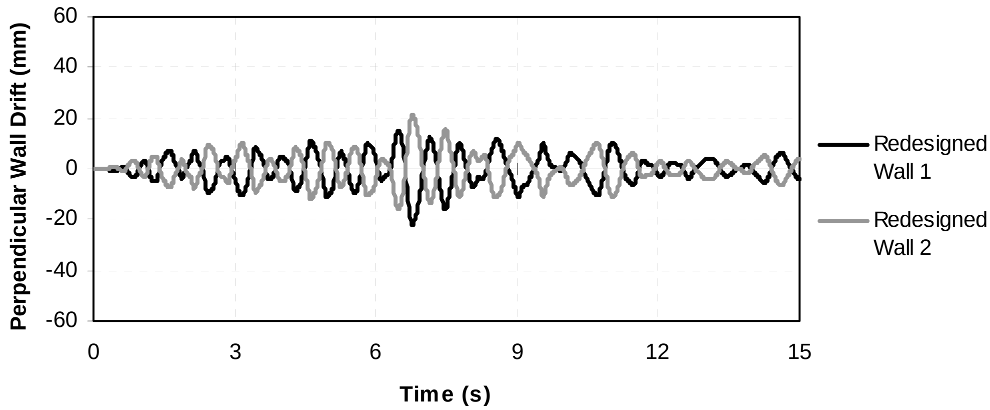

Figure C.43 Drifts of Perpendicular Walls (Redesigned Case 4_1_0)

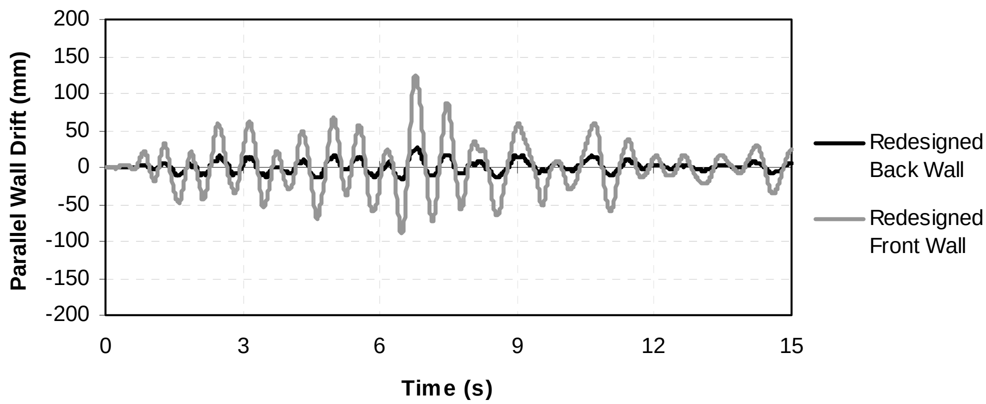

Figure C.44 Drifts of Parallel Walls (Redesigned Case 4_1_0)

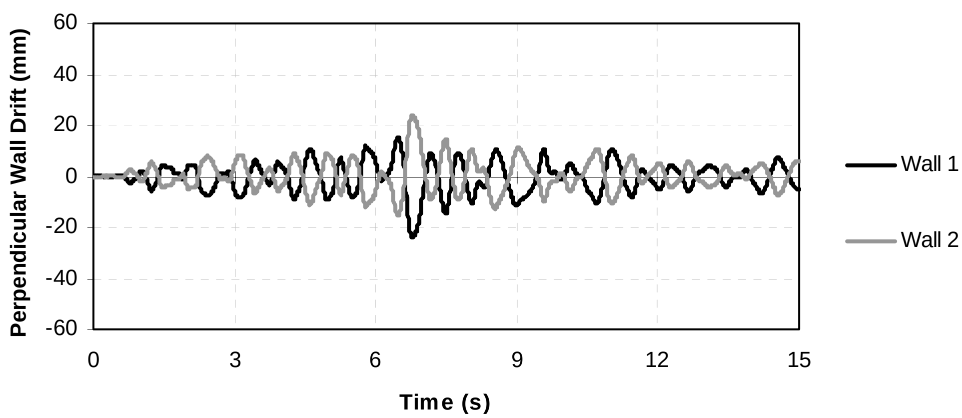

Figure C.45 Drifts of Perpendicular Walls (Case 4_1_25)

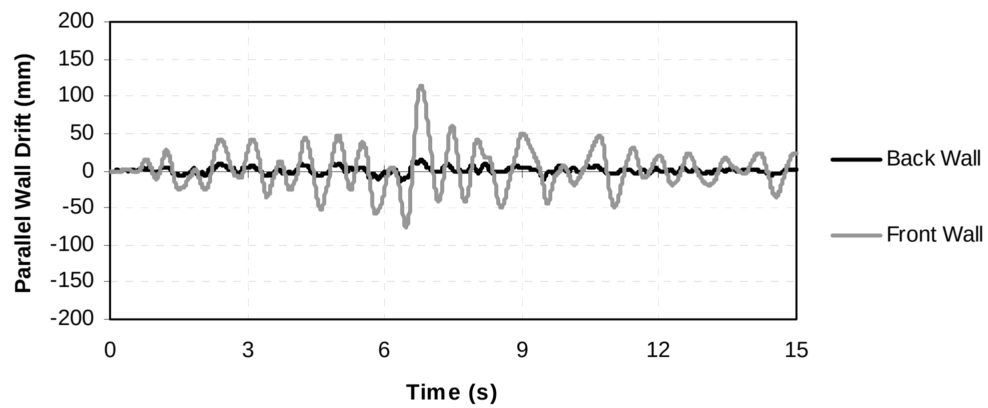

Figure C.46 Drifts of Parallel Walls (Case 4_1_25)

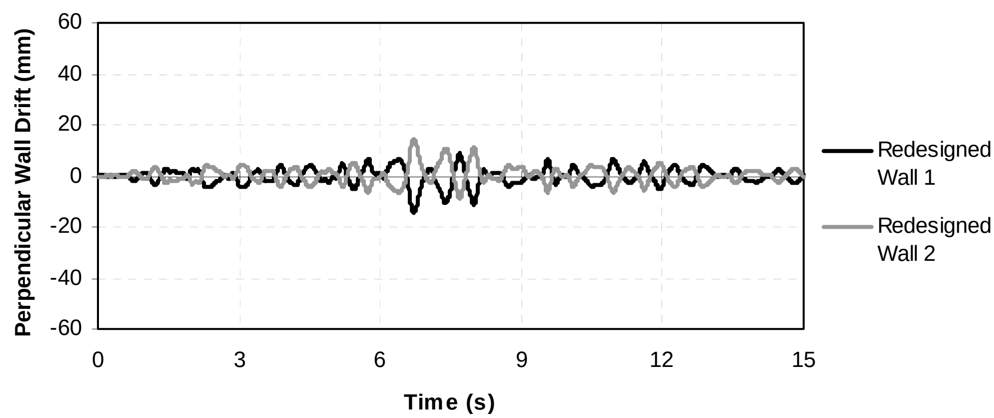

Figure C.47 Drifts of Perpendicular Walls (Redesigned Case 4_1_25)

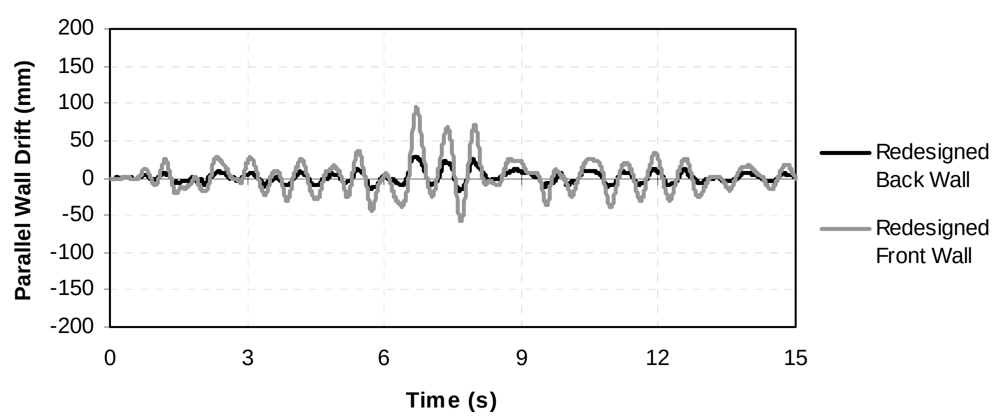

Figure C.48 Drifts of Parallel Walls (Redesigned Case 4_1_25)

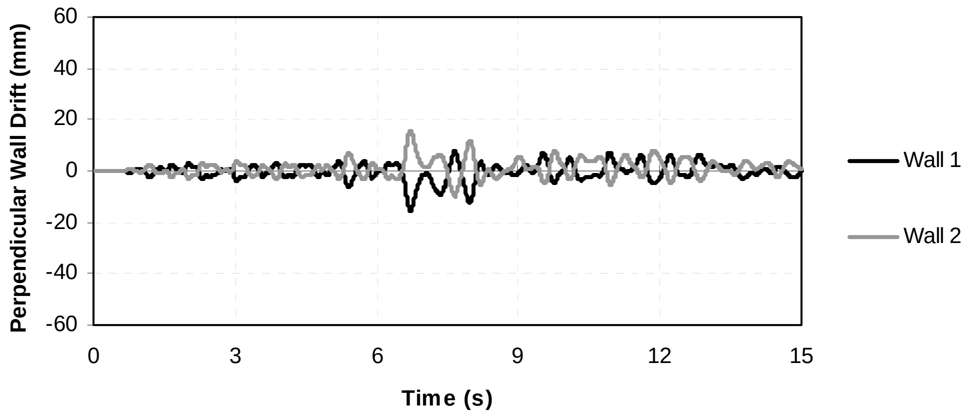

Figure C.49 Drifts of Perpendicular Walls (Case 4_1_50)

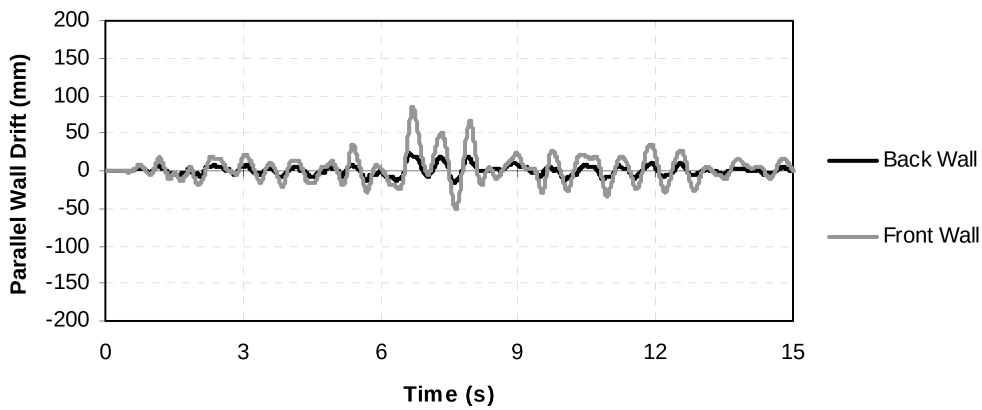

Figure C.50 Drifts of Parallel Walls (Case 4_1_50)

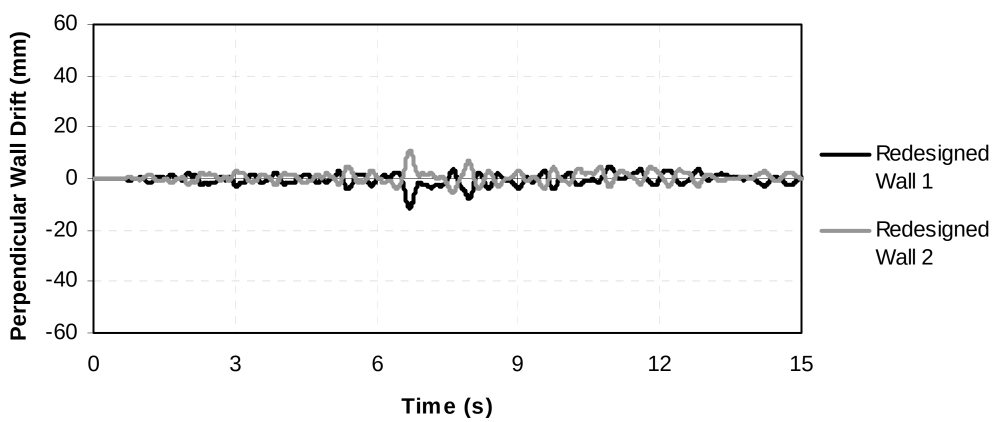

Figure C.51 Drifts of Perpendicular Walls (Redesigned Case 4_1_50)

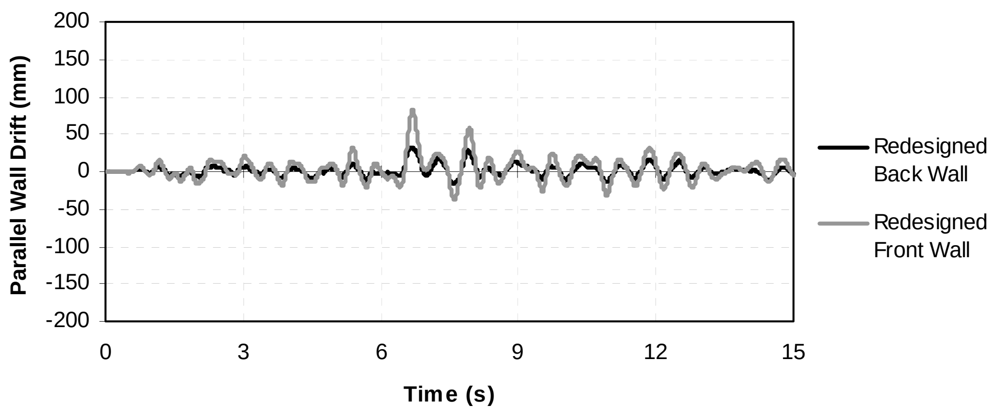

Figure C.52 Drifts of Parallel Walls (Redesigned Case 4_1_50)

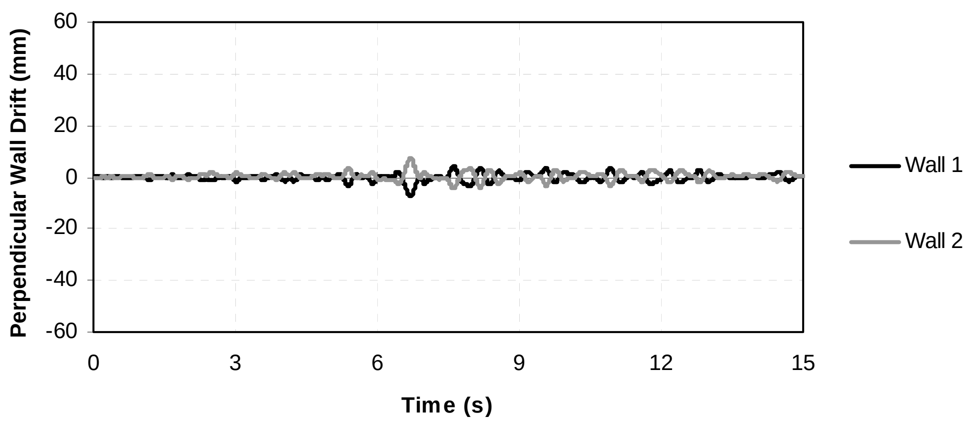

Figure C.53 Drifts of Perpendicular Walls (Case 4_1_75)

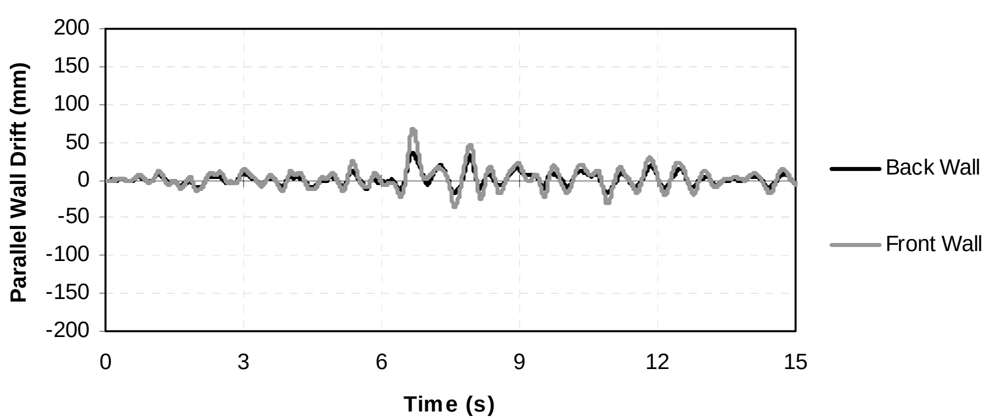

Figure C.54 Drifts of Parallel Walls (Case 4_1_75)

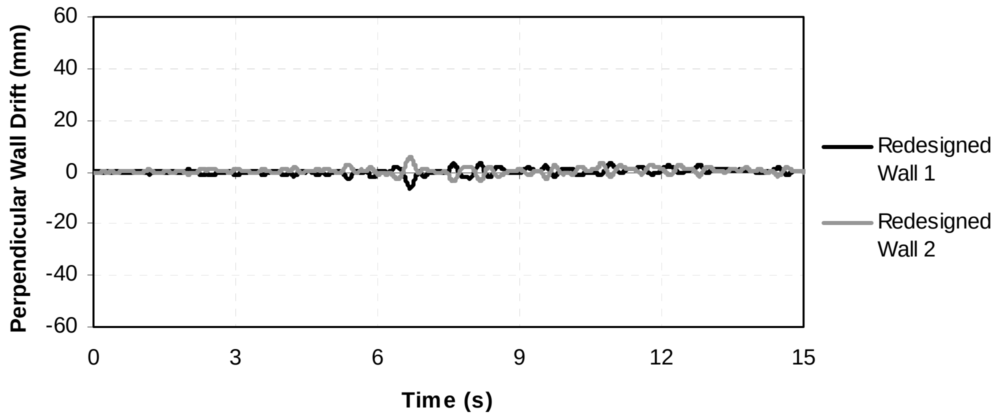

Figure C.55 Drifts of Perpendicular Walls (Redesigned Case 4_1_75)

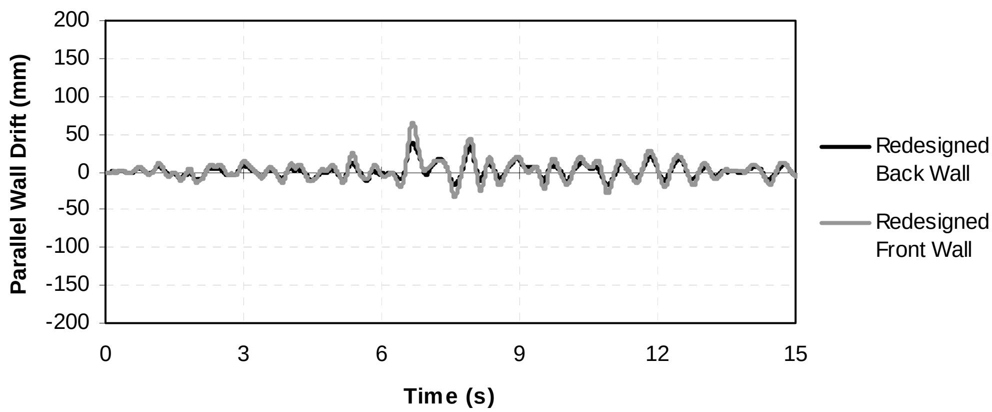

Figure C.56 Drifts of Parallel Walls (Redesigned Case 4_1_75)

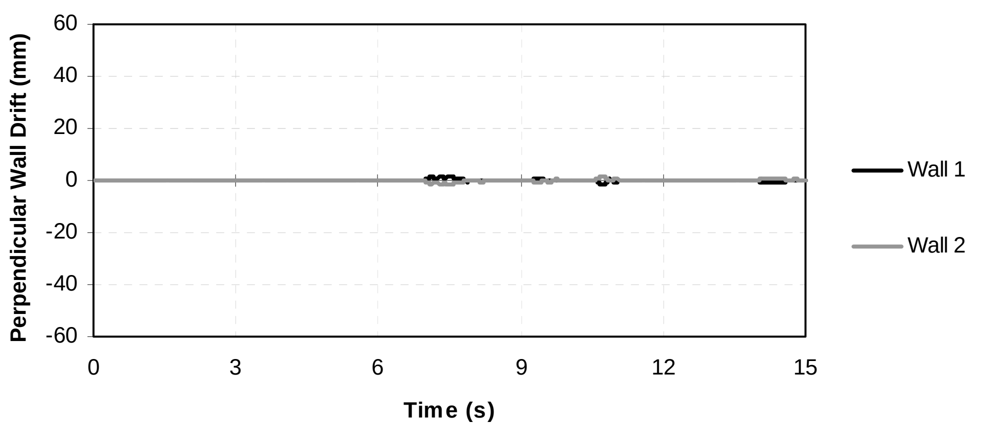

Figure C.57 Drifts of Perpendicular Walls (Case 4_1_100)

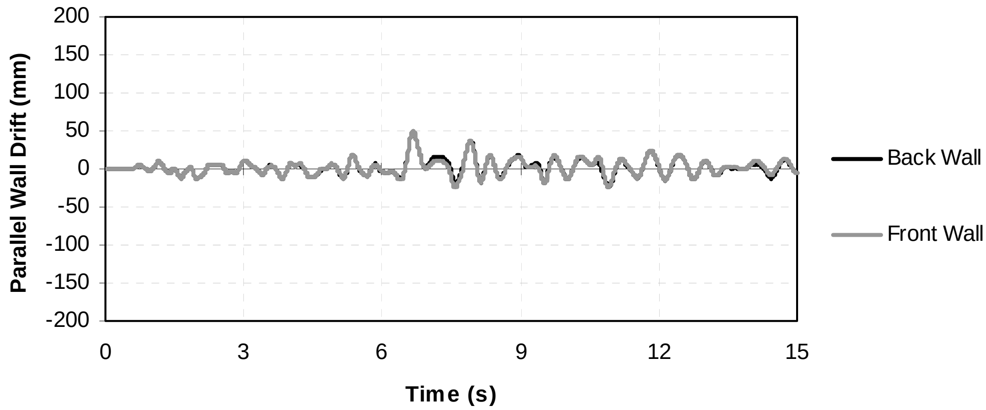

Figure C.58 Drifts of Parallel Walls (Case 4_1_100)

Table C.9 Peak Drifts of the Shear Walls (Group 4_1)

Front/Back Wall ratio (%)		Peak Perpendicular Wall Drift (mm)						Peak Parallel Wall Drift (mm)					
		Wall 1			Wall 2			Back Wall			Front Wall		
		+	-	MAX	+	-	MAX	+	-	MAX	+	-	MAX
Original	0	27.68	-40.79	**40.79**	45.18	-27.91	**45.18**	11.85	-12.59	**12.59**	185.93	-117.96	**185.93**
	25	15.54	-23.82	**23.82**	23.88	-15.59	**23.88**	14.28	-13.44	**14.28**	113.97	-75.63	**113.97**
	50	7.80	-15.42	**15.42**	15.74	-9.77	**15.74**	22.73	-15.58	**22.73**	85.70	-50.79	**85.70**
	75	4.16	-7.50	**7.50**	7.50	-4.37	**7.50**	36.59	-18.22	**36.59**	68.01	-35.93	**68.01**
	100	1.69	-1.82	**1.82**	1.89	-1.73	**1.89**	49.39	-23.78	**49.39**	49.71	-24.48	**49.71**
Redesigned	0	15.37	-21.84	**21.84**	21.33	-16.15	**21.33**	25.86	-16.52	**25.86**	125.20	-89.24	**125.20**
	25	8.71	-14.35	**14.35**	14.51	-8.86	**14.51**	28.35	-16.56	**28.35**	94.08	-57.19	**94.08**
	50	4.71	-11.44	**11.44**	10.88	-5.71	**10.88**	32.81	-15.88	**32.81**	82.04	-36.99	**82.04**
	75	3.28	-6.21	**6.21**	5.62	-3.66	**5.62**	39.58	-18.43	**39.58**	65.28	-33.65	**65.28**

Table C.10 Peak Imposed Loads and Load Ratios in the Shear Walls (Group 4_1)

Front/Back Wall ratio (%)		Peak Perpendicular Imposed Loads (kN)								Peak Parallel Imposed Loads (kN)							
		Wall 1				Wall 2				Back Wall				Front Wall			
		+	-	MAX	Load Ratio	+	-	MAX	Load Ratio	+	-	MAX	Load Ratio	+	-	MAX	Load Ratio
Original	0	35.78	-31.43	**35.78**	**2.43**	32.70	-36.47	**36.47**	**2.477**	44.98	-36.38	**44.98**	**1.53**	0.00	0.00	**0.00**	**N/A**
	25	33.27	-22.87	**33.27**	**2.26**	22.91	-33.29	**33.29**	**2.261**	32.44	-39.01	**39.01**	**1.66**	14.76	-16.29	**16.29**	**2.77**
	50	26.55	-19.34	**26.55**	**1.803**	18.80	-27.04	**27.04**	**1.837**	35.11	-43.29	**43.29**	**2.21**	24.46	-26.47	**26.47**	**2.7**
	75	16.03	-12.59	**16.03**	**1.089**	12.22	-16.98	**16.98**	**1.154**	31.76	-41.73	**41.73**	**2.48**	27.06	-33.68	**33.68**	**2.67**
	100	5.10	-4.50	**5.10**	**0.347**	4.34	-4.76	**4.76**	**0.323**	29.06	-37.94	**37.94**	**2.58**	27.24	-38.00	**38.00**	**2.58**
Redesigned	0	94.648	-68.67	**94.65**	**2.14**	69.63	-94.58	**94.58**	**2.14**	47.76	-62.94	**62.94**	**2.14**	0	0.00	**0.00**	**N/A**
	25	58.864	-45.30	**58.86**	**1.82**	45.67	-59.11	**59.11**	**1.83**	42.8	-52.28	**52.28**	**2.22**	14.59	-16.23	**16.23**	**2.76**
	50	36.069	-23.63	**36.07**	**1.47**	22.85	-36.32	**36.32**	**1.48**	35.4	-46.07	**46.07**	**2.35**	21.43	-26.51	**26.51**	**2.70**
	75	17.519	-13.21	**17.52**	**0.92**	13.4	-17.00	**17.00**	**0.90**	32.16	-42.03	**42.03**	**2.50**	26.93	-33.56	**33.56**	**2.66**

Group 4_2 (L:W=2:1, w/ parallel partition wall)

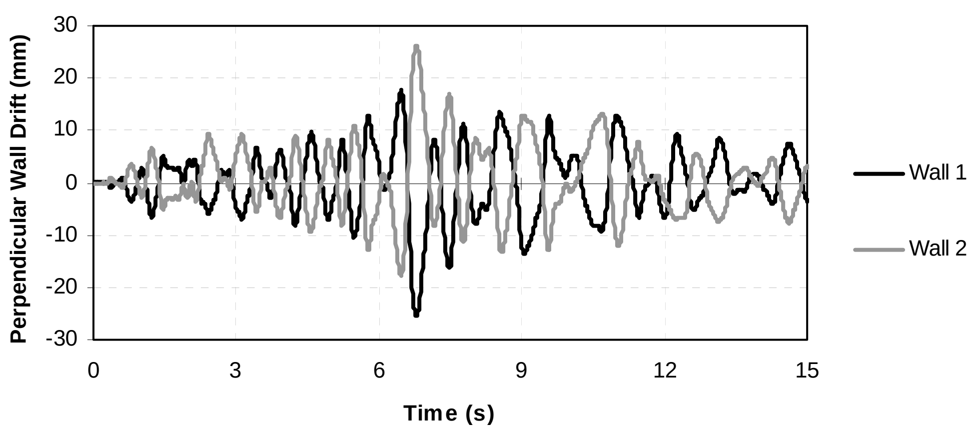

Figure C.59 Drifts of Perpendicular Walls (Case 4_2_0)

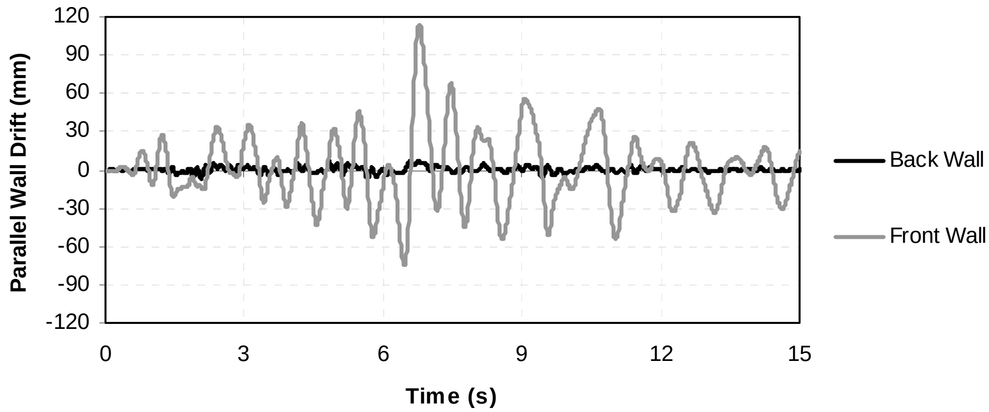

Figure C.60 Drifts of Parallel Walls (Case 4_2_0)

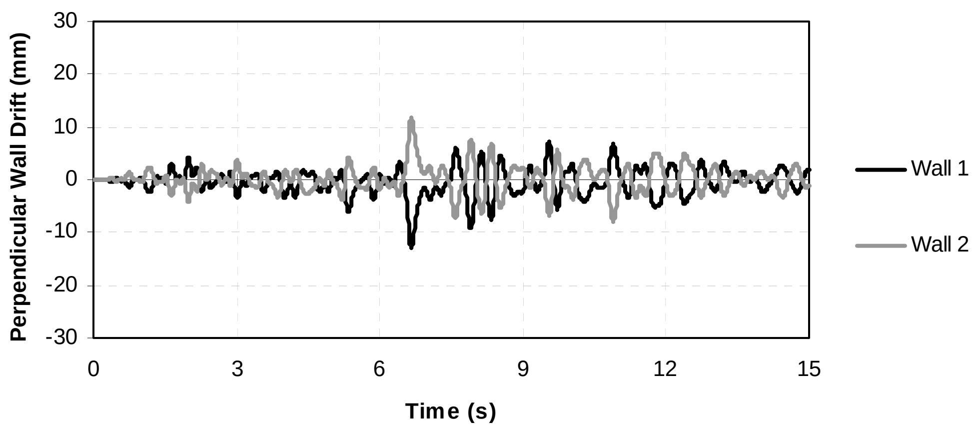

Figure C.61 Drifts of Perpendicular Walls (Case 4_2_25)

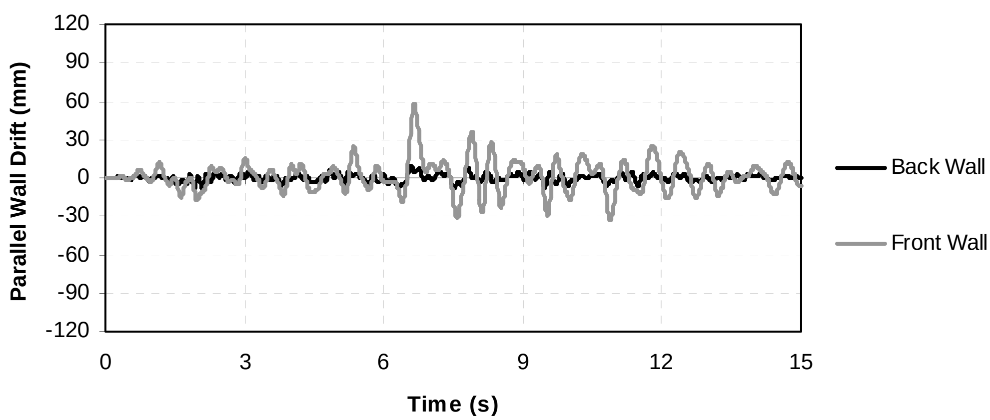

Figure C.62 Drifts of Parallel Walls (Case 4_2_25)

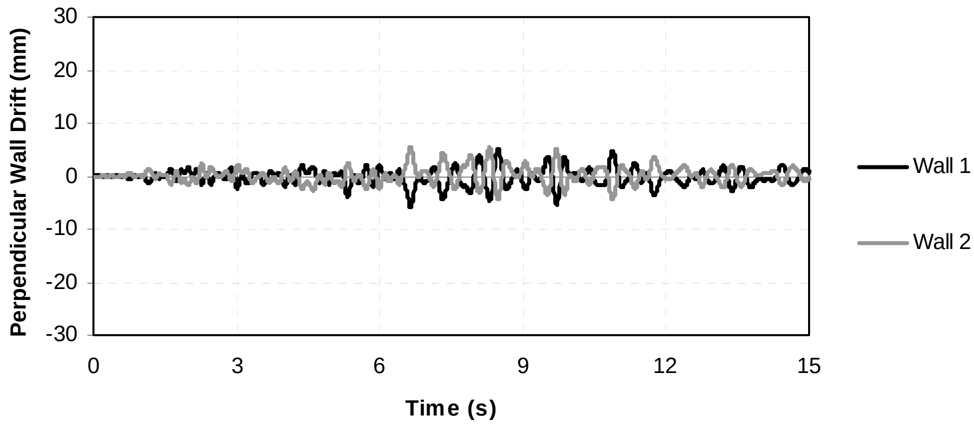

Figure C.63 Drifts of Perpendicular Walls (Case 4_2_50)

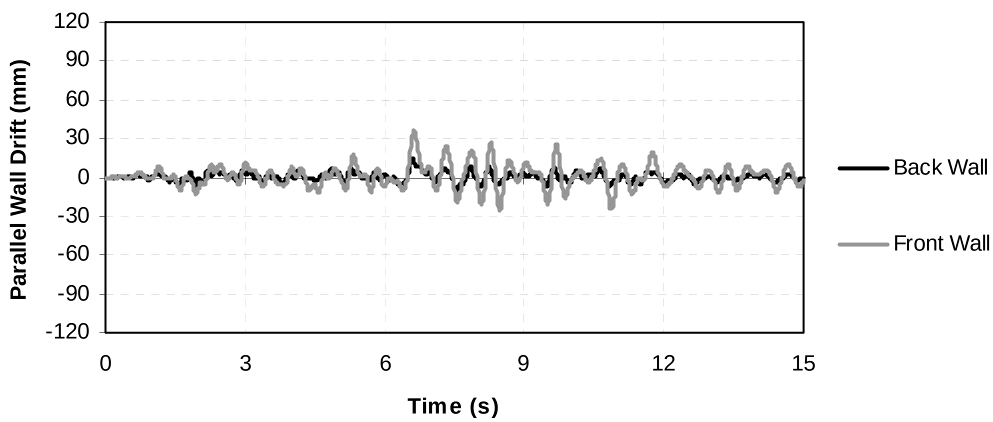

Figure C.64 Drifts of Parallel Walls (Case 4_2_50)

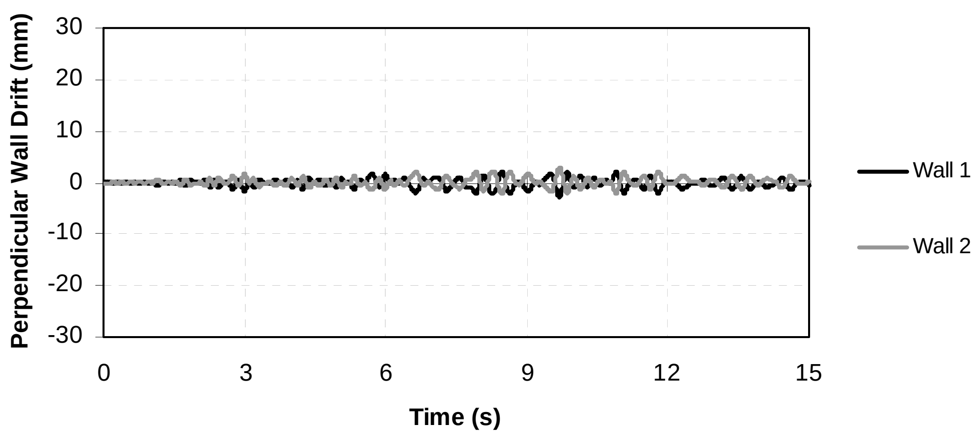

Figure C.65 Drifts of Perpendicular Walls (Case 4_2_75)

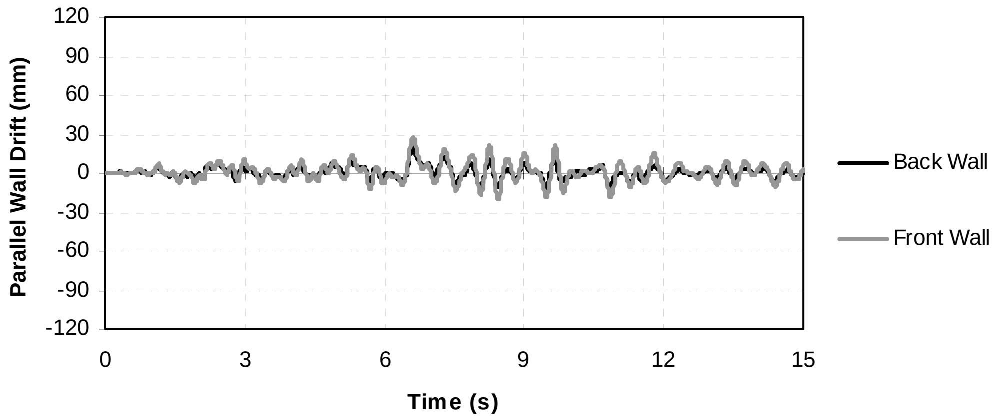

Figure C.66 Drifts of Parallel Walls (Case 4_2_75)

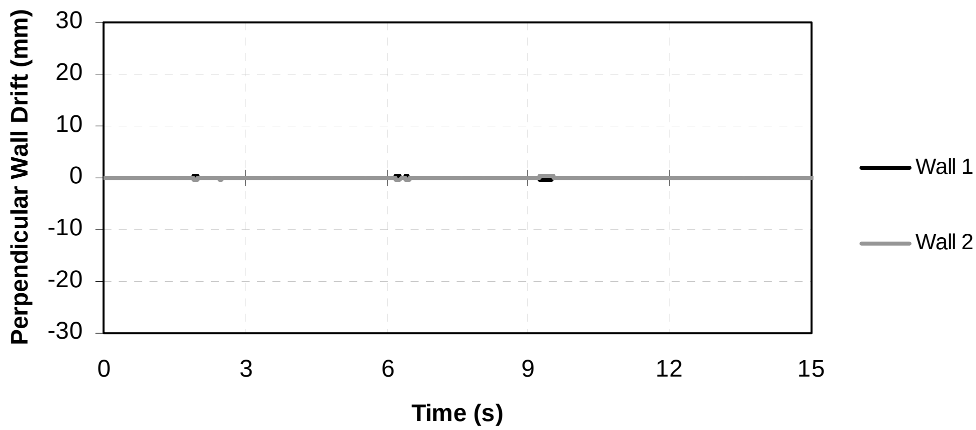

Figure C.67 Drifts of Perpendicular Walls (Case 4_2_100)

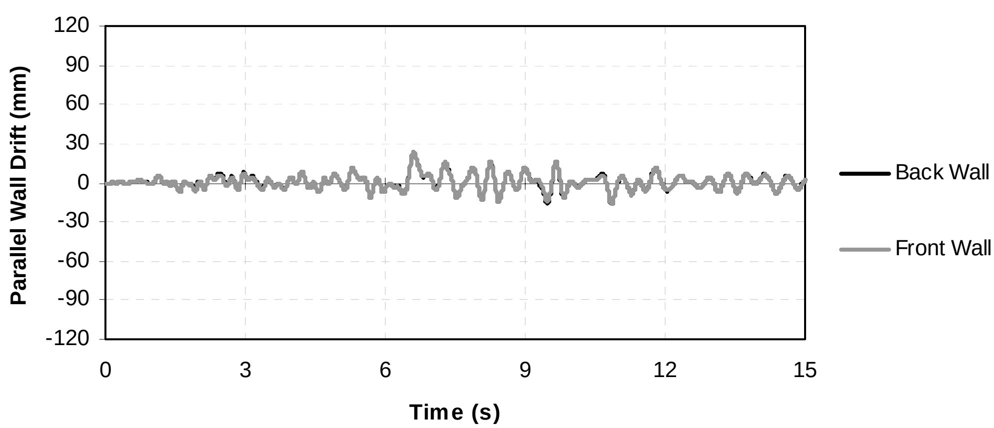

Figure C.68 Drifts of Parallel Walls (Case 4_2_100)

Table C.11 Peak Drifts of the Shear Walls (Group 4_2)

Front/Back Wall ratio (%)		Peak Perpendicular Wall Drift (mm)						Peak Parallel Wall Drift (mm)					
		Wall 1			Wall 2			Back Wall			Front Wall		
		+	-	MAX	+	-	MAX	+	-	MAX	+	-	MAX
Original	0	17.60	-25.52	**25.52**	26.27	-17.76	**26.27**	6.70	-6.80	**6.80**	114.45	-75.10	**114.45**
	25	7.11	-12.94	**12.94**	11.72	-7.86	**11.72**	9.77	-8.45	**9.77**	57.46	-33.01	**57.46**
	50	5.17	-5.80	**5.80**	5.42	-4.50	**5.42**	14.24	-10.24	**14.24**	36.08	-25.09	**36.08**
	75	2.24	-2.84	**2.84**	2.87	-2.32	**2.87**	19.70	-11.70	**19.70**	28.31	-19.73	**28.31**
	100	0.34	-0.45	**0.45**	0.45	-0.39	**0.45**	23.88	-16.27	**23.88**	23.65	-16.13	**23.65**

Table C.12 Peak Imposed Loads and Load Ratios in the Shear Walls (Group 4_2)

Front/Back Wall ratio (%)		Peak Perpendicular Imposed Loads (kN)								Peak Parallel Imposed Loads (kN)							
		Wall 1				Wall 2				Back Wall				Front Wall			
		+	-	MAX	Load Ratio	+	-	MAX	Load Ratio	+	-	MAX	Load Ratio	+	-	MAX	Load Ratio
Original	0	33.94	-24.09	**33.94**	**2.31**	24.26	-34.08	**34.08**	**2.31**	26.12	-24.81	**26.12**	**0.89**	0.00	0.00	**0.00**	**N/A**
	25	23.68	-14.46	**23.68**	**1.61**	16.21	-22.62	**22.62**	**1.54**	26.73	-35.29	**35.29**	**1.50**	12.39	-15.65	**15.65**	**2.66**
	50	13.47	-12.28	**13.47**	**0.91**	12.24	-13.53	**13.53**	**0.92**	25.38	-34.22	**34.22**	**1.74**	19.75	-23.46	**23.46**	**2.39**
	75	6.34	-6.48	**6.48**	**0.44**	6.56	-6.41	**6.56**	**0.45**	23.38	-33.15	**33.15**	**1.97**	23.66	-27.97	**27.97**	**2.22**
	100	1.24	-1.04	**1.24**	**0.08**	1.07	-1.24	**1.24**	**0.08**	24.39	-31.22	**31.22**	**2.12**	24.28	-31.53	**31.53**	**2.14**

Group 5_1 (L:W=3:1, w/o parallel partition wall)

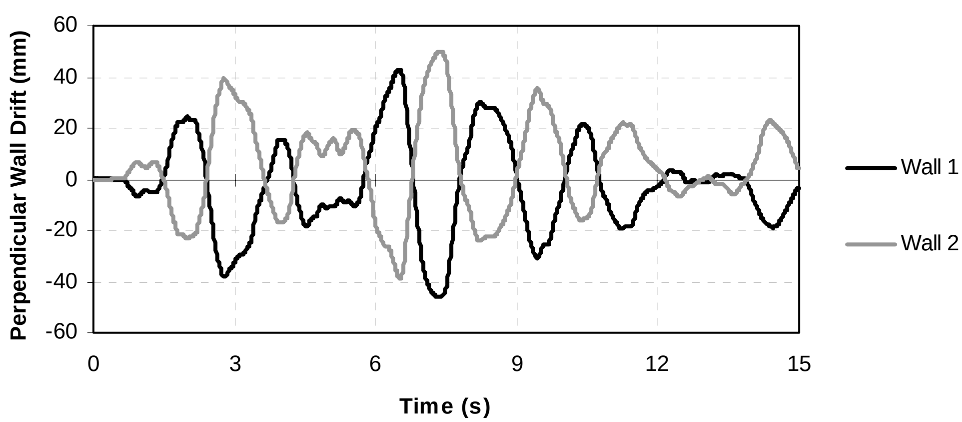

Figure C.69 Drifts of Perpendicular Walls (Case 5_1_0)

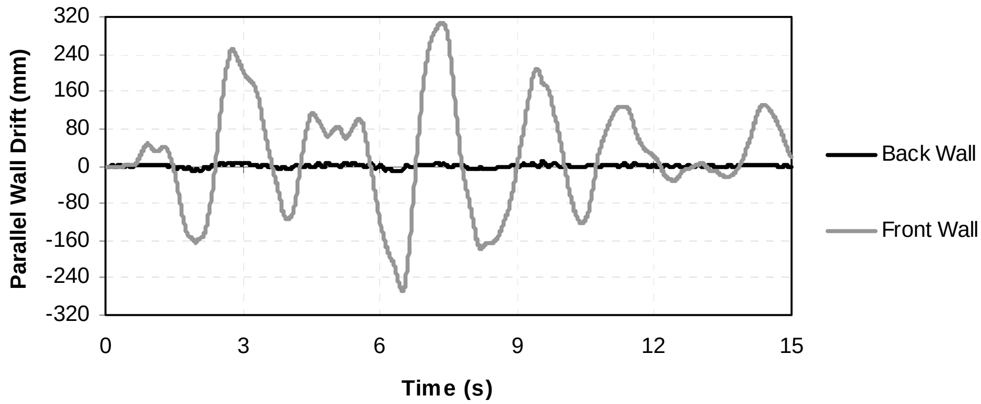

Figure C.70 Drifts of Parallel Walls (Case 5_1_0)

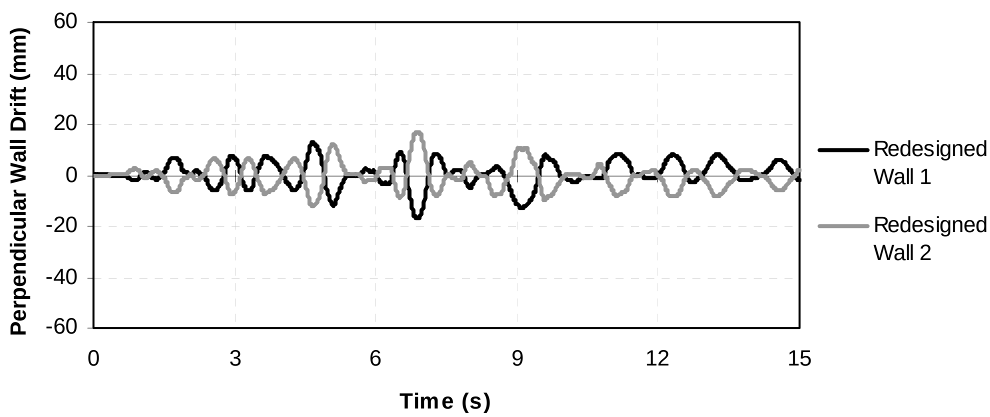

Figure C.71 Drifts of Perpendicular Walls (Redesigned Case 5_1_0)

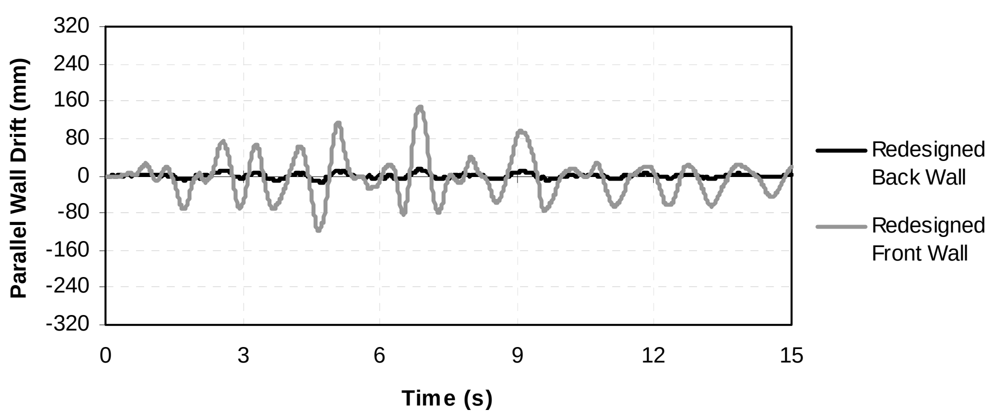

Figure C.72 Drifts of Parallel Walls (Redesigned Case 5_1_0)

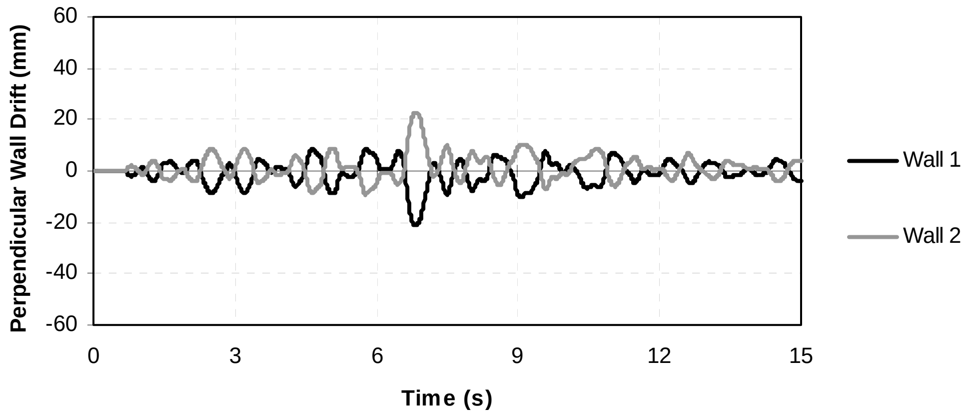

Figure C.73 Drifts of Perpendicular Walls (Case 5_1_25)

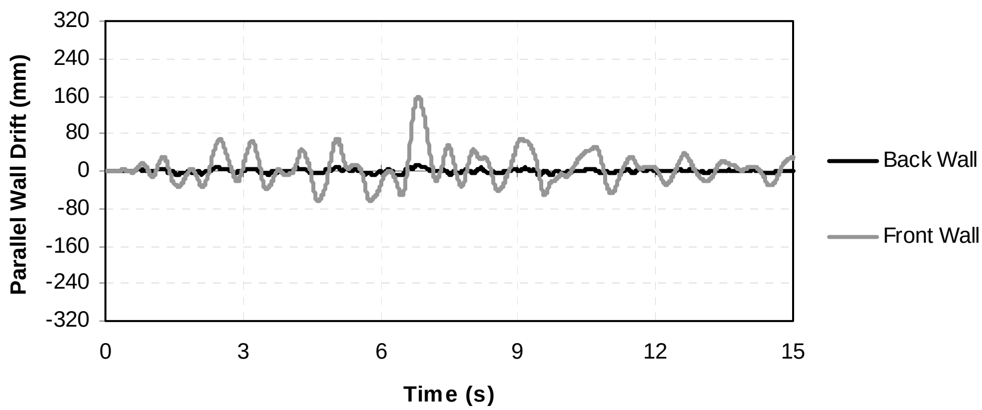

Figure C.74 Drifts of Parallel Walls (Case 5_1_25)

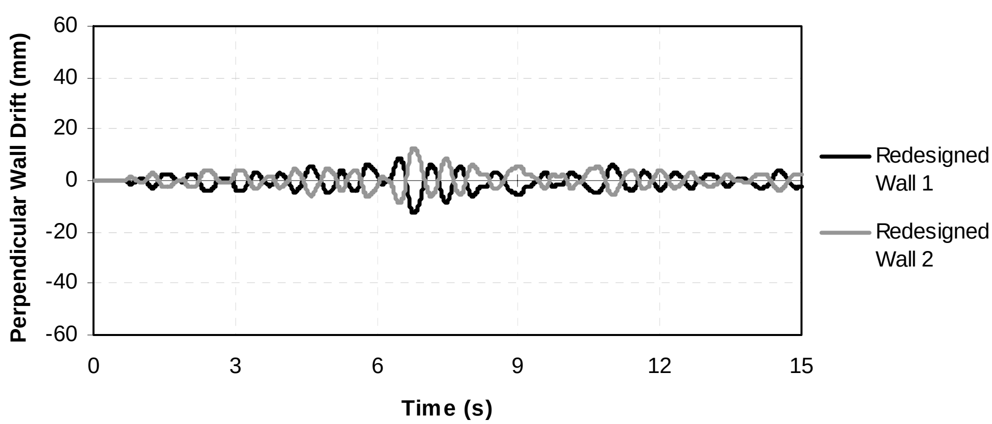

Figure C.75 Drifts of Perpendicular Walls (Redesigned Case 5_1_25)

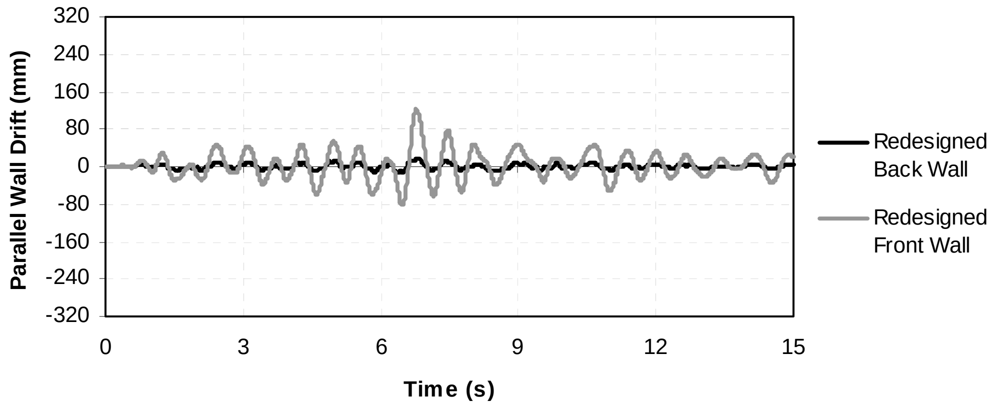

Figure C.76 Drifts of Parallel Walls (Redesigned Case 5_1_25)

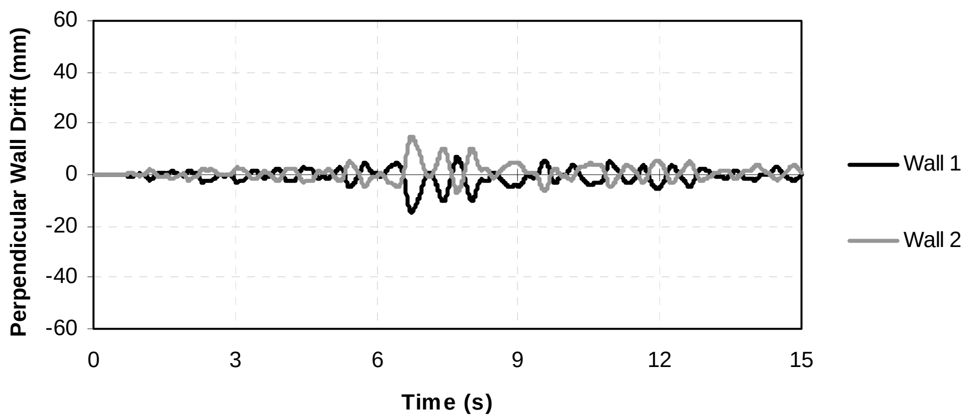

Figure C.77 Drifts of Perpendicular Walls (Case 5_1_50)

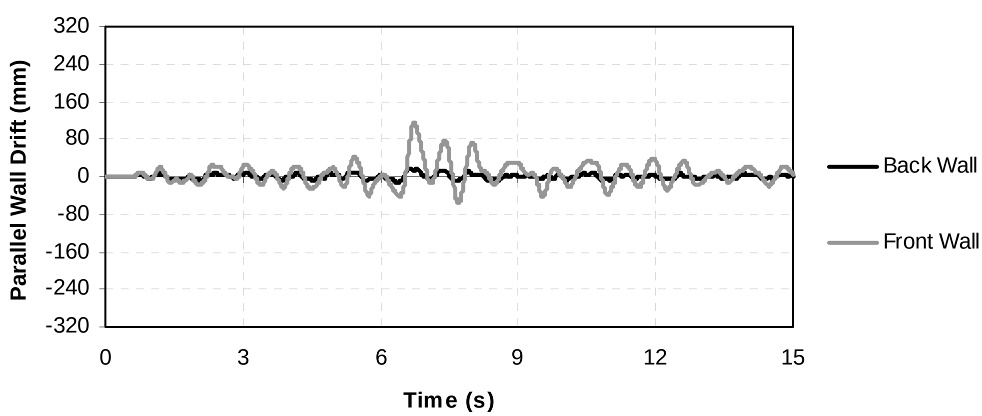

Figure C.78 Drifts of Parallel Walls (Case 5_1_50)

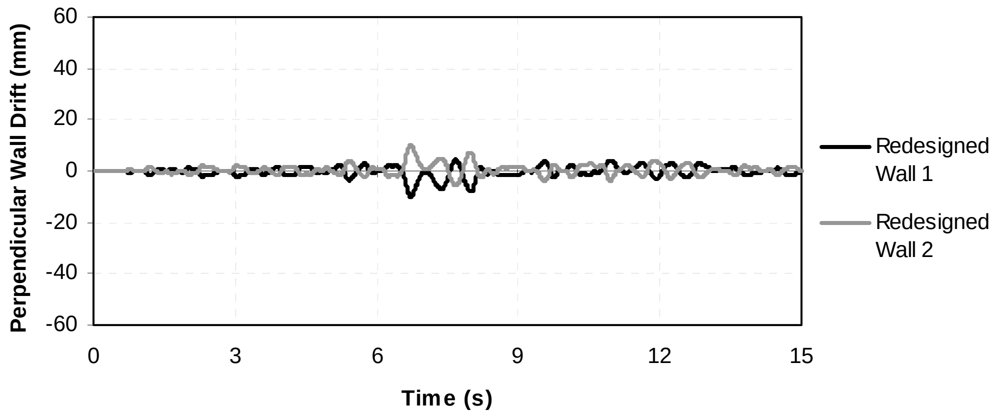

Figure C.79 Drifts of Perpendicular Walls (Redesigned Case 5_1_50)

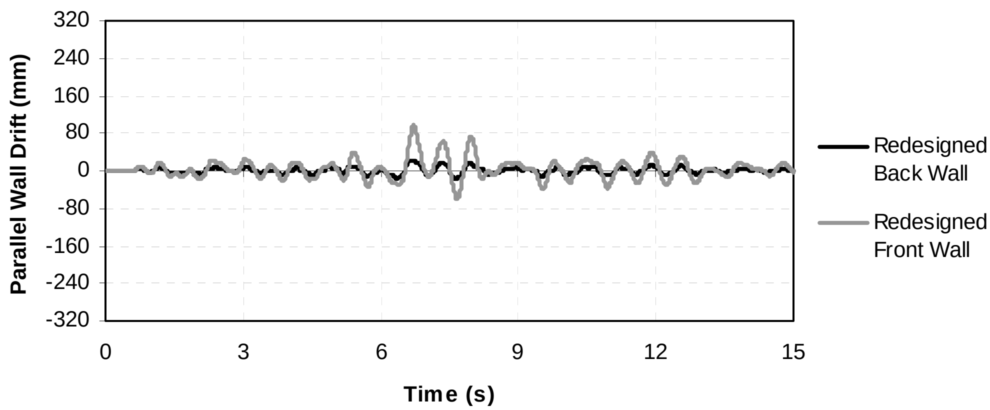

Figure C.80 Drifts of Parallel Walls (Redesigned Case 5_1_50)

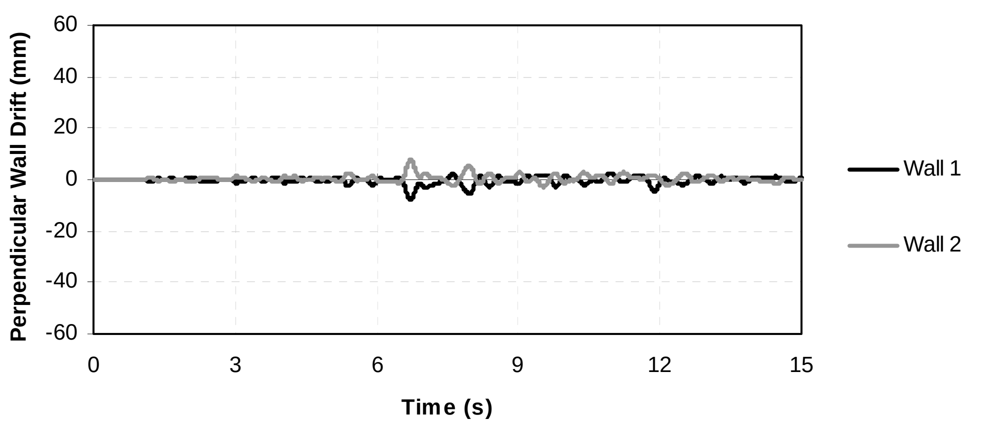

Figure C.81 Drifts of Perpendicular Walls (Case 5_1_75)

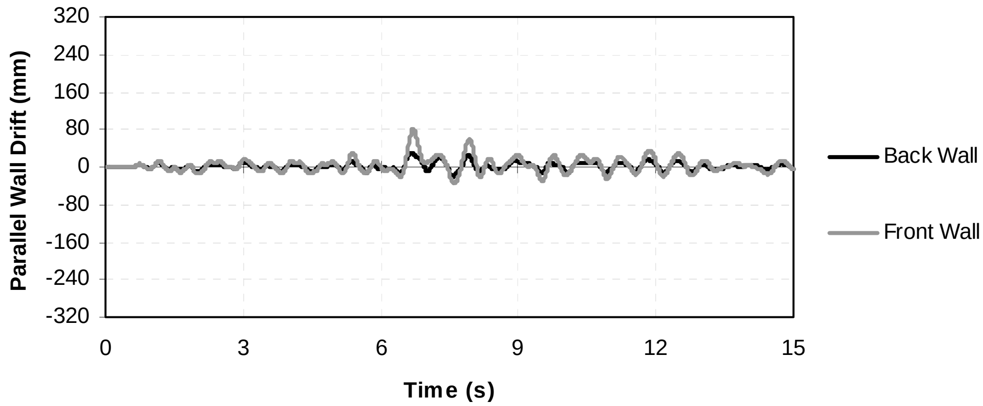

Figure C.82 Drifts of Parallel Walls (Case 5_1_75)

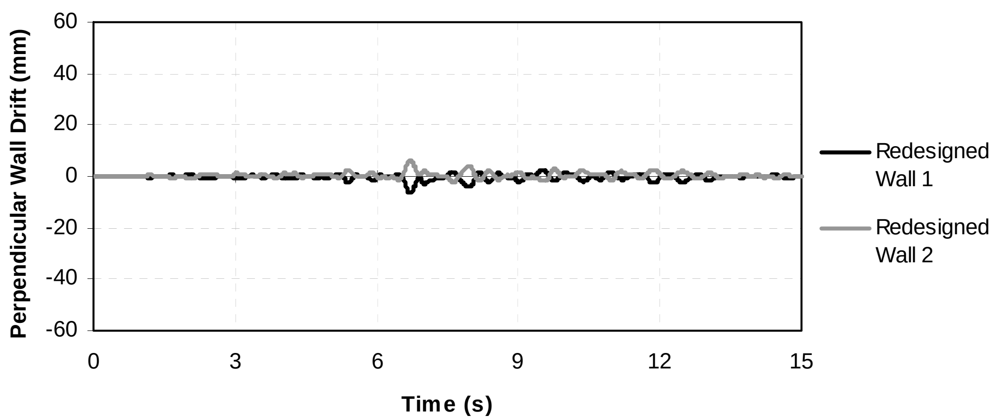

Figure C.83 Drifts of Perpendicular Walls (Redesigned Case 5_1_75)

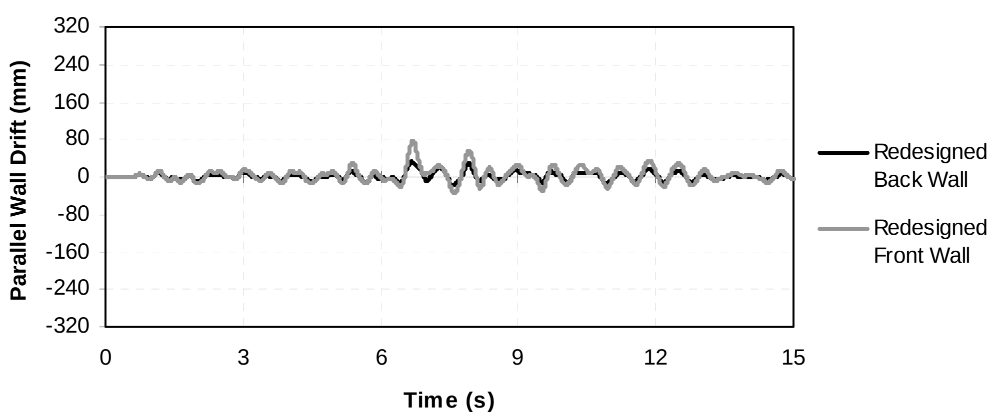

Figure C.84 Drifts of Parallel Walls (Redesigned Case 5_1_75)

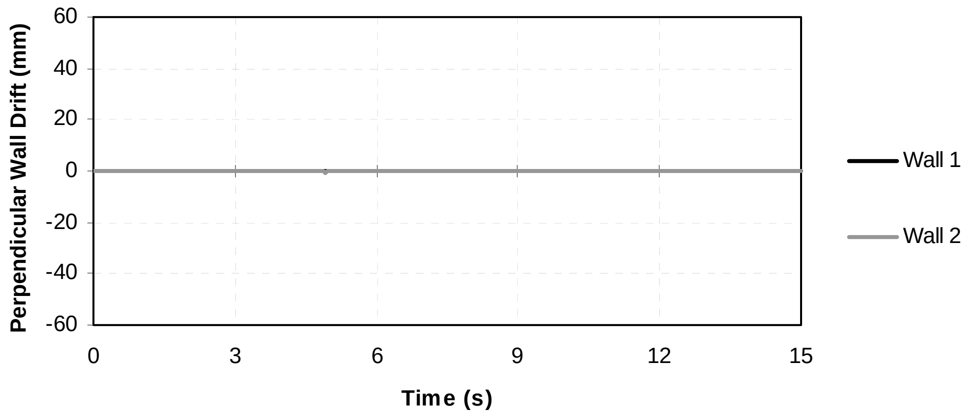

Figure C.85 Drifts of Perpendicular Walls (Case 5_1_100)

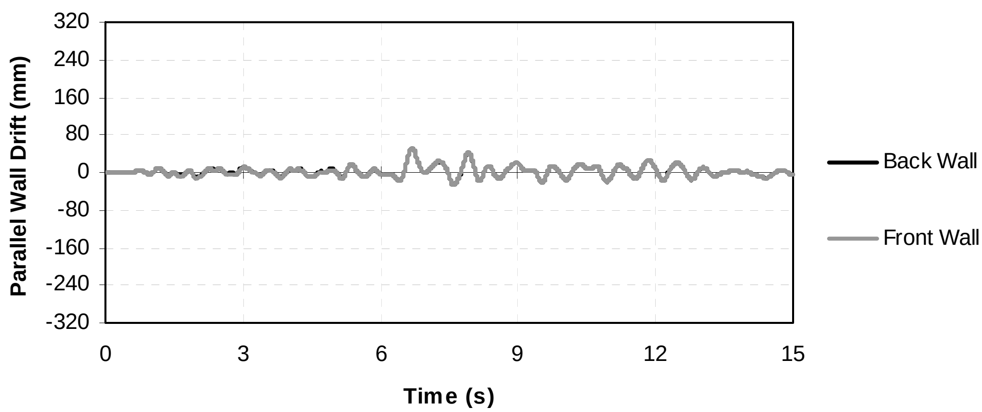

Figure C.86 Drifts of Parallel Walls (Case 5_1_100)

Table C.13 Peak Drifts of the Shear Walls (Group 5_1)

Front/Back Wall ratio (%)		Peak Perpendicular Wall Drift (mm)						Peak Parallel Wall Drift (mm)					
		Wall 1			Wall 2			Back Wall			Front Wall		
		+	-	MAX	+	-	MAX	+	-	MAX	+	-	MAX
Original	0	43.02	-46.14	**46.14**	50.14	-38.75	**50.14**	9.01	-12.67	**12.67**	306.99	-267.35	**306.99**
	25	8.81	-21.10	**21.10**	22.96	-8.97	**22.96**	12.86	-9.84	**12.86**	157.04	-65.40	**157.04**
	50	6.79	-14.68	**14.68**	14.82	-6.76	**14.82**	17.27	-13.05	**17.27**	115.08	-56.16	**115.08**
	75	2.48	-7.75	**7.75**	7.51	-2.74	**7.51**	30.61	-19.28	**30.61**	81.22	-35.01	**81.22**
	100	0.37	-0.18	**0.37**	0.14	-0.41	**0.41**	52.14	-26.43	**52.14**	52.45	-26.64	**52.45**
Redesigned	0	12.60	-16.88	**16.88**	16.99	-12.19	**16.99**	13.94	-14.66	**14.66**	149.92	-116.79	**149.92**
	25	8.91	-12.84	**12.84**	12.82	-8.92	**12.82**	17.15	-11.48	**17.15**	121.88	-83.05	**121.88**
	50	4.57	-9.78	**9.78**	9.85	-5.81	**9.85**	21.74	-17.75	**21.74**	96.33	-59.09	**96.33**
	75	2.56	-6.61	**6.61**	6.13	-2.34	**6.13**	32.43	-18.73	**32.43**	77.74	-35.33	**77.74**

Table C.14 Peak Imposed Loads and Load Ratios in the Shear Walls (Group 5_1)

Front/Back Wall ratio (%)		Peak Perpendicular Imposed Loads (kN)								Peak Parallel Imposed Loads (kN)							
		Wall 1				Wall 2				Back Wall				Front Wall			
		+	-	MAX	Load Ratio	+	-	MAX	Load Ratio	+	-	MAX	Load Ratio	+	-	MAX	Load Ratio
Original	0	57.02	-52.59	**57.02**	**2.58**	52.49	-57.12	**57.12**	**2.59**	60.89	-43.59	**60.89**	**1.38**	0.00	0.00	**0.00**	**N/A**
	25	46.44	-28.93	**46.44**	**2.10**	28.94	-46.62	**46.62**	**2.11**	40.53	-49.10	**49.10**	**1.39**	22.38	-24.38	**24.38**	**2.76**
	50	41.03	-28.22	**41.03**	**1.86**	28.23	-41.14	**41.14**	**1.86**	43.99	-57.21	**57.21**	**1.94**	36.42	-40.35	**40.35**	**2.74**
	75	24.34	-13.50	**24.34**	**1.10**	12.65	-25.14	**25.14**	**1.14**	49.55	-59.81	**59.81**	**2.37**	42.23	-51.08	**51.08**	**2.70**
	100	0.59	-1.70	**1.70**	**0.08**	1.72	-0.60	**1.72**	**0.08**	47.23	-57.61	**57.61**	**2.61**	47.45	-57.65	**57.65**	**2.61**
Redesigned	0	129.66	-117.49	**129.66**	**1.47**	117.21	-129.28	**129.28**	**1.46**	64.82	-69.63	**69.63**	**1.58**	0.00	0.00	**0.00**	**N/A**
	25	109.97	-66.98	**109.97**	**1.78**	66.97	-109.93	**109.93**	**1.78**	46.39	-59.80	**59.80**	**1.69**	22.21	-24.61	**24.61**	**2.79**
	50	62.32	-43.61	**62.32**	**1.41**	40.07	-61.75	**61.75**	**1.40**	52.37	-63.72	**63.72**	**2.16**	37.22	-39.85	**39.85**	**2.71**
	75	30.54	-17.64	**30.54**	**0.97**	17.93	-29.56	**29.56**	**0.93**	48.91	-60.78	**60.78**	**2.41**	41.94	-50.90	**50.90**	**2.69**

Group 5_2 (L:W=3:1, w/ parallel partition wall)

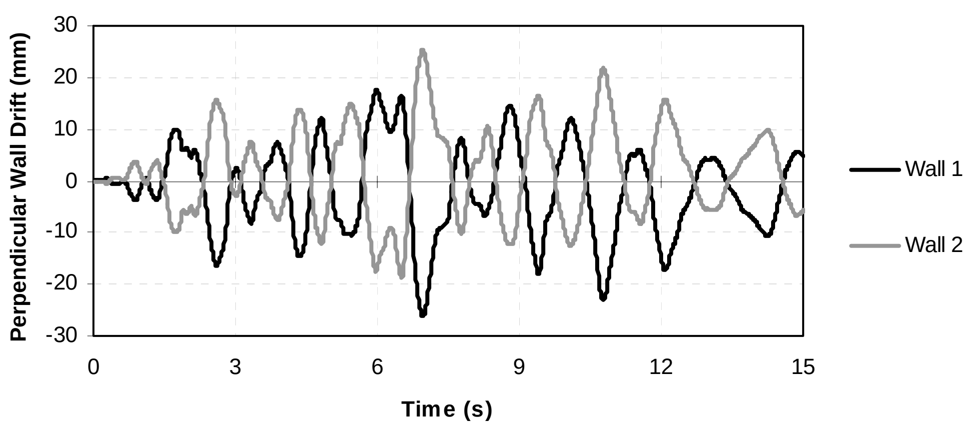

Figure C.87 Drifts of Perpendicular Walls (Case 5_2_0)

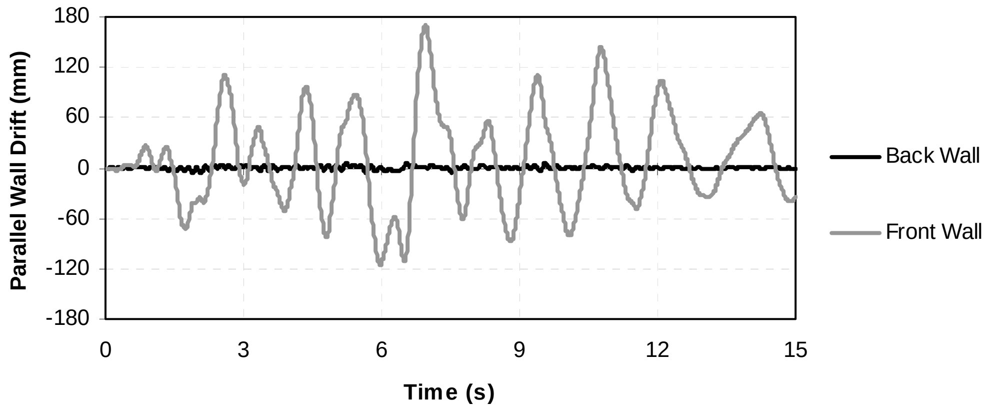

Figure C.88 Drifts of Parallel Walls (Case 5_2_0)

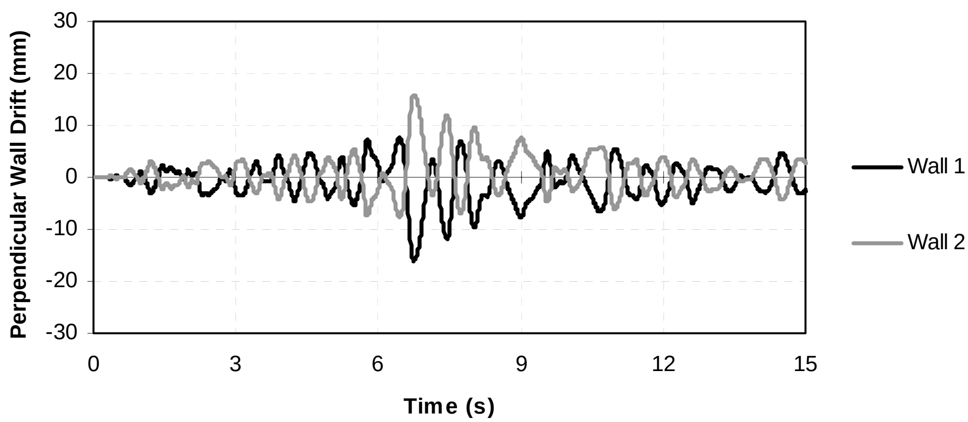

Figure C.89 Drifts of Perpendicular Walls (Case 5_2_25)

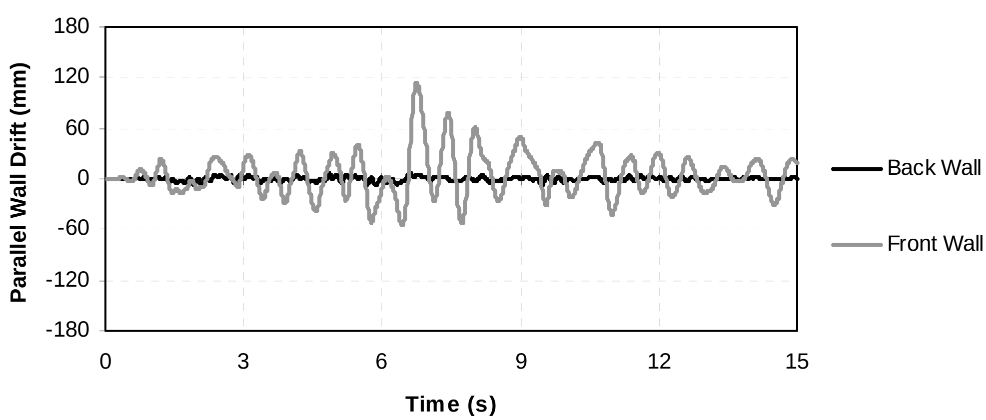

Figure C.90 Drifts of Parallel Walls (Case 5_2_25)

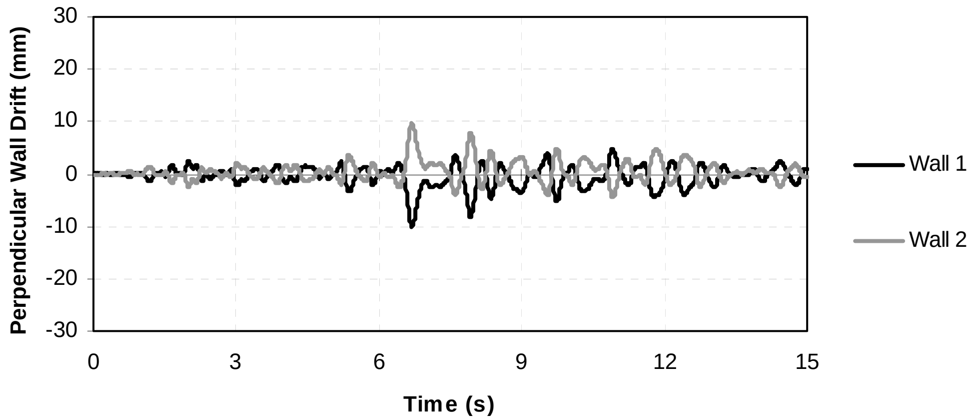

Figure C.91 Drifts of Perpendicular Walls (Case 5_2_50)

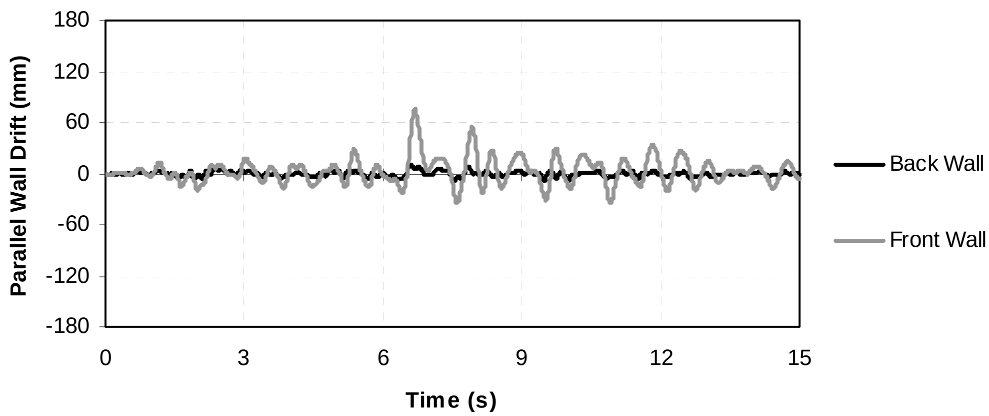

Figure C.92 Drifts of Parallel Walls (Case 5_2_50)

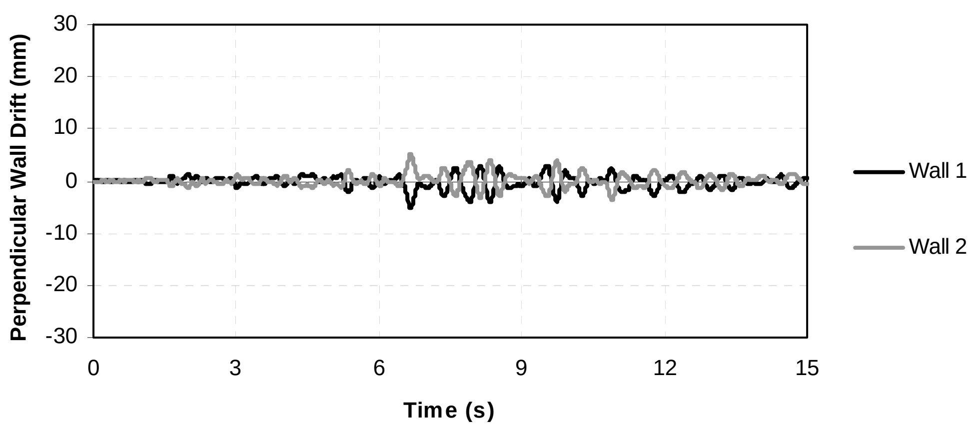

Figure C.93 Drifts of Perpendicular Walls (Case 5_2_75)

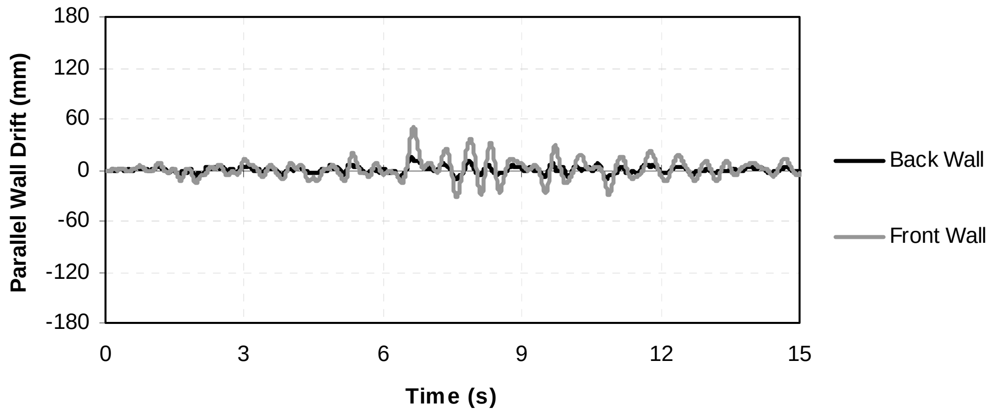

Figure C.94 Drifts of Parallel Walls (Case 5_2_75)

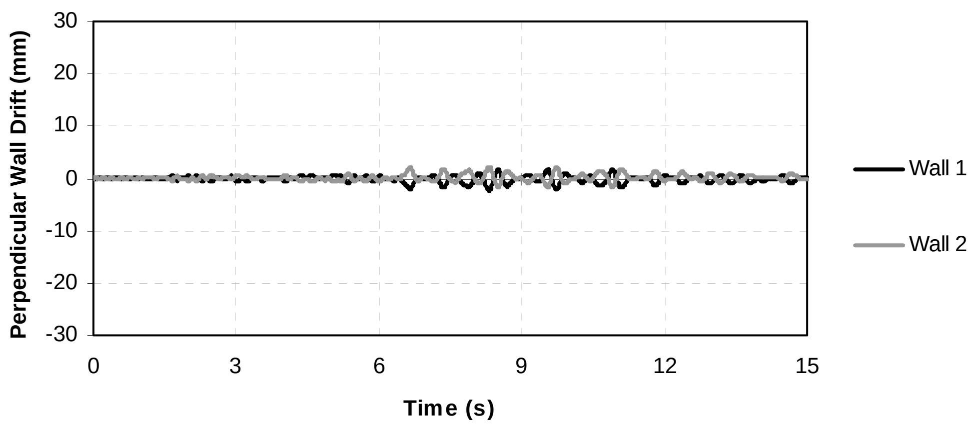

Figure C.95 Drifts of Perpendicular Walls (Case 5_2_100)

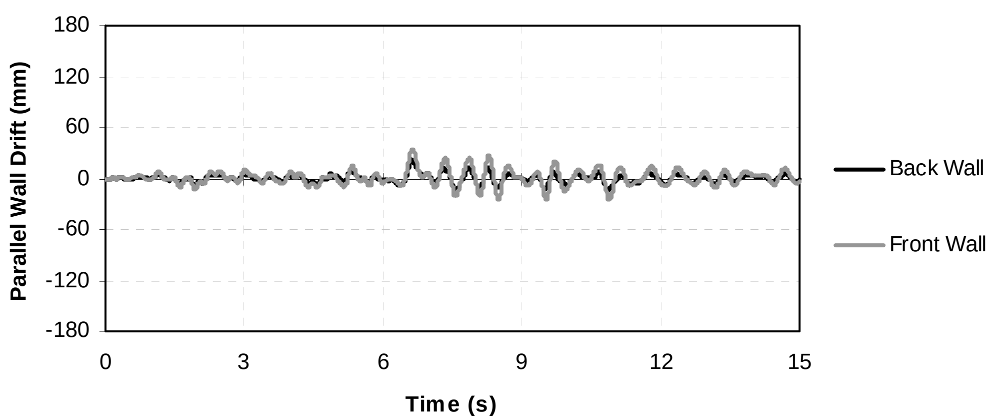

Figure C.96 Drifts of Parallel Walls (Case 5_2_100)

Table C.15 Peak Drifts of the Shear Walls (Group 5_2)

Front/Back Wall ratio (%)		Peak Perpendicular Wall Drift (mm)						Peak Parallel Wall Drift (mm)					
		Wall 1			Wall 2			Back Wall			Front Wall		
		+	-	MAX	+	-	MAX	+	-	MAX	+	-	MAX
Original	0	17.70	-26.16	**26.16**	25.28	-18.73	**25.28**	5.52	-6.87	**6.87**	169.46	-115.76	**169.46**
	25	7.58	-15.99	**15.99**	15.96	-7.61	**15.96**	7.31	-7.42	**7.42**	114.15	-55.47	**114.15**
	50	4.73	-10.07	**10.07**	9.83	-4.42	**9.83**	11.12	-8.18	**11.12**	75.45	-35.03	**75.45**
	75	2.97	-5.19	**5.19**	5.15	-3.62	**5.15**	15.82	-11.39	**15.82**	49.63	-30.80	**49.63**
	100	1.74	-2.32	**2.32**	2.23	-1.79	**2.23**	21.24	-14.89	**21.24**	35.25	-25.60	**35.25**

Table C.16 Peak Imposed Loads and Load Ratios in the Shear Walls (Group 5_2)

Front/Back Wall ratio (%)		Peak Perpendicular Imposed Loads (kN)								Peak Parallel Imposed Loads (kN)							
		Wall 1				Wall 2				Back Wall				Front Wall			
		+	-	MAX	Load Ratio	+	-	MAX	Load Ratio	+	-	MAX	Load Ratio	+	-	MAX	Load Ratio
Original	0	49.23	-39.14	**49.23**	**2.23**	42.24	-49.23	**49.23**	**2.23**	41.03	-33.27	**41.03**	**0.93**	0.00	0.00	**0.00**	**N/A**
	25	43.29	-27.49	**43.29**	**1.96**	27.47	-43.28	**43.28**	**1.96**	33.36	-41.58	**41.58**	**1.18**	20.90	-24.92	**24.92**	**2.82**
	50	29.94	-22.18	**29.94**	**1.36**	21.37	-30.29	**30.29**	**1.37**	35.46	-45.76	**45.76**	**1.55**	31.19	-39.74	**39.74**	**2.70**
	75	17.93	-13.42	**17.93**	**0.81**	13.98	-17.78	**17.78**	**0.81**	35.82	-47.21	**47.21**	**1.87**	42.81	-48.77	**48.77**	**2.58**
	100	8.46	-7.81	**8.46**	**0.38**	7.83	-8.50	**8.50**	**0.38**	37.47	-47.05	**47.05**	**2.13**	45.99	-53.00	**53.00**	**2.40**